

FRICTION STIR WELDING AND PROCESSING IX



Edited by
Yuri Hovanski • Rajiv Mishra
Yutaka Sato • Piyush Upadhyay • David Yan

TMS

 Springer

The Minerals, Metals & Materials Series

Yuri Hovanski · Rajiv Mishra · Yutaka Sato
Piyush Upadhyay · David Yan
Editors

Friction Stir Welding and Processing IX

TMS

 Springer

Editors

Yuri Hovanski
Brigham Young University
Provo, UT
USA

Piyush Upadhyay
Pacific Northwest National Laboratory
Richland, WA
USA

Rajiv Mishra
University of North Texas
Denton, TX
USA

David Yan
University of Wisconsin—Green Bay
Green Bay, WI
USA

Yutaka Sato
Tohoku University
Sendai
Japan

ISSN 2367-1181 ISSN 2367-1696 (electronic)
The Minerals, Metals & Materials Series
ISBN 978-3-319-52382-8 ISBN 978-3-319-52383-5 (eBook)
DOI 10.1007/978-3-319-52383-5
TMS owns copyright; Springer has full publishing rights

Library of Congress Control Number: 2016963430

© The Minerals, Metals & Materials Society 2017

This work is subject to copyright. All rights are reserved by the Publisher, whether the whole or part of the material is concerned, specifically the rights of translation, reprinting, reuse of illustrations, recitation, broadcasting, reproduction on microfilms or in any other physical way, and transmission or information storage and retrieval, electronic adaptation, computer software, or by similar or dissimilar methodology now known or hereafter developed.

The use of general descriptive names, registered names, trademarks, service marks, etc. in this publication does not imply, even in the absence of a specific statement, that such names are exempt from the relevant protective laws and regulations and therefore free for general use.

The publisher, the authors and the editors are safe to assume that the advice and information in this book are believed to be true and accurate at the date of publication. Neither the publisher nor the authors or the editors give a warranty, express or implied, with respect to the material contained herein or for any errors or omissions that may have been made. The publisher remains neutral with regard to jurisdictional claims in published maps and institutional affiliations.

Printed on acid-free paper

This Springer imprint is published by Springer Nature
The registered company is Springer International Publishing AG
The registered company address is: Gewerbestrasse 11, 6330 Cham, Switzerland

Preface

Friction stir welding (FSW) was invented by TWI (formerly The Welding Institute), Cambridge, UK and patented in 1991. The real growth in this field started in 1995. In the last 21 years, FSW has seen a very significant growth in both technology implementation and scientific exploration. This is the ninth symposium on Friction Stir Welding and Processing (FSW/P) held under the auspices of The Minerals, Metals & Materials Society (TMS). The interest and participation in this symposium is an indirect testimony of the growth of this field. This year, a total of 72 abstracts have been accepted, and presentations will require seven oral sessions with an additional poster session with 14 unique posters. The presentations cover all aspects of friction stir welding and processing from fundamentals to design and applications. Thirty manuscripts are published in the conference proceedings. The field has reached a critical new phase; this is the first symposium after the expiry of the TWI friction stir welding patent.

This symposium and the accompanying proceedings honors the contributions of Murray W. Mahoney to the field of FSW/P. As we reflect back, we see how instrumental he was to the scientific endeavor associated with FSW/P. He organized the first TWI International Symposium on Friction Stir Welding at the Rockwell Science Center, where at that time he was the manager of the structural materials group. Among many firsts, his first paper in *Metallurgical and Materials Transactions A* is a classic in the field. He was instrumental in starting the TMS Friction Stir Welding and Processing symposium in 2001. This has been a remarkable career full of contributions to the field of FSW/P.



Murray W. Mahoney, a champion of friction stir welding and processing

The organizers would like to thank the Shaping and Forming Committee of the TMS Materials Processing and Manufacturing Division for sponsoring this symposium.

Yuri Hovanski
Rajiv Mishra
Yutaka Sato
Piyush Upadhyay
David Yan

Contents

Part I High Temperature Applications I

Effect of Thermal Aging on the Corrosion and Mechanical Properties of Friction Stir Welded 250 Grade Maraging Steel	3
Bharat K. Jasthi, Todd Curtis, Christian A. Widener, Michael West and Brendan Kellogg	
Friction Stir Processing of 304L Stainless Steel for Crack Repair	13
M.P. Miles, C. Gunter, F. Liu and T.W. Nelson	
Influence of Underwater Operation on Friction Stir Welding of Medium Carbon Steel	23
Tomoko Miyamori, Yutaka Sato and Hiroyuki Kokawa	
Feasibility of Iridium Containing Nickel Based Superalloy Tool to Friction Stir Spot Welding of High Strength Steel	29
Kunihiro Tanaka, Tatsuya Nakazawa, Koichi Sakairi, Yutaka Sato, Hiroyuki Kokawa, Toshihiro Omori and Kiyohito Ishida	

Part II High Temperature Applications II

Development of Friction Stir Processing for Repair of Nuclear Dry Cask Storage System Canisters	39
Ken Ross, Ben Sutton, Glenn Grant, Gary Cannell, Greg Frederick and Robert Couch	
Performance of Tungsten-Based Alloy Tool Developed for Friction Stir Welding of Austenitic Stainless Steel	47
Yutaka Sato, Ayuri Tsuji, Tomohiro Takida, Akihiko Ikegaya, Akinori Shibata, Hiroshi Ishizuka, Hideki Moriguchi, Shinichi Susukida and Hiroyuki Kokawa	

Investigation of Process Parameters for Friction Stir Processing (FSP) of Ti-6Al-4V Alloy	53
Sandip Chougule, Digvijay Sheed, R.K.P. Singh, N. Prabhu, B.P. Kashyap and Kaushal Jha	
Part III Derivative Technologies	
Solid-State Joining of Thick-Section Dissimilar Materials Using a New Friction Stir Dovetailing (FSD) Process	67
Md. Reza-E-Rabby, Ken Ross, Scott Whalen, Yuri Hovanski and Martin McDonnell	
Joining Aerospace Aluminum 2024-T4 to Titanium by Friction Stir Extrusion	79
William Todd Evans, George E. Cook and Alvin M. Strauss	
Dissimilar Metal T-Joint of Aluminum and Steel Formed by Friction Stir Extrusion	91
Adam W. Jarrell, Alvin M. Strauss and George E. Cook	
Part IV Lightweight Applications	
Friction Stir Welding of Thick Section Aluminium Alloys—New Techniques	99
Jonathan Peter Martin	
Friction Stir Weld Lap Joint Properties in Aeronautic Aluminium Alloys	109
Egoitz Aldanondo, Ekaitz Arruti and Alberto Echeverria	
Friction Stir Welding of Thick Aluminium Welds—Challenges and Perspectives	119
Murshid Imam, Yufeng Sun, Hidetoshi Fujii, Yasuhiro Aoki, Ninshu MA, Seiichiro Tsutsumi and Hidekazu Murakawa	
High-Speed FSW Aluminum Alloy 7075 Microstructure and Corrosion Properties	125
Jingyi Zhang, Piyush Upadhyay, Yuri Hovanski and David P. Field	
Flow Features in Shoulder Zone During Scroll Tool Friction Stir Welding Thick 6061 Aluminum Plates	137
David Yan, Xiaoming Wang and Guy Littlefair	
Part V Dissimilar Applications	
Joining Dissimilar Material Using Friction Stir Scribe Technique	147
Piyush Upadhyay, Yuri Hovanski, Blair Carlson, Eric Boettcher, Robert Ruokolainen and Peter Busuttill	

Influence of Stir Flow on Joint Quality During Friction Stir Lap Al-to-Cu Welding	157
D. Parningotan, M. Tarrant, Z.W. Chen, A. Hilton and T. Pasang	
A Numerical Simulation for Dissimilar Aluminum Alloys Joined by Friction Stir Welding	167
Carter Hamilton, Mateusz Kopyściański, Aleksanda Węglowska, Stanisław Dymek and Adam Pietras	
Realization of Ultrasound Enhanced Friction Stir Welded Al/Mg- and Al/Steel-Joints: Process and Robustness, Mechanical and Corrosion Properties	179
Marco Thomä, Guntram Wagner, Benjamin Straß, Christian Conrad, Bernd Wolter, Sigrid Benfer and Wolfram Fürbeth	
Part VI Industrial Applications	
Friction Stir Welding Process Development of AA7075 for Hot Stamping Applications	197
François Nadeau and Nia R. Harrison	
A Novel Approach for Joining EN AW 1050 Stranded Wire and EN CW 004A Contact Elements by Friction Stir Spot Bonding	211
Anna Regensburg, René Schürer, Jan Ansgar Gerken, Helmut Steinberg and Jean Pierre Bergmann	
Joining Al 6061 to ZE41A Mg Alloy by Friction Stir Welding Using a Cold Spray Transition Joint	221
Todd R. Curtis, Victor K. Champagne III, Michael K. West, Reza Rokni and Christian A. Widener	
Refill Friction Stir Spot Joining for Aerospace Aluminum Alloys	237
Enkhsaikhan Boldsaikhan, Shintaro Fukada, Mitsuo Fujimoto, Kenichi Kamimuki, Hideki Okada, Brent Duncan, Phuonghanh Bui, Michael Yeshiambel, Brian Brown and Alan Handyside	
Part VII Control and Simulation	
Depth and Temperature Control During Friction Stir Welding of 5 cm Thick Copper Canisters	249
Lars Cederqvist, Olof Garpinger and Isak Nielsen	
Predicting Lap Shear Strength for Friction Stir Scribe Joining of Dissimilar Materials	261
Erin Iesulauro Barker, Piyush Upadhyay, Yuri Hovanski and Xin Sun	

Simultaneous Independent Control of Tool Axial Force and Temperature in Friction Stir Processing	269
Ken Ross, Glenn Grant, Jens Darsell and David Catalini	
Process Force Reduction During Robotic Friction Stir Welding of Aluminum Alloys with Reduced Tool Aspect Ratios	277
Anna Regensburg, Michael Grätzel, René Schürer, Michael Hasieber and Jean Pierre Bergmann	
Part VIII Poster Session	
Friction Stir Processing of 2507 Super Duplex Stainless Steel: Microstructure and Corrosion Behaviour	289
M.K. Mishra, G. Gunasekaran, A.G. Rao, B.P. Kashyap and N. Prabhu	
Effect of Heat Treatment on Friction-Stir-Processed Nanodispersed AA7075 and 2024 Al Alloys	297
I. El-Mahallawi, M.M.Z. Ahmed, A.A. Mahdy, A.M.M. Abdelmotagaly, W. Hoziefa and M. Refat	
Numerical Analysis of FSW Employing Discrete Element Method	311
Kenta Mitsufuji, Masahito Nambu and Fumikazu Miyasaka	
Author Index	321
Subject Index	323

About the Editors



Yuri Hovanski is Associate Professor of Manufacturing Engineering at Brigham Young University. He earned a B.S. Degree in Mechanical Engineering at Brigham Young University, and then completed his Masters and Doctorate degrees at Washington State University. He is a member of Tau Beta Pi Engineering Honors Society, and actively participates in AWS, ASM, and TMS serving as the Chair for the Shaping and Forming Committee, and the incoming secretary for the ASM Joining Committee. He has participated in friction stir related research for more than a decade as a senior research engineer at Pacific Northwest National Laboratory where he investigated weld formability, the influence of post-weld microstructure and texture on mechanical properties, and low-cost solutions for industrial implementation of friction stir technologies. Working with numerous industrial suppliers around the world, Dr. Hovanski has introduced cost-efficient solutions for thermal telemetry, new low-cost tool materials, high volume production techniques aluminum tailor-welded blanks, and is a co-inventor of friction stir scribe technology used for joining dissimilar materials. As an active researcher, Dr. Hovanski received the R&D 100 award in 2011, the DOE Vehicle Technologies Office Distinguished Achievement award in 2015, and a western region FLC award for technology transfer in 2015. He actively reviews friction stir related literature for numerous publications and has documented his work in more than 50 publications.



Rajiv Mishra is Distinguished Research Professor of Materials Science and Engineering in the Department of Materials Science and Engineering at the University of North Texas and Director of the Advanced Materials and Manufacturing Processes Institute (AMMPI). He is also the UNT Site Director of the NSF I/UCRC for Friction Stir Processing and a Fellow of ASM International. His highest degree is Ph.D. in Metallurgy from the University of Sheffield, UK (1988). He has received a number of awards which include the Firth Pre-doctoral Fellowship from the University of Sheffield, the Brunton Medal for the best Ph.D. dissertation in the School of Materials from the University of Sheffield in 1988, the Young Metallurgist Award from the Indian Institute of Metals in 1993, Associate of the Indian Academy of Sciences in 1993, and the Faculty Excellence Awards from the University of Missouri-Rolla in 2001, 2002, 2003, 2004, 2005, 2006, and 2007. He has authored or co-authored 290 papers in peer-reviewed journals and proceedings and is principal inventor of four U.S. patents. His current publication-based h-index is 44 and his papers have been cited more than 8900 times. He has co-edited a book on friction stir welding and processing, and edited or co-edited 13 TMS conference proceedings. He is founding editor of a short book series on Friction Stir Welding and Processing and co-author of seven short books. He is the past chair of the TMS Structural Materials Division (SMD) and served on the TMS Board of Directors as the SMD Director. He serves on the editorial board of *Materials Science and Engineering A* and *Science and Technology of Welding and Joining*.



Yutaka Sato is Associate Professor in the Department of Materials Processing at Tohoku University, Japan. He earned a Ph.D. in Materials Processing at Tohoku University (2001). His Ph.D. thesis was titled “Microstructural Study on Friction Stir Welds of Aluminum Alloys.” He participated in friction stir research of steels at Brigham Young University for a year in 2003. He is a member of Sub-commission III-B WG-B4 at IIW, which is a working group to build international standardization of friction stir spot welding. His work has focused on metallurgical studies of friction stir welding and processing for about 20 years. He has

obtained fundamental knowledge on development of grain structure, texture evolution, joining mechanism, behavior of oxide layer on surface, properties–microstructure relationship, and so on. Recently, he has centered on developing friction stir welding of steels and titanium alloys, and new tool materials. He has received a number of awards including the Kihara Award from the Association for Weld Joining Technology Promotion in 2008, Prof. Koichi Masubuchi Award from AWS in 2009, Murakami Young Researcher Award from the Japan Institute of Metals in 2010, Aoba Foundation Award in 2010, Honda Memorial Young Researcher Award in 2011, and The Japan Institute of Metals and Materials Meritorious Award in 2015. He has authored or co-authored more than 220 papers in peer-reviewed journals and proceedings.



Piyush Upadhyay is a scientist at Pacific Northwest National Laboratory. He obtained his Ph.D. in Mechanical Engineering from the University of South Carolina in 2012 in “Boundary Condition Effects on Friction Stir Welding of Aluminum alloys”. For the past 8 years he has been primarily involved in research and development of FSW and allied technologies to join similar and dissimilar materials. Currently, he leads efforts on friction stir welding of alloys in dissimilar thickness and dissimilar materials including combinations of aluminum, steels, and polymers for automotive application. He has received several awards and recognitions including Aid Nepal Scholarship for undergraduate study in 2001, Happy House Foundation research fellowship at Kathmandu University in 2007, and the DOE Energy Efficiency & Renewable Energy Recognition for Innovation in 2015. He has authored or co-authored more than 20 papers in peer-reviewed journals and proceedings and is actively involved in peer review of several technical journals and conference sub-committees.



David Yan is a tenure-track Assistant Professor of Mechanical Engineering at University of Wisconsin-Green Bay. He earned his Ph.D. degree in Mechanical Engineering from Deakin University, Melbourne, Australia (2014). Prior to that, he received his M.Phil. (1st Hons) and B.E. (Hons) degree in Mechanical Engineering from Auckland University of Technology, New Zealand. His current research focuses on friction stir deposition of metal powders. Previously, he centered his postgraduate research topics on the characterizations of material flow formation during scroll tool friction stir welding Al alloys and has gained more than ten years of research experience in friction stir processing and metal cutting. In addition, he actively partakes in ASME and The Minerals, Metals & Materials Society serving as a member in the Shaping and Forming Committee, Additive Manufacturing Committee, Titanium Committee, as well as symposium co-organizer. Dr. Yan reviews machining and solid-state joining related literature for several journals and has authored more than ten publications including books, journal papers, and peer-reviewed conference proceedings. He has received a number of awards including Research for Industry Awards (2008), Australian Postgraduate Awards (2010), and Grants-In-Aid of Research Award (2015).

Part I
High Temperature Applications I

Effect of Thermal Aging on the Corrosion and Mechanical Properties of Friction Stir Welded 250 Grade Maraging Steel

Bharat K. Jasthi, Todd Curtis, Christian A. Widener, Michael West and Brendan Kellogg

Abstract The main objective of this work is to investigate the microstructure and mechanical properties of friction stir welded 250 grade Maraging steel. Successful welds were made using W-25%Re-4%HfC pin tools in forge control mode at a rotational speed of $200 \text{ rev} \cdot \text{min}^{-1}$ and a travel speed of $50.8 \text{ mm} \cdot \text{s}^{-1}$. Retained austenite was identified in the weld nugget. Formation of retained austenite in the weld nugget is strongly influenced by the weld process parameters. The effects of post weld aging on the corrosion and mechanical properties of the welds were evaluated and compared to the parent material. Post-weld aging at $482 \text{ }^\circ\text{C}$ for 15 h resulted in peak hardness across the weld nugget.

Keywords Maraging steel • Friction stir welding • W-Re pin tool

Introduction

Maraging steels are a class of iron-nickel alloys designed for applications requiring high strength, excellent fracture toughness and good weldability. These steels are used for several critical applications such as the landing gears, rocket motor cases, powder shafts, submarine hulls and low temperature tooling [1]. The properties are achieved through age-hardening of a low carbon, iron-nickel alloy which results in precipitation of intermetallic phases such as Ni_3Mo and Ni_3Ti in the martensite matrix. The morphology and crystal structure of these intermetallic phases depends on the aging temperature and time. The unique ability of being weldable without any preheating in the aged condition makes these steels attractive for the fabrication of large structures [2, 3].

B.K. Jasthi · T. Curtis (✉) · C.A. Widener · M. West · B. Kellogg
Arbegas Materials Processing and Joining Laboratory, Department of Materials
and Metallurgical Engineering, South Dakota School of Mines and Technology,
501 E. St. Joseph St, Rapid City, SD 57701, USA
e-mail: Todd.Curtis@sdsmt.edu

© The Minerals, Metals & Materials Society 2017
Y. Hovanski et al. (eds.), *Friction Stir Welding and Processing IX*,
The Minerals, Metals & Materials Series, DOI 10.1007/978-3-319-52383-5_1

Some studies had demonstrated that the martensite in the maraging steel could revert to austenite during the aging process [4–6]. A small fraction of this metastable martensite can transform into ferrite and austenite if enough time and temperature are given during the aging treatment. Since the nickel content of these alloys is very high (18 wt%), the austenite formed does not transform back to martensite on cooling to room temperature and thus results in incomplete precipitation hardening after aging treatment [7].

The maraging steels have demonstrated excellent weldability using a variety of fusion welding techniques including laser, electron beam, plasma and gas tungsten arc welding [8–11]. Most of the fusion welding techniques showed excellent joint efficiencies (up to 90%), but the toughness in the fusion zone is considerably lower than that of the parent material. The decrease in the toughness in the fusion welds can be attributed to the presence of reverted austenite, which is formed due to microsegregation of alloying elements in the interdendritic regions of the fusion welds [1].

As a solid state joining process, friction stir welding (FSW) can avoid the problems associated with segregation of alloying elements and austenite reversion. Absence of austenite reversion can also improve corrosion and precipitation hardening behavior during the subsequent aging process. There is only one report concerning the FSW application to 250 grade maraging (Mar 250) steel by Meshram et al. [12] and the results showed an improvement in toughness of the friction stir welds over the base material. However, the effects of thermal aging on the corrosion and hardening behavior were not systematically studied. Therefore, the main objective of this work is to investigate the effect of thermal aging on the corrosion and hardening response of friction stir welded 250 grade maraging steel.

Experimental

High-temperature pin tools made of W-25%Re-4%HfC (W-Re) were used to make friction stir welds on 6.35 mm thick Mar 250 steel plates. These W-Re pin tools have a convex shoulder and tapered pin design. Two pin tools with different pin lengths (4 mm and 5.8 mm) were used for the welding experiments as shown in Fig. 1. Initial developmental welds were made with 4 mm pin tool and production welds were made with 5.8 mm pin tool. All the welds were made using an *i*-stir-10[®] FSW system equipped with a Megastir[®] water-cooled, high-temperature pin tool (HTPT) adapter. This multi-axis machine is fitted with an AdAPT[®] (adjustable and adaptable pin tool) head that has the advantage of welding complex shapes. The tools and the Mar 250 plates were shielded with Ar gas during welding to prevent oxidation. All the welds were made in force control mode with varying forge force. The feed rate ranged from 50.8 to 101.6 mm · s⁻¹ and the spindle speed

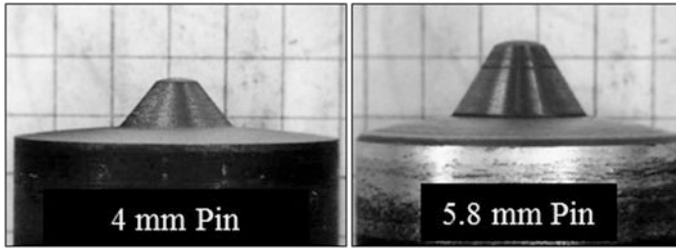


Fig. 1 W-Re-HfC pin tools

ranged from 200 to 400 $\text{rev} \cdot \text{min}^{-1}$. Forge force was varied between 15.5 and 28.9 kN. The final parameters chosen were 200 $\text{rev} \cdot \text{min}^{-1}$, 50.8 $\text{mm} \cdot \text{s}^{-1}$, 28.9 kN forge force, and 1° lead angle with the 5.8 mm pin tool.

The parent material received in the solution annealed condition. Therefore, friction stir welding was performed in this condition. After welding, the plates were sectioned perpendicular to the welding direction and prepared for metallographic examination using standard metallographic polishing procedures. Aging treatment was performed on the parent and welded specimens with the objective of determining the corrosion behavior as a function of aging temperature and time. Three aging treatments H800 (426 °C), H900 (482 °C) and H1000 (538 °C) were performed for 1, 5 and 15 hours. The polished specimens were etched with modified Fry's reagent (50 ml HCl, 25 ml HNO₃, 1 g CuCl₂, and 150 ml H₂O) to reveal the macro and microstructures. The specimens were examined using a metallurgical microscope. Vickers microhardness measurements were made across the weld nugget across the polished metallographic weld cross sections. The measurements were made at a load of 500 g and a loading time of 20 s in accordance with ASTM E92-82.

Electrochemical corrosion potential measurements were conducted in 1% NaCl solution using a potentiostat (GAMRY 600) and a Flat cell (K0235). The experimental setup is shown in Fig. 2. A platinum counter electrode and a silver chloride (Ag-AgCl/KCl-Saturated) reference electrode were used for the electrochemical measurements. The reference electrode potential is +197 mV relative to the normal hydrogen electrode (NHE). The as-welded and heat treated corrosion specimens were prepared by polishing with different SiC abrasive papers (wet grinding-240 grit and wet polishing-600 grit). This polishing was intended to remove any oxide layer on the surface and to minimize the surface roughness effects on the results. The standard specimen exposed area is 1 cm². However in this investigation, the specimen exposed area was restricted to 0.18 cm² by placing 2.1 mm thick Teflon disc between the specimen and the standard Teflon gasket as shown in Fig. 2. By limiting the exposed area of the specimen, the corrosion potentials could be precisely measured from the weld nugget region as shown in Fig. 2.

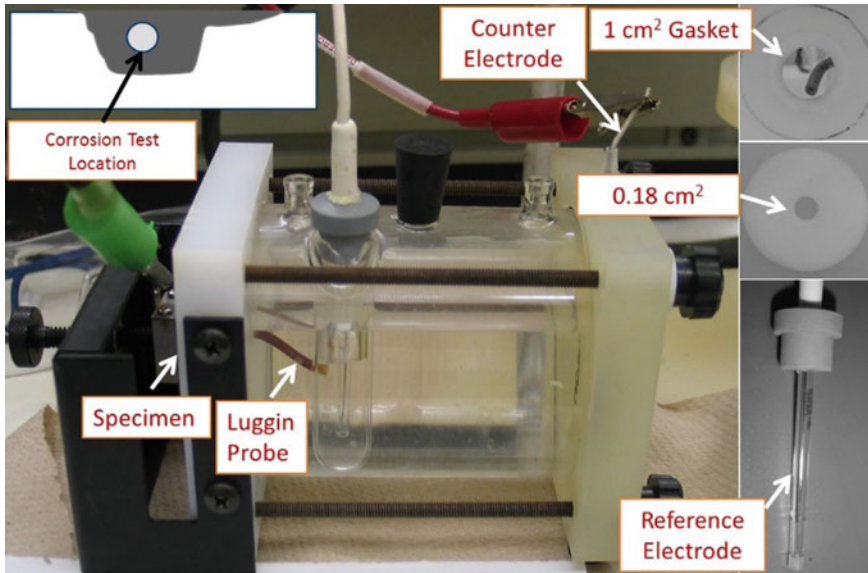


Fig. 2 Electrochemical testing setup

Results and Discussion

The W-25%Re-4%HfC pin tools used for this investigation produced good quality welds. Successful defect free welds were produced with 5.8 mm pin tool when processed at $200 \text{ rev} \cdot \text{min}^{-1}$, $50.8 \text{ mm} \cdot \text{s}^{-1}$, 28.9 kN forge force. However, the welds made with 4 mm pin tool resulted in a small wormhole defects as shown in Fig. 3. Increasing the applied forge force during welding or decreasing the weld travel speed can eliminate these wormhole defects in a friction stir weld. Previous investigation on friction stir welding of maraging steels by Meshram et al. [12] reported significant wear on WC, W-Fe and W-Mo pin tools. However, no significant wear was identified in this investigation with both 4 mm and 5.8 mm pin tools. The improved wear performance of these tools can be attributed to the presence of HfC in the pin tools. The addition of hafnium carbide along with

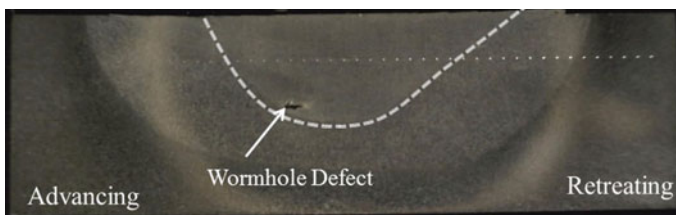


Fig. 3 Macrograph showing the cross-section of Mar 250 friction stir weld

rhenum to tungsten is known to improve ductility at room temperature and strength at high temperature.

Tool life is a very important consideration for friction stir welding of any high melting temperature materials. An ideal pin tool should have high toughness, good strength, excellent wear resistance, and be chemically inert at welding temperatures. Pin tools made of polycrystalline cubic boron nitride (PCBN) have excellent wear resistance and appear to meet all the requirements of a high temperature pin tools. However, premature cracking and the cost of the pin tool limits its use. W-based tools on the other hand have good fracture toughness, but these tools can experience severe wear and degradation during welding of high temperature materials. The addition of HfC to W-Re appears to improve the wear resistance of W-Re pin tools [13]. The tool life can also be extended by lowering the process forces during welding. W-Re tools in general have lower process forces during welding compared to PCBN tools. A comparative study of PCBN and W-Re tools performed by Jasthi et al. [14], on another iron-nickel alloy (Fe-36%Ni) showed significant lower process forces for W-Re tools when compared with PCBN pin tools. The lower forces observed for W-Re tools is believed to be the consequence of its lower thermal conductivity, which translates to lower heat loss through the tool and higher weld temperatures [14].

Microstructures of the solution annealed (parent) and friction stir welded material are shown in Fig. 4. The solution annealed parent had a lath martensite microstructure with prior austenite grain size (martensite packet size) of $\sim 35 \mu\text{m}$. The weld microstructure looks similar to the parent material with a fine martensite structure and with an average grain size of $\sim 9 \mu\text{m}$. Reverted austenite with average grain size of $\sim 5 \mu\text{m}$ was observed in specific regions of the weld nugget as shown in Fig. 5. It is interesting to note that reverted austenite was only observed on the advancing side near the weld-heat affected zone (HAZ) interface and also in the flow arm region (beneath the shoulder) of the weld nugget, where the temperatures are believed to be high compared to the other parts of the weld nugget. The average hardness in the weld nugget in the as-welded condition is $\sim 316 \text{HV}$, whereas the average hardness of the reverted austenite formed in the weld nugget is $\sim 220 \text{HV}$.

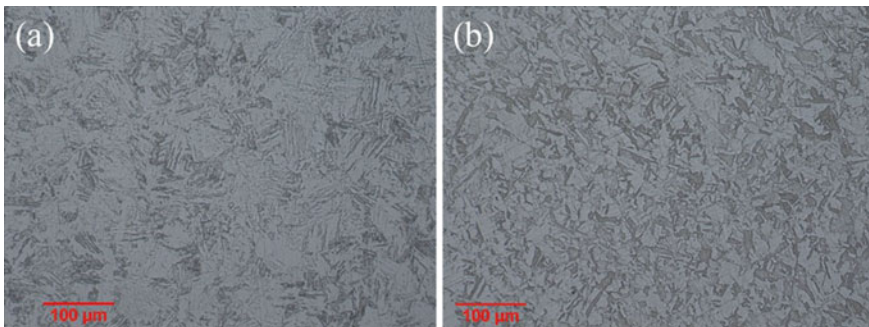


Fig. 4 Micrographs of Mar 250 steel showing: **a** solution annealed; **b** FSW Nugget

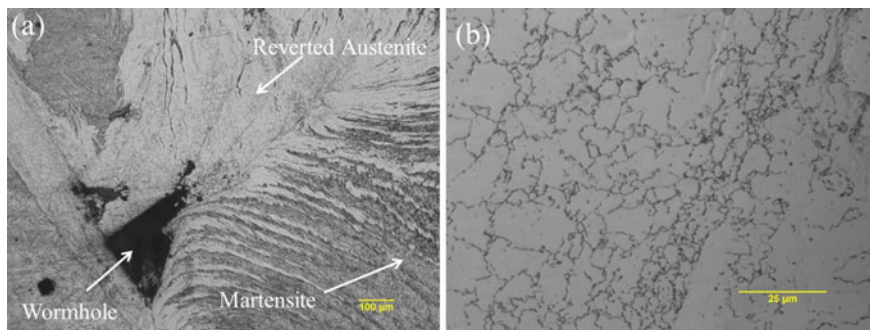


Fig. 5 Micrographs of Mar 250 weld nugget showing: **a** austenite reversion (white regions) on the advancing side of the weld nugget; **b** recrystallized reverted austenite

Nickel is an austenite stabilizer and the presence of nickel in higher proportions (18 wt%) in the alloy can stabilize the austenite phase during welding and does not transform back to martensite on cooling to room temperature. The presence of reverted austenite in the weld nugget will result in incomplete precipitation hardening after the subsequent aging process. It is also interesting to note that reverted austenite was only observed for the welds that were made with hotter process parameters (higher forge loads). No reverted austenite was observed for the welds made with colder process parameters (lower forge forces), which suggests that formation of reverted austenite in the weld nugget can be controlled with the friction stir welding process variables.

Microhardness evaluations were performed across the weld nugget in the as-welded condition as shown in Fig. 6. The average hardness of the parent material in the solution annealed condition is ~ 310 HV, whereas the average hardness of the weld nugget is same as the parent material which is ~ 316 HV. The hardness in the HAZ had increased to ~ 420 HV on both advancing and retreating sides of the weld nugget. The increase in hardness is most likely caused by the aging of the martensite structure of the parent material which is in the solution annealed condition before welding.

The average microhardness in the weld nugget as a function of aging temperature is shown in Fig. 7. The average hardness increased with aging temperature and time for specimens aged at 426 °C (H800) and 482 °C (H900). Whereas for the specimens aged at 538 °C (H1000), the hardness increased initially with aging time, but decreased eventually when specimen was aged for 15 h. The decrease in the average nugget hardness for the specimens aged at 538 °C for 15 h is most likely caused by the over aged condition, which can lead to coarsening of precipitates. Peak hardness of 575 HV in the weld nugget was achieved when aging was performed at 482 °C for 15 h.

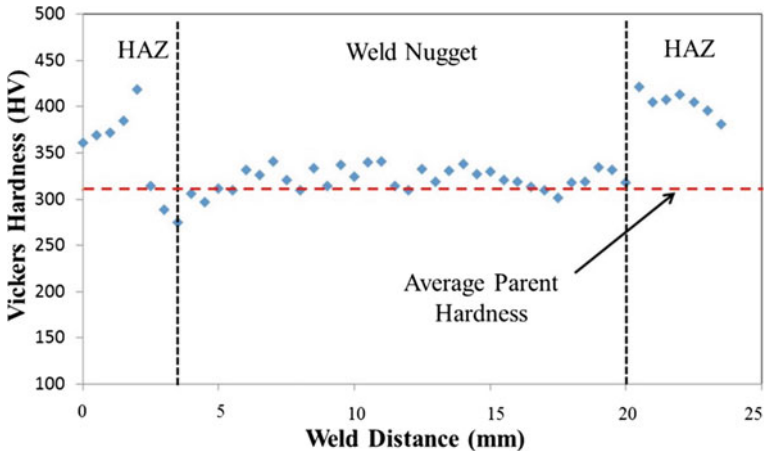


Fig. 6 Microhardness across the weld nugget in the as-welded condition

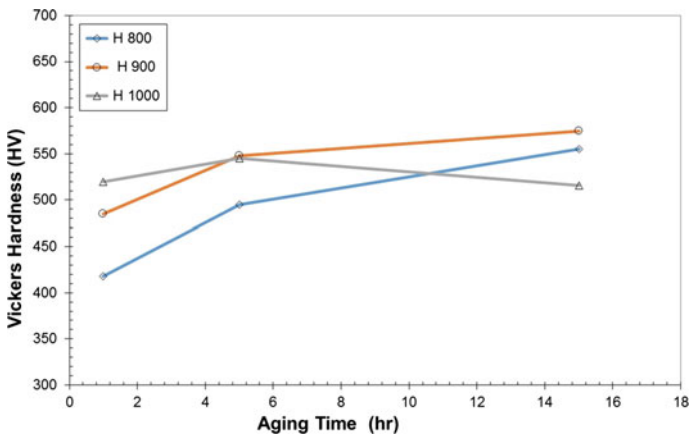


Fig. 7 Microhardness in the weld nugget as function of aging temperature and time

Electrochemical corrosion potentials were measured for both parent and friction stir welded Mar 250 specimens. The corrosion potentials of the post weld aged specimens were also measured and compared with the as received parent material as shown in Fig. 8. This figure shows that the as-welded specimens showed a more anodic corrosion potentials when compared to the parent material which is in the solution annealed condition. The corrosion potentials of the aged specimens (426 °C and 538 °C) for 15 h were much more anodic to both parent and as-welded conditions. A complete list of electrochemical potentials for as-received and aged specimens are tabulated in Table 1. The results show the corrosion potentials decreased with increasing aging temperature and time.

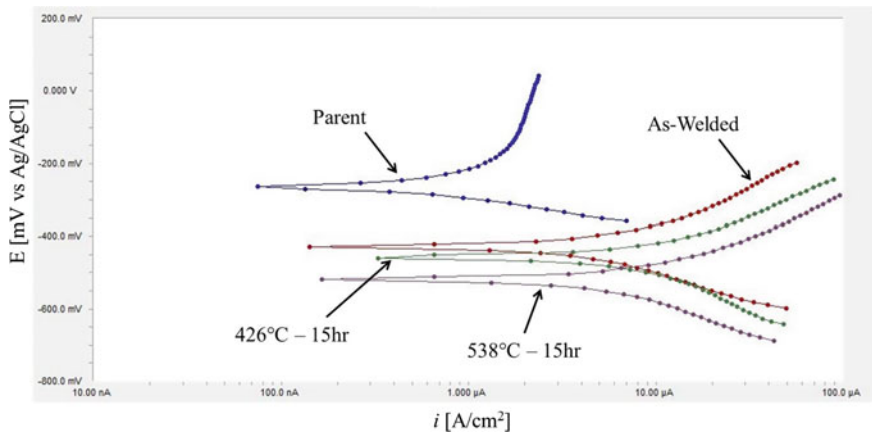


Fig. 8 Tafel scan comparisons for parent, as-welded and aged specimens

Table 1 Electrochemical potentials for Mar 250 specimens

Sample	Corrosion potential (mV)
Parent (solution annealed)	-0.266
As-welded (FSW)	-0.429
FSW + H800-1 h	-0.46
FSW + H800-15 h	-0.457
FSW + H1000-1 h	-0.486
FSW + H1000-15 h	-0.520

Conclusions

The effect of Post-weld artificial aging on the corrosion resistance and mechanical properties of friction stir welded grade 250 maraging was investigated. Successful welds were made using W-25%Re-4%HfC pin tools in forge control mode at a rotational speed of $200 \text{ rev} \cdot \text{min}^{-1}$ and a travel speed of $50.8 \text{ mm} \cdot \text{s}^{-1}$. Formation of retained austenite in the weld nugget is strongly influenced by the weld process parameters. Cold process parameters eliminated the formation of reverted austenite in the weld nugget. Average hardness in the weld nugget increased with aging temperature and time. Similarly, the corrosion potentials for the aged specimens decreased with aging temperature and time.

Acknowledgements The authors gratefully acknowledge the financial support provided by the National Science Foundation under the contract number 157074. The authors also acknowledge the graduate students (Sushma Karanam, Lukmon Aminu, Reeha Budatla, and Oladimeji Oladepo) for their help with the specimen preparation.

References

1. Shamantha C, Narayanan R, Iyer K, Radhakrishnan V, Seshadri S, Sundararajan S, Sundaresan S (2000) Microstructural changes during welding and subsequent heat treatment of 18Ni (250-grade) maraging steel. *Mater Sci Eng, A* 287(1):43–51
2. Blauel J, Smith H, Schulze G (1974) Fracture toughness study of a grade 300 maraging steel weld joint. *Weld J Res Suppl* 53:211
3. Rajkumar V, Arivazhagan N, Ramkumar KD (2014) Studies on welding of maraging steels. *Procedia Eng* 75:83–87
4. Höring S, Abou-Ras D, Wanderka N, Leitner H, Clemens H, Banhart J (2009) Characterization of reverted austenite during prolonged ageing of maraging steel CORRAX. *Steel Res Int* 80(1):84–88
5. Schnitzer R, Radis R, Nöhner M, Schober M, Hochfellner R, Zinner S, Povoden-Karadeniz E, Kozeschnik E, Leitner H (2010) Reverted austenite in PH 13–8 Mo maraging steels. *Mater Chem Phys* 122(1):138–145
6. Viswanathan U, Dey G, Sethumadhavan V (2005) Effects of austenite reversion during overageing on the mechanical properties of 18 Ni (350) maraging steel. *Mater Sci Eng, A* 398(1):367–372
7. Fanton L, Abdalla AJ, Lima M (2014) Heat treatment and ybfiber laser welding of a maraging steel. *Weld J* 93:362–368
8. Tariq F, Baloch RA, Ahmed B, Naz N (2010) Investigation into microstructures of maraging steel 250 weldments and effect of post-weld heat treatments. *J Mater Eng Perform* 19(2): 264–273
9. Ramana PV, Reddy GM, Mohandas T (2013) Microstructure, hardness and residual stress distribution in maraging steel gas tungsten arc weldments. *Sci Technol Weld Joining*
10. Quintino L, Costa A, Miranda R, Yapp D, Kumar V, Kong C (2007) Welding with high power fiber lasers—a preliminary study. *Mater Des* 28(4):1231–1237
11. Sakai P, Lima M, Fanton L, Gomes C, Lombardo S, Silva D, Abdalla A (2015) Comparison of mechanical and microstructural characteristics in maraging 300 steel welded by three different processes: LASER PLASMA and TIG. *Procedia Eng* 114:291–297
12. Meshram SD, Reddy GM, Pandey S (2013) Friction stir welding of maraging steel (Grade-250). *Mater Des* 49:58–64
13. Thompson BT (2010) Tool degradation characterization in the friction stir welding of hard metals. The Ohio State University
14. Jasthi BK, Arbegast WJ, Howard SM (2009) Thermal expansion coefficient and mechanical properties of friction stir welded invar (Fe-36% Ni). *J Mater Eng Perform* 18(7):925–934

Friction Stir Processing of 304L Stainless Steel for Crack Repair

M.P. Miles, C. Gunter, F. Liu and T.W. Nelson

Abstract Friction stir processing (FSP) was investigated as a method for repairing cracks in 304L stainless steel. Healing feasibility was demonstrated by processing a tapered crack and a series of randomly sequenced cracks with different widths. It was possible to heal a crack that begins narrow and then progressively widens, but processing a crack that starts too wide created voids that could not be closed up. Tension and hardness testing of 304L plates processed under different conditions were performed in order to assess the effect of processing on weld and heat affected zone properties. Corrosion testing was also carried out, in order to evaluate the effect of FSP on potential sensitization of the stir zone. After 1000 h of testing in saline solution at room temperature it was found that no corrosion products formed on the base material controls or on any of the friction stir processed specimens.

Keywords 304L stainless steel • Friction stir processing • Crack healing

Introduction

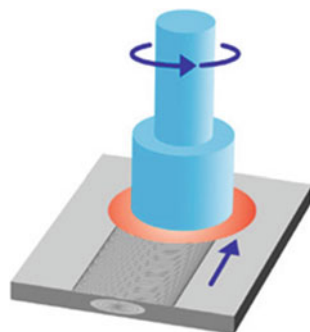
The nuclear industry is facing challenges in repair or replacement of stainless steel reactor components, which have been exposed to neutron irradiation. Irradiated stainless steel contains helium, which forms primarily by n/α reactions with alloying elements nickel and boron [1–6]. Helium gas is insoluble in metals, so it precipitates and forms bubbles (at the nanoscale), nucleating at dislocations, point defects, and grain boundaries [4]. When conventional fusion welding is used for weld repair, the high temperatures and thermal stresses inherent in the process

M.P. Miles (✉) · C. Gunter
Manufacturing Engineering Technology, Provo, USA
e-mail: mmiles@byu.edu

F. Liu · T.W. Nelson
Mechanical Engineering, Provo, USA

© The Minerals, Metals & Materials Society 2017
Y. Hovanski et al. (eds.), *Friction Stir Welding and Processing IX*,
The Minerals, Metals & Materials Series, DOI 10.1007/978-3-319-52383-5_2

Fig. 1 FSP could be used to repair a crack by processing an existing arc weld



enhance the growth of helium bubbles, causing intergranular cracking in the heat-affected zone (HAZ) [6–8].

Repair of nuclear components encompasses both the replacement of a failed component, in which case a new component must be joined to existing structures, and the in situ repair of arc welds that have developed stress corrosion cracks in service [2, 9, 10]. In both cases the issue of helium embrittlement, accelerated by the temperatures and stresses of fusion welding, presents a serious difficulty that must be overcome. While low heat input laser welding can be a partial solution to the problem [7], reactors with 30–40 years of service may have irradiated components which cannot be repaired by any of the conventional methods [11]. It is anticipated that many nuclear reactors will function for up to 80 years [12], so the reparability of irradiated stainless steel is of great importance to this industry.

Friction stir processing (FSP) is similar to friction stir welding (FSW), except that its purpose is not to join parts together, but to modify material microstructures and properties. The repair of a stress corrosion crack in an existing weld could be done by passing a tool along an existing weld or HAZ and “healing” the crack. The process of FSP is shown in Fig. 1.

Much of the prior work done in FSW can be applied to FSP. Both FSW and FSP have been studied extensively for their ability to create favorable properties in metal alloys [13–19], most of which have been aluminum alloys. While we have not found research literature on the use of FSP to “heal”, or repair, stress corrosion cracks in existing welds, one study by Sterling demonstrated that FSP can be used to process over existing arc welds in austenitic stainless steel, to enhance the mechanical properties of the weld [20]. For stress corrosion crack repair of irradiated stainless steel, lower peak temperatures would favor the use of FSP over fusion welding processes like GTAW, because the helium bubbles present in the material would have a lower driving force to diffuse to grain boundaries in the HAZ. But if FSP is a potential solution for weld repair of irradiated stainless steel, there remains the potential challenge of sigma phase and chromium carbide formation, which have been reported in friction stir welded 304L stainless steel along the advancing side of the stir zone [21]. Although others have reported preferential etching along this same region of the stir zone, they also report large variability, depending on the welding conditions [20, 22]. Sigma and chromium carbide phases

are well known to reduce the corrosion resistance of austenitic stainless steel [21–23], and need to be suppressed if FSP is to be employed for weld repair.

Experimental Procedures

FSP experiments were performed on 12 mm thick 304L stainless steel using a tool speed of 250 rpm and a feed rate of 100 mm/min. The tool, provided by Megastir Technologies, was composed of 70% PCBN and 30% W-Re, with a pin length of 8 mm and a convex 25 mm diameter shoulder, as shown in Fig. 2. The pin was threaded and the shoulder had scrolls, in order to promote the stirring of material.

The microstructure in the initial plate exhibited an average grain size of about 40 μm , but some grains were as small as 5 μm , as measured by electron backscatter diffraction (EBSD), shown in Fig. 3.

Fig. 2 Friction stir processing tool (70% PCBN/30% W-Re), with an 8 mm long conical pin and 25 mm diameter convex shoulder



Fig. 3 304L stainless steel microstructure for as-received plate

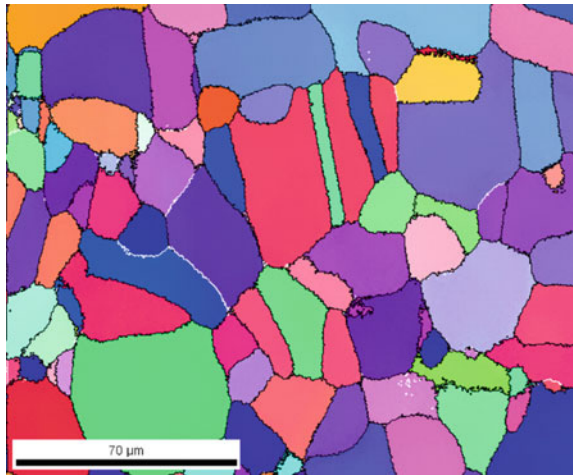


Table 1 Composition of 304L stainless steel (wt%)

C	Mn	P	S	Si	Cr	Ni	N	Fe
0.08	2.00	0.045	0.030	0.75	18–20	8–12	0.10	Balance

The composition of the plates that were processed is shown in Table 1.

Experiments were done in order to assess both the crack healing capability of FSP and to measure the mechanical properties of specimens that had been processed using a variety of different tool feeds and speeds.

Results and Discussion

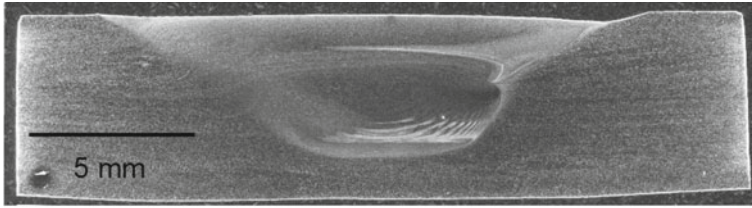
Two different crack healing experiments were carried out. The first one employed a plate with a variety of different machined cracks, randomly placed along a straight line in a 304L plate. Each crack was 30 mm long and went through the full thickness of the plate. The crack widths, in sequence, were: 3 mm, 0.5 mm, 2.0 mm, 2.5 mm, 1.5 mm, 1.0 mm, 0.33 mm. With random ordering, the 3 mm crack was the first one in the sequence, which proved to be too wide to heal. Therefore, the first experiment didn't provide much information about crack healing feasibility using FSP. A second experiment was performed on a tapered crack, where the tool started processing at the narrow end and finished processing at the wide end (0 mm at the beginning and 2 mm at the end). The simulated crack was cut by wire EDM and was 400 mm long.

Figure 4 shows a sequence of cross sections spaced along the length of the crack. The oxide layer at the joint interface is clearly seen in each cross section. The stir zone shows adequate healing of the crack throughout the sequence; however, as the crack approaches a width of 2 mm, there is less material to be consolidated and a depression develops on the top of the plate, on the advancing side (right side) of the stir zone.

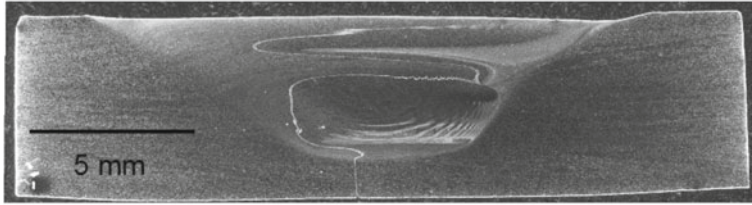
From these results it appears that cracks in 304L can be healed by FSP, up to about 2 mm in width, using the tool design shown in Fig. 2 and parameters of 250 rpm—100 mm/min. Further work is needed to characterize properties of specimens where crack healing has taken place by FSP.

In addition to crack healing, some bead-on-plate FSP experiments were performed at different feeds and speeds. Mechanical properties and hardness of the stir zone were assessed for each set of parameters, and grain sizes were measured on the advancing side (AS), center (C), and retreating side (RS) of the stir zone.

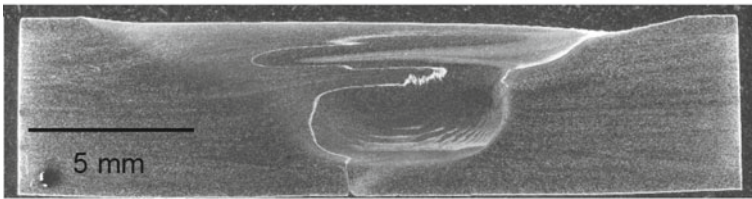
Cross sections of the plates processed at different feeds and speeds are shown in Fig. 5. Most of the parameters resulted in a consolidated stir zone except for the plates processed at 125 rpm—150 mm/min (easily visible) and 175 rpm—150 mm/min (much smaller voids), both of which had voids in the lower portion of the advancing side nugget (Fig. 5b).



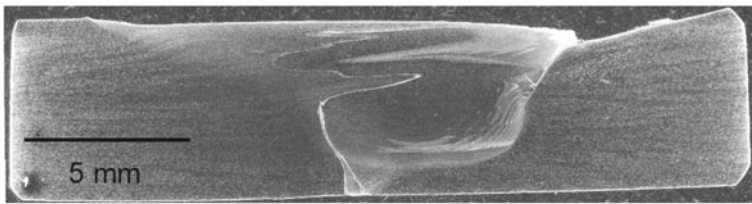
(a)



(b)



(c)



(d)

Fig. 4 Cross sections of tapered crack healing experiment. **a** base material just before the crack, **b** 45 mm from beginning of tapered crack, **c** 205 mm from beginning of crack, **d** 385 mm from beginning of crack

Transverse tensile testing (weld transverse to major strain axis) was carried out, using three specimens for each set of parameters. A summary of the testing is shown in Table 2, along with the power measured at the spindle of the machine during the FSP experiments.

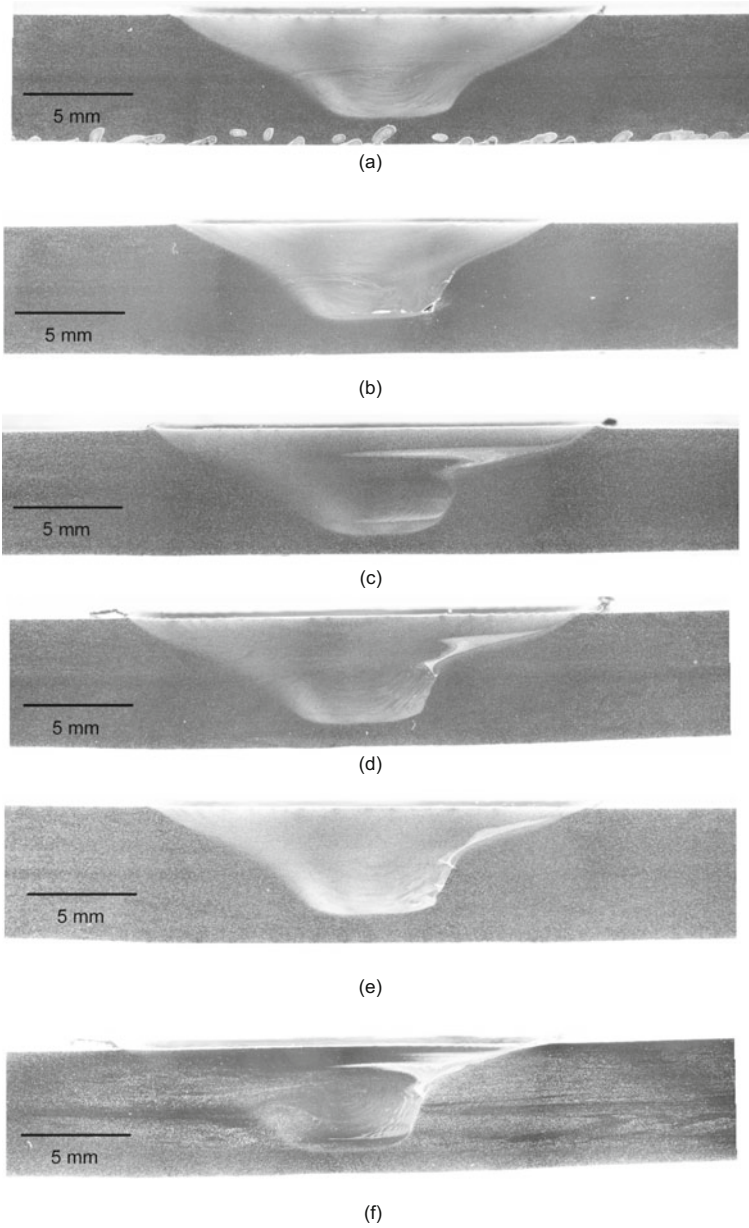
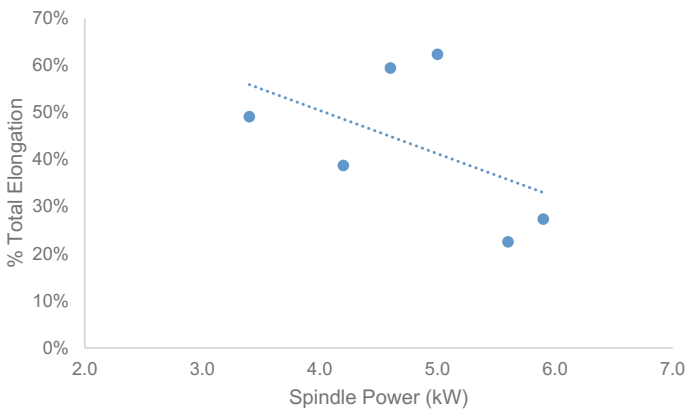


Fig. 5 Cross sections of bead-on-plate stir zones for different parameters. **a** 80 rpm—50 mm/min, **b** 125 rpm—150 mm/min, **c** 150 rpm—50 mm/min, **d** 150 rpm—100 mm/min, **e** 175 rpm—150 mm/min, **f** 250 rpm—100 mm/min

Table 2 Mechanical properties for transverse tensile specimens (average of 3 specimens)

FSP parameters	FSP power (kW)	% Total elongation	Ultimate tensile strength (MPa)
Base metal	–	76	622
80 rpm—50 mm/min	3.3	49	696
125 rpm—150 mm/min	4.8	39	683
150 rpm—50 mm/min	4.9	59	684
150 rpm—100 mm/min	6.3	62	429
175 rpm—150 mm/min	4.8	22	675
250 rpm—100 mm/min	6.3	27	605

**Fig. 6** Total elongation in transverse tensile test as a function of FSP power

From an elongation viewpoint, the worst performance corresponded to the parameters that generated the greatest power at the welding spindle. Although temperatures in the stir zone cannot be measured directly, power correlates positively with welding temperature. Tensile elongation correlated negatively with welding power ($R^2 = 0.44$) in this case, as seen in Fig. 6. All welded specimens had elongations that were less than the base material, while four of the specimens had a UTS higher than the base material.

Grain sizes in the stir zone were measured by EBSD, while microhardness measurements were made in the stir zone and in the base material. The data from these measurements are shown in Table 3, along with spindle power for each case.

For a given set of parameters grain sizes varied but were essentially similar on the retreating side, center, and advancing side of the stir zone, given the large standard deviations in the measurements. All grain sizes in the stir zone represent grain refinement compared to the base material average grain size of about 40 μm .

Table 3 Grain sizes in stir zone and microhardness ranges across stir zone, heat affected zone, and base material

Feed rate (mm/min)	RPM	Spindle power (KW)	Grain size			μ-Hardness (HV)	
			RS	C	AS	Min	Max
50	80	3.3	2.72 ± 1.39	2.91 ± 1.54	2.77 ± 1.42	186	318
50	150	4.8	7.97 ± 4.16	9.03 ± 4.87	9.32 ± 4.94	184	246
100	150	4.9	5.63 ± 2.86	6.47 ± 3.41	5.51 ± 2.78	188	272
100	250	6.3	9.25 ± 5.5	9.70 ± 5.27	11.35 ± 6.17	184	265
150	125	4.8	2.04 ± 0.94	2.63 ± 1.46	2.43 ± 1.18	180	340
150	175	6.3	4.73 ± 2.37	5.61 ± 3.09	5.63 ± 2.86	182	302

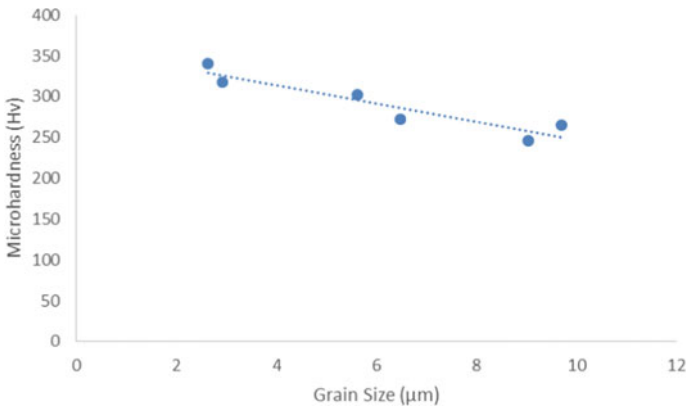


Fig. 7 Stir zone microhardness as a function of grain size

However, across the different parameter sets grain sizes were larger for cases of greater spindle power, although the relationship is not linear. Maximum hardness values did correlate somewhat negatively with spindle power ($R^2 = 0.10$). But as expected from the Hall-Petch relationship, finer grain size was strongly correlated with greater microhardness, as seen in Fig. 7.

Conclusions

Feasibility of crack repair by FSP was demonstrated in 12 mm thick 304L stainless steel plate. The repair of a tapered, straight crack, machined through the plate thickness by wire EDM, was evaluated visually by examining cross sections along the length of the stir zone. In this case, it appears that 2 mm crack width is the

practical limit for repair, since the top of the stir zone exhibited a depression on the advanced side, owing to the lack of material represented by the crack. Bead on plate FSP experiments on 12 mm 304L plate showed a negative relationship between spindle power and total elongation in transverse tensile specimens, while the UTS of the same specimens were greater than that of the base material in 4 out of 6 cases. Inhomogeneity of hardness in the friction stir processed specimens is the reason for lower total elongations compared to the base material. Finer grain size in the stir zone was strongly correlated with greater levels of hardness, as would be expected from the Hall-Petch relationship.

Acknowledgements This work was supported by National Science Foundation grant CMMI-1405508.

References

1. Asano K et al (1999) Weldability of neutron irradiated austenitic stainless steels. *J Nucl Mater* 264(1–2):1–9
2. Kanne WR et al (1999) Weld repair of irradiated materials. *Mater Charact* 43(2–3):203–214
3. Tsuchiya K, Kawamura H, Kalinin G (2000) Re-weldability tests of irradiated austenitic stainless steel by a TIG welding method. *J Nucl Mater* 283:1210–1214
4. Li S et al (2011) The effect of helium on welding irradiated materials. *Weld J* 90(1):19S–26S
5. Tosten MH et al (2007) Repair techniques for fusion reactor applications. *Weld J* 86(8):245S–252S
6. Feng Z, Wilkowski G (2002) Repair welding of irradiated materials: modeling of helium bubble distributions for determining crack-free welding procedures. *Medium: X; Size: 8 pp*
7. Yurioka N, Horii Y (2006) Recent developments in repair welding technologies in Japan. *Sci Technol Weld Joining* 11(3):255–264
8. Kanne WR et al (1995) Welding irradiated stainless-steel. *J Nucl Mater* 225:69–75
9. Wang CA et al (1996) The effect of an applied stress on the welding of irradiated steels. *J Nucl Mater* 239(1–3):85–89
10. Wang CA et al (1996) Welding of irradiated stainless steel. *J Nucl Mater* 233:213–217
11. Willis, E., *Electrical Power Research Institute (EPRI)*. 2013
12. Li S et al (2011) The effect of helium on welding of irradiated materials. *Weld J* 90:7
13. Yang Q, Xiao BL, Ma ZY (2012) Influence of process parameters on microstructure and mechanical properties of friction-stir-processed Mg-Gd-Y-Zr casting. *Metall Mater Trans a-Phys Metall Mater Sci* 43A(6):2094–2109
14. Tsai FY, Kao PW (2012) Improvement of mechanical properties of a cast Al-Si base alloy by friction stir processing. *Mater Lett* 80:40–42
15. Sun N, Apelian D (2011) Friction stir processing of aluminum cast alloys for high performance applications. *JOM* 63(11):44–50
16. Feng XL, Liu HJ, Babu SS (2011) Effect of grain size refinement and precipitation reactions on strengthening in friction stir processed Al-Cu alloys. *Scripta Mater* 65(12):1057–1060
17. Liu FC, Ma ZY (2010) Contribution of grain boundary sliding in low-temperature superplasticity of ultrafine-grained aluminum alloys. *Scripta Mater* 62(3):125–128
18. Liechty BC, Webb BW (2008) Modeling the frictional boundary condition in friction stir welding. *Int J Mach Tools Manuf* 48(12–13):1474–1485
19. Mishra RS, Ma ZY (2005) Friction stir welding and processing. *Mater Sci Eng: R: Rep* 50(1–2):1–78

20. Sterling CJ et al (2004) Effects of friction stir processing on the microstructure and mechanical properties of fusion Welded 304L Stainless Steel, in Research Report. Office of Naval Research. p 7
21. Park SHC et al (2003) Rapid formation of the sigma phase in 304 stainless steel during friction stir welding. *Scripta Mater* 49(12):1175–1180
22. Sorensen CD, Nelson TW (2005) Sigma phase formation in friction stirring of iron-nickel-chromium alloys. In: proceedings of the 7th international conference on trends in welding research. Pine Mountain, GA: ASM
23. Park SHC et al (2004) Corrosion resistance of friction stir welded 304 stainless steel. *Scripta Mater* 51(2):101–105

Influence of Underwater Operation on Friction Stir Welding of Medium Carbon Steel

Tomoko Miyamori, Yutaka Sato and Hiroyuki Kokawa

Abstract Friction stir welding (FSW) would be effective as an underwater repairing process of the defective steel structures. In this study, underwater and conventional FSW trials were performed on 5.5 mm thick medium carbon steel at various welding parameters, and then the feasibility of underwater FSW to steels, and the microstructures and hardness profile of the welds were examined. Underwater FSW could produce defect-free welds, and exhibited higher torque and Z-axial load than conventional one. The stir zone was composed of ferrite and pearlite after conventional FSW, while underwater FSW produced a microstructure consisting of bainite with ferrite and pearlite in the stir zone, resulting in higher hardness than the conventional one. This difference could be explained by the cooling rate and the continuous cooling transformation diagram of the steel.

Keywords FSW · Carbon steel · Underwater operation

Introduction

To secure safety during the decommissioning of nuclear power plants, especially of the Fukushima nuclear power plant, temporary repairing of steel structures is required. There is a possibility that the defective steel structures are placed in water or in an explosive gas atmosphere, thus the underwater repairing process in the solid state would be preferred.

Friction stir welding (FSW), which was developed in 1991 at The Welding Institute (TWI), is a solid-state welding process using frictional heat and the material flow arising from the rotation of the inconsumable tool [1]. FSW is often used as a process to eliminate solidification defects in cast materials [2]. Recently, several kinds of aluminum alloys have been subjected to underwater FSW,

T. Miyamori (✉) · Y. Sato · H. Kokawa
Department of Materials Processing, Graduate School of Engineering,
Tohoku University, Sendai, Japan
e-mail: tomoko.miyamori.r7@dc.tohoku.ac.jp

successfully producing sound welds [3–5]. Zhang et al. [3] examined the mechanical properties and the microstructure of the aluminum alloy 2216-T6 subjected by underwater FSW, showing that the reduction of hardness in the heat affected zone was suppressed through the rapid cooling of underwater FSW. According to these results, underwater FSW could be used as a repairing process of the defective steel structures placed in water, but systematic studies on underwater FSW of steels have hardly been done.

In the present study, underwater and conventional FSW trials of medium carbon steel were carried out, and then the microstructure and hardness profile of the welds were examined. Moreover, the microstructural evolution of the stir zone was discussed with thermal history during FSW.

Experimental Procedures

Underwater and conventional FSW trials were performed on 0.45 wt% medium carbon steel plate, 5.5 mm in thickness. All FSW trials were conducted on the bead-on-plate configuration with a Q60 composite tool consisting of 60% cBN (cubic boron nitride) and 40% W-Re alloy. The appearance and dimension of the tool used are shown in Fig. 1. Tilting of the tool axis was not employed in this study. The rotational speed varied from 150 to 300 rpm, while the travel speed was constant at 1.0 mm/s. The underwater FSW was conducted in an acrylic box filled with flowing water (292 K). During the FSW trials, machine outputs, such as torque and the Z axial load, were continuously recorded. Moreover, the thermal history of the weld was measured with an R-type thermocouple embedded in the steel plate.

After the FSW trials, the Vickers hardness profile of the weld across the stir zone was measured on the cross-section perpendicular to the welding direction with a

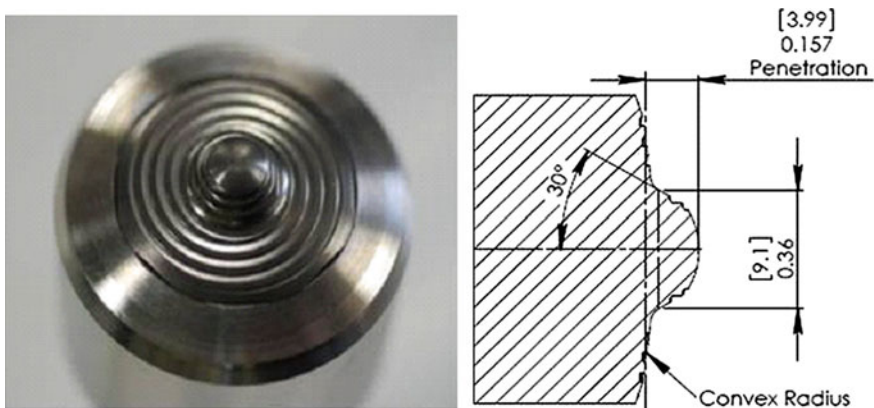


Fig. 1 Appearance and dimension of the tool used in this study. Unit: [mm] inch

load of 1 kgf for 10 s. The microstructure in the stir zone was observed by scanning electron microscopy (SEM) after etching using a Nital solution.

Results and Discussion

The surface appearances and cross sections of the underwater and conventional friction stir welds are shown in Fig. 2. The underwater FSW resulted in a slightly rougher appearance than the conventional one. The underwater FSW could produce the defect-free welds at most of the welding parameters used in this study as well as the conventional one, although the probe was broken at the rotational speed of 150 rpm during underwater FSW. This result suggests that underwater FSW exhibits slightly narrower process window than conventional one.

Vickers hardness profiles of the welds across the stir zones are presented in Fig. 3. All the stir zones are hardened, and underwater FSW leads to higher hardness values in the stir zone than conventional one, suggesting that cooling was faster during underwater FSW.

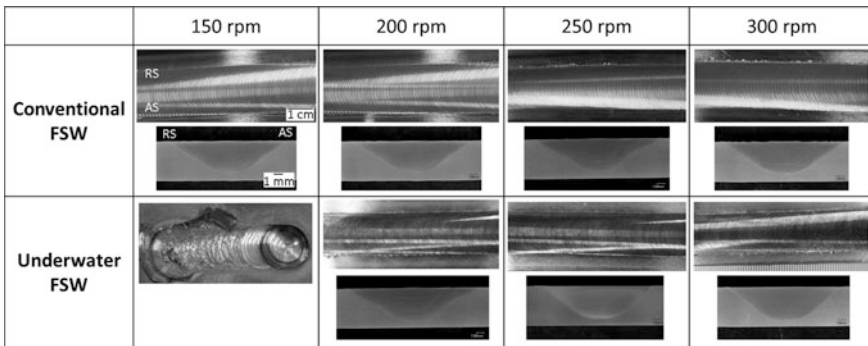


Fig. 2 Surface appearances and cross sections of the welds

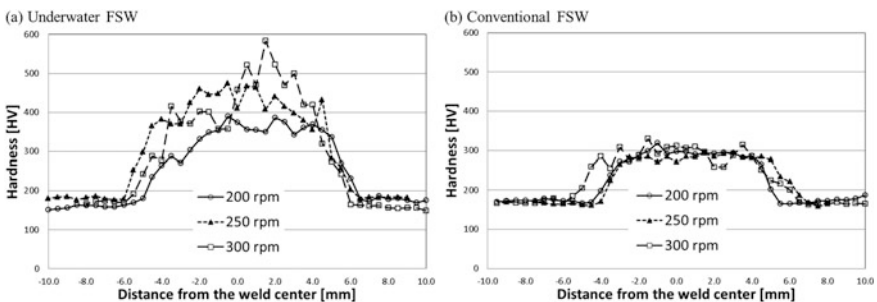


Fig. 3 Effect of rotational speed on the hardness distribution of the weld

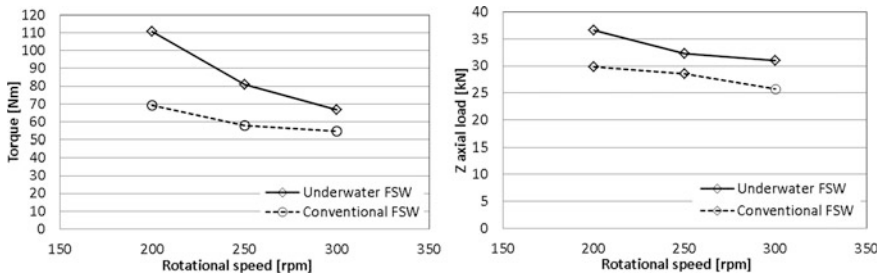
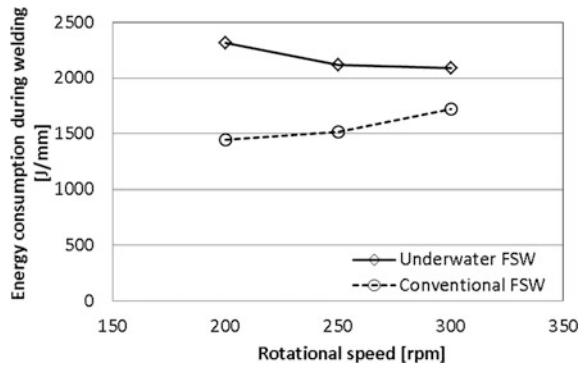


Fig. 4 Effect of rotational speed on torque and Z-axial load during FSW

Fig. 5 Effect of rotational speed on energy consumption during FSW



The torque and Z-axial load measured during underwater and conventional FSW trials are shown in Fig. 4. They decrease with increasing rotational speed. It is interesting that underwater FSW resulted in a higher torque and Z-axial load than conventional one. The energy consumption per unit length during FSW, which can be calculated using the torque, rotational speed and travel speed [6], was compared between underwater and conventional FSW trials (Fig. 5). The effect of rotational speed on the energy consumption was negligible, but the energy consumption of the underwater FSW was larger than that of the conventional one. This result implies that water cooling reduces temperature of the stirred material around the welding tool, and the peak temperature of the stir zone.

Thermal histories of the stir zone during the underwater and conventional FSW trials are given in Fig. 6. The peak temperatures of underwater FSW were somewhat lower than those of conventional one. Moreover, it is clearly shown that the heating and cooling rates during underwater FSW were significantly higher than those during conventional one.

The microstructures of the base material, and the stir zones produced at 250 rpm are shown in Fig. 7. The stir zone was composed of ferrite and pearlite after conventional FSW, while underwater FSW produced a microstructure consisting of ferrite, pearlite and bainite. This difference can be explained with the continuous cooling transformation (CCT) diagram of 0.45%C steel and difference in the

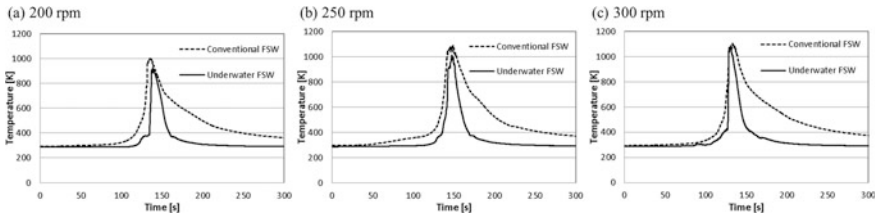


Fig. 6 Thermal histories during the underwater and conventional FSW trials

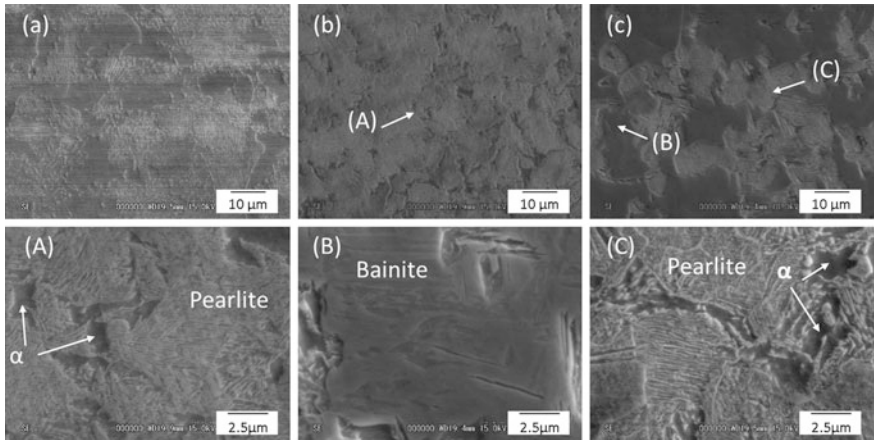


Fig. 7 SEM images of base material (a), and stir zones produced by conventional FSW (b) and underwater FSW (c) (250 rpm). Higher magnified images of regions A–C in (b) and (c) are shown in (A)–(C), respectively

cooling rate during FSW. From Fig. 6b, the cooling rates were estimated to be 312 and 290 K/s in the underwater and conventional FSW trials at 250 rpm, respectively. According to the CCT diagram [7], bainite formation requires the cooling rate higher than 296 K/s, suggesting that the formation of bainite is possible only during the cooling of underwater FSW. The formed bainite causes the higher hardness in the stir zones produced by underwater FSW.

Conclusions

Underwater FSW successfully produced the defect-free welds on 0.45 wt% medium carbon steel. Underwater FSW resulted in higher consumed energy, lower peak temperature and higher cooling rate than the conventional one. The stir zone produced by underwater FSW consisted of bainite, ferrite and pearlite causing the high hardness.

Acknowledgements The authors are grateful to Mr. A. Honda for technical assistance. This study was partially supported by the Center of World Intelligence Project for Nuclear S&T and Human Resource Development entrusted by the Ministry of Education, Culture, Sports, Science and Technology of Japan.

References

1. Thomas WM, Nicholas ED, Needham JC, Murch MG, Templesmith P, Dawes CJ International patent application no. PCT/GB92/02203
2. Santella ML et al (2005) Effects of friction stir processing on mechanical properties of the cast aluminum alloys A319 and A356. *Scripta Mater* 53:201–206
3. Zhang HJ et al (2012) Effect of water cooling on the performances of friction stir welding heat-affected zone. *J Mater Eng Perform* 21(7):1182–1187
4. Zhang HJ et al (2011) Microstructure and mechanical properties as a function of rotation speed in underwater friction stir welded aluminum alloy joints. *Mater Des* 32:4402–4407
5. Upadhyay P, Reynolds AP (2010) Effects of thermal boundary conditions in friction stir welded AA7050-T7 sheets. *Mater Sci Eng, A* 527:1537–1543
6. Pew JW et al (2007) Torque based weld power model for friction stir welding. *Sci Technol Weld Joining* 12(4):341–347
7. Totten G et al (2002) *Handbook of residual stress and deformation of steel*. ASM International, Materials Park, OH, p 249

Feasibility of Iridium Containing Nickel Based Superalloy Tool to Friction Stir Spot Welding of High Strength Steel

Kunihiro Tanaka, Tatsuya Nakazawa, Koichi Sakairi, Yutaka Sato, Hiroyuki Kokawa, Toshihiro Omori and Kiyohito Ishida

Abstract The authors have developed an Ir-containing Ni based superalloy tool, strengthened by γ' precipitation, for friction stir welding (FSW) of steel and titanium alloys. The Ir-containing Ni based superalloy tool exhibited an acceptable performance during FSW of 304 stainless steel and Ti-6Al-4 V. In this study, feasibility of Ir-containing Ni based superalloy tool to friction stir spot welding (FSSW) of high strength steel was examined. FSSW was conducted on the lapped sheets of 1.2 mm-thick DP590 steel. The Ir-containing Ni base superalloy tool with 1.2 mm long probe successfully produced the spot welds on DP590 steel without macroscopic deformation. Even after 600 FSSW trials, the tool shape was hardly changed, suggesting that the Ir-containing Ni based superalloy tool is appropriate for FSSW of high strength steel.

Keywords FSSW · Ir · Ni-base superalloy · Welding tool

Introduction

Ni-based superalloy exhibits high high-temperature strength, being one of the most widely used materials in high-temperature applications, such as aerospace, nuclear power generators and turbine engines. This alloy is strengthened by the precipitation of a fine γ' (Ni_3Al) phase with a L1_2 structure in the γ matrix. The strengthening effect of this γ' phase exhibits a positive correlation with temperature in Ni-based superalloy, but the service temperature of polycrystalline Ni-based alloy is generally lower than 1000 °C due to the relatively low melting point of Ni (1455 °C).

K. Tanaka (✉) · T. Nakazawa · K. Sakairi
Tanaka Kikinzoku Kogyo K.K., Hiratsuka, Kanagawa, Japan
e-mail: kuni-tanaka@ml.tanaka.co.jp

Y. Sato · H. Kokawa · T. Omori · K. Ishida
Tohoku University, Sendai, Japan

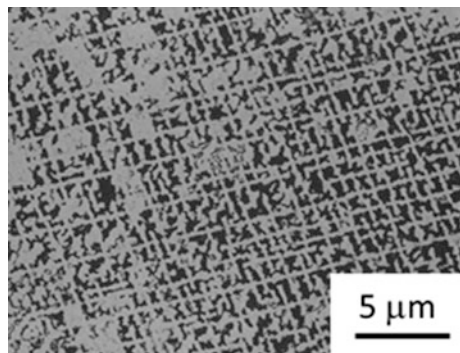
Friction stir welding (FSW) of steels has been achieved using various tools made of high melting point materials, such as W-Re alloy [1], W carbide [2], Co-base alloy [3], polycrystalline cubic boron nitride (cBN), and composites consisting of cBN and W-Re alloy [4], but these tools often experience problems such as excessive wear, oxidation and deformation. Gan et al. [5] have also demonstrated that a strength of at least 400 MPa at 1000 °C is needed for tool materials for FSW of steels to prevent tool deformation.

It is well known that platinum group metals (PGM) have a high melting point, as well as excellent corrosion resistance at temperatures above 1000 °C. Both Pt and Ir are often used in high temperature applications, such as crucibles for crystal growth, spark plug electrodes and glass melting equipment, because of their high heat-resistance property.

Previous researchers have developed a tool made of Ir-containing Ni base superalloy strengthened by precipitation of the stable γ' phases, $(\text{Ni, Ir})_3(\text{Al, W})$ with the L1_2 structure [6]. A typical microstructure of Ir-containing Ni based superalloy containing cuboidal γ' phases is shown in Fig. 1. The temperature dependence on the 0.2% yield strength of the Ir-containing Ni based superalloy and typical as-cast Ni based superalloy Mar-M247, obtained by compression testing, is shown in Fig. 2. The Ir-containing Ni based alloy exhibits much higher strength at high temperatures than Mar-M247, because the $(\text{Ni, Ir})_3(\text{Al, W})$ has higher stability than the Ni_3Al due the high phase stability of $\text{Ir}_3(\text{Al, W})$ [7] which meets the minimum requirement to prevent the tool deformation during FSW of steels.

According to the high high-temperature strength, the authors preliminarily attempted to use the Ir-containing Ni based superalloy tool for FSW of carbon steel, 304 stainless steel, and Ti-6Al-4 V alloy [8, 9], confirming the acceptable performance of the Ir-containing Ni based superalloy tool. In this study, feasibility of the Ir-containing Ni based superalloy tool to FSSW of high strength steel was examined.

Fig. 1 Microstructure of γ' phases of Ir-containing Ni based superalloy



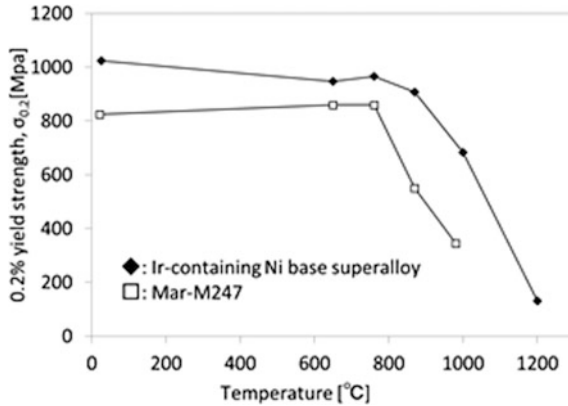


Fig. 2 Results of compression test of Ir-containing Ni based superalloy and Mar-M247

Experimental Procedures

Chemical composition of the Ir-containing Ni base superalloy used in this research is shown in Table 1. This chemical composition was determined based on that of Mar-M247 which is a representative as-cast Ni base superalloy. The alloy button was initially produced via arc melting. Subsequently, it was re-melted in an oxide crucible using a high-frequency melting furnace and then rapidly solidified into a Cu mold with an appropriate tool shape using tilt casting equipment. The as-cast alloy with the tool shape was solution-heat-treated at 1300 °C for 3 h under vacuum, followed by a heat-treatment for at 800 °C for 24 h for the γ' precipitation. The heat-treated alloys were precisely machined to the final tool shape. The final tool shape were probe length of 1.2 mm, probe diameter of 3.5 mm, and shoulder diameter of 10 mm, as shown in Fig. 3.

The material subjected to FSSW was DP590 steel, 1.2 mm in thickness. The lapped DP590 steels were welded at a tool rotation speed of 200 rpm, plunge depth of 1.6 mm, and holding time of 2.0 s. To evaluate the tool wear, change in 3-D tool shape during FSSW was captured using digital microscope and then loss of cross-sectional area was quantified, as shown in Fig. 4. When the tool experienced cracking or chipping, FSSW trial was terminated.

Table 1 Chemical composition of Ir-containing Ni-base superalloy (wt%)

Ni	Ir	Al	W	C	Other
38	25	4	14	0.1	18.9



Fig. 3 Appearance of tool with 1.2 mm-long probe used in this study

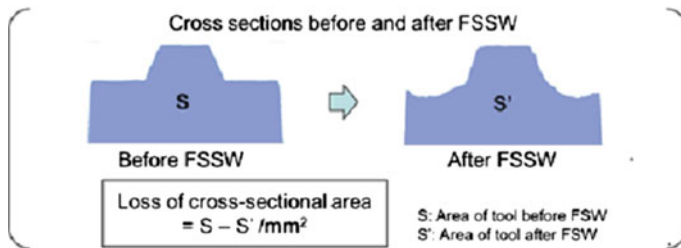


Fig. 4 Quantification of the tool wear

Results and Discussion

Appearance of DP590 steel with spot welds is shown in Fig. 5. Smooth welds without excessive flash were obtained on DP590 steel using a Ir-containing Ni base superalloy tool.

A typical cross-sectional overview of the spot weld is shown in Fig. 6. It is clearly shown that FSSW produced the defect-free spot weld on the DP590 steel. Appearances of the tool taken at regular intervals are shown in Fig. 7. Chipping, cracking and macroscopic tool wear were not found even after 600 spot welding.

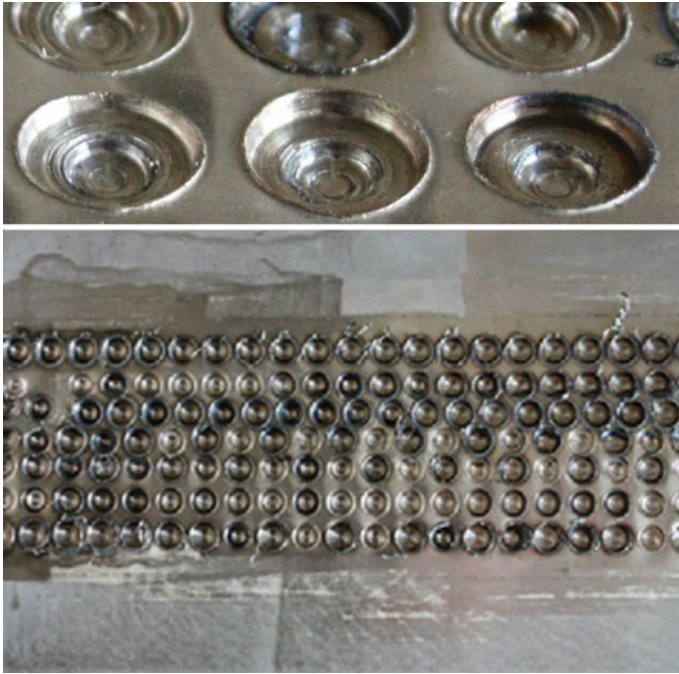


Fig. 5 Appearance of DP590 steel with friction stir spot welds

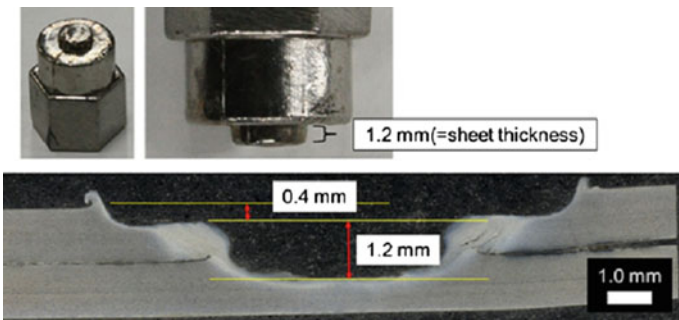


Fig. 6 Cross-sectional overview of spot weld

Change in tool shape and quantified loss of cross-sectional area during FSSW are shown in Figs. 8a and b, respectively. The cross-sectional area was hardly changed even after 600 FSSW trials.

To examine the microstructural change in tool surface during FSSW trial, the microstructure was analyzed on the cross-section of the tool subjected to 50 spot welding. The cross-sectional micrographs are shown in Fig. 9. The probe surface hardly experienced the microstructural change during FSSW, although it is found

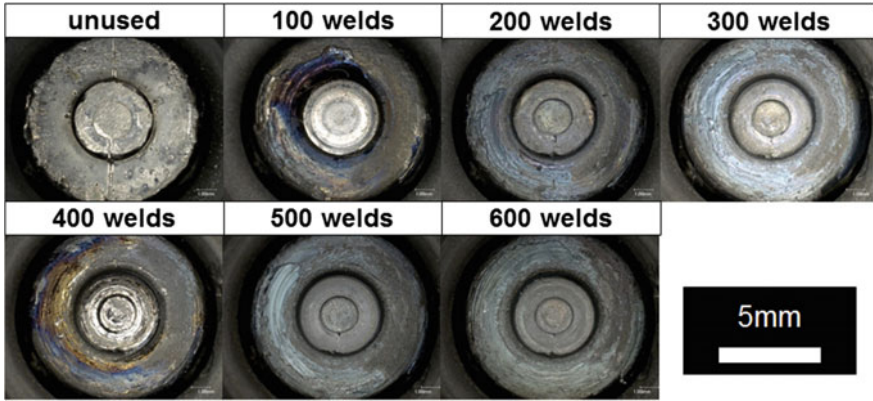


Fig. 7 Change in tool appearance during FSSW

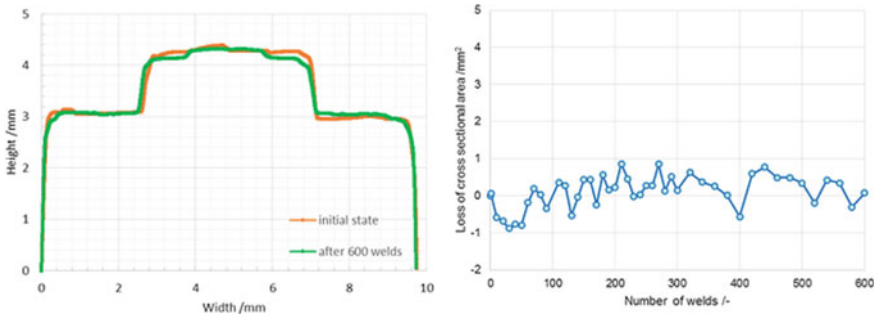


Fig. 8 a Change in tool profile during FSSW, b effect of number of welds on loss of cross-sectional area

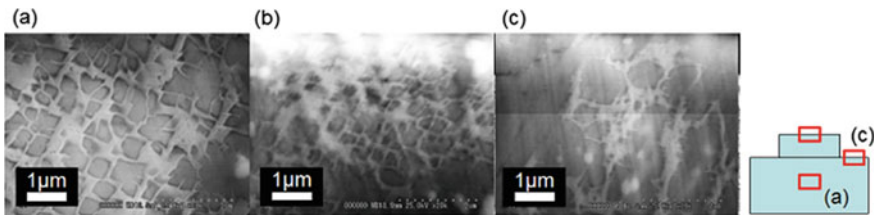


Fig. 9 SEM images of the tool after 50 spot welding

that the γ' precipitates slightly grew in the vicinity of the shoulder surface. This result suggests that the microstructural change slightly occurred in the vicinity of the tool surface.

Conclusion

Ir-containing Ni based superalloy tool with 1.2 mm long probe successfully produced the spot welds on DP590 steel without macroscopic deformation. Even after 600 FSSW trials, the tool shape was hardly changed, and severe wear was not found on the Ir-containing Ni base superalloy tool.

Acknowledgements We would like to acknowledge our sincere regards to Mr. K. Hosoi for their contribution to this research.

References

1. Liu H, Zhou L (2007) Progress in friction stir welding of high melting point materials. *Trans China Weld Inst* 28:101–104
2. Ouyang JH et al (2002) Application of laser-based additive manufacturing to production of tools for friction stir welding. In: *Proceedings of 13th solid freeform fabrication symposium*, Austin, TX. University of Texas, pp 65–72
3. Sato YS et al (2011) Development of a cobalt-based alloy FSW tool for high-softening-temperature materials. *Friction Stir Welding and Processing VI* (Wiley. NJ, TMS, Hoboken, pp 3–9
4. Packer S et al (2003) Tool and equipment requirements for FSW ferrous and other high melting temperature alloys. In: *Proceedings of 4th International Symposium on Friction Stir Welding*, Park City, UT, USA, CD-ROM
5. Gan W et al (2007) Tool materials selection for friction stir welding of L80 steel. *Sci Technol Weld Joining* 12:610–613
6. Sato J et al (2006) Cobalt-base high-temperature alloys. *Science* 7(312):90–91
7. Omori T et al (2014) Phase equilibria and mechanical properties of the Ir-W-Al system. *Intermetallics* 55:154–161
8. Nakazawa T et al (2015) “Friction stir welding of steels using a tool made of iridium containing nickel base superalloy”, *Friction Stir Welding and Processing VIII* (Wiley. NJ, TMS, Hoboken, pp 77–82
9. Nakazawa T et al (2016) Performance of iridium containing nickel base superalloy tool for friction stir welding of Ti-6Al-4 V alloy. In: *Proceedings of 11th international symposium on friction stir welding*, Cambridge, UK, CD-ROM

Part II
High Temperature Applications II

Development of Friction Stir Processing for Repair of Nuclear Dry Cask Storage System Canisters

Ken Ross, Ben Sutton, Glenn Grant, Gary Cannell, Greg Frederick and Robert Couch

Abstract The Nuclear Regulatory Commission has identified chloride-induced stress corrosion cracking (CISCC) of austenitic stainless steel dry cask storage systems (DCSS) as an area of great concern. Friction stir processing (FSP) was used to repair laboratory-generated stress corrosion cracking (SCC) in representative stainless steel 304 coupons. Results of this study show FSP is a viable method for repair and mitigation CISCC. This paper highlights lessons learned and techniques developed to apply FSP to crack repair in sensitized thick section stainless steel 304. These include: development of process parameters, welding at low spindle speed, use of weld power and temperature control and optimization of these controls. NDE and destructive analysis are also presented to demonstrate effectiveness of the developed methods for SCC crack repair.

Keywords Friction stir • Stress corrosion crack • Sensitization • Repair • Temperature control

Introduction

In the United States spent nuclear fuel is typically placed into austenitic stainless steel DCSS canisters near the power plant that generated the waste. DCSS canisters were intended to be temporary storage. Because no permanent storage facilities are

B. Sutton • G. Frederick • R. Couch
Electric Power Research Institute, 1300 W WT Harris Blvd,
Charlotte, NC, USA

K. Ross (✉) • G. Grant
Pacific Northwest National Laboratory, 902 Battelle Blvd,
Richland, WA, USA
e-mail: kenneth.ross@pnnl.gov

G. Cannell
Fluor Enterprises, Inc., 1200 Jadwin Ave, Richland, WA, USA

available in the United States, electric utilities must find a way to extend licenses beyond the original 20 year license period.

The United States Department of Energy [1] and Nuclear Regulatory Commission [2] determined sensitization and residual stresses produced by fusion welds in austenitic DCSS canisters put the fusion weld areas at high risk for CISC. This work explores the use of FSP to repair CISC damage and remediate HAZ sensitization produced by fusion welding.

Experimental Approach

SCC Repair

Two type 304 stainless steel coupons with controlled levels of SCC exposure were created to demonstrate the feasibility of FSP for repair of DCSS canisters. Each coupon is $500 \times 300 \times 25$ mm and each was furnace sensitized to create a continuous network of grain boundary chromium depletion by precipitation of $M_{23}C_6$ carbides. To produce two levels of SCC severity, plates were installed in a three point bending mechanical fixture and exposed to an SCC environment for 7 h and 277 h, respectively. Details regarding furnace sensitization and SCC exposure for generating the coupons used in this work are given by Sutton et al. [3]. Surface cracking was identified using liquid penetrant inspection. Phased array ultrasonic inspection was used to characterize the length and depth of surface and sub-surface cracking in each test coupon.

FSP was done on a high stiffness, precision friction stir welding machine located at the Pacific Northwest National Laboratory (PNNL). Process development was carried out by executing relay tuning [4] to determine PID gains for temperature control at 850 °C. Welds were run at various travel speeds, tilt angles and tool axial forces at 850 °C. The parameters that produced micrographs with the least amount of preferential etching in the stir zone were 38.1 mm/min, 55.6 kN tool axial force, and 0° spindle tilt using a Megastir Q70 tool. Relay tuning was then repeated with these parameters to optimize PID gains for temperature control. All crack repair welds were run with these parameters and optimized gains. PNNL's robust temperature control algorithms were used to hold the weld at a temperature of 850 °C \pm 2 °C for all repair welds. Argon shielding and a liquid cooled tool holder were used for all welds.

Post-FSP analysis was performed using non-destructive evaluation techniques and subsequent microscopy. Similar to the evaluation prior to FSP, liquid penetrant inspection determined the effectiveness of FSP to seal SCC. Phased array ultrasonic inspection quantified remnant subsurface cracking and detected any FSP-related defects. FSP cross-sections were cut from each coupon, polished using standard metallographic techniques, electrolytically etched with a 10% aqueous oxalic acid solution, and imaged using laser scanning confocal microscopy.

Results and Discussion

Process Development

Preliminary experimentation showed that that the least amount of preferential etching in the stir zone occurred at low feed rates and high forces. 38.1 mm/min traverse speed, 55.6 kN tool axial force, 850 °C tool temperature and 0° spindle tilt were chosen as final process parameters. To optimize temperature control for these parameters, relay tuning was repeated with these parameters to identify optimal gains. The relay tuning weld started in temperature control with non-optimized gains, once the weld traversed 48 mm at 850 °C, relay tuning was engaged. Output from the relay tuning, Fig. 1, was analyzed using methods presented by Marshall and Sorensen [4] to yield PID gains for the temperature controller optimized for final weld parameters.

Nondestructive analysis showed that SCC was successfully produced in the furnace sensitized and stressed 304 stainless steel plates. Liquid penetrant inspection detected surface cracks. Subsurface SCC growth and crack branching was detected and characterized via phased array ultrasonic inspection. Table 1 summarizes the crack characterization results. The number of cracks, length of cracks, and maximum crack depths increased substantially from the 7 h to the 277 h exposure condition.

The 7 h exposure condition produced a plate with a single crack running along the center of the plate with a maximum depth of 2 mm. This represents an ideal SCC condition where a surface-connected crack is shallower than the stir zone of the tool used in this study. There is negligible SCC branching, and there is no curvature to the crack plane. These conditions enable the crack to be fully consumed within the stir zone with a linear FSP path. This plate was selected for demonstration of complete crack healing by a single FSP pass.

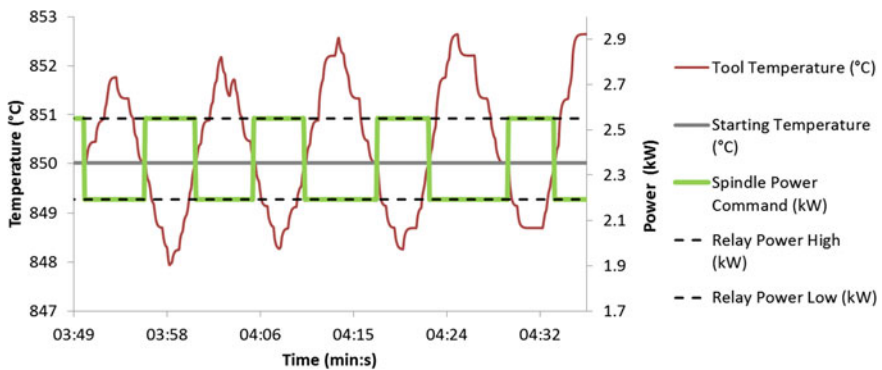


Fig. 1 Relay tuning data output for weld run at 38.1 mm/min traverse speed, 55.6 kN tool axial force, 850 °C starting tool temperature and 0° spindle tilt

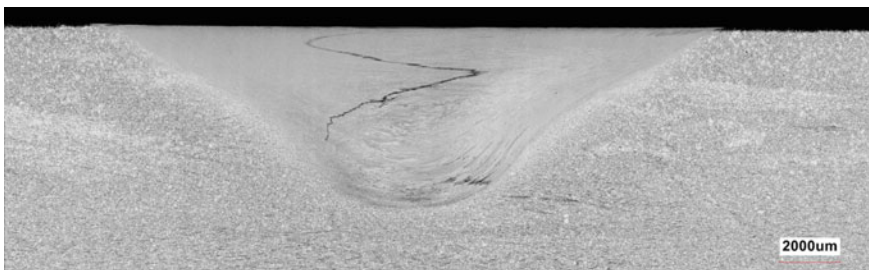
Table 1 Measured SCC dimension before and after FSP

Exposure duration (h)	Crack number	Pre-FSP crack length (mm)	Pre-FSP maximum crack height (mm)	Post-FSP crack length (mm)	Post-FSP maximum embedded crack height (mm)
7	1	58	2	Undetectable	
277	1	129	12	129	8
	2	152	17	152	10
	3	66	8	66	2

Post-FSP analysis of the 7 h exposure condition resulted in a fully consumed crack within the stir zone. No defects of any kind were detected by liquid penetrant examination or phased array ultrasonic inspection. An etched FSP cross-section of the 7 h test piece is presented in Fig. 2. The dark swirl pattern contained within the center of the stir zone is likely a redistribution of corrosion products from the crack surfaces. Further analysis is needed to confirm the cause of the swirl pattern.

Liquid penetrant and ultrasonic inspection of the 277 h test plate indicated that a raster pattern of 63.5 mm by 203.2 mm would be required to seal all of the cracks in the 277 h test plate. This pattern was made by 9 FSP passes 203.2 mm long, spaced 7.93 mm apart. An extra 12.7 mm was added to the start and stop of the raster pattern to enter and exit the raster pattern. A graphical representation of the raster pattern is given in Fig. 5.

Post-FSP inspection of the 277 h test plate showed that all cracks within the stir zones were successfully healed and remnant cracking below the FSP zone was unaffected. No surface cracks were identified via liquid penetrant inspection of the FSP zone. Phased array ultrasonic examination showed no defects formed within the stir zones and remnant subsurface cracking did not propagate during FSP. Table 1 presents the crack characterization results before and after FSP. A cross-section of the 277 h test plate post-FSP is shown in Fig. 3. A dark etching pattern exists in each FSP pass that fully or partially consumed a crack, similar to the swirl pattern seen in the 7 h exposure test piece. The remnant subsurface cracking is connected to these swirl features and substantiates the

**Fig. 2** Micrograph of fully consumed SCC following single-pass FSP

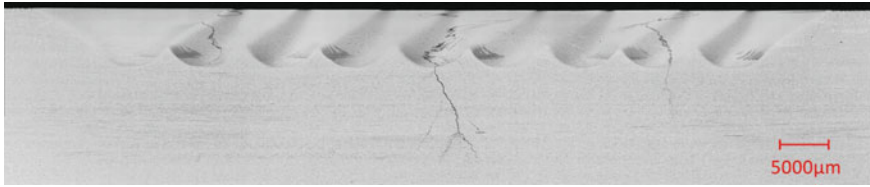


Fig. 3 Micrograph of partially consumed SCC in 277 h exposure condition plate

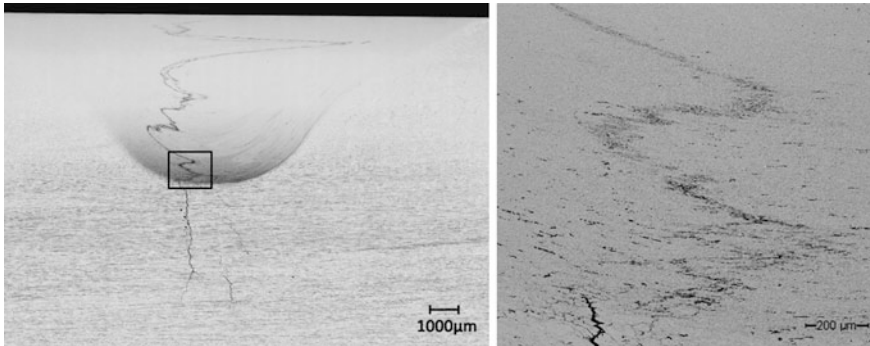


Fig. 4 Redistribution of corrosion products likely cause dark swirl pattern contained in the center of the stir zone; (left) micrograph of stir zone and crack remnant; (right) magnified view of intersection of stir zone and crack remnant marked by the box on the left hand image

conclusion that the swirl pattern is a redistribution of preexisting corrosion products from the crack faces (Fig. 4). Further analysis is needed to verify this conclusion. No additional analysis was done to characterize regions that were preferentially etched in the cross-section.

The combined use of temperature control and force control resulted in a well controlled weld. Weld depth is uniform. Figure 3, shows that size, shape and features of the stir zone appear to be similar across the raster pattern. Some differences in the preferential etching exist and should be investigated. The stir zone on the far right hand side of Fig. 3 is traversing into the page with the advancing side on the right and the retreating side on the left of the stir zone. The second stir zone from the right is traversing out of the page with the advancing side on the left and the retreating side on the right of the stir zone. The pattern continues across the entire rastered area.

Temperature control results for FSP repair of the 277 h exposure condition plate are shown in Fig. 5 and Fig. 6. Tool temperature was held to $850\text{ }^{\circ}\text{C} \pm 2\text{ }^{\circ}\text{C}$ for the entire weld after the initial plunge and traverse. During the weld, spindle speed varied from 120 RPM to 50 RPM. When using robust temperature control, spindle speed is a process output [5].

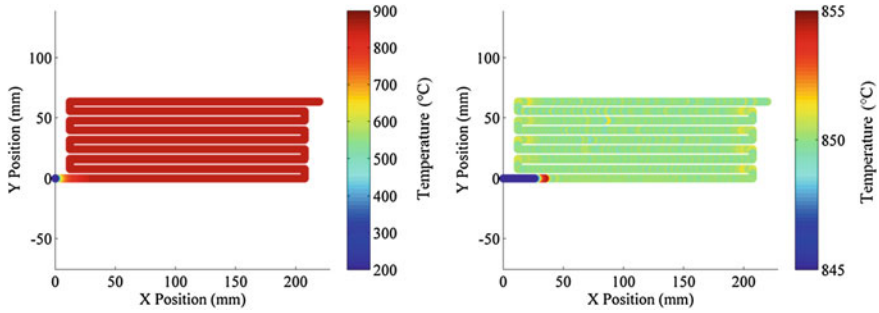
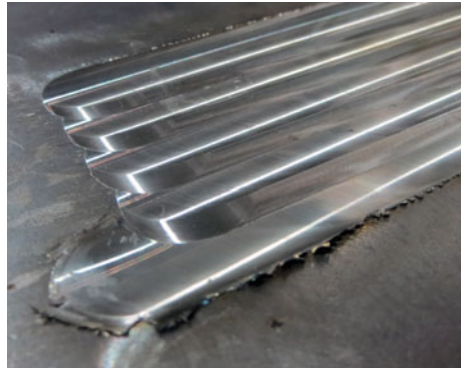


Fig. 5 Temperature feedback during FSP repair of plate with 277 h exposure condition; (left) 200–900 °C scale showing initial traverse transient, (right) 845–855 °C scale showing tight control of temperature

Fig. 6 Surface finish of FSP repair of plate with 277 h exposure duration



Controlling at low motor speeds and high motor torques is problematic for induction motors. Significantly lowering weld temperature at the traverse rate used in this study may require gearing down the spindle drive or replacing the induction motor with a servo control motor to enable adequate spindle control at low speeds and high torque.

Heat Affected Zone Sensitization Remediation

In order to study the ability of FSP to remediate sensitization, bead on plate fusion welds using stainless steel 308 rod were run on 304L coupons. An FSP pass was run along the fusion boundary on one side of the weld on each coupon, consuming the HAZ. These coupons are being evaluated according to ASTM A262 to quantify

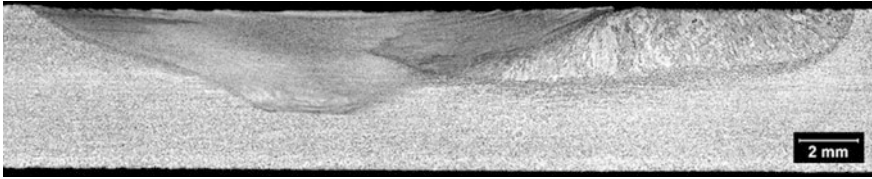


Fig. 7 Micrograph of sensitized 304L weldment following FSP of the GTAW HAZ

sensitization remediation. A cross section of a sensitization remediation coupon is shown in Fig. 7. Attention is given to carbide formation and distribution in the stir zone and FSP HAZ. Carbide formation and distribution will be compared to the original GTAW fusion weld HAZ. It is anticipated that FSP will improve corrosion performance based on results reported by Cannell et al. [6] that showed improvements in localized and general corrosion performance in thin-section 304L friction stir welds compared to GTAW welds [6].

Tool Life

Initially Megastir MS-90 tools were used for this study. Two new MS-90 tools had all features worn away within the first 101.6 mm of welding in sensitized 304 coupons. The poor performance of the MS-90 tools in sensitized 304 stainless steel was surprising because MS-90 tools have performed well in other steel alloys. Megastir Q-70 tools had excellent performance. The FSP repair of the 277 h exposure condition plate lasted 56 min and traversed 1925.3 mm. The Q-70 tool used experienced minor wear after completing this FSP repair.

Future Work

Additional characterization is needed better understand microstructures seen in the SCC repair coupons. This should include Electron microscopy and energy-dispersive X-ray spectroscopy of heavily etched regions and swirl patterns. Both single- and double-loop electrochemical potentiodynamic reactivation analysis, additional ASTM A262 testing, and accelerated atmospheric SCC testing should be conducted to understand the corrosion performance of the sensitization remediation FSP test coupons relative to fusion welding.

Additional FSP sensitization repair coupons should be made at lower temperatures to determine if additional improvements in corrosion performance can be gained through FSP repair at increasingly lower temperatures.

Conclusions

Results presented demonstrate that SCC repair and sensitization remediation of DCSS canisters via FSP is feasible. Two laboratory generated coupons, one with high SCC severity and one with low SCC severity were characterized before and after FSP repair. Liquid penetrant inspection, ultrasonic inspection and destructive metallographic analysis show that: Crack growth does not occur during FSP repair operations, cracks of a depth less than that of the stir zone are fully consolidated by FSP repair; cracks extending deeper than the stir zone are dimensionally stable and successfully embedded within the test coupon during FSP repair. FSP using tool temperature and tool axial force control resulted in a stable and uniform stir zone in single pass repair and large multi-pass raster patterns.

References

1. Hanson B, Alsaed H, Stockman C, Enos D, Meyer R, Sorenson K (2012) Gap analysis to support extended storage of used nuclear fuel. <http://www.energy.gov/sites/prod/files/Gap%20Analysis%20Rev%200%20Final.pdf>
2. (2012) NRC INFORMATION NOTICE 2012-20: potential chloride-induced stress corrosion cracking of austenitic stainless steel and maintenance of dry cask storage system canisters. <http://www.nrc.gov/docs/ML1231/ML12319A440.pdf>
3. Sutton B, Ross K, Grant G, Cannell G, Frederick G, Couch R (2017) Friction stir processing of degraded austenitic stainless steel nuclear fuel dry cask storage system canisters. In: Friction stir weld and processing IX, San Diego
4. Marshall D, Sorensen C (2013) System parameter identification for friction stir processing. In: Friction stir welding and processing VII, San Antonio, TX
5. Ross KA, Sorensen CD (2013) Paradigm shift in control of the spindle axis. In: Friction stir welding and processing VII, San Antonio, TX
6. Cannell G, Grant G, Adams T (2015) Demonstration of friction stir welding (FSW) technology for packaging of used nuclear fuel. In: Waste management, Pheonix, Arizona

Performance of Tungsten-Based Alloy Tool Developed for Friction Stir Welding of Austenitic Stainless Steel

Yutaka Sato, Ayuri Tsuji, Tomohiro Takida, Akihiko Ikegaya, Akinori Shibata, Hiroshi Ishizuka, Hideki Moriguchi, Shinichi Susukida and Hiroyuki Kokawa

Abstract As the cost-effective tool material, W-based alloys containing hard particles, exhibiting high strength, ductility, and thermal conductivity at high temperatures, were newly developed for FSW of austenitic stainless steel in this study. The W-based alloy tools containing various hard-particles were employed in FSW of type 304 austenitic stainless steel, and the wear behavior was examined. The W-based alloy tools coated by a ceramic exhibited the good performance during FSW, but the tool wear could not be completely prevented. Degree of the tool wear depended on the high-temperature strength, i.e., it decreased with increasing high-temperature strength. The tool wear was significantly suppressed in the W-based alloy with the higher high-temperature strength, and the tool shape was hardly changed even after the 20 m travel on the tool with 1.7 mm long probe.

Keywords FSW · Tungsten-based alloy · Welding tool · Stainless steel

Introduction

The tool damage associated with mechanical wear, deformation, fatigue, fracture and chemical reactions is a critical issue in friction stir welding (FSW) of steels [1–3]. After a preliminary result on FSW of steels reported [4], various tool materials, such as W-Re alloy, polycrystalline cubic boron nitride (PCBN), and composite consisting of W-Re alloy and cBN powders, have been developed for FSW of steels [1, 5]. These materials exhibit the good tool performance during

Y. Sato (✉) · S. Susukida · H. Kokawa
Tohoku University, Sendai, Japan
e-mail: ytksato@material.tohoku.ac.jp

A. Tsuji · T. Takida · A. Ikegaya
Allied Material Corporation, Toyama, Japan

A. Shibata · H. Ishizuka · H. Moriguchi
Nippon ITF, Inc., Kyoto, Japan

FSW of steels, but their usage is still limited in the practical applications because of the low cost-effectiveness.

To expand the practical applications of FSW of steels, development of cost-effective tool materials which are hardly damaged during the FSW operation is required. Since the metallic-based material might be preferred for prevention of cracking and chipping of the tool during FSW, the authors have attempted to develop Mo-based and W-based alloys exhibiting the good performance as the tool materials that enable welding of steels. To alleviate the tool deformation during FSW, these alloys containing hard particles, such as ceramic and/or intermetallic particles, were designed so as to achieve the high-temperature strength higher than 400 MPa at 1000 °C, which is a requirement reported by Gan et al. [6]. A preliminary study using various Mo-based alloys designed [7] revealed that the tool damage was effectively suppressed on the Mo-based alloy tool having both the high ductility and thermal-conductivity at high temperatures during FSW of 304 stainless steel.

In this study, W-based alloy tools containing hard particles were designed for FSW of austenitic stainless steels based on the requirements of the material factors obtained using Mo-based alloy tools. Since W has the superior physical and mechanical properties than Mo [8], W-based alloy expectedly exhibits the better tool performance than Mo-based one. FSW trials were carried out on 304 stainless steel with these tools, and the tool wear behaviors were examined.

Experimental Procedures

Two W-based alloys containing the different hard-particles were newly designed and produced by sintering. To examine mechanical properties of the alloys themselves, three-point bend testing was conducted at 1200 °C. 0.2% proof stress and fracture displacement were obtained through three-point bend testing to evaluate high-temperature strength and toughness. In addition, the thermal conductivity was examined by laser flash method.

FSW tools with 1.7 mm-long probe were made of the designed W-based alloys. Some of the tools were coated with a ceramic by physical vapor deposition to examine effect of ceramic coating on tool wear. Appearance and dimension of the tool used is shown in Fig. 1. FSW trials were conducted on a 4 mm-thick 304 austenite stainless steel at a tool rotational speed of 200 rpm and a travel speed of 1 mm/s. Argon gas shielding was employed to prevent the oxidization of both the tool and welded material. A weld length of an FSW pass was 450 mm, which was repeated to increase the total weld length. The 3-dimensional tool shape was captured after each FSW pass using a digital microscope to examine the tool wear behavior during FSW. The degree of tool wear was quantified by a decrease in cross-sectional area of the tool, as shown in Fig. 2.

Fig. 1 Appearance and dimension of the W-based alloy tool used in this study

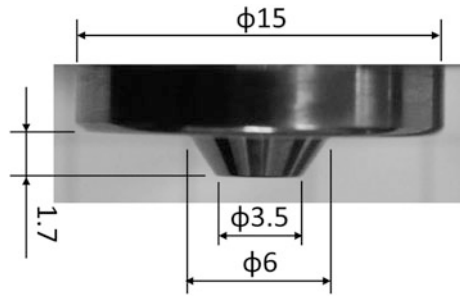


Fig. 2 Quantification of degree of tool wear

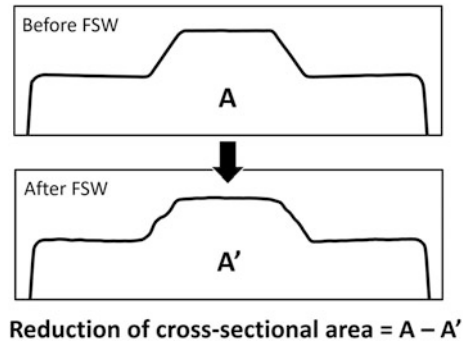


Table 1 Properties of W-based alloys

Properties	W alloy 1	W alloy 2	Mo alloy
0.2% proof stress at 1200 °C (MPa)	588	950	491
Displacement at fracture at 1200 °C (mm)	>6.0	>6.0	3.6
Thermal conductivity at 1000 °C (W/mK)	100.4	69.3	64

Results and Discussion

Properties of the designed W-based alloys are shown in Table 1. For comparison, properties of the Mo-based alloy showing the best tool performance in the preliminary study [7] are also given in this table. The preliminary study using Mo-based alloy tools having the thermal conductivity between 24 and 46 W/mK showed that the tool wear significantly occurred on Mo-based alloy with the thermal conductivity lower than 30 W/mK because of the overheating of the tool probe. Moreover, the displacement higher than 3.5 mm in the three-point bend testing was needed to prevent the cracking and chipping on the tool. Two W-based alloys designed in this study showed the higher strength, displacement and thermal conductivity at high temperatures than the Mo-based alloy. In W-based alloys, W alloy 1 exhibited the lower strength and higher thermal conductivity than W alloy 2. An example of scanning electron microscopic (SEM) image of the developed W alloy is shown in Fig. 3.

Fig. 3 A typical SEM image of developed W-based alloy

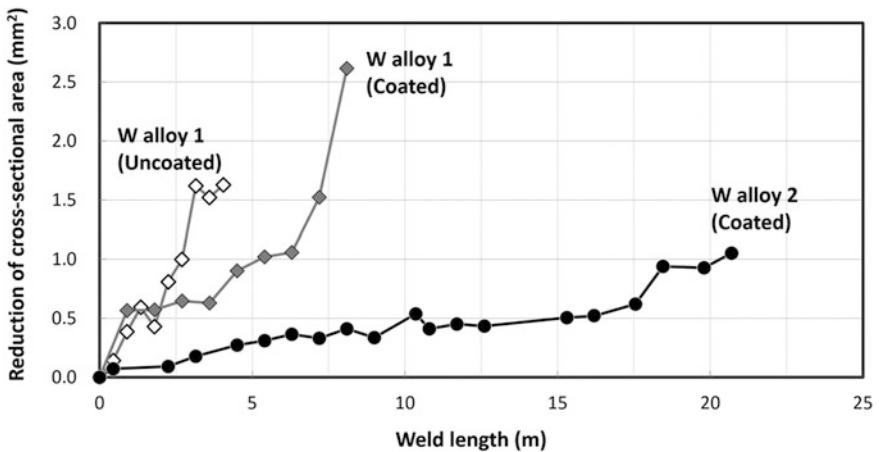
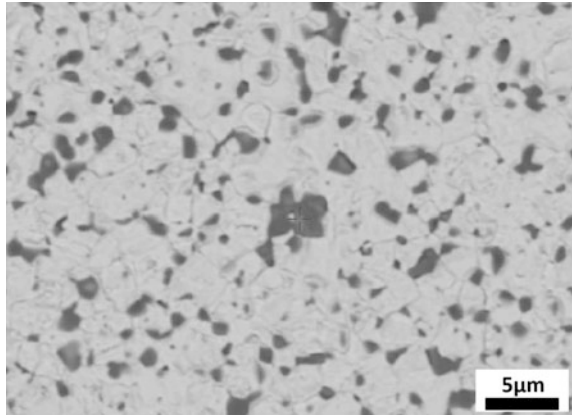


Fig. 4 Effect of weld length on reduction of cross-sectional area of W-based alloy tools

Black phases, i.e., hard particles, are uniformly distributed in the W matrix. Volume fraction of hard particles was about 10%.

Effect of weld length on decrease in cross-sectional area of W-based alloy tools is shown in Fig. 4. The decrease in cross-sectional area increased with the weld length on all tool materials. This means that all tools were worn during FSW. However, degree of tool wear depends on the presence of ceramic coating and the tool material. It is clearly shown that the uncoated tools experienced the severer tool wear than the coated ones, meaning that the ceramic coating is effective to suppress the wear of the tool material. In the coated W-based alloy tools, W alloy 2 exhibited the more excellent wear resistance than W alloy 1. W alloy 1 exhibited low degree of tool wear up to the weld length of about 4 m, beyond which its wear became severe. Shape profiles of the tools made of W alloys 1 and 2 at the weld length of

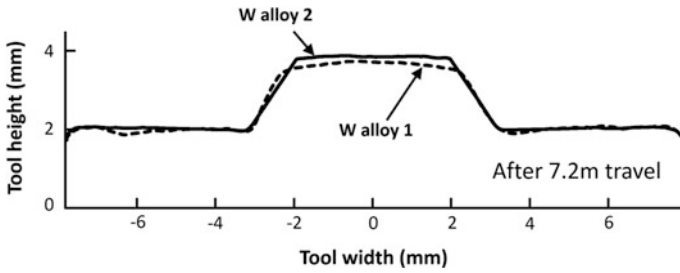


Fig. 5 Shape profiles of the tools made of W alloys 1 and 2 at the weld length of 7.2 m

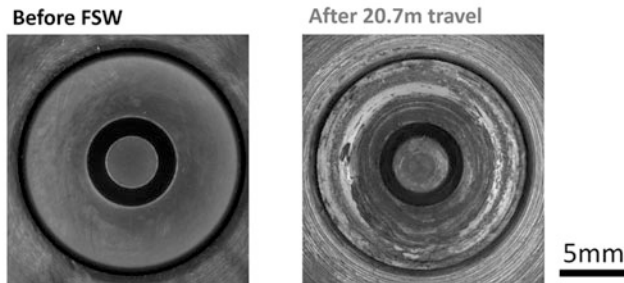
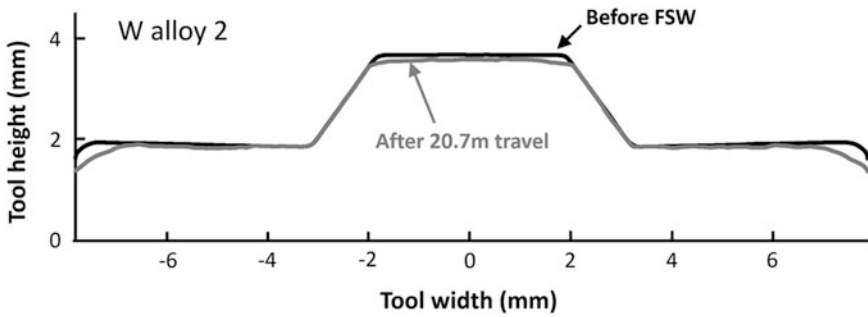


Fig. 6 Changes in shape profile and surface appearance of the tool made of W alloy 2 during FSW

7.2 m are shown in Fig. 5. The probe was deformed on the coated tool made of W alloy 1 although the deformation hardly occurred on the coated tool made of W alloy 2. The precise examination of the tool damage revealed that peeling of the ceramic coating was partly found on only the tool made of W alloy 1. This result implies that the tool deformation results in the peeling of the ceramic coating on the tool made of W alloy 1 because W alloy 1 has the lower high-temperature strength than W alloy 2, resulting in reduction of the wear resistance on the tool made of W alloy 1.

On the other hand, the coated tool made of W alloy 2 exhibited the excellent tool performance. Changes in shape profile and surface appearance of the coated tool made of W alloy 2 during FSW is presented in Fig. 6. In the tool made of W alloy 2, the decrease in cross-sectional area was less than 1 mm^2 , and any cracks and drastic deformation were not found even at the weld length of 20 m. The workpiece used in this study was 304 stainless steel, usually causing severer tool wear than carbon steels, because 304 stainless steel has the higher high-temperature strength. Therefore, this result implies that the coated tool made of W alloy 2 would exhibit the much excellent wear-resistance on carbon steels. In this study, a new tool exhibiting the excellent performance during FSW of 304 stainless steel was successfully developed using the W-based alloy containing hard particles with a ceramic coating.

Summary

In this study, the wear behaviors of the newly developed W-based alloy tools with a ceramic coating were examined during FSW of 304 austenite stainless steel. The FSW tool made of the W-based alloy having higher high-temperature strength exhibited the more excellent performance on 304 stainless steel. The tool hardly experienced macroscopic wear, deformation and cracking even after the 20.7 m travel.

References

1. Sorensen CD, Nelson TW (2007) Friction stir welding of ferrous and nickel alloys. In: Mishra RS, Mahoney MW (eds) Friction stir welding and processing. ASM International, Materials Park, OH, pp 111–121
2. Bhadeshia H, DebRoy T (2009) Critical assessment: friction stir welding of steels. *Sci Technol Weld Join* 14:193–196
3. Thompson B, Babu SS (2010) Tool degradation characterization in the friction stir welding of hard metals. *Weld J* 89:256–261
4. Thomas WM, Threadgill PL, Nicholas ED (1999) Feasibility of friction stir welding steel. *Sci Technol Weld Join* 4:365–372
5. Sorensen CD (2010) Tool wear measurements for PCBN tools used in FSW of structural steel. In: Proceedings of 8th international friction stir welding symposium, Timmendorfer Strand, Germany, CD-ROM
6. Gan W, Li ZT, Khurana S (2007) Tool materials selection for friction stir welding of L80 steel. *Sci Technol Weld Joining* 12:610–613
7. Sato YS, Susukida S, Kokawa H, Yamazaki S, Tsuji A, Uenishi N, Ikegaya A, Moriguchi H, Ishizuka H (2015) Effect of tool material properties on tool life of Mo-based alloy FSW tool for steels. Preprints of the national meeting of japan welding society, vol 96, pp 60–61
8. Shabalín IL (2014) Ultra-high temperature materials I. Springer Science + Business Media B. V., Dordrecht, The Netherlands

Investigation of Process Parameters for Friction Stir Processing (FSP) of Ti-6Al-4V Alloy

Sandip Chougule, Digvijay Sheed, R.K.P. Singh, N. Prabhu, B.P. Kashyap and Kaushal Jha

Abstract In the current work friction stir processing of the Ti-6Al-4V alloy was carried out. Various process parameters (tool traverse speed and tool rotation speed) were studied for successful FSP of Ti-6Al-4V. The process parameters were identified using macrostructure observation on the surface of processed plate and microstructure evolution in the stir zone (SZ) of the FSP specimen. The effect of tool traverse speed and tool rotation speed on microstructure evolution in the SZ, thermo-mechanically affected zone (TMAZ) and heat affected zone (HAZ) were studied. The microstructure transformation from initial elongated α structure to prior β grains, with α layer grain boundary consisting of mixture of acicular α' and very fine lamellar α/β colonies, was observed at SZ. This was the case for wide range of variations in parameters except for the tool rotation speed of 600 rpm and traverse speed of 60 and 100 mm/min. Under this combination of parameters, the bands of DRX α and transformed β structure were observed to evolve at SZ.

Keywords Friction stir processing · Process parameter · Microstructure · Ti-6Al-4V alloy

S. Chougule (✉) · D. Sheed · R.K.P. Singh
Bharat Forge, Kalyani Centre for Technology and Innovation, Pune 411036, India
e-mail: Sandip.chougule@bharatforge.com

D. Sheed
e-mail: Digvijay.sheed@bharatforge.com

R.K.P. Singh
e-mail: RajkumarSingh@bharatforge.com

N. Prabhu · B.P. Kashyap
Department of Metallurgical Engineering and Materials Science,
Indian Institute of Technology, Bombay, Mumbai 400076, India
e-mail: nprabhu@iitb.ac.in

B.P. Kashyap
e-mail: bpk@iitb.ac.in

K. Jha
Engineering Design and Development Division, BARC, Mumbai 400085, India
e-mail: kaushal@barc.gov.in

Introduction

Friction stir welding (FSW) is solid state joining technique. Based on the basic principles of FSW friction stir processing (FSP) is carried out. The FSP technique is emerging as a very effective solid-state processing technique has been used for many applications like to produce surface composites, microstructural refinement and homogenization, microstructural modification of metal matrix composites, superplasticity, and mechanical property enhancement [1–12]. This process is successfully applied to low melting point materials like aluminum alloys, copper alloys, magnesium alloys [7–9, 13–16], but it has been facing difficulties with high melting point materials like titanium alloys, inconel alloys and steel due to difficulties in identifying tool materials and equipment capable of withstanding the high forces and temperatures involved with welding or processing these alloys [1]. Researchers taken up the challenge to overcome the difficulties in high melting point materials processing and tried different and advanced tool materials like tungsten-lanthanum oxide, tungsten-rhenium, tungsten carbides, Polycrystalline cubic boron nitride (PCBN) etc. for titanium alloys, inconel alloys and steel materials [1, 17]. Titanium alloys, especially Ti-6Al-4V alloy has been widely used in industries including aerospace, bio-medical, transportation, marine and offshore, petrochemical, architecture, and household due to its outstanding properties, such as high strength-to-weight ratio, good corrosion resistance, high thermal stability and better mechanical properties at high working temperature [18, 19]. Generally Ti-6Al-4V alloy has been joined by conventional welding processes like gas tungsten arc welding (GTAW), plasma arc welding, electron beam welding (EBW) etc. The problems of melting & solidification, large thermal distortion & residual stresses generated during fusion welding are overcome by friction stir welding technique [20]. Researchers processed Ti-6Al-4V alloy plates ranging from 1.5 to 15 mm with various combination of tool rotating speed and tool traverse speed with different starting microstructures [20–31]. The weld quality or processed surface mostly affected by tool rotating speed and tool feed rate, so one has to experiment with these processing parameters.

In present work friction stir processing of the Ti-6Al-4V alloy was carried out. The effect of various process parameters (tool rotation speed and tool traverse speed) on the microstructure evolution of Ti-6Al-4V alloy was studied and suitable process parameters are identified for successful FSP of Ti-6Al-4V alloy.

Material and Experimental Work

Material Composition and FSP Parameters

The material used in this study was mill annealed Ti-6Al-4V alloy plates of 6 mm with the chemical composition: Al 6.29, V 3.96, C 0.007, Fe 0.18, N 0.001, O 0.18

Table 1 Process parameters selected for FSP

Tool rotating speed (rpm)	Tool traverse speed (mm/min)	Tool rotating speed (rpm)	Tool traverse speed (mm/min)
600	60	400	140
	80		160
	100		180
	120		200
	140		220
	160		
	180		

and balanced Ti (all in weight %). Considering low thermal conductivity of Ti-6Al-4V alloy, a tungsten based tool alloyed with 1 percent (wt%) lanthanum oxide ($W-1\%L_2O_3$) was used for FSP. The tool design had a shoulder of 25 mm diameter and a tapered pin of length 5.5 mm & major diameter of 6 mm. In present work the tool head was stationary and tilted 2° opposite to the traveling direction of table/workpiece. The processing parameters used for FSP are given in Table 1.

After FSP, specimens were cut along transverse direction of processed plates at corresponding locations for microstructure characterization. Specimens were prepared for microstructure analysis by polishing on automatic polishing machine Tegamin-30. After polishing specimens were etched using Kroll's reagent and examined under optical microscopy (OM) & scanning electron microscopy (SEM) Carl Zeiss make. Hardness testing was carried out on the Vickers hardness tester using diamond indenter. The 500 g load was used with dwell time 10 s.

Tool Design

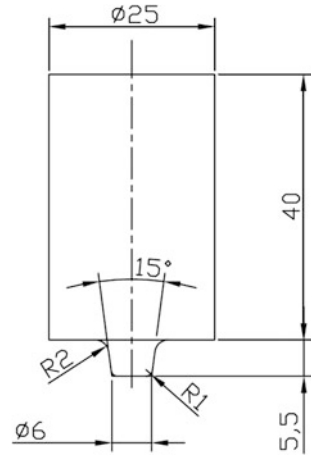
Tool Material

Requirements of the tool for FSP/FSW are high hardness, good wear resistant and high melting point. Hence tungsten 25 pct rhenium alloy or tungsten 1 pct lanthanum oxide was selected as the tool material for FSP process.

Tool Geometry

Tool geometry is one of the important process parameter. For the FSP tool shoulder and tool pin profile are important factors which affects the quality of weld. Selected tool geometries are very simple. Tool is having flat shoulder and taper pin profile. The diameter of the shoulder is set to 25 mm and the pin diameter is 6 mm. The length of the pin is 5.5 mm from the surface of the shoulder. Figure 1 shows drawing of tool geometry for FSP.

Fig. 1 Drawing of tool geometry for FSP



Results and Discussion

Process Window for FSP

In FSP, heat generated by tool and material friction during process is mainly controlled by processing parameters that are tool rotation and tool traverse speed. Thus, appropriate combinations of tool rotation and tool traverse speed could produce defect-free joints. In the present study, single pass FSP carried out on Ti-6Al-4V alloy of 6 mm thick plate with different combinations of tool rotation and tool traverse speed as tabulated in table to find out the optimum processing conditions. Based on visual inspection of FSP surface and macrostructure of the cross-section of the FSP runs of process windows as shown in the Fig. 2 were established.

In FSP for 400 rpm tool rotation defect free runs was observed for 160, 180, 200, and 220 mm/min except at 140 mm/min tool traverse speed. Similarly for 600 rpm tool rotation defect free runs were observed for 140, 160 and 180 mm/min against defective FSP runs at 60, 80, 100 and 120 mm/min tool traverse speed.

Fig. 2 Processing windows for Ti-6Al-4V Alloy FSP (Triangle represent parameters with visual discontinuities, square represent parameters with no visually detectable discontinuities)

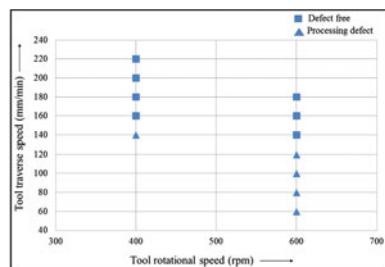


Table 2 shows FSP surfaces and respective macrostructure of the cross-section of the FSP runs for all sets of parameters used in the current study.

Defect like flash formation, irregular FSP surface and tunneling voids inside the SZ were observed for traverse speed 60, 80, 100 and 120 mm/min at tool rotation of 600 rpm. Same defects were also observed for tool traverse speed 140, 160, 180, 200, 220 mm/min at tool rotation of 400 rpm. Defects in the FSP process are mainly associated with the metal flow during the process which is direct function of the tool tilt angle and tool penetration during FSP.

It is well established that maximum temperature possible during FSP is proportional to tool rotational speed and the rate of heating or dwell time is proportional to tool traverse speed. By using analytical and numerical approach researchers proposed various 2-dimensional as well as 3-dimensional models in order to understand the actual metal flow during FSP [32]. These models were further validated by experimental methods. So in current study the defects like flash formation, irregular FSP surface could be formed mainly due to imbalance in material flow from advancing side of the tool to retreating side of tool.

Microstructure Evolution

The as-received Ti-6Al-4V alloy used in this study contained elongated α structure with β phase at the grain boundary as shown in Fig. 3.



















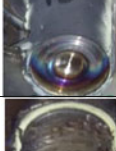
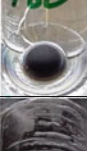
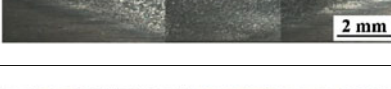
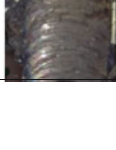


During FSP, the temperature measured on the surface of specimen is shown in Fig. 4 which indicates that the average temperature observed on surface of FSP specimen exceeded the β transus temperature ($995 \pm 5^\circ\text{C}$).

There are some important observations to be made upon viewing micrographs in Fig. 5. For the parameters 600 rpm, 60 and 100 mm/min, the initial elongated α structure transformed to bands of DRX α and transformed β structure in the stir zone (SZ). The diameter of the equiaxed α grain formed in the stir zone is significantly smaller than the diameter of the original as received base metal α phase. There are large bands of transformed β -phase begins to form in the portion of the stir zone upon increasing the feed rate for both rotational speeds.

In thermo-mechanically affected zone (TMAZ), prior β grains got decorated with α layer at grain boundary consisting of lamellar α colonies. TMAZ shows martensitic structure formation as the temperature in stir zone gone beyond the β transus temperature. As we increase feed rate beyond 120 mm/min for 600 rpm rotational speed & 160 mm/min for 400 rpm rotational speed the microstructures in the SZ are characterized by a fully transformed β structure in the form of lamellar α/β structure. This suggests that the peak temperatures in the SZ exceeded the β -transus temperature during processing, and $\beta \rightarrow \alpha + \beta$ phase transformation occurred during cooling at all the performed processing conditions. However, the prior β grain size is significantly influenced by the processing parameters.

It is known that β grain growth is rapid in the β phase field because of high temperature and absence of second-phase particle. The prior β grain size depends on

Table 2 Images of FSP runs along with macrostructure in transverse direction of the each parameter

Parameters	After FSP surface	After flash removal surface	Macrostructure
600/60			
600/80			
600/100			
600/120			
600/140			
600/160			
600/180			
400/140			

(continued)

(continued)

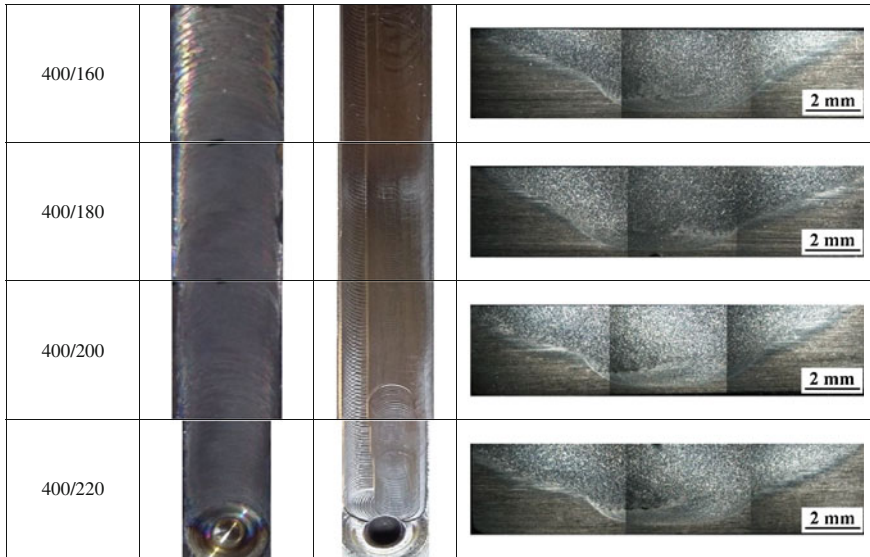


Fig. 3 SEM image showing microstructure of as-received Ti-6Al-4V alloy

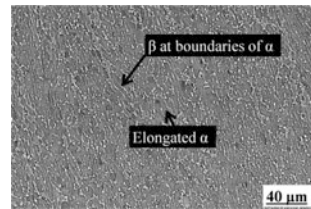
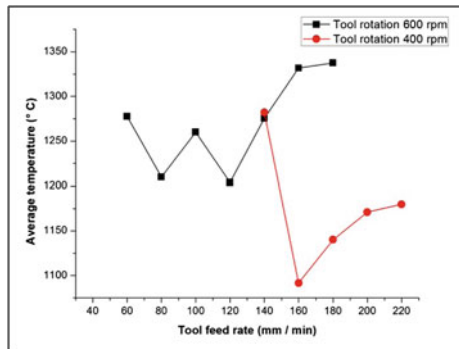


Fig. 4 Average surface temperature profile of FSP specimen



the temperature and exposure time above the β -transus temperature, which are controlled by the processing parameters. Increase in tool rotational rate and decrease in traverse speed can produce higher processing peak temperature and longer exposure time at high temperature, resulting in larger prior β grain in the SZ.


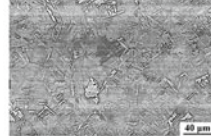
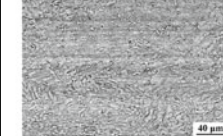

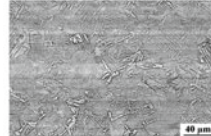
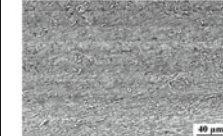
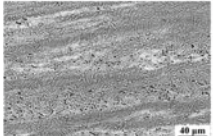

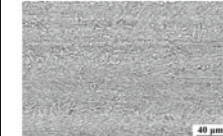


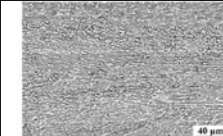


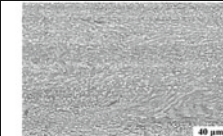

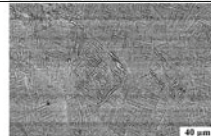
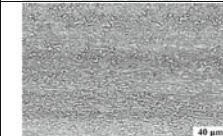

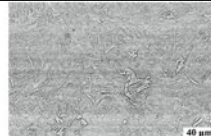

Zone RPM/(mm/min)	(a) Stir zone	(b) Thermo-mechanically affected zone	(c) Heat affected zone
600/60			
600/80			
600/100			
600/120			
600/140			
600/160			
600/180			

Fig. 5 SEM micrographs showing microstructure of **a** SZ, **b** TMAZ and **c** HAZ of studied parameters

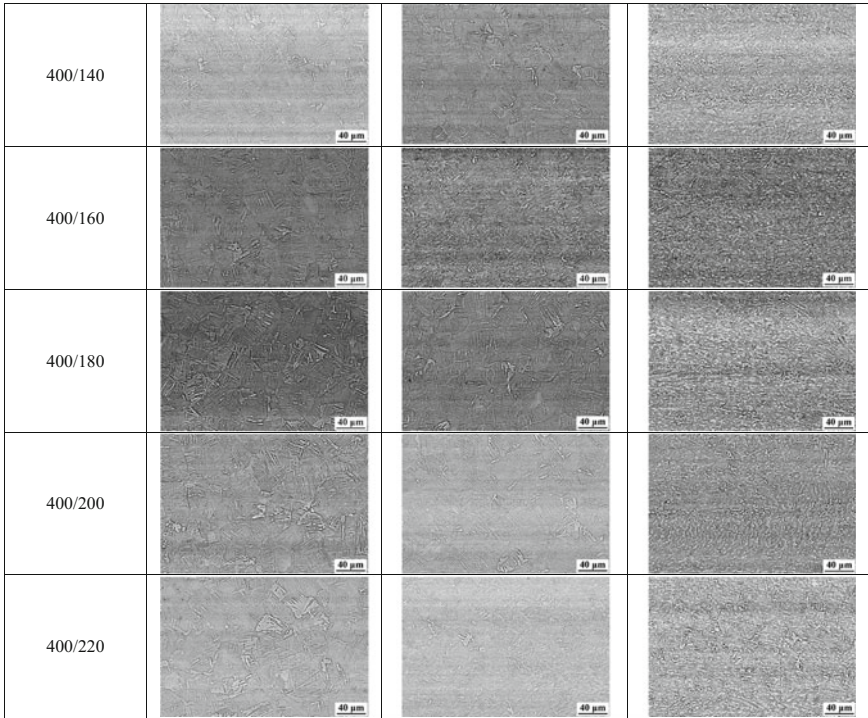


Fig. 5 (continued)

Micro-Hardness

Vickers hardness profiles across the welds are shown in Fig. 6a, b. The SZ has a higher hardness value than the BM. The HAZ & BM have the almost same hardness value in each sample. The prior β grain size is a dominant factor governing

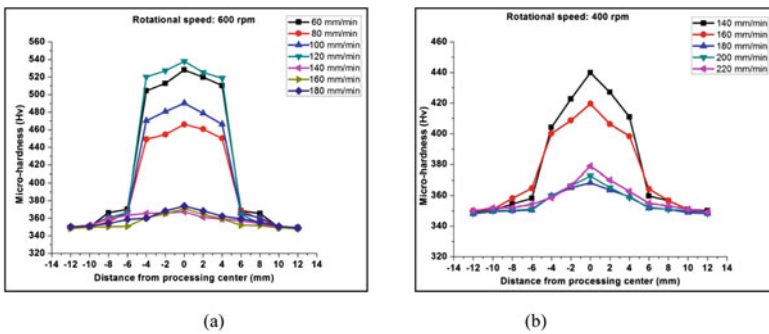


Fig. 6 Vickers hardness profiles across the SZ of the FSP **a** rotational speed 600 rpm, **b** rotational speed 400 rpm

mechanical properties, and smaller β grain size leads to greater strength and ductility [33]. This would be a reason why the hardness in the HAZ less as compared to SZ. The mean hardness value of the SZ also decreases with increasing rotational speed keeping feed rate constant. The parameters with 600 rpm/60 mm/min, 600 rpm/80 mm/min & 600 rpm/100 mm/min SZs were characterized by more or less refined microstructure, as shown in Fig. 4. For such refined microstructures hardness value is higher as per Hall patch relationship, smaller the grain sizes higher the hardness. It is observed that upon increasing the feed rate hardness decreases keeping rotational speed constant.

Conclusions

- Design of experiment developed to investigate processing parameters suitable for friction stir processing of Ti-6Al-4V. After investigating the various processing parameters a processing window was established for successful FSP.
- Metallographic study revealed the occurrence of three distinct zones namely SZ, TMAZ & HAZ. Microstructure of each zone is distinct. SZ showed bands of DRX α with intermediate transformed β grains for higher rotational speed and lower tool traverse speed. Fully transformed β structure in the form of lamellar α/β structure was observed for lower rotational speed and higher tool traverse speed. SZ has basin like shape. TMAZ is in between SZ & HAZ. TMAZ microstructure showed fully lamellar α/β colony with prior α phase formed at boundaries of the colony structure. HAZ is very small in size as compared to the other two zones. It appears in between TMAZ & BM. It showed the mixture of transformed β grain structure and undeformed α grains.
- The SZ has a higher hardness value than the BM. The HAZ & BM have the almost same hardness value in all samples. The mean hardness value of the SZ decreases with increasing rotational speed at constant feed rate. Smaller the grain size higher is the hardness. It is observed that upon increasing the feed rate at constant rotational speed hardness decreases.

References

1. Mishra Rajiv S, Ma ZY (2005) Friction stir welding and processing. *Mater Sci Eng R* 50:1–78
2. Pilchak AL, Juhas MC, Williams JC (2007) Microstructural changes due to friction stir processing of investment-cast Ti-6Al-4V. *Metall Mater Trans A* 38:401–408
3. Pilchak AL, Norfleet DM, Juhas MC, Williams JC (2008) Friction stir processing of investment-cast Ti-6Al-4V: microstructure and properties. *Metall Mater Trans A* 39:1519–1524
4. Sharma SR, Ma ZY, Mishra RS (2004) Effect of friction stir processing on fatigue behavior of A356 alloy. *Scripta Materialia* 51:237–241

5. Kwon YJ, Saito N, Shigematsu I (2002) Friction stir process as a new manufacturing technique of ultrafine grained aluminum alloy. *J Mater Sci Lett* 21:1473–1476
6. Ma ZY, Sharma SR, Mishra RS (2006) Effect of multiple-pass friction stir processing on microstructure and tensile properties of a cast aluminum–silicon alloy. *Scripta Materialia* 54:1623–1626
7. Johannes LB, Mishra RS (2007) Multiple passes of friction stir processing for the creation of superplastic 7075 aluminum. *Mater Sci Eng A* 464:255–260
8. Rao AG, Katkar VA, Gunasekaran G, Deshmukh VP, Prabhu N, Kashyap BP (2014) Effect of multipass friction stir processing on corrosion resistance of hypereutectic Al–30Si alloy. *Corros Sci* 83:198–208
9. Feng AH, Ma ZY (2007) Enhanced mechanical properties of Mg–Al–Zn cast alloy via friction stir processing. *Scripta Mater* 56:397–400
10. Charit I, Mishra RS (2003) High strain rate superplasticity in a commercial 2024 Al alloy via friction stir processing. *Mater Sci Eng A* 359:290–296
11. Ma ZY, Mishra RS, Mahoney MW, Grimes R (2003) High strain rate superplasticity in friction stir processed Al–Mg–Zr alloy. *Mater Sci Eng A* 351:148–153
12. Ma ZY, Mishra RS, Mahoney MW (2002) Superplastic deformation behavior of friction stir processed 7075Al alloy. *Acta Materialia* 50:4419–4430
13. Liu G, Murr LE, Niou C-S, McClure JC, Vega FR (1997) Microstructural aspects of the friction-stir welding of 6061-T6 aluminum. *Scripta Materialia* 37:355–361
14. Soon PH, Kimura T, Murakamic T, Naganod Y, Nakata K, Ushio M (2004) Microstructures and mechanical properties of friction stir welds of 60% Cu–40% Zn copper alloy. *Mater Sci Eng A* 371:160–169
15. Su J-Q, Nelson TW, McNelley TR, Mishra RS (2011) Development of nanocrystalline structure in Cu during friction stir processing (FSP). *Mater Sci Eng A* 528:5458–5464
16. Lee W-B, Kim J-W, Yeon Y-M, Jung S-B (2003) The joint characteristics of friction stir welded AZ91D magnesium alloy. *Mater Trans* 44:917–923
17. Rai R, De A, Bhadeshia HKDH, DebRoy T (2011) Review: friction stir welding tools. *Sci Technol Weld Join* 16:325–342
18. Gerd L, Williams JC (2003) *Titanium*, vol 2. Springer, Berlin
19. Christoph Leyens, Peters Manfred (2003) *Titanium and titanium alloys*. Wiley-VCH, Weinheim
20. Su J, Mishra RS, Wang J, Xu R, Baumann JA (2013) Microstructure and mechanical properties of a friction stir processed Ti–6Al–4V alloy. *Mater Sci Eng A* 573:67–74
21. Davies PS, Wynne BP, Rainforth WM, Thomas MJ, Threadgill PL (2011) Development of microstructure and crystallographic texture during stationary shoulder friction stir welding of Ti–6Al–4V. *Metall Mater Trans A* 42:2278–2289
22. Edwards PD, Ramulu M (2009) Investigation of microstructure, surface and subsurface characteristics in titanium alloy friction stir welds of varied thicknesses. *Sci Technol Weld Joining* 14:476–483
23. Paola L, Cerri E (2014) Friction stir welding of Ti–6Al–4V alloy. *Mater Sci Forum* 783:574–579
24. Zhang Y, Sato YS, Kokawa H, Park SHC, Hirano S (2008) Microstructural characteristics and mechanical properties of Ti–6Al–4V friction stir welds. *Mater Sci Eng A* 485:448–455
25. Liu HJ, Zhou L, Liu QW (2010) Microstructural characteristics and mechanical properties of friction stir welded joints of Ti–6Al–4V titanium alloy. *Mater Des* 31:1650–1655
26. Zhou L, Liu HJ, Liu QW (2010) Effect of rotation speed on microstructure and mechanical properties of Ti–6Al–4V friction stir welded joints. *Mater Des* 31:2631–2636
27. Pilchak AL, Tang W, Sahiner H, Reynolds AP, Williams JC (2011) Microstructure evolution during friction stir welding of mill-annealed Ti–6Al–4V. *Metall Mater Trans A* 42:745–762
28. Ramirez AJ, Juhas MC (2003) Microstructural evolution in Ti–6Al–4V friction stir welds. *Mater Sci Forum* 426:2999–3004
29. Edwards P, Ramulu M (2010) Identification of process parameters for friction stir welding Ti–6Al–4V. *J Eng Mater Technol* 132:031006

30. Edwards P, Ramulu M (2010) Peak temperatures during friction stir welding of Ti-6Al-4V. *Sci Technol Weld Joining* 15:468–472
31. Ma ZY (2008) Friction stir processing technology: a review. *Metall Mater Trans A* 39:642–658
32. Mishra RS, Mahoney MW (2007) Friction stir welding and processing. Editors ASM International, pp 37–49
33. Sirilar P, Srichandr P (2006) Grain refinement of α/β phase Ti-6Al-4V alloy by thermomechanical treatment. In: Proceedings of the 4th Thailand materials science and technology conference, paper M13

Part III
Derivative Technologies

Solid-State Joining of Thick-Section Dissimilar Materials Using a New Friction Stir Dovetailing (FSD) Process

Md. Reza-E-Rabby, Ken Ross, Scott Whalen, Yuri Hovanski
and Martin McDonnell

Abstract Solid-state joining of thick section aluminum to steel plate has been achieved using a new process called friction stir dovetailing (FSD). In FSD, a custom designed pin tool is used to flow a lower melting point material (AA6061) into dovetail grooves machined into the surface of an underlying material that has a higher melting point (rolled homogeneous armor [RHA]). Repeating dovetails form a mechanical interlocking structure akin to metallic Velcro. In this study, 38.1 mm (1.5 in.) thick AA6061 was joined to 12.7 mm (0.5 in.) thick RHA plates. The effectiveness of FSD is demonstrated through tensile test data that shows specimens failing in the processed aluminum rather than at the joint interface. Numerical simulations that highlight the importance of optimizing dovetail geometry are presented. The effect of process parameters on joint strength and microstructure also are discussed.

Keywords Friction stir dovetailing • FSW • Aluminum • RHA • Dissimilar metals

Introduction

In friction stir welding (FSW), a non-consumable tool pin with counter clockwise helical features (threads and/or flutes) rotates in a clockwise direction (and *ceteris paribus*) results in a downward flow of material that leads to effective consolidation near the weld root [1]. Using the driving mechanism of the tool pin, FSW has been used to extrude the upper material (aluminum [Al]) into the pre-machined grooves

Md. Reza-E-Rabby (✉) · K. Ross · S. Whalen · Y. Hovanski
Applied Materials and Processing Group, Pacific Northwest
National Laboratory, 902 Battelle Blvd., Richland, WA 99352, USA
e-mail: md.reza-e-rabby@pnl.gov

M. McDonnell
U.S. Army Tank Automotive Research Development
and Engineering Center, 6501 E 11 Mile Road, Warren, MI 48397, USA

of an underlying material (steel) to construct lap joint of dissimilar materials [2–4]. By plastically deforming and forging aluminum into the grooves, a mechanical interlock was achieved without forming a metallurgical bond between the aluminum and steel. However, the ability to form an intermetallic bond at the aluminum-steel interface while simultaneously filling the dovetail would greatly improve joint strength. Studies have shown that the joint strength of the dissimilar material between Al and steel increases as the thickness of intermetallic compound (IMC) layer decreases [5, 6]. As reported in other studies, a minimum IMC layer thickness essentially improves the mechanical properties of dissimilar material such as Al and steel joined using the FSW process [7, 8]. In the conventional FSW process, tooling cost significantly increases when both Al and steel are involved in plastic deformation. In this approach, overheating of Al resulted in uncontrolled growth of IMCs while stirring the two materials (Al-steel) in the nugget zone, hence decreasing the joint strength [9, 10]. Numerous studies have been conducted to join Al to steel using FSW by (1) offsetting the tool from the weld center line (toward the Al) when forming a butt joint [5, 9, 11, 12], (2) decreasing the tool plunge depth for a lap joint [6–8], and (3) simultaneously machining and joining using a friction stir scribe technology [13]. The goal of those techniques was to enhance joint properties while minimizing heat generation and extending tool life. The current study, friction stir dovetailing (FSD) is a new process attempted to resolve challenges associated with forming Al to steel joints. This paper explores the use of FSD to join dissimilar materials (AA6061 and RHA) by plastically deforming the lower melting point material (AA6061) into dovetail grooves machined into the higher melting point material (RHA) to form mechanical interlocks while simultaneously forming an intermetallic bond to further strengthen the joint. A set of welding parameters and dovetail geometric variables were examined to investigate the mechanical and microstructural properties of joints. Finite element analysis (FEA) was used to optimize the dovetail geometric dimensions and the number of grooves to the maximum mechanical properties of the joint with the minimum number of passes.

Materials and Experimental Procedure

Plates of RHA procured to MIL-DTL-12560J were dual disc ground to a thickness of 12.7 mm and pre-machined dovetail grooves with the dimensions shown in Fig. 1a. The RHA plates were inserted into AA6061-T651 sandwich structures having a total thickness of 38.1 mm as illustrated in the Fig. 1b. FSD was performed using a tool made from H13 tool steel that was heat treated to obtain RHC 45. The one-piece FSW tool consists of a scrolled shoulder and a frustum shaped (6.1°) threaded + 3 flatted pin as shown in Fig. 1c. FSD was performed using a tool rotational speed of 275 RPM and welding speed ranging between 25–50 mm/min. The reason for selecting these welding parameter combinations was to examine the formation of IMCs along the interface of Al and RHA within the dovetail regions.

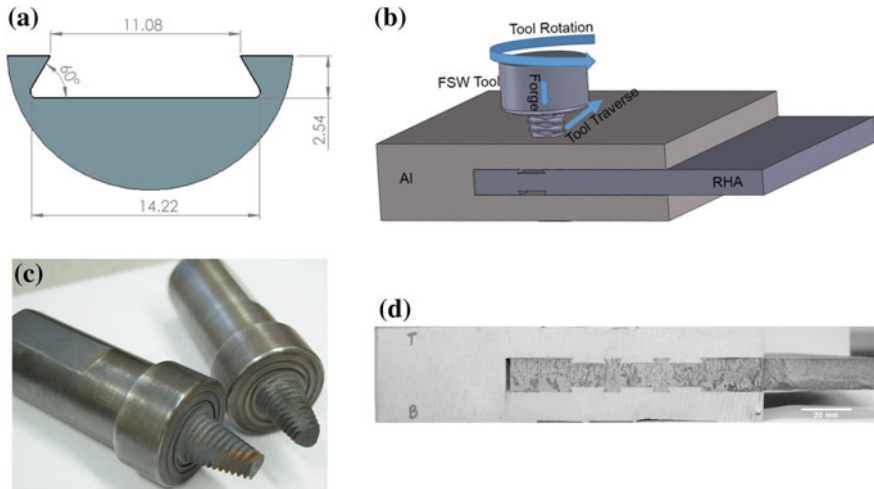


Fig. 1 FSD process. **a** Dovetail geometric dimensions, **b** double-side FSW of Al-RHA sandwich structure, **c** FSD tools, and **d** cross section of sandwich for mechanical and microstructural analysis

All welding was performed using a position control mode where the forge force is a response variable of the commanded plunge depth. Welds were made on the top side, then machined flat, and the assembly was turned over to weld the bottom side. Tensile specimens were cut from the welded Al-steel to an average thickness of 12.0 mm using a water jet as shown in Fig. 1d. Standard grinding and polishing sequences were followed for metallographic sample preparation and final polished surface was obtained using colloidal silica ($<0.05 \mu\text{m}$). A scanning electron microscope (SEM) equipped with energy dispersive spectroscopy (EDS) was employed to investigate the intermetallic formation. Tensile testing of sandwich plates (specimen shown in Fig. 1d) was performed using a 50 kip MTS test frame.

Modeling and Simulation

Optimization of Dovetail Numbers and Weld Passes

Structural analysis of a dovetail joints between AA6061 and RHA subjected to tensile load was simulated using LS DYNA finite element software. The simulation predicted the failure of tensile specimens with, and without, the formation of IMCs along Al and RHA dovetail interface. Cases for 1, 2 and 3 dovetails having the geometry in Fig. 1a were structurally analyzed using FEA. It should be noted that the number of dovetail joints dictates the number of FSD passes require for the sandwich in order for the joint to break in the base Al rather than at the Al-RHA interface. Since the temperature cycle during FSD resulted in microstructural changes from precipitation hardened condition of AA6061-T6 to an annealed

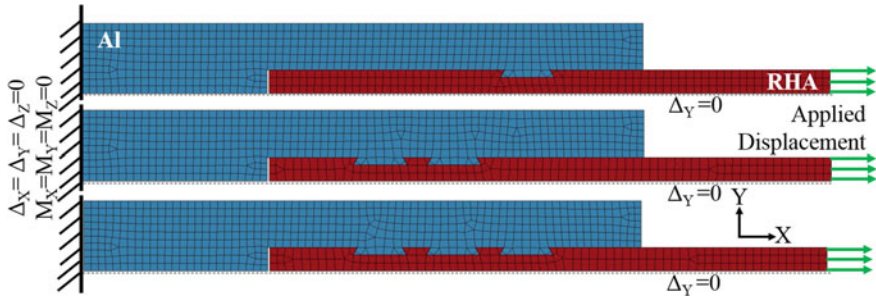


Fig. 2 Two-dimensional view of finite element model (symmetric with respect to the X-axis) of three tensile specimens with 1, 2 and 3 dovetails

condition [14], the material properties of AA6061-O [15] were utilized in the simulation. In addition, RHA (density—7840 kg/m³, elastic modulus—210 GPa and Poisson's Ratio—0.28) was considered as elastic material in this structural analysis since the yield strength of RHA (820 MPa) is much higher than the UTS of AA6061-O (56 MPa). The two-dimensional view of the meshed finite element models (half of the tensile specimen since the structure is symmetric with respect to the X-axis) having 1, 2 and 3 dovetails and applied boundary conditions are shown in Fig. 2. To simulate the tensile test, a prescribed linear displacement was applied to the right farthest nodes of RHA (Fig. 2) with a displacement value of 20 mm. The translational and rotational constraints relative to the X, Y and Z axis were applied to the left farthest nodes of the Al. The translational constraint to the nodes along the axis of symmetry (X-axis) was also applied with $\Delta Y = 0$.

The interfaces between Al and RHA, within the dovetails, were defined as contact pairs using an algorithm available in LS DYNA for two conditions: (a) without IMCs formation and (b) with IMCs formation. In the case of no IMC along the Al-RHA dovetail interface, the contact interaction was modeled with the coefficient of static friction as 0.3 and dynamic friction as 0.2 between Al and steel. For the conditions under which IMC form along the Al-RHA dovetail interface, a surface contact was defined between the upper, lower and side skin of the Al-RHA interface within the dovetails faces. The master segment of RHA and slave nodes of Al (and vice versa) was constrained by assuming both the normal and shear force for failure of Al-RHA IMC would be 500 N, which is much less than the minimum tensile strength of a lap joint published in the literature [8].

Results and Discussion

From the finite element simulations shown in Fig. 3a, it was observed that shear failure of the Al dovetail occurred for configuration with one, two and three dovetails when no IMC is present. Therefore, simple dovetail interlock without

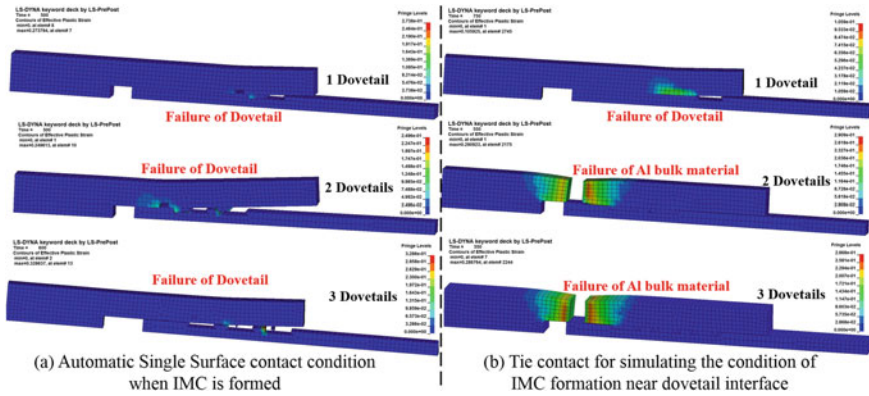


Fig. 3 Effective plastic strain contours from the LS DYNA structural analyses. **a** Without IMC formation and **b** with IMC layer formation along the Al-RHA dovetail interface

bonding doesn't have impact on structural integrity regardless of the number of dovetails. Figure 3b shows that joint strength is improved when IMC is present at the Al-RHA interface within the dovetail. In the case of IMC being present, only two dovetail features are required to cause failure in the bulk Al. In general, the results of this structural analysis indicate that, the presence of IMCs formation improves joint efficiency in the FSD process. As a result, steps were taken to generate an IMC at the Al-RHA interface while simultaneously filling the dovetail grooves.

Weld Microstructural Analysis

Transverse macro sections of Al-RHA joints with different dovetail geometries are shown in Fig. 4. The macro-sections clearly demonstrate the effective filling of Al into the dovetail grooves regardless of dovetail geometric variations. The FSD process is quite robust in terms being able to fully fill the grooves. For example, welds were performed (from 200 to 275 rpm and 25 to 100 mm/min) with the tip of the tool ranging from 2 mm above the RHA surface to having the tool tip in contact with the bottom of the dovetails in Fig. 4b, c. In all cases, the grooves were fully filled with no voids observed.

While Fig. 4 provides a macro-view of weld cross sections in terms of defect formation and dovetail filling, metallographic analysis is needed to determine the bonding state along the Al-RHA interface. SEM analysis at the Al-RHA interface of specimens in Fig. 4a, b are shown in Figs. 5 and 6 respectively.

The data indicates that interfacial bonding has occurred due to the formation of an IMC measuring 0.5–1 μm thick in narrow dovetail grooves (Fig. 5) and 1.0–2.0 μm thick in wider dovetail grooves (Fig. 6). The SEM micrographs suggest

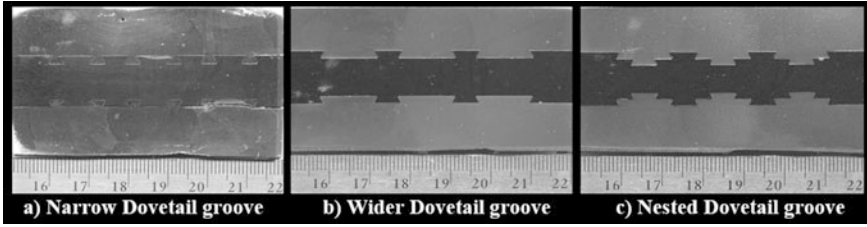


Fig. 4 Transverse sections of as polished specimens for different dovetail geometries

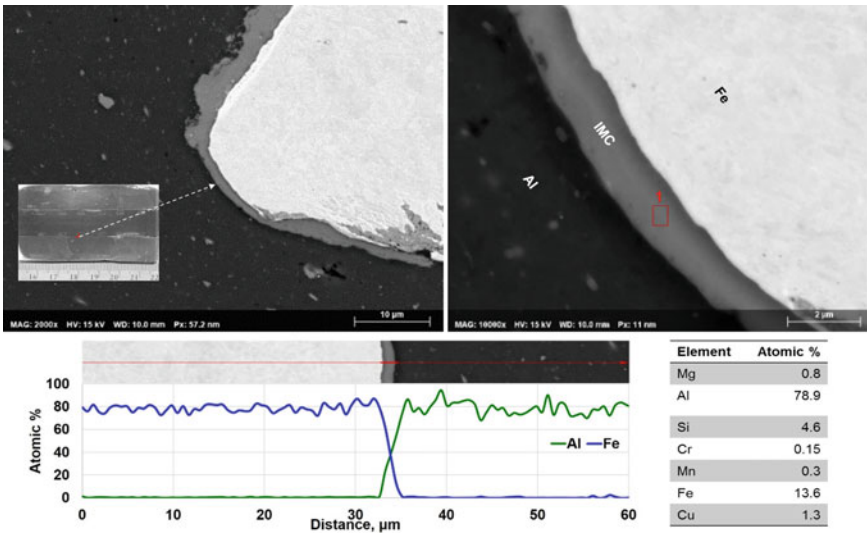


Fig. 5 SEM micrographs for the specimen in Fig. 4a exhibiting IMC formation in the narrow dovetail region and EDS elemental analysis for quantification

that incipient melting of AA6061 during FSD might cause bonding between RHA and Al with the formation of an intermediate transition layer which will be further confirmed as IMCs from energy dispersive spectroscopy (EDS) analysis. The formation of IMCs was confirmed by elemental quantitative analysis using EDS. The spot (area) and line scanning energy spectrum results are combined with the SEM micrograph in Fig. 5. The atomic percentage of corresponding line scans of Al and Fe at the intermediate transition layer indicate a diffusion profile of Al and Fe across the interface suggesting IMC formation. Moreover, the EDS spot analysis of this layer showed 79 at.% Al and 14 at.% Fe. In FSD, intense plastic deformation of AA6061 by the stirring tool might cause incipient melting of Al in close proximity to the RHA due to high localized temperature. The increased heat input caused by the tool contacting and deforming the RHA resulted in the formation of possible multiple IMCs ($AlFe$, Al_3Fe , $FeAl_2$, Al_4Fe , $Al_{13}Fe_4$, Al_5Fe_2 etc.) at the bonding

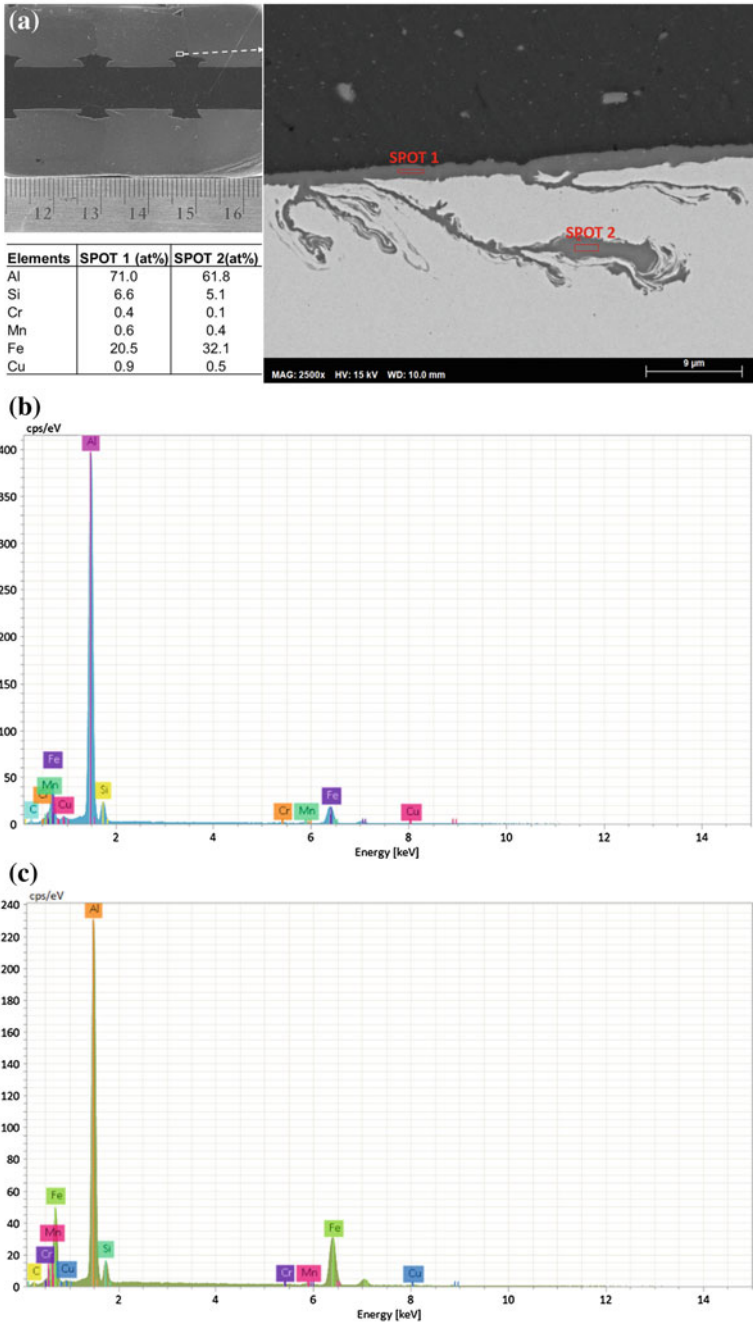


Fig. 6 SEM analysis and EDS quantification of FSD process for wider dovetail while tool plunge depth was such that dovetail peak of RHA was deformed. **a** Macro cross section, SEM micrograph detecting the IMC and spot elemental composition, **b** EDS Spectra of elemental analysis in SPOT 1, **c** EDS Spectra of elemental analysis in SPOT 2

interface which might be further confirmed from temperature measurement during FSD, phase diagram analysis and corresponding X-ray diffraction analysis.

The macro cross section in Fig. 6a shows the deformed layer of RHA near the upper region of dovetails where the stir tool intentionally contacted the RHA during processing to locally increase temperature and promote IMC formation. Consequently, the growing of IMCs were evident outside the dovetail in the SEM and EDS analysis shown in Fig. 6a. Frictional heating due to contact between the stir tool and RHA may result in the Al being melted locally, thereby resulting in the formation of IMCs. Figure 6b, c presents the EDS spectral analysis for two different spots on the IMC layers. According to the EDS spectra and elemental composition mentioned in Fig. 6, the intermetallic compounds $FeAl_2$, Fe_3Al or Fe_2Al might form in the Al-RHA interlayer.

Tensile Tests

Tensile testing of sandwich structures shown in Fig. 1d was conducted for specimens having the dovetail geometries shown in Fig. 4. For these specimens, tool speed was held constant at 275 rpm and the welding speed was 25 and 50 mm/min. Figure 7 presents the maximum tensile load per unit length of weld (i.e. specimen thickness) plotted against different dovetail grooves and welding conditions. At least 4 specimens of each category were tested.

It was observed from Fig. 7 that nested dovetails result in higher strength than single wider dovetails regardless of welding speed. The higher load carrying

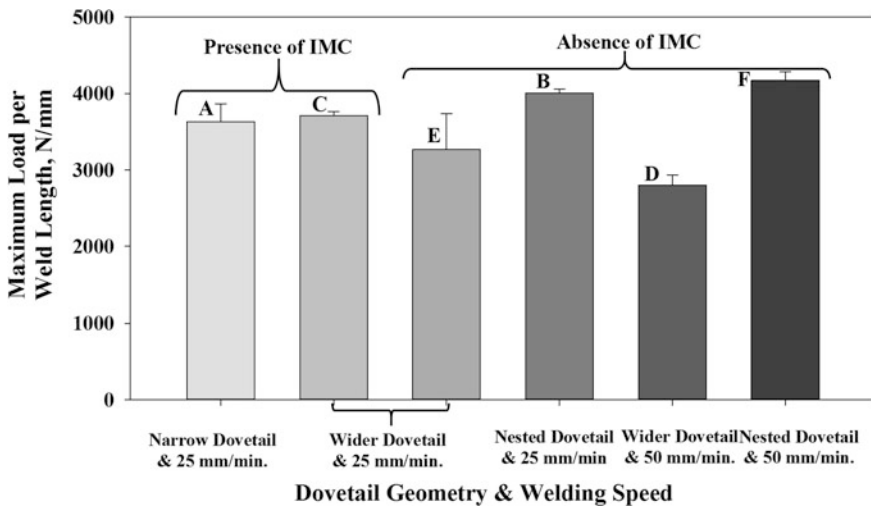


Fig. 7 Maximum tensile load per unit length as a function of dovetail geometry and welding speed

capacity provided by nested dovetails is due to the additional interlocking that resists deformation in the tensile and transverse directions. In the absence of IMC, there does not appear to be a statistical difference in the load at failure on the weld speed range of 25–50 mm/min. However, inclusion of the IMC within the wider single dovetail at 25 mm/min was found to increase strength compared to the case of no IMC. This speaks to the important role of IMC formation for improving joint strength. The narrow dovetails welded at 25 mm/min have IMC formation outside the dovetail (see Fig. 5) and interestingly show higher strength than the wider dovetails with IMC. From this data, we concluded that the formation of IMCs significantly improves joint strength. An ongoing focus of the research is to develop tooling and process conditions that result in formation of IMCs within wider and nested dovetail geometries.

Interestingly, the dovetail geometries play a significant role in tensile test failure which is described using Fig. 8. The normalized load (load per unit weld length) as a function of extension for different dovetail geometries is plotted in Fig. 8. The images of the failed specimens for corresponding load versus extension curves are also presented in Fig. 8. Failure of the narrower dovetail specimen (A) occurred due to fracture of the brittle intermetallic layer on one side of the sandwich structure at peak load which is followed by ductile failure (Curve A) of bulk Al due to eccentric loading. For the load curves D and E, successive separation of dovetails occurred after reaching the maximum load as the dovetails tend to unzip one pair after another. This phenomenon is indicated by the sharp changes in slope of the load curves on their descending part as tensile testing progress to joint failure. For the nested dovetail welded at 25 mm/min corresponding to load curve C, failure

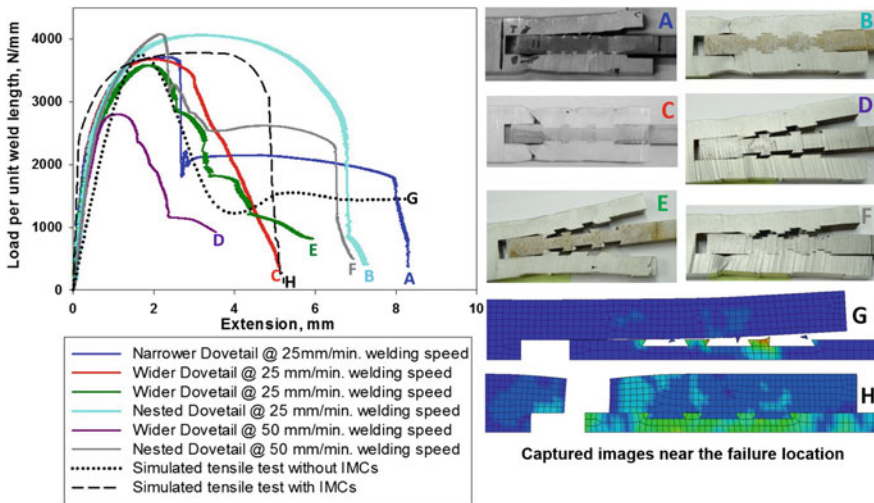


Fig. 8 Representative load versus displacement curves of the tensile test on different welding speed and dovetail geometries (*left*). *Right* Tensile samples illustrating the fracture pattern

occurred in the processed Al rather than at the dovetail interlock. As mentioned earlier the volume of the filled Al in the nested dovetail is high enough to encounter the tensile loading near the region of the additional interlock, resulting in failure in the Al with the failure plane perpendicular to the loading direction. The failure of the tensile specimen corresponding to load curve C is also similar to Curve B. However, an additional contribution of bonding between Al and RHA with the formation of IMCs resulted in a bulk Al failure, which was also confirmed from Fig. 6. This failure mode was also predicted using FEA in which it was suggested that simultaneous process of FSD and intermetallic formation improve the joint efficiency.

The predicted force-displacement graphs were also compared in Fig. 8 using curves G and H for no IMC and with IMC bonding respectively. In both simulated tensile test results, the load increases to peak indicating the initial failure in dovetail (curve G) or necking of bulk Al (curve H). However, the descending part of the curve behave differently as load beings to drop. Beyond the peak load, simulated curve G captures the successive failure of dovetail followed by the ductile behavior of the lap joint before the complete collapse of all three dovetails. Moreover, curve H captures the general characteristics of the stress-strain curve for AA6061-O [15]. This is because the IMC bonding along dovetail interfaces of Al-RHA resulted in a ductile failure of bulk Al rather than at joint.

Conclusions

The following conclusions can be drawn from this study:

1. FSD is capable of extruding aluminum into dovetail grooves of a bottom RHA plate in the lap joint configuration.
2. Structural analysis using FEA indicates that IMC formation improves joint efficiency in the FSD process.
3. Formation of IMCs along the Al-RHA dovetail interface requires physical contact between the stir tool and RHA.
4. Nested dovetails result in higher joint strength than single dovetails.

From the results obtained in this study it is anticipated that, the FSD process can be extended to a wide range of material stack-up (50 mm or higher thickness) to form dovetail interlock.

Acknowledgements This work was supported by the US Army Tank Automotive Research, Development and Engineering Center. The Pacific Northwest National Laboratory is operated by the Battelle Memorial Institute for the United States Department of Energy under contract DE-AC06-76LO1830.

References

1. Thomas WM (1998) Friction stir welding and related friction process characteristics. In: Paper presented at the 7th international conference on joints in aluminum, Abington, Cambridge, United Kingdom
2. Nishihara T (2003) Development of friction stir forming. *Mater Sci Forum* 426–432: 2971–2978
3. Lazarevic S, Miller SF, Li J, Carlson BE (2013) Experimental analysis of friction stir forming for dissimilar material joining application. *J Manuf Process* 15:616–624
4. Evans WT, Gibson BT, Reynolds JT, Strauss AM, Cook GE (2015) Friction stir extrusion: a new process for joining dissimilar materials. *Manuf Lett* 5:25–28
5. Tanaka T, Morishige T, Hirata T (2009) Comprehensive analysis of joint strength for dissimilar friction stir welds of mild steel to aluminum alloys. *Scripta Mater* 61:756–759
6. Kimapong K, Watanabe T (2005) Lap joint of A5083 aluminum alloy and SS400 steel by friction stir welding. *Mater Trans* 46(4):835–841
7. Movahedi M, Kokabi AH, Reihani SMS, Cheng WJ, Wang CJ (2013) Effect of annealing treatment on joint strength of aluminum/steel friction stir lap weld. *Mater Des* 44:487–492
8. Ogura T, Saito Y, Nishida T, Nishida H, Yoshida T, Omichi N, Fujimoto M, Hirose A (2012) Partitioning evaluation of mechanical properties and the interfacial microstructure in a friction stir welded aluminum alloy/stainless steel lap joint. *Scripta Mater* 66:531–534
9. Watanabe T, Takayama H, Yanagisawa A (2006) Joining of aluminum alloy to steel by friction stir welding. *J Mater Process Technol* 178:342–349
10. Chen CM, Kovacevic R (2004) Joining of Al 6061 alloy to AISI 1018 steel by combined effects of fusion and solid state welding. *Int J Mach Tools Manuf* 44:1205–1214
11. Kundu S, Roy D, Bhola R, Bhattacharjee D, Mishra B, Chatterjee S (2013) Microstructure and tensile strength of friction stir welded joints between interstitial free steel and commercially pure aluminum. *Mater Des* 50:370–375
12. Lee W-B, Schmuecker M, Mercardo UA, Biallas G, Jung S-B (2006) Interfacial reaction in steel–aluminum joints made by friction stir welding. *Scripta Mater* 55:355–358
13. Patterson EE, Hovanski Y, Field DP (2016) Microstructural characterization of friction stir welded aluminum–steel joints. *Metall Mater Trans A* 47(a):2815–2829
14. Sato YS, Kokawa H, Enomoto M, Jogan S (1999) Microstructural evolution of 6063 aluminum during friction-stir welding. *Metall Mater Trans A* 30(A):2429–2437
15. Abood AN, Saleh AH, Abdullah ZW (2013) Effect of heat treatment on strain life of aluminum alloy AA 6061. *J Mater Sci Res* 2(2):51–59

Joining Aerospace Aluminum 2024-T4 to Titanium by Friction Stir Extrusion

William Todd Evans, George E. Cook and Alvin M. Strauss

Abstract The welding of titanium and aluminum is difficult due to differences in their material properties and the formation of intermetallic compounds (IMCs) which can weaken the weld. A new process, Friction Stir Extrusion (FSE), has been used to join dissimilar materials by using Friction Stir Processing to extrude a top sheet of material into a pre-made, concave groove in the bottom sheet of material. FSE has been used to create a strong, mechanically interlocking joint between aluminum 6061 and steel that eliminates IMCs. However, FSE hasn't been applied to any other material combinations. This current research applies the FSE process to join aluminum 2024-T4 to commercially pure titanium. The process was optimized by adjusting the RPM, traverse rate, and groove geometry. The Al-Ti joints are evaluated based on shear strength and ultimate tensile strength. The groove geometry proved to be the most important parameter as different geometries can enhance the strength by mechanical means and by optimizing the volume and shape of the material extruded. Successful joints were created by the FSE process and can be used as a viable alternative for joining aluminum to titanium.

Keywords Friction stir processing • Aluminum • Titanium • Joining • Friction stir welding

W.T. Evans (✉) · G.E. Cook · A.M. Strauss
Department of Mechanical Engineering, Vanderbilt University,
Nashville, TN 37235, USA
e-mail: William.T.Evans@Vanderbilt.edu

G.E. Cook
e-mail: Al.Strauss@Vanderbilt.edu

A.M. Strauss
e-mail: George.E.Cook@Vanderbilt.edu

Introduction

High strength aluminum alloys are used extensively in the aerospace, automotive and ship building industries due to their strong mechanical properties and low weight compared to other materials such as steel. Titanium also has a high strength to weight ratio in addition to corrosion resistance which makes it another widely used material in these fields. With increasing use of these materials, there is a need to find more effective and innovative ways of joining these two dissimilar materials.

The welding of titanium and aluminum is difficult due to differences in their material properties and the formation of intermetallic compounds (IMCs) which can weaken the weld. Numerous joining techniques have been proposed such as diffusion bonding [1–3], laser welding [4], friction welding [5, 6], friction stir welding [7, 8], and ultrasonic welding [9] to name a few. Each of these methods provides a way to join aluminum and titanium and can be used for different geometries and material thicknesses. Previous research introduced a new technique called Friction Stir Extrusion [10] that showed a new way to join aluminum 6061 to steel. This process relies on the Friction Stir Welding (FSW) process to extrude material into a preformed concave groove. The process eliminates the issues of IMCs by creating a mechanical joint of dissimilar materials. The formation of intermetallic compounds has limited the strength of most aluminum to titanium friction stir welds and therefore is a prime candidate to test the feasibility of an aluminum/titanium joint formed by FSE. This research seeks to prove the ability to use the fundamentals of the FSE process to join aluminum 2024-T4 to commercially pure titanium.

Materials and Methods

The materials used in this research are commercially available 2024-T4 Aluminum and Grade 2, 99% pure titanium bars. The 2024 material was rated at 324 Mpa yield strength and the titanium was 275 Mpa. The bars of each material were cut into 155 mm by 52 mm by 6.35 mm thick sections. The titanium bar was prepared for Friction Stir Extrusion (FSE) by creating a concave groove 15 mm from the edge of the material. The initial size of the groove was chosen based on the previous research in FSE of 6061 to steel and was an o-ring groove of 3 mm depth, 48° included angle and a neck diameter of 3 mm. As will be discussed later, this groove setup did not create successful FSE joints and additional groove geometries were implemented.

The 2024-T4 aluminum was positioned in a lap joint configuration over the titanium with 35 mm of overlap. This positioning kept the entire width of the FSW tool on the titanium and allowed enough overhang for tensile shear testing. The tool was chosen to maximize the flow of material. The tool was made of 25.4 mm O1 hardened tool steel with a 7° convex shoulder with six scrolls and a 6.35 mm diameter threaded probe of 4.6 mm length. The setup can be seen in Fig. 1.

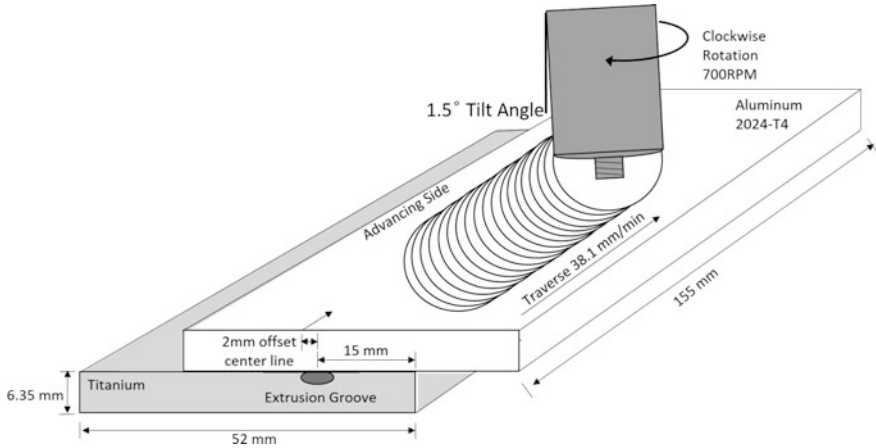


Fig. 1 Friction stir extrusion setup for joining aluminum to titanium

FSE is, essentially, a bead on plate FSW that extrudes the material into the groove. Therefore, similar FSW welding parameters from successful 2024-T4 welds were chosen. The best tensile properties obtained by Mohammed of FSW welded 2024-T4 were found at an RPM of 710 RPM and 20 mm/min traverse rate. [11] This was used as an initial starting point and FSE joints were performed at 500, 700, and 900 RPM with traverse rates of 38, 50.8, 76.2, and 101.6 mm/min. The tool was positioned at both a 0 and 1.5° tilt angle. The tool was plunged 5.3 mm into the aluminum to allow maximum engagement of the tool shoulder. This also kept the probe just above the aluminum titanium interface to prevent tool wear by only engaging the 2024 with the probe. The tool was offset from the center of the groove by 2 mm to the advancing side. This both prevents the probe from inhibiting the flow of aluminum into the groove, as was noted in FSSW welds by Lazaveric [12] and maximizes material flow into the groove.

Results and Discussion

Groove Shapes

Figure 2 shows the surface features of the FSE joint with a full o-ring groove as was presented in the previous research on FSE joining of 6061 to steel [10]. While the process was successful with the 6061 and a smooth, classic onion ring pattern was formed, this extruded volume proved to be too large to allow proper consolidation of the 2024. The extra volume of aluminum extruded into the groove left extra space in the weld zone. Some material from the advancing side was extruded down into the groove and additional material flowed behind the pin in rough

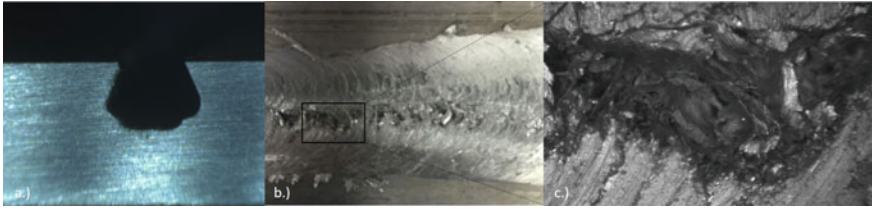


Fig. 2 O-ring groove results. **a** Full o-ring groove shape. **b** Surface finish of FSE joint with non consolidated material. **c** Magnified image of voids showing chunks of aluminum that have not been consolidated by the shoulder

chips/clumps. Since there was less material behind the tool, this material accumulated at the bottom of the nugget zone at a level below the back edge of the tool. The tool shoulder could not fully engage the aluminum in the nugget area and therefore could not stir and consolidate the aluminum into a smooth surface as evidenced in Fig. 2b, c. This convex tool was designed to operate at a 0° tilt angle to compensate for any thermal expansion or uneven surface features. To improve the performance of the tool, the tilt angle was changed to 1.5° lead angle. This improved the ability to consolidate the material since the back edge of the shoulder was engaged deeper in the material, but it still could not overcome the volumetric void issue.

To address this problem, 3 new groove shapes that required less volume were created, as pictured in Fig. 3. For the first groove, a slit saw was used to create two opposing slits, 2 mm deep at 45° angle to the surface. This left behind a triangular wedge of titanium to help direct the extruded aluminum into both slits. The second groove shape created a modified dovetail by widening the cross-sectional area at the surface of the slot to 3 mm and milling out the triangular wedge of material. This groove left a small section of the slit intact while allowing for more material to flow into the groove. The third adjusted groove shape was created by raising the o-ring cutter depth from 3 to 2 mm. This reduced the volume of the full o-ring cut by about 30% but still allowed a slightly concave region in the groove to hold the 2024. These changes allowed for successful FSE joints with a good surface finish to be achieved.

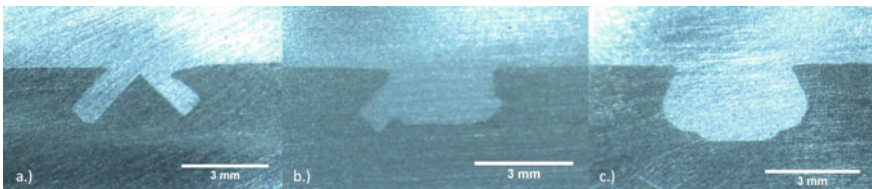


Fig. 3 Friction stir extrusion groove shapes. **a** Slit saw groove. **b** Modified slit saw groove. **c** Modified o-ring groove

RPM and Traverse

Figures 4, 5 and 6 show the effects of RPM and traverse rate on the surface of the joints. Figure 5 shows the full depth of the top plate of aluminum with the surface shape of the joint and the extruded region. Successful joints were formed at both 500 and 700 RPM at 50.8 mm/min. However, the surface of the joint was more evenly distributed across the width of the weld and better consolidated at 700 RPM as can be seen in Fig. 6 represented by the solid orange line with square markers. At 900 RPM and 50.8 mm/min visible voids/worm holes were formed in the weld as noted on Figs. 4 and 6. At 900 RPM the tool creates coarser onion rings and deposits more of the aluminum on the retreating side. This deposit of material on the retreating side does not leave enough material to be fully consolidated back into the FSE joint in the nugget region on the advancing side which leads to void formation.

700 RPM was set as successful parameter for consolidated joints and three additional traverse rates were tried to see their impact on the joint. Successful FSE joints were produced at 700 RPM and 38.1, 50.8, 76.2, and 101.6 mm/min. The slower rate of 38.1 mm/min produced a very smooth finish that covered almost the entire width of the joint. At the higher traverse rates, the onion rings were not as consistent and smooth and did not cover the entire width of the joint as seen in Fig. 6 where the right side of the joint has more material built up on it. This shows that the shoulder did not engage as evenly with the material on the advancing and retreating side. These results indicate that as the tool traverses more quickly, there is less time to stir the material and less heat input into the joint for the material to be sufficiently plasticized and stirred evenly across the width of the weld. In addition, the faster traverse rates led to higher axial forces in the x and y directions that started to approach the safety limits of the dynamometer. Given these results 700 RPM and 38.1 mm/min were chosen as parameters that led to the best joints.

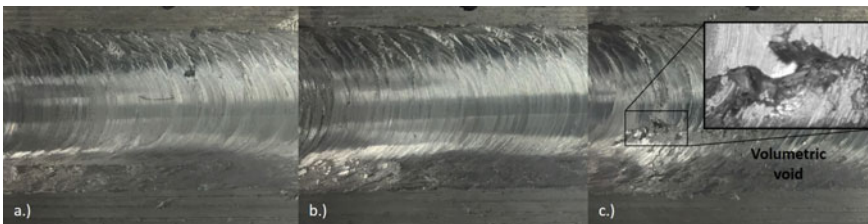


Fig. 4 Surface finish of FSE joints at 50.8 mm/min. **a** 500 RPM. **b** 700 RPM. **c** 900 RPM

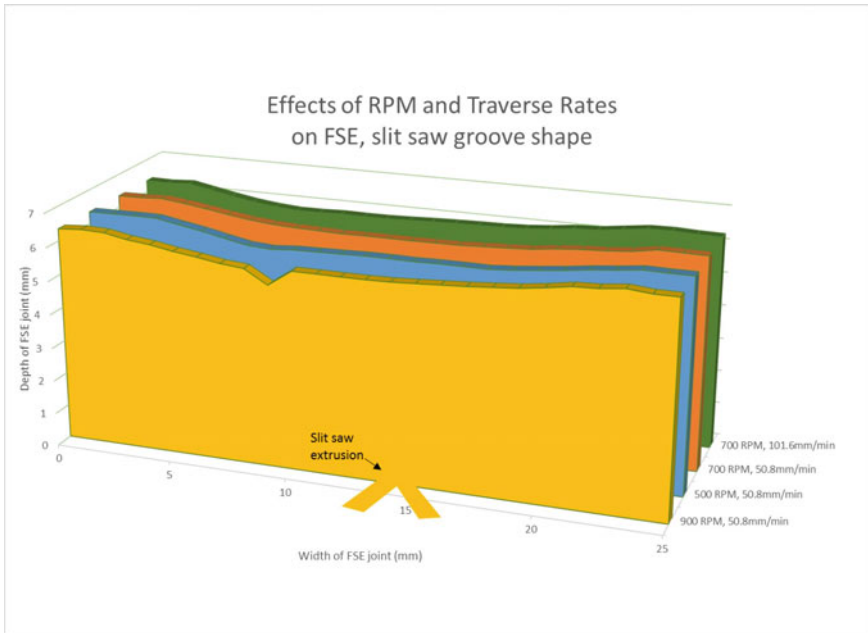


Fig. 5 Surface finish of FSE joints at different RPMs and traverse rates

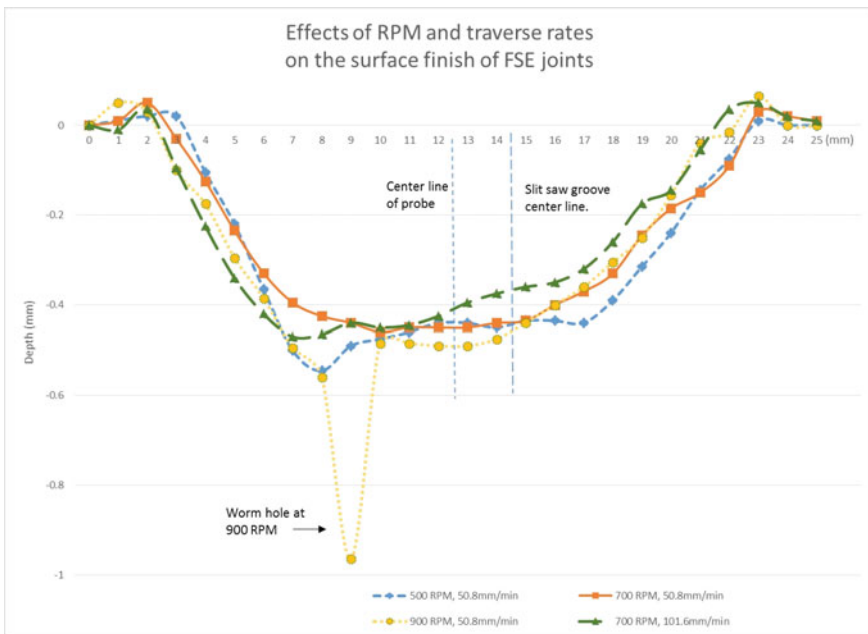


Fig. 6 Surface plot of effects of RPM and traverse rates for FSE joints

Tensile Results

Samples of the three modified grooves were cut into smaller samples for tensile testing. Tensile shear testing was completed on an Instru-met Model TTC-102MC tensile testing machine with a 5,000 kg capacity. The samples were tested at a rate of 5 mm/min and sampled at 10 Hz.

The cross-sectional area of the material in shear dictates the shear strength of the joint. For consistency across the groove shapes, the widest area of the neck at the surface of the steel plate was used to calculate the cross-sectional area used to determine the shear strength. For the first modified groove with the slit saw cuts and the triangular section of titanium, the average shear strength was 198.9 Mpa, which is 70% of the parent material. For the second modified dovetail groove with the widened opening and the triangular feature milled out, the average shear strength of the material was 164 Mpa, which is 58% of the parent material. The third modified groove created with a shallower o-ring cut had an average shear strength of 170.5 Mpa, which is 60% of the parent material. These results can be seen and compared in Fig. 7.

The shear strength gives a good way to compare the strength of the cross-sectional area of the extruded material to that of the parent material, but load bearing applications will also need to know the peak load strength of the joint. Therefore, the peak load strength for a 6.35 mm wide specimen was used to evaluate the overall strength of the joint. All peak load strength values were normalized to this value of 6.35 mm to account for small variations in actual sample width. The highest average peak load obtained was 386 kgf for the modified o-ring.

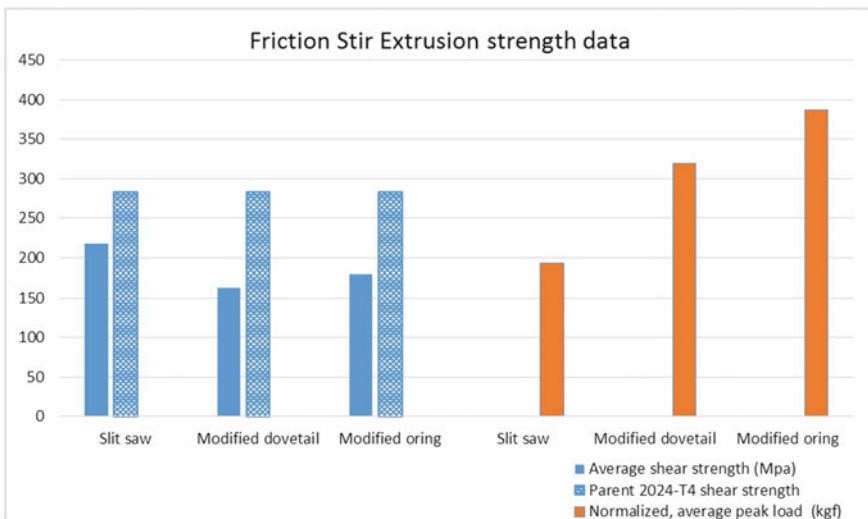


Fig. 7 Friction stir extrusion shear strength and peak loads for different groove geometries

The modified slit saw groove had a peak load of 319 kgf and the slit saw groove was 193 kgf. So, while the slit saw groove had the best shear properties at 70% of the parent material, the average peak load was 50% less than that of the modified o-ring groove. This makes sense physically given that the distance across the neck of the modified o-ring groove is just over twice that of slit saw groove and this extra cross-sectional area contributes to the much higher peak load of the joint.

Discussion

Examination of the joints after fracture reveals that no intermixing or bonding occurred between the aluminum and titanium. This eliminates the concern over IMCs at the interface weakening the joint and provides a good way to join the materials. These results also show that the strength of the FSE joint for this particular setup is determined only by the physical properties of the joint. The main contributions to the strength based on the physical setup in this research are frictional forces, clinching, volume of material, and cross-sectional area of the smallest region.

The two basic types of geometries of the shaped slit saw versus the extruded volume of the modified dovetail/o-ring give further insight into the optimization of the FSE process. The slit saw groove represents a groove geometry that leads to better overall strength per volume of material extruded. It does this by adding other mechanical elements that contribute to the strength of the joint. First, the opposing slit saw angles act as anchors that increase the surface area in contact between the two materials. This adds to the overall strength both by keeping the material in true shear with no bending until close to failure, and by increasing the frictional and mechanical resistance. Secondly, it can be seen in the polished groove section in Fig. 3a that the titanium at the lip of the joint has been deformed downward by the z force of the FSE machine. This acts as a clinching force that also helps keep the joint in line while in tension and thus, increases the overall strength. This result is both a limiting factor and an opportunity to increase the strength. It is limiting because materials must be chosen that can withstand the strong z force of the FSE process, as well as, dictating limits on how much overhang can be designed into the groove edge geometry. However, it also provides an opportunity to use the natural deflection, clinching or other mechanical deformation features to enhance the strength of the weld.

In contrast to the slit saw, the o-ring groove uses more volume and increases the cross-sectional area. It resembles a solid chunk of material and its strength is almost entirely dependent on the cross-sectional area of the material. Figure 8b, c show that before joint failure, the aluminum is elongated and a space forms at the back side of the groove. This space eventually negates the ability of the concave shape to hold the material. This creates a rotation of the extruded material that adds stress to the material and quickly leads to failure.

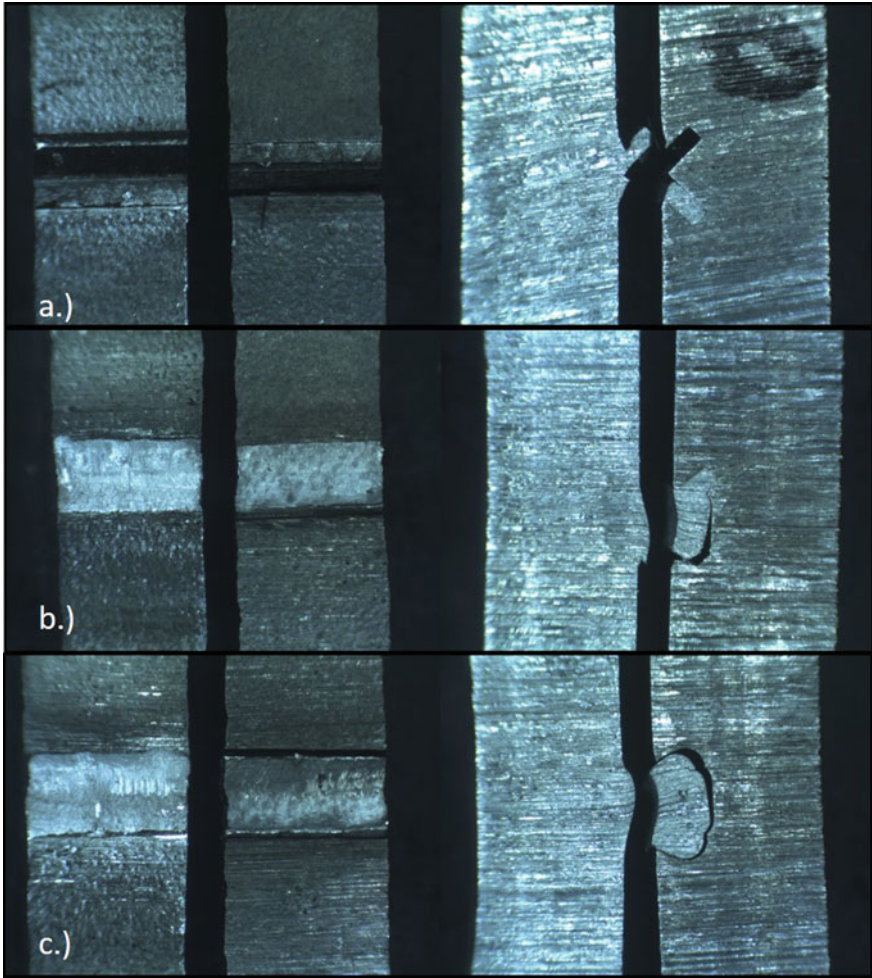


Fig. 8 Failure surfaces and profiles of 3 FSE groove shapes. **a** Slit saw groove. **b** Modified slit saw groove. **c** Modified o-ring groove

These results show that the ultimate tensile strength of the joint can be increased by increasing the cross-sectional area. However, increasing the cross-sectional area can necessitate a larger volume, unless the volume of the groove is decreased by other means such as making a shallower cut. Shallower cuts can lead to less depth and less ability to create a concave region to extrude into. Therefore, each of these considerations must be assessed for the individual application. In this research the plates were thick to allow for more volume of material to be available for extrusion into the weld. Therefore, the geometry that could form a successful joint and create the largest cross-sectional area will be the most successful as can be seen is the case for the modified o-ring in this paper. However, many applications such as the

aerospace industry use thinner sheet material. Thinner sheets have less material available for extrusion into the groove and groove geometry will become a key design component. Geometries like the slit saw groove that add mechanical properties to the joint and enhance the overall strength will likely prove more effective for most applications. In addition, other materials could be used as an interlayer between the materials in order to add additional strength. This could be achieved by using a material that can be brazed during the process to provide a better locking or adding a sealant that can increase the rigidity of the joint.

Conclusions

The Friction Stir Extrusion process was used to join aluminum 2024-T4 to commercially pure titanium. It has been shown that:

1. Successful Friction Stir Extrusion joints were formed at 700 RPM and 38.1 mm/min.
2. Joints exhibited a shear strength of up to 70% of the parent material.
3. No intermixing of aluminum and titanium occurred, minimizing concerns of IMCs.
4. Three different groove geometries were successfully used while one was unsuccessful. The groove geometry is the most significant factor in both the success and strength of FSE joints.
5. FSE joint strength is a combination of cross-sectional area of the extruded material and mechanical attributes that contribute to the overall strength.
6. The process was applied to thick sheet material to allow for more material extrusion, but optimized joint geometries should allow for application to thin sheet materials and increases in overall strength.

Acknowledgements This work was supported by the NASA Tennessee Space Grant Consortium.

References

1. Jiangwei R, Yajiang L, Tao F (2002) Microstructure characteristics in the interface zone of Ti/Al diffusion bonding
2. Miyagawa K, Tsubaki M, Yasui T, Fukumoto M (2009) Spot welding between aluminium alloy and Zn-coated steel by friction stirring. *Weld Int*
3. Wilden J, Bergmann JP (2004) Manufacturing of titanium/aluminium and titanium/steel joints by means of diffusion welding 3(5):285–290
4. Anawa EM, Olabi AG, Elshukri FA (2009) Modeling and optimization of tensile shear strength of titanium/aluminum dissimilar welded component. *J Phys: Conf Ser* 181:12033
5. Fuji A (2002) In situ observation of interlayer growth during heat treatment of friction weld joint between pure titanium and pure aluminium. *Sci Technol Weld Join* 7(6):413–416

6. Fuji A, Ameyama K, North TH (1995) Influence of silicon in aluminium on the mechanical properties of titanium/aluminium friction joints. *J Mater Sci* 30(20):5185–5191
7. Chen YC, Nakata K (2008) Microstructural characterization and mechanical properties in friction stir welding of aluminum and titanium dissimilar alloys
8. Aonuma M, Nakata K (2011) Dissimilar metal joining of 2024 and 7075 aluminium alloys to titanium alloys by friction stir welding. *Mater Trans* 52(5):948–952
9. Zhang CQ, Robson JD, Prangnell PB (2016) Dissimilar ultrasonic spot welding of aerospace aluminum alloy AA2139 to titanium alloy TiAl6V4. *J Mater Process Technol* 231:382–388
10. Evans WT, Gibson BT, Reynolds JT, Strauss AM, Cook GE (2015) Friction stir extrusion: a new process for joining dissimilar materials. *Manuf Lett* 5:25–28
11. Kassim Mohammed H (2011) A comparative study between friction stir welding and metal inert gas welding of 2024-t4 aluminum alloy 6(11)
12. Lazarevic S, Miller SF, Li J, Carlson BE (2013) Experimental analysis of friction stir forming for dissimilar material joining application. *J Manuf Process* 15(4):616–624

Dissimilar Metal T-Joint of Aluminum and Steel Formed by Friction Stir Extrusion

Adam W. Jarrell, Alvin M. Strauss and George E. Cook

Abstract This paper extends the capabilities of the Friction Stir Extrusion process by demonstrating the ability to join aluminum and steel in a T-joint configuration. Friction Stir Welding techniques are used to extrude aluminum into a concave groove cut into the top edge of a steel plate. The Friction Stir Extrusion process forms a mechanical joint avoiding many of the detrimental effects from the formation of intermetallic compounds. Also, eliminating many of the issues of rapid tool wear associated with the Friction Stir Welding of steel. The T-joint configuration would allow joining of dissimilar materials in a variety of applications, such as joining an aluminum skin to a steel/titanium frame. Such construction would allow for a strong, lightweight, and corrosion resistant structures. Strength of the joint was tested in tension to determine the quality of the weld. The average failure strength of the joint was 47.66 Kgf/mm.

Keywords Friction stir welding • Friction stir processing • Friction stir extrusion • T-joint • Dissimilar metals • Low carbon steel • 6061 aluminum

Introduction

In recent years, manufactures in the auto, aerospace, and other industries have been moving to the production of more energy efficient products. Energy efficiency can be achieved by weight reduction. To realize this goal, lighter materials, like composites, aluminum, and titanium, are replacing heavier steel. The new diversity of materials used led a need for effective methods of joining dissimilar materials.

A.W. Jarrell (✉) • A.M. Strauss • G.E. Cook
Vanderbilt University, Nashville, USA
e-mail: adam.w.jarrell@vanderbilt.edu

A.M. Strauss
e-mail: al.strauss@vanderbilt.edu

G.E. Cook
e-mail: george.e.cook@vanderbilt.edu

Welding dissimilar materials with common welding methods is difficult or impossible, because of differences in materials properties. In addition, bolts, screws, rivets, and adhesives have limited use and can add costs.

Friction Stir Welding has produced limited success. Some success has been found using assisted FSW [1]. Other attempts to weld two materials directly with FSW have encountered two issues. The formation of intermetallic compounds weaken the joint [4], or the tool will experience rapid wear due to contact with the harder material.

Friction Stir Extrusion is a promising technique to joint dissimilar materials. FSE is a technique that uses Friction Stir Welding to join material by extrusion into a preformed structure [2]. The softer of the two materials is extruded into a preformed structure in the harder material. The interlocking of the two materials forms a permanent mechanical joint. It shares many of the benefits of FSW. There are no consumables used in the process, because there is no need for a shielding gas or filler material. Since the tool stays in the softer of the two materials, there is little tool wear, and the formation of intermetallic compounds is avoided by the tool only interacting one material. Finally, the process can be preformed with little to know special set up over a typical weld.

This contribution extends the Friction Stir Extrusion process by demonstrating its use to form a T-Joint between steel and aluminum.

Method

Dovetail grooves were cut in a 50.8×9.525 mm low carbon steel bar stock using an O-ring dovetail cutter. The cutter had a neck diameter of 2.946 mm and included angle of 48° . The grooves were cut to a depth of 2.794 mm, Fig. 1. A 76.2×6.35 mm aluminum bar was laid on top the steel in a T-Joint configuration.

Fig. 1 The O-ring groove cut into the edge of low carbon steel plates to a depth on 2.794 mm

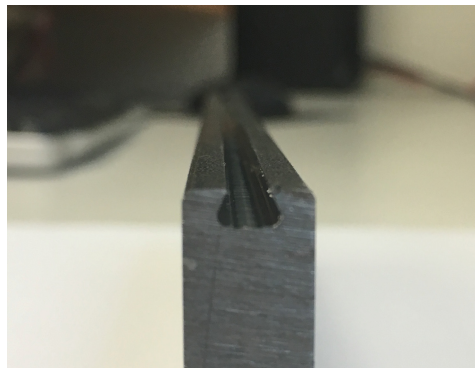


Fig. 2 Modified milwaukee milling machine used to weld the T-joints

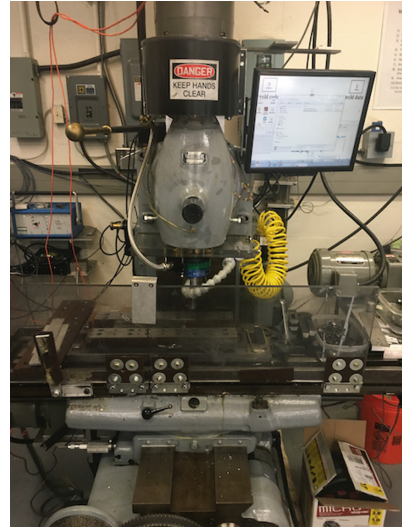
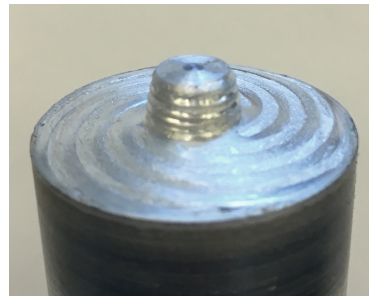


Fig. 3 Convex tool with scrolls and threaded pin used in the FSE process



The welds were done using a Milwaukee #2K Universal Horizontal Milling Machine modified for FSW, Fig. 2. The milling machine has three motorized axis and position control based upon in-house code. The metal plates were clamped to the table of the milling machine using an in-house fixture.

The tool used has a convex shoulder with shallow scrolls and a threaded pin. The scrolls and threaded pin create an downward flow of plasticized aluminum that should be forced into the groove. The tool is 25.4 mm diameter, and the pin is 7 mm in diameter with a length of 4.06 mm, Fig. 3.

The welding parameters were varied until the material extruded into the groove was roughly maximized. The tool was offset 2.03 mm to the advancing side from the center of the groove. Its been found that the pin can act as a plug, preventing material from flowing into the groove, [2, 3]. The tool rotation speed and transverse rate were 1500 RPM and 76.2 mm/min. The tool was plunged 5 mm into the aluminum. The tool was set at a lead angle of 1.5 degrees, Fig. 4.

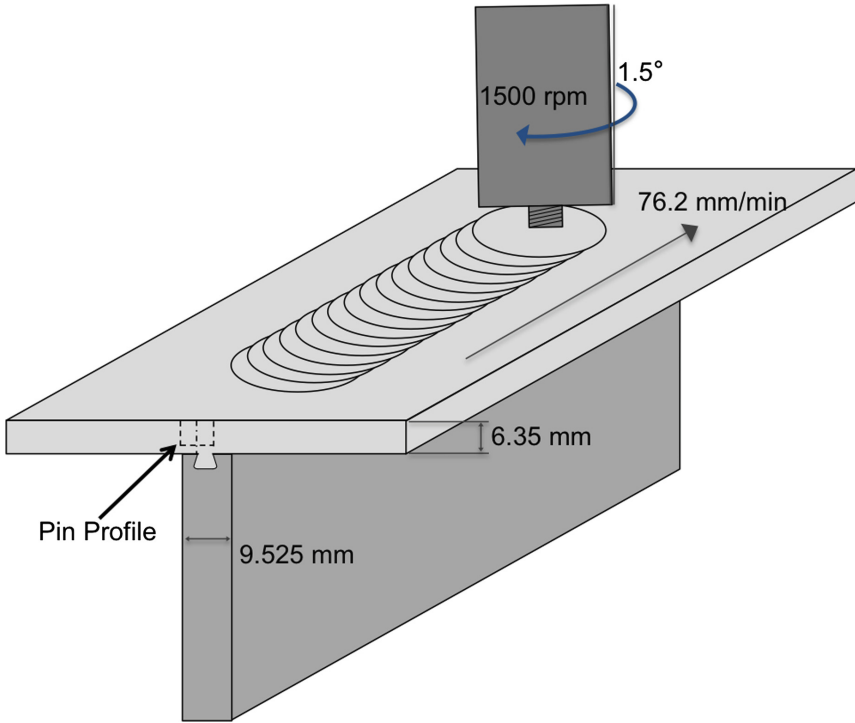


Fig. 4 The configuration of the tool with the dissimilar materials

Results and Discussion

The welds were cut into cross sections to inspect the quality of the extrusion. The weld was completely filled except for a small void on the lower left side of the groove, Fig. 5b. The left side of the weld in the image corresponds to the side closest to the pin during the weld. So, the void could be due to the pin obstructing the flow into the groove, or insufficient time under the tool for the aluminum to flow into the groove.

Also, thinning of the aluminum can be seen in Fig. 5a. The material was thinned the most on the advancing side of the tool indicating that a substantial amount of the material extruded into the joint came from the advancing side.

Samples, approximately 6.35 mm in thickness, were tested in tension by a tensile tester. The ultimate tensile strength of the joints were scaled by the measured width of the sample to account for variations. The average failure strength of the samples was 47.66 Kgf/mm, Fig. 6a. The samples failed by deformation of the aluminum fill into the steel groove, instead of the samples failing at the neck of the dovetail, Fig. 6b.

The failure of the joints doesn't seem to prefer either side. The deformation of the groove fill didn't appear to be uneven. So, the void in the lower corner of the groove had little effect on strength.

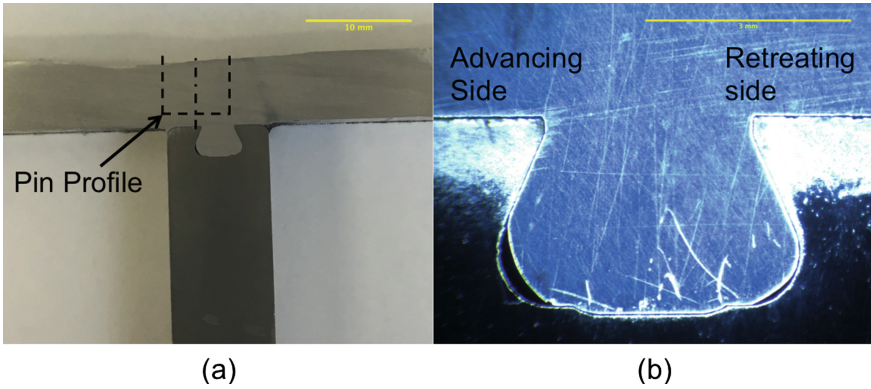


Fig. 5 **a** Cross section of the weld displaying the thinning of the aluminum from the extrusion. An overlay of the pin profile is shown. **b** Micrograph displaying the incomplete fill on the left side of the groove

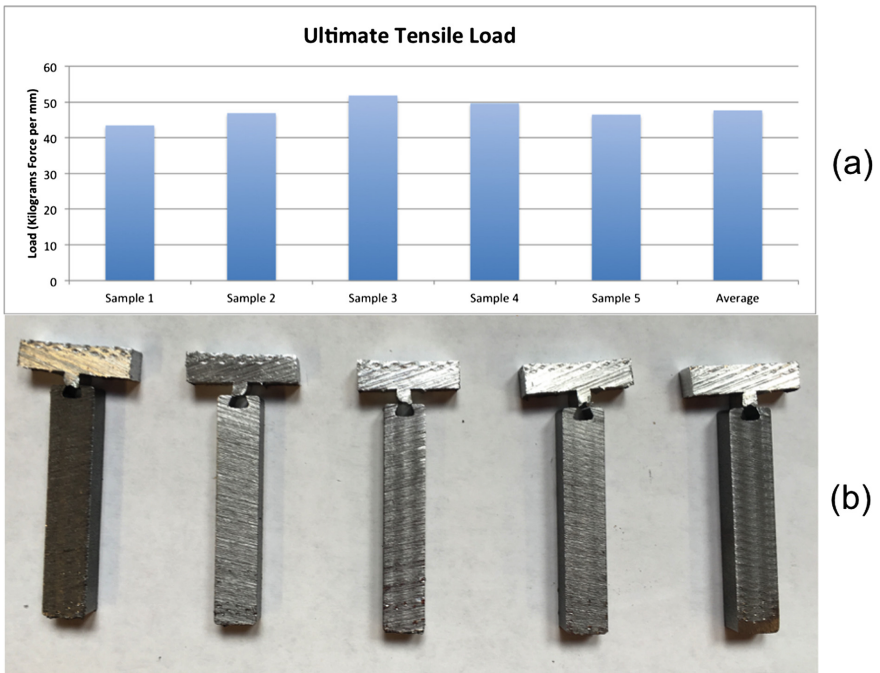


Fig. 6 **a** The ultimate tensile strength in Kgf of 6.35 mm samples. **b** The samples after tensile testing. The welds were performed at 1500 rpm and 76.2 mm/min with a lead angle of 1.5 degrees. The tool was offset 2.08 mm to the advancing side

One of the benefits of convex tools is that they can be used with little to no lead angle in typical friction stir welding operation. However, it was found that a relatively steep lead angle was required for good weld quality in this application. Large wormholes were formed when the weld was preform without a large lead angle. It is hypothesized that the tool wasn't providing sufficient welding pressure due to the material thinning. The material thinning caused the tool to lose contact with the surface when low lead angles are used.

Conclusions

FSE is a versatile process and is capable of producing strong joints between two materials with dissimilar properties without special fixtures. Successful T-Joints were created with the process, and were found to have a tensile strength of 47.66 Kgf/mm.

Because the joint failed under plastic deformation, a wider inclusion angle in the dovetail groove might produce a stronger joint. However, joints with larger cross sectional area increase the volume extruded and the thinning of the top plate. This could become an issue with thinner top plates. The process could be improved by optimizing the groove shape by considering the strength of the final joint. Other methods of offsetting the thinning could be by adding materials in process or by using welding tools with larger diameters.

Acknowledgements This work was supported by the NASA Tennessee Space Grant Consortium.

References

1. Bang H, Bang H, Jeon G et al (2012) Gas tungsten arc welding assisted hybrid friction stir welding of dissimilar materials Al6061-T6 aluminum alloy and STS304 stainless steel. *Mater Des* 37:48–55
2. Evans W, Gibson B, Reynolds J et al (2015) Friction stir extrusion: a new process for joining dissimilar materials. *Manuf Let* 5:25–28
3. Lazarevic S, Miller S, Li J et al (2013) Experimental analysis of friction stir forming for dissimilar material joining application. *J Manuf Process* 15:616–624
4. Mubiayi M, Esther A (2013) Friction stir welding of dissimilar materials: an overview. *Mech Manuf Eng Tech* 7:635–640

Part IV
Lightweight Applications

Friction Stir Welding of Thick Section Aluminium Alloys—New Techniques

Jonathan Peter Martin

Abstract There are many applications for which joining of thick section aluminium components is required; these include aircraft wing spars, liquefied natural gas tanks, armour plate, and railway headstocks. Using conventional fusion welding techniques can be challenging. Recent innovations at TWI, using the unique twin headed capabilities of the Powerstir™ friction stir welding (FSW) machine, have demonstrated several techniques that have the potential to minimise production cycle times, making joining of thick section aluminium alloys both technically and commercially advantageous. This paper describes these techniques and the work undertaken at TWI to develop them. Process benefits and weld properties are discussed highlighting the potential benefits including reduce component processing times through quicker welding and minimal part handling; improve weld quality through use of reduced and uniform heat input and increase tool life leading to reduced tooling costs.

Keywords FSW • New techniques • Thick section

Introduction

There are many applications for which joining of thick section aluminium components is required. These include aircraft wing spars, LNG tanks, armour plate, and railway headstocks. Using conventional fusion welding techniques can be challenging, as typically:

- A multi-pass technique is required, leading to low productivity;
- Component edge preparation and a shielding gas are necessary;

J.P. Martin (✉)

TWI Technology Centre (Yorkshire) Ltd, Rotherham, UK

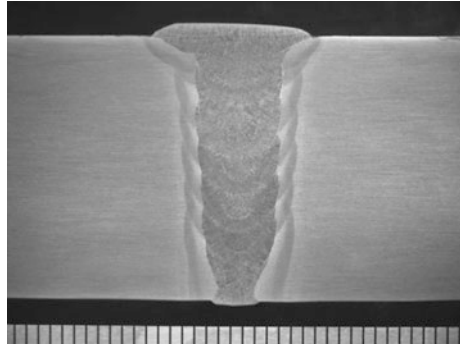
e-mail: jonathan.martin@twi.co.uk

© The Minerals, Metals & Materials Society 2017

Y. Hovanski et al. (eds.), *Friction Stir Welding and Processing IX*,

The Minerals, Metals & Materials Series, DOI 10.1007/978-3-319-52383-5_11

Fig. 1 Section through a thick section fusion weld.
 'Reproduced courtesy of TWI Ltd'



- The process is difficult to control;
- Preheat is required;
- Welds are prone to porosity and cracking;
- Welding can lead to component distortion;
- Multi-pass technique can lead to increased NDT complexity more interfaces generated by successive passes
- Some aerospace alloys in the 2xxx and 7xxx series are difficult, or impossible, to fusion weld.

A transverse section taken from a thick section fusion weld is shown in Fig. 1 showing the multi-pass weld build up.

Friction stir welding (FSW) has been the subject of rapid development and application across the world since its invention, by TWI, in 1991 [1], and is now a well-established joining technique for aluminium alloys. The majority of industrial applications involve joining components in the thickness range of 2–8 mm. Companies gain many benefits from using this technique; however, the technical and commercial benefits of joining thicker aluminium alloys are less well established. TWI has demonstrated that thick section FSW is possible and can bring many benefits; however, there are several issues:

- Short tool life due to high forces;
- Very slow welding traverse rates;
- High heat input leading to loss of weld strength;
- Uneven heat input into the weld leading to variations in hardness, weld strength and component distortion.

Typically, to weld thicker plate, a Weld-Flip-Weld approach is used. This consists of using a FSW tool with half thickness component penetration. After the first weld has been made, it is normally necessary to remove any flash from the weld surface before releasing the component from the fixture. Some plate distortion can occur, so once the partially fabricated plate has been lifted and turned, it must be placed back in the fixture and forced into position prior to completing the second weld. These additional operations (component cleaning, pilot holes, handling, and

refixturing), especially when fabricating large and heavy components, can be a very significant portion of the total time required to fabricate the component.

TWI has been developing several new FSW techniques to minimise cost, production cycle time, and weld heat input, making joining thick section aluminium alloys both technically and commercially more advantageous. All these techniques require the unique capabilities of the PowerStir FSW machine (Fig. 2) at the TWI Technology Centre. This multi-functional R&D machine has opposed, synchronised spindles. Although there are many FSW machines with opposed spindles, it is believed that this is the only machine that can run tooling capable of at least 50 mm penetration on each head. The machine specification is given in Table 1. The upper and lower spindle, housing the two FSW tools, and the slotted fixture used for welding in a simultaneous configuration, is shown in Fig. 3.

Initial trials, when simultaneously welding from either side of 50 mm thickness aluminium alloy plates, have shown that the welding speed can be significantly increased when compared with the Weld–Flip–Weld joining technique. This is explained by the additional energy from the two tools and the slotted fixture not conducting the heat away. This local heat produces a softer plasticised region around the FSW tool, providing less resistance to the passage of the tool through the material for the same tool traverse rate.

TriFlat™ probes have been used during these trials. The tools are typically operated in a staggered configuration with probe paths overlapping producing a volume of double processed material in the component midplane. A typical weld section is shown in Fig. 4. However it is possible to run the tools directly opposed

Fig. 2 TWI's PowerStir FSW machine. 'Reproduced courtesy of TWI Ltd'



Table 1 PowerStir specifications

Parameter	Unit	Upper spindle	Lower spindle
Rotation speed	RPM	1000	1000
Torque	Nm	2350	1300
Downforce force capacity	kN	15	10
Welding force capability	kN	10	10

'Reproduced courtesy of TWI Ltd'

Fig. 3 Welding in a simultaneous configuration. 'Reproduced courtesy of TWI Ltd'

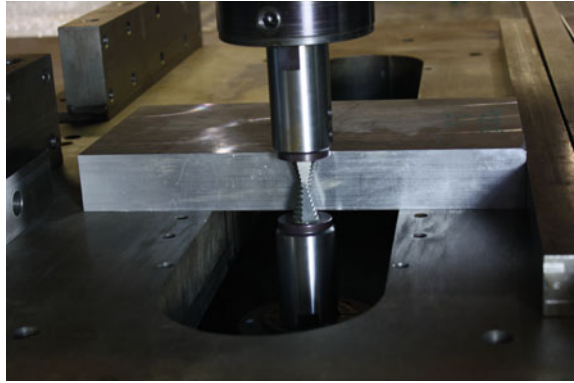


Fig. 4 Simultaneous welding with probe overlap (transverse weld section). 'Reproduced courtesy of TWI Ltd'

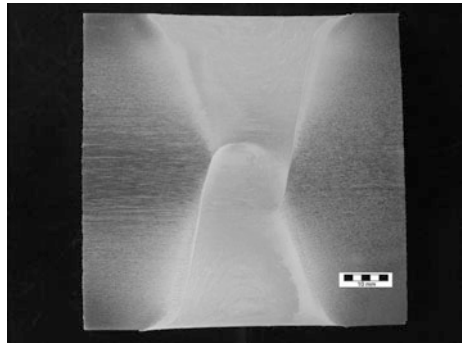
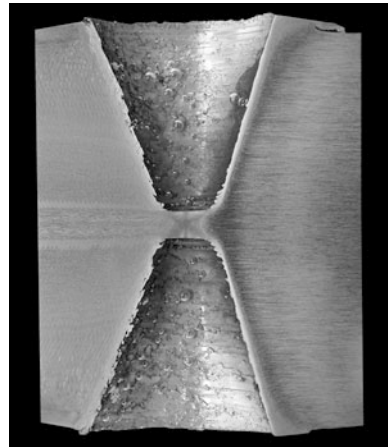


Fig. 5 Simultaneous welding with probe gap (longitudinal weld section). 'Reproduced courtesy of TWI Ltd'



leaving a small gap between them. A longitudinal weld section taken where the two tools have exited the component is shown in Fig. 5. This clearly shows the wrought rolled component macrostructure in advance of the tools and how this has been

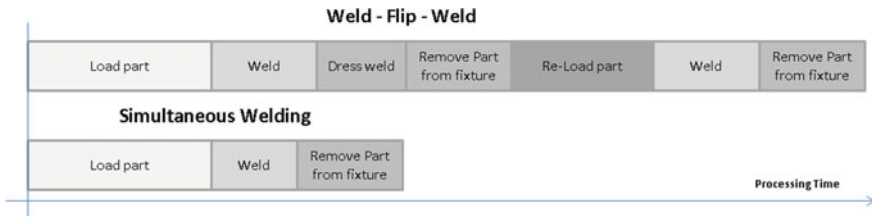
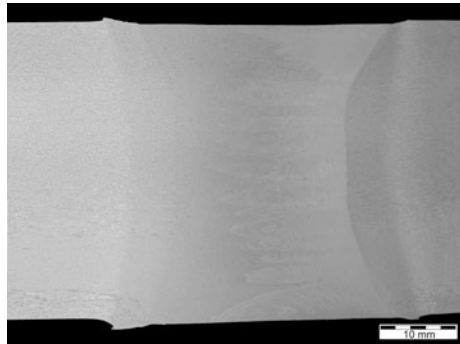


Fig. 6 Total processing time using Weld-Flip-Weld and simultaneous welding techniques

Fig. 7 A macrograph taken from a bobbin weld made in 40 mm thickness AA6082-T6. 'Reproduced courtesy of TWI Ltd'



processed to a finer more equiaxed grain structure by the passage of the tools and the interaction between the two probe tips.

The effect on the total process cycle time using simultaneous welding is very significant, as shown in Fig. 6. Not only is the welding time reduced, but also secondary operations such as handling, dressing, and refixturing of a potentially distorted component are eliminated. However, these benefits have to be considered against the increased capital cost of ownership of a more capable FSW machine.

TWI are developing other techniques for welding thick section components in a single setup. The first of these techniques is called supported bobbin FSW. TWI has developed the floating bobbin FSW technique, which has many advantages over conventional FSW; however, as the component thickness increases, it becomes increasingly difficult to control the position of the bottom bobbin shoulder. Figure 7 shows a macrograph taken through a weld made in 40 mm thickness AA6082-T6, which shows that the upper and lower weld surfaces are not parallel. There is a narrowing of the section on the weld advancing side (right) and a thickening on the retreating side. This phenomenon was termed 'wedging'. The probe connecting the upper and lower shoulder of the bobbin is therefore rotating in an abnormal manner during welding, which leads to premature tool failure. In the supported bobbin FSW technique, the bottom shoulder is radially restrained by a bearing in the under head as shown in Fig. 8. An example of a weld made using this technique is shown in Fig. 9. This weld was made in 50 mm thick AA5083-O, produced using a welding speed of 85 mm/min, without tool failure, and the upper and lower weld surfaces

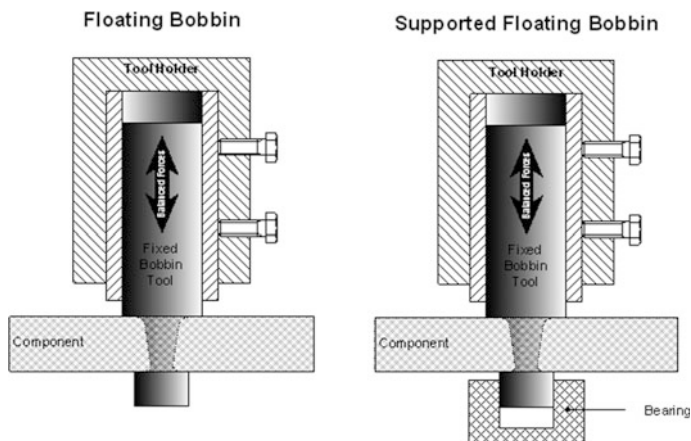
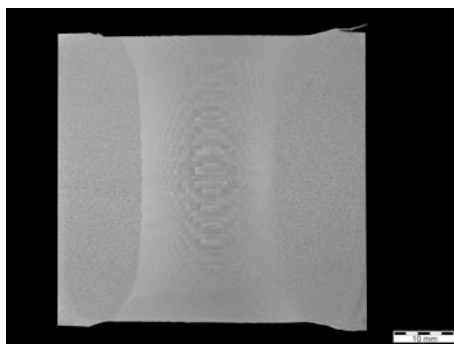


Fig. 8 Schematic drawing of floating bobbin FSW and supported bobbin FSW. ‘Reproduced courtesy of TWI Ltd’

Fig. 9 Macrograph taken from a supported bobbin weld in 50 mm thickness AA5083-O. ‘Reproduced courtesy of TWI Ltd’



were nominally parallel. A comparison on the potential benefits of the supported bobbin FSW technique to fusion welding 50 mm thickness AA5083-O is given in Table 2.

Further trials were undertaken to assess the performance of smaller sized bobbin tools. Using conventional floating bobbin tools to join 25 mm thickness AA5083-O, the maximum welding speed which could be realised was 100 mm/min without wedging. Using a bobbin tool design featuring a smaller probe and shoulders, it was possible to increase the tool rotation speed, and also welding speed to 180 mm/min, using the supported bobbin technique. The calculated spindle energy required to make these welds reduced from 4.7 kJ/mm for the larger tool to 2.5 kJ/mm for the supported smaller tool. Macrographs taken from these welds are shown in Figs. 10 and 11 respectively.

The benefits of using smaller tooling were demonstrated, as welds could be made at higher traverse speeds. Supporting the lower shoulder assisted in reducing

Table 2 Comparison between fusion and FSW welding a 1-m long component 50 mm thickness AA5083-O

Fusion	FSW
Recommended double sided weld (Pre heating)	One setup welding technique
V-Prep on both sides (~2h)	None
Consumable wire diameter 1.2 mm; weight around 10 kg	None
25 passes each side (Total of 50 passes for both sides)	1 pass
Flip plate over after each pass (To reduce distortion)	None
Average weld speed 1 m/min	Weld speed 85 mm/min
50 min welding time	12 min welding time
Total of 6 h including prep and handling	Total of 1 h including handling
Weld UTS around 95% of parent material	Weld parent strength
Expected distortion in transverse plane, around 10°	Expected distortion in transverse plane, less than 1°

'Reproduced courtesy of TWI Ltd'

Fig. 10 Macrograph taken from a supported bobbin weld in 25 mm thickness AA5083-O using a 24 mm diameter probe. 'Reproduced courtesy of TWI Ltd'

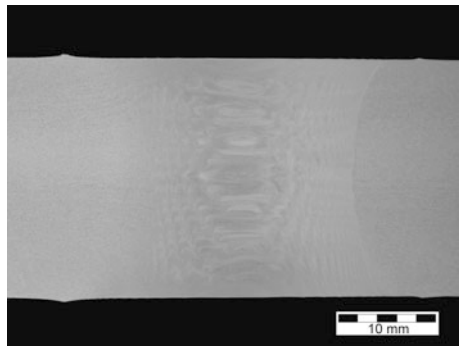


Fig. 11 Macrograph taken from a supported bobbin weld in 25 mm thickness AA5083-O using a 16 mm diameter probe. 'Reproduced courtesy of TWI Ltd'

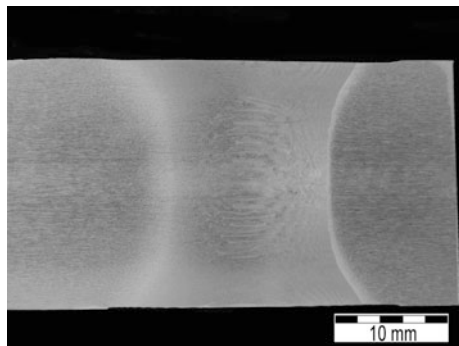
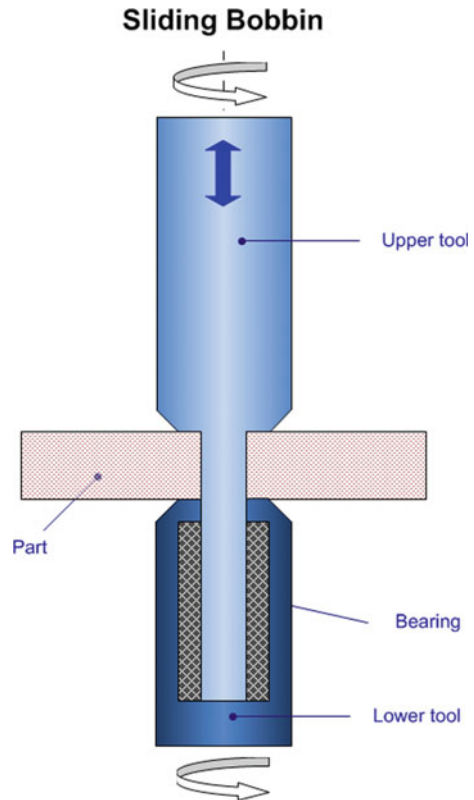


Fig. 12 Schematic drawing of sliding bobbin FSW.
 'Reproduced courtesy of TWI Ltd'



tool bending; however, as the probe size reduced, it had insufficient tensile strength to contain the plasticised materials leading to probe failure. To try to reduce/eliminate the tensile stress on the probe a new FSW variant was designed called sliding bobbin. A schematic drawing of this technique is shown in Fig. 12. In this technique, both upper and lower shoulders are driven. The probe is held in the upper shoulder but the lower end of the probe is located and held radially in the bottom shoulder but allowed to slide longitudinally. The lower tool is operated in position control with the upper tool in force control. Only limited welds have been made using this technique. Similar results have been obtained to supported bobbin using the 16 mm diameter probe; smaller diameter probes have yet to be assessed. Although this technique requires two driven heads, sliding bobbin has the following potential benefits over simultaneous double sided welding.

- Use of small diameter probe/shoulders, and therefore increased welding speed;
- Lower heat input;
- More even heat input;
- No double processed area in the weld reducing the number of weld zones, simplifying NDT assessment.

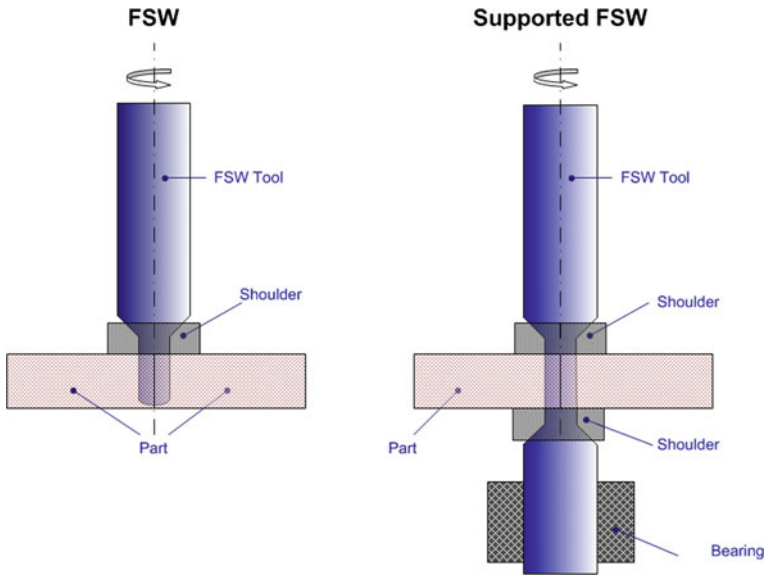


Fig. 13 Schematic drawing of supported FSW. ‘Reproduced courtesy of TWI Ltd’

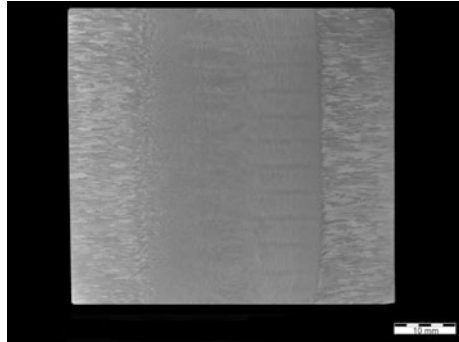
The third technique is called supported FSW, and is based on the dual-rotation FSW technique. In these trials, the shoulders were kept stationary, and only the probe rotated. A schematic diagram of this technique is shown in Fig. 13.

The basic principle uses two stationary shoulders, top and bottom, with the FSW probe passing through the shoulders and component, and then supported by a bearing in the lower head. It was expected that this technique, similar to the supported bobbin technique, would:

- Increase the weld depth possible by a single weld;
- Use small diameter probes/shoulders, and therefore increase welding speeds;
- Be impossible to get lack of penetration defects.

However, with this technique, as heat is generated only by the probe, a lower weld heat input is expected. This may be beneficial when joining aluminium alloys, which obtain their strength by solution heat treatment and aging, as less thermal damage to the material properties would occur. A limited number of welds have been made using this technique, and it has been demonstrated that it is possible to make sound welds as shown in Fig. 14. The weld nugget is nominally parallel, consisting of a fine grain structure with clear rings relating to the probe features. There is a sharp transition to the wrought plate microstructure on the advancing side of the weld (right). The weld thermo-mechanically affected zone which is typically formed with a conventional FSW tool is almost non-existent.

Fig. 14 A welding made using supported FSW in 50 mm thickness AA6082-T6. 'Reproduced courtesy of TWI Ltd'



Conclusion

Recent innovations at TWI, using the unique twin headed capabilities of the PowerStir FSW machine, have demonstrated several techniques which have the potential to minimise production cycle times, making joining of thick section aluminium alloys both technically and commercially advantageous. These techniques need further development to understand more fully the extents of the process window, weld properties, and limits on tool geometry; however, this work has demonstrated the potential to:

- Reduce component processing times through shorter weld times and minimal part handling;
- Improve weld quality through use of reduced and uniform heat input;
- Increase tool life leading to reduced tooling cost;
- Reduce distortion.

Reference

1. Thomas WM et al (1991) Improvements relating to friction welding (European Patent Specification 0 615 480 B1, Dec 1991)

Friction Stir Weld Lap Joint Properties in Aeronautic Aluminium Alloys

Egoitz Aldanondo, Ekaitz Arruti and Alberto Echeverria

Abstract A study of properties of Friction Stir Weld lap joints performed with the AA7075-T6 aluminum alloy used in aerospace manufacturing are presented in this work. The effects of different tool designs and welding parameters in the weld cross sectional and mechanical properties of the joints were investigated. The weld cross sectional features were analyzed by metallographic examination while the mechanical properties were studied by microhardness measurements. Typical features of Friction Stir Weld lap joints have been identified such as hook features, cold lap defects or joint line uplifting. The extension of Heat Affected Zone regions and mechanical property reduction was evaluated depending on the welding parameters used to perform the Friction Stir Weld joints. The tool design as well as welding conditions that minimize defects such as effective sheet thinning, hardness drops or wide Heat Affected Zone regions were established.

Keywords Friction stir welding • Lap joints • Aluminium • AA7075-T6

Introduction

Aircraft structures are commonly manufactured using high strength aluminium alloys such as 2XXX and 7XXX series which are typically combined in lap joint configurations to form skin-stringer stiffened parts. The limitations and difficulties that present such alloys in traditional fusion welding processes resulted in the use of riveting as the main joining technology in the manufacturing of structural elements for aircrafts. However the irruption of a solid state welding technique such as Friction Stir Welding (FSW) opened up new possibilities and many novel structures have been developed in the aerospace industry over the last years [1–5]. The industrial implementation of FSW technology in the manufacturing of primary

E. Aldanondo (✉) · E. Arruti · A. Echeverria
IK4 LORTEK, Arranomendia kalea 4A, 20240 Ordizia, Spain
e-mail: Egoitz@lortek.es

© The Minerals, Metals & Materials Society 2017
Y. Hovanski et al. (eds.), *Friction Stir Welding and Processing IX*,
The Minerals, Metals & Materials Series, DOI 10.1007/978-3-319-52383-5_12

aircraft structures in some of those developments [3–5] evidences the suitability of the technology for this type of application.

One of the most promising application of FSW in aerostructures is the manufacturing of fuselage panels which are generally composed by lap joints between stringer and skin parts. Therefore issues relevant to FSW lap joints have to be dealt with and solved in order to produce joints and parts that comply with the stringent quality requirements of the aeronautic industry. There has been a number of studies focused on that end [6–13] which have shown the main characteristics of joints and the main influential elements that are responsible for such characteristics. Thus typical defects such as hooking, sheet thinning or cold lap defects are well known and some strategies to avoid them or reduce their severity have been described. Among these strategies are the use of double passes [6, 9] as well as the optimization of tool designs and welding parameters in order to maximize the quality of the obtained joints [6–13]. Although some general trends can be extracted from all those works, a general solution for the elimination of the hook features has not been achieved yet and further work is needed for that purpose.

The main results achieved in a work investigating the characteristics of FSW lap joints are presented in this paper. A comparison is made in lap joints produced using a AA7075-T6 aluminium alloy, two different tool designs and several welding parameters. The characteristics of joints are analyzed by metallographic examination and microhardness measurements, which have demonstrated to be useful means to perform a preliminary evaluation of the joint characteristics and investigate the role of the used tool designs and welding parameters in those characteristics.

Experimental Details

A series of FSW trials was made in AA7075-T6 aluminium alloy overlapping a 2 mm thick sheet on top of another 3 mm thick sheet. All trials were made in an I-STIR PDS4 machine for FSW process development with the possibility to be operated in position or force control using two different tool designs. Thus a tool containing a conventional threaded, cylindrical probe and a tool containing a probe with three flats and a mixed thread were used as shown in Fig. 1. The dimensions for both tools were similar having a shoulder diameter of 10 mm, a probe diameter of 4 mm and a probe length of 2.5 mm. Therefore the penetration of the probe in the bottom sheet is 0.5 mm in all cases. After an initial welding parameter investigation, two welding conditions were selected representing two heat input conditions. A rotational speed of 1200 rpm and welding speed of 152 mm/min were used as high heat input condition resulting in a weld pitch of 0.13 mm/rev; while 800 rpm and 254 mm/min were used as rotational speed and welding speed as cold heat input conditions giving a weld pitch of 0.32 mm/min. Welds were produced using the two welding conditions and two tool designs under force control,

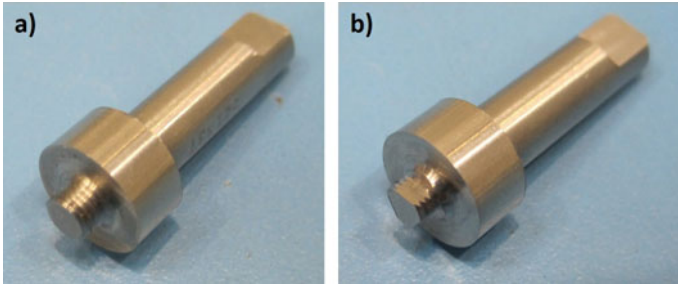


Fig. 1 FSW tools used to produce the welds. **a** Conventional threaded tool and **b** tool with 3 flats

adjusting the applied force depending on the welding speed and the rotational speed for each case.

Metallographic examination of the welds was conducted with cross-section specimens that were prepared following standard metallographic procedures. These included polishing to a mirror like finish and etching by submerging the specimens into a Keller's reagent for approximately 5 s, rinse in water and drying in a warm airflow. Weld cross sectional features of the FSW lap joints were investigated by an Olympus GX51 light optical microscope.

Microhardness measurements were performed using a Vickers indenter, a load of 500 g and a load application time of 15 s. The indentations were made with a spacing of 0.5 mm between them, at the midplane of the top sheet and along the transverse cross-section of the welds taking the weld centerline as reference. A length of at least 20 mm (10 mm from the centerline in both directions) was analyzed in order to characterize all relevant microstructural zones. All microhardness measurements were performed in the as welded condition and allowing a time of approximately 30 days between the production of the welds and the measurements.

Results and Discussion

Weld cross sectional features and local mechanical properties of the produced FSW lap joints were analyzed by means of metallographic examination and microhardness measurements. The following sections summarize the main results obtained in this work:

Weld Cross Sectional Characterization

Cross-sections of FSW lap joints produced by the employed tools and welding conditions are shown in Figs. 2 and 3. The only case where major volumetric defects were found was in the weld performed by the conventional threaded tool operated at 0.13 mm/rev (image “a” at Fig. 2). In this case a continuous wormhole defect can be observed at the advancing side resulting from the inappropriate material flow and consolidation. This major defect can be eliminated by using a weld pitch of 0.32 mm/rev (image “a” at Fig. 3) or by using the tool with three flats as shown by the volumetric defect-free joints (image “b” at Fig. 2 and image “b” at Fig. 3). Therefore the tool with three flats seems to produce a more appropriate plasticized material flow and consolidation being able to eliminate major defects and increasing the process envelope.

The volume of stirred material during FSW is mainly dependent on the tool design and the welding parameters. This volume for the investigated joints is highlighted in Figs. 2 and 3, then superposed for comparisons in Fig. 4. It can be observed that using the tool with three flats the volume of the stir zone is slightly larger than the volume obtained with the conventional threaded tool for similar welding parameters. This suggests that material flow and consolidation capacity offered by the tool with three flats is more intense and appropriate in comparison to the conventional threaded tool. Thus the process envelope where defect free joints can be obtained is larger for the tool with three flats so that volumetric defect free

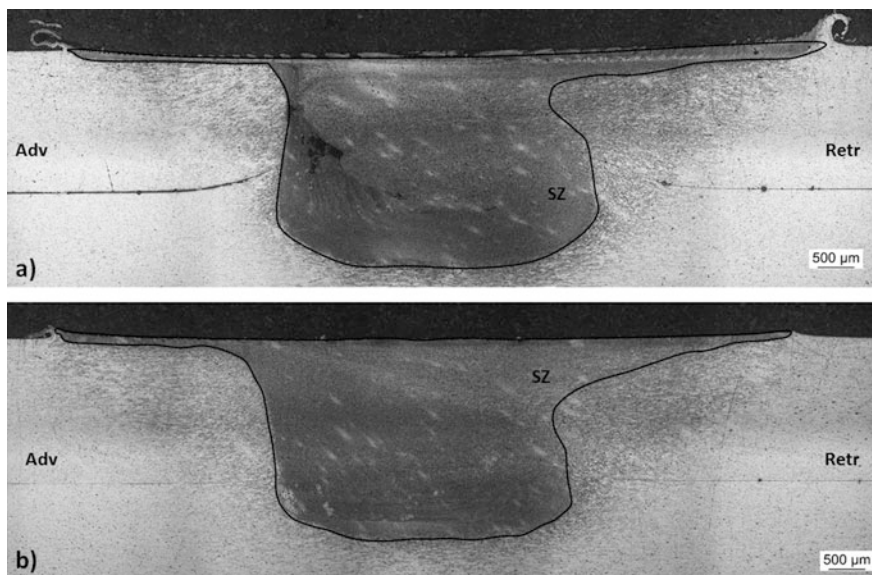


Fig. 2 Cross-sections of FSW laps joints produced at 1200 rpm and 152 mm/min (0.13 mm/rev) with **a** conventional threaded tool and **b** tool with 3 flats

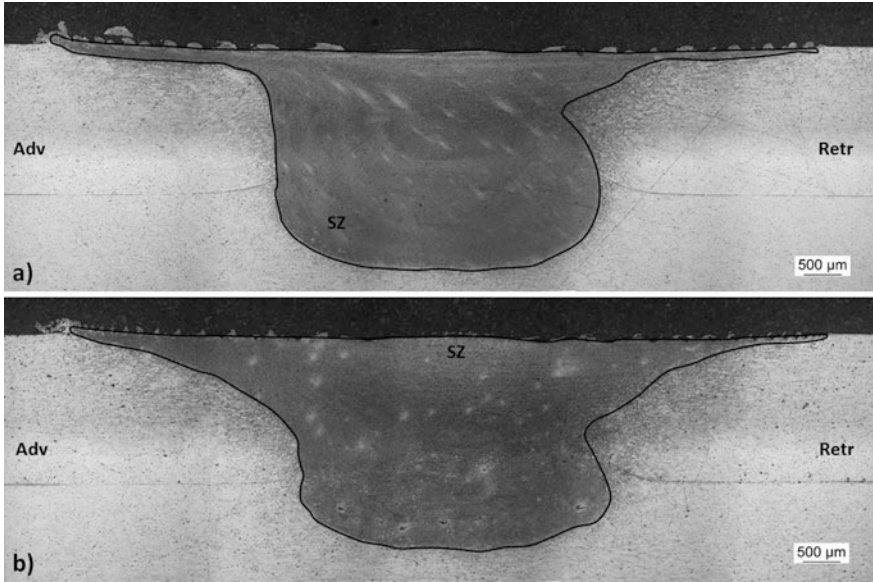


Fig. 3 Cross-sections of FSW laps joints produced at 800 rpm and 254 mm/min (0.32 mm/rev) with **a** conventional threaded tool and **b** tool with 3 flats

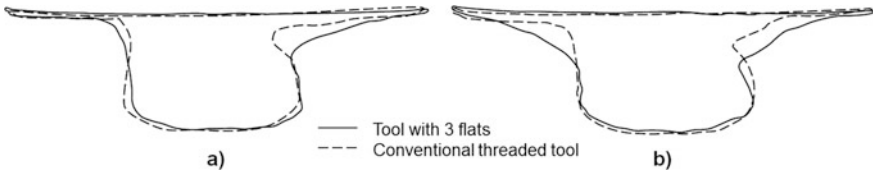


Fig. 4 Superposed stir zone regions in FSW lap joints made with different tools and produced at **a** 1200 rpm and 152 mm/min (0.13 mm/rev); and **b** 800 rpm and 254 mm/min (0.32 mm/rev)

joints were obtained even at the welds produced under high heat input conditions (0.13 mm/rev in Fig. 2 “b”).

Typical weld cross sectional features of FSW lap joints such as hook features at the advancing side or joint line uplifting as well as cold lap defects at the retreating side were observed in the investigated welds, although their size was found to be generally reduced. The severity and size of those defects was found to be different for different tool designs and welding parameters. As previously reported [13], generally larger hooks and joint line uplifts were found in the welds made by the conventional threaded tool in comparison with those made with the tool with three flats (Figs. 2 and 3). Therefore the effective sheet thickness of the top sheet was larger in the welds made by the tool with three flats which seems to be beneficial for the joint properties.

Microhardness Analysis

Comparisons of microhardness distributions along the welds obtained in the investigated FSW lap joints are shown in Figs. 5, 6, 7 and 8. W shaped hardness distributions which are typical in FSW of precipitation hardening aluminium alloys can be observed in all cases, although significant differences were found depending on the welding parameters and tool designs used for performing the welds.

The comparison between FSW lap joints made using a different weld pitch of 0.13 and 0.32 mm/rev (Figs. 5 and 6) showed the great influence of the welding parameters in the material softening. The use of high heat input parameters, i.e. 1200 rpm and 152 mm/min (0.13 mm/rev), produced lower minimum hardness values and wider heat affected zone (HAZ) regions. This effect results from the higher temperatures and heating of the material achieved at 0.13 mm/rev, which produced a larger overaging effect of the material resulting in hardness drop. The same effect was observed in the welds performed with the conventional threaded tool (Fig. 5) as well as with the tool containing three flats (Fig. 6). Thus minimum hardness values in the range of 125–130 HV0.5 (~27% drop relative to the base material hardness) were measured in welds performed using a weld pitch of 0.13 mm/rev; while 130–135 HV0.5 was found to be the range for minimum hardness values in welds made at 0.32 mm/rev (~24% drop relative to the base material hardness).

The comparison of hardness distributions along the welds obtained using the same welding parameters for the investigated two tool designs are shown in Figs. 7 and 8. Very similar profiles were obtained for both tools in welds performed using the two investigated weld pitch conditions (0.13 mm/rev in Fig. 7 and 0.32 mm/rev in Fig. 8), although some trends could be observed. In both cases the welds made

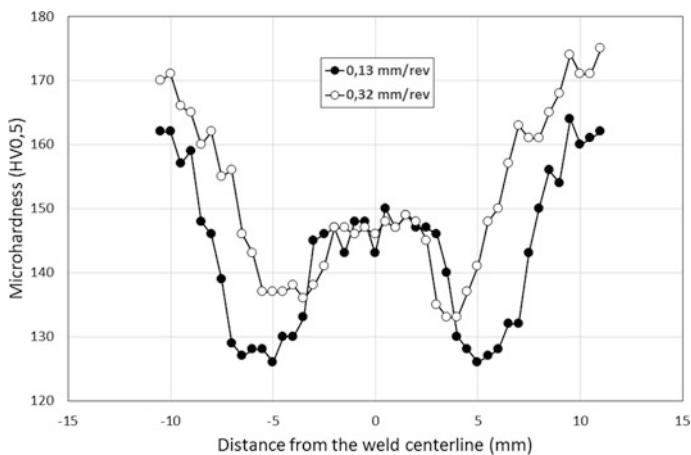


Fig. 5 Microhardness values in welds made at 0.13 and 0.32 mm/rev with a conventional threaded tool

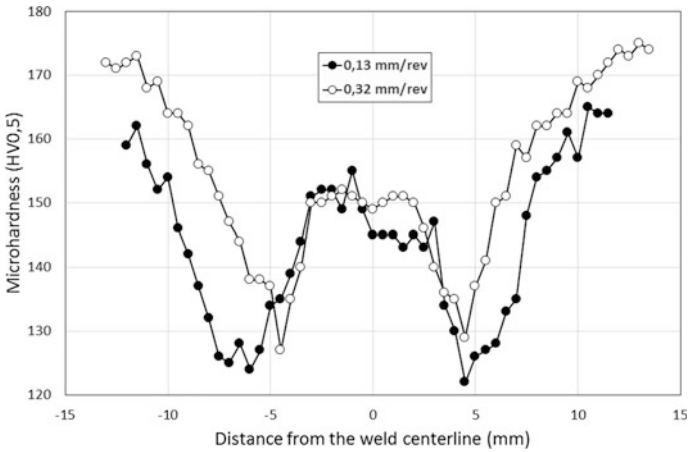


Fig. 6 Microhardness values in welds made at 0.13 and 0.32 mm/rev with a threaded tool with 3 flats

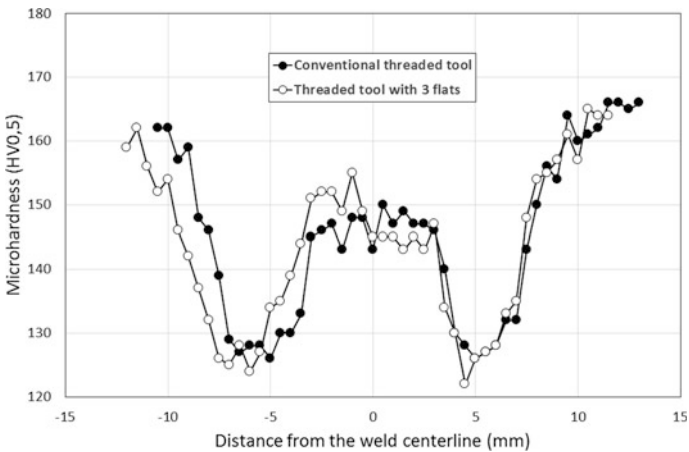


Fig. 7 Microhardness values in welds made at 0.13 mm/rev with different tool designs

by the tool with three flats showed lower minimum hardness values as well as wider HAZ extensions in comparison with the welds made by the conventional threaded tool. This could be explained by a slightly higher overaging effect occurred if the tool with three flats is used. The higher degree of stirring and plastic deformation promoted by this tool, as previously discussed in the weld cross sectional characterization (Fig. 4), could be responsible for the achievement of higher temperatures resulting in a higher overaging degree and lower hardness values.

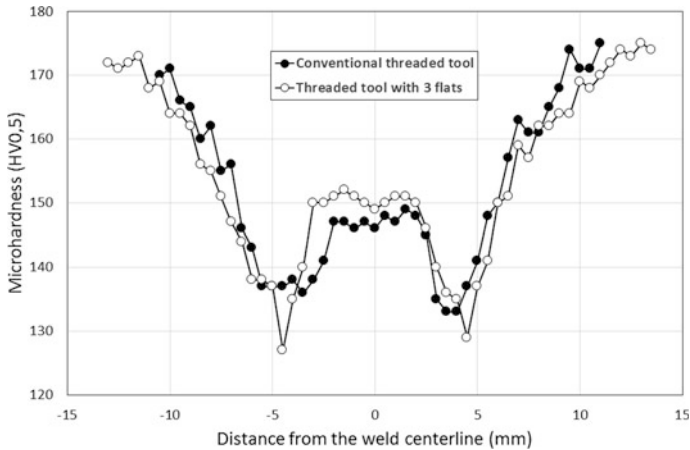


Fig. 8 Microhardness values in welds made at 0.32 mm/rev with different tool designs

Conclusions

In the present work weld cross sectional features and mechanical properties of FSW lap joints were investigated in a series of welds made in aluminium alloy AA7075-T6, using different tool designs and welding parameters. The following observations regarding relationships of tool designs, welding parameters and joint properties have been attained:

- The use of low heat input welding parameters, i.e. 800 rpm and 254 mm/min – 0.32 mm/rev, produced volumetric defect free welds.
- When high heat input parameters were used, i.e. 1200 rpm and 152 mm/min – 0.13 mm/rev, the tool with three flats produced defect free welds while a wormhole defect was found in welds made with the conventional threaded tool.
- The tool with three flats showed a higher capacity to promote the appropriate stirring, material flow and consolidation of the plasticized material resulting in a larger process envelope or welding parameter range where defect free joints are obtained.
- Smaller hook features and joint line uplifts were produced by the tool with three flats in comparison with the conventional threaded tool, resulting in a larger effective sheet thickness of the top sheet.
- Lower hardness values and wider HAZ regions were observed in welds made using the high heat input parameters, i.e. 1200 rpm and 152 mm/min – 0.3 mm/rev, for the two tool designs investigated.
- Very similar hardness distribution profiles along the weld were observed in welds performed under same welding parameters for the two tool designs investigated.

Based on the previous observations, it seems clear that better results would be obtained regarding FSW lap joint properties using a tool with three flats rather than using a conventional threaded tool. Although the use of low heat input parameters was found to produce better local mechanical properties, i.e. higher hardness values and smaller HAZ extension, further research is needed in order to evaluate the general mechanical properties of FSW lap joints, as other weld cross sectional features such as hook size or joint line uplifting were found to be in the same range in welds made with low and high heat input welding parameters and the tool with three flats.

References

1. Booker MJ et al.(2000) Applying friction stir welding to the ariane 5 main motor thrust frame. In: 2nd international symposium on friction stir welding, Gothenburg, Sweden, 27–29 June 2000
2. Talwar R et al. (2000) Friction stir welding of airframe structures. In: 2nd international symposium on friction stir welding, Gothenburg, Sweden, 27–29 June 2000
3. Christner B (2002) Development and testing of friction stir welding (FSW) as a joining method for primary aircraft structure. In: 23rd ICAS congress, Toronto, Canada, 8–13 September 2002
4. Christner B (2016) A friction stir welded jet aircraft: from concept to reality. In: 11th international symposium on friction stir welding, Cambridge, UK, 17th May 2016
5. Fernandez F (2010) FSW applied on mid-size aircraft. In: 8th international symposium on friction stir welding, Timmendorfer Strand, Germany, 18–20th May 2010
6. Cederquist L, Reynolds AP (2001) Factors affecting the properties of friction stir welded aluminium lap joints. *Weld J Res Suppl* 80:281
7. Aldanondo E et al (2013) Mechanical and microstructural properties of lap joints. In: 142nd TMS annual meeting and exhibition—friction stir welding and processing VII, San Antonio, USA, March 2013, pp 195–205
8. Buffa G et al (2009) Friction stir welding of lap joints: Influence of process parameters on the metallurgical and mechanical properties. *Mater Sci Eng A* 519:19–26
9. Dubourg L et al (2010) Process optimisation and mechanical properties of friction stir lap welds of 7075-T6 stringers on 2024-T3 skin. *Mater Des* 31:3324–3330
10. Ji S et al (2016) Effect of reverse-threaded pin on mechanical properties of friction stir lap welded alclad 2024 aluminum alloy. *J Mater Sci Technol* 32:671–675
11. Yang X et al (2014) Defect features and mechanical properties of friction stir lap welded dissimilar AA2024-AA7075 aluminum alloy sheets. *Mater Des* 55:9–18
12. Liu H et al (2016) The effect of interface defect on mechanical properties and its formation mechanism in friction stir lap welded joints of aluminum alloys. *J Mater Process Technol* 238:244–254
13. Aldanondo et al (2016) Microstructural features in friction stir welded lap joints. In: 10th international conference on trends in welding research, Tokyo, Japan, 10–14th October 2016

Friction Stir Welding of Thick Aluminium Welds—Challenges and Perspectives

Murshid Imam, Yufeng Sun, Hidetoshi Fujii, Yasuhiro Aoki, Ninshu MA, Seiichiro Tsutsumi and Hidekazu Murakawa

Abstract The present paper describes the main challenges faced by the heavy metal industries in the adoption of the friction stir welding of thick section. The requirement of higher forge axis load necessitates the use of a massive and expensive FSW machine, powerful fixtures and improved tool material technology to withstand the higher bending stresses. The thicker sections are also responsible for the significant variations in the joint properties such as grain size, precipitates morphology, distribution of secondary phase particles and hardness due to the noticeable differences in the temperature distribution along the weld thickness. To address these typical challenges in the friction stir welding of thicker sections, a preheating technique along with a composite backing plate is developed. The main advantages of the present approach are to reduce the requirements of the higher forge axis load, power consumption of the FSW machine, tool wear, and improved weld productivity and joint properties through a thermal balance along the thickness of the weld. The present approach can also be extended to the thicker plates of the high strength materials.

Keywords Friction stir welding · Thick plate · Weld thermal management · Hybrid friction stir welding · Low diffusivity backing plate

Introduction

There has been growing interest in the heavy metal industries with the recent progress in the friction stir welding of thick aluminium welds, especially constructing large aluminium structures such as oil and gas tanks, offshore platforms, and military parts [1]. However, despite the recent progress in this area, many challenges still need to be overcome before it comes to full scale industrial use. With an increased thickness, the requirement of a higher power, load bearing ability of the tool, axial

M. Imam (✉) · Y. Sun · H. Fujii · Y. Aoki · S. Tsutsumi · H. Murakawa
Joining and Welding Research Institute, Osaka University, Osaka, Ibaraki 567-0047, Japan
e-mail: imam@jwri.osaka-u.ac.jp

N. MA
JSOL Corporation, Engineering Technology Division, Nishi-ku, Osaka 550-0001, Japan

© The Minerals, Metals & Materials Society 2017
Y. Hovanski et al. (eds.), *Friction Stir Welding and Processing IX*,
The Minerals, Metals & Materials Series, DOI 10.1007/978-3-319-52383-5_13

load, and welding and clamping forces make the task more challenging in terms of the selection of the process control parameters, FSW machine, tool material technology and design. In addition, a significant variation in the dynamic parameters such as the strain rate and peak temperature along the weld thickness, poor stirring effect and heat loss to the backing plate material at the weld root creates more complexities. Therefore, the weld thermal management along the thickness of the weld must be taken into consideration to extend the process window, minimizing the weld defects, reducing the tool wear, optimizing the joint properties and minimizing the weld distortion. In previous reported studies, the preheating techniques were limited to the smaller sheet thicknesses [2–4]. They reported that the preheating techniques can reduce the tool wear and improve the weld productivity. Also, Imam et al. [5] and Upadhyay and Reynolds [6] suggested that low diffusivity backing plate materials can be used to reduce the heat loss to the backing plate material and hence improve weld productivity. The effect of the combined approach of the preheating along with the low diffusivity backing plate placed in the central region surrounded by a high or moderate diffusivity backing plate material has not yet been studied, especially for thicker sections of aluminium alloys. Therefore, to overcome the challenges stated above for thicker sections, a modified laser preheating system with a composite backing plate was developed. It is believed that this approach will push the application of friction stir welding in thicker section materials and can be done with relatively simple and inexpensive FSW systems.

Experimental Procedure

An experiment was conducted using a 20-mm thick 5083-O aluminium alloy plate. The as-received plates were cut into $400 \times 90 \times 20$ mm pieces and friction stir butt welded using a recently developed Triflat™ design FSW tool. This type of tool has a scrolled shoulder and probe in the shape of a truncated cone with threads and three flats. A laser preheating setup was installed along with the head of the FSW machine. A defocused beam of a 1 cm diameter light spot ahead of the rotating probe was used to preheat the workpiece. The backing plate used in the central region is made from ceramic. The other two surrounding backing plates were made from steel. Online temperature monitoring was made using the thermocouples inserted in the workpiece both along the thickness of the weld in the SZ and on the surface. The online monitoring of the weld during the plunging and welding process was also made using a thermovision camera FLIR system, ThermoCAM P640. Note that the use of infrared thermography is a useful technique for the identification of the tool failure during welding, temperature in the heat affected zones (HAZs), temperature conducted to the FSW tool material, and thereby provide useful information regarding the selection of the process control parameters. Also, it helps to monitor the weld from a farther distance and protect the operator from exposure to harmful laser radiation.

Results and Discussion

Table 1 shows the welding parameters and calculated heat input for the friction stir welded thick aluminium alloys. It can be clearly seen from this table that, as compared to thin section welds, the selection of the primary process control parameters such as forge axis load, tool rotational and welding speeds are different and requires more fundamental knowledge of the physical mechanisms occurring at the tool/workpiece interface and thermal boundary conditions in the thicker section materials. The thicker section material requires a higher torque and forge axis load to overcome the material resistance provided by the larger material volume and to ensure adequate material mixing along the thickness of the weld. To avoid melting, particularly at the shoulder/workpiece interface, the increase in the frictional heat input due to the higher forge axis load is compensated by the decrease in the tool rotational speed. The higher welding speed can be used to ensure the optimum balance of the heat input both in the shoulder and probe affected regions. However, it poses another challenge in the friction stir welding of the thick section. The tool material should be strong enough withstanding the large bending stresses when the welding speed increases. Also, fancier or intricate tool geometrical features are

Table 1 A summary of the chosen welding parameters and calculated heat input in the friction stir welding of thicker section aluminium alloys

Material	Sheet thickness	Maximum torque (Nm)	Maximum axial load (kN)	Rotational speed (rpm)	Welding speed (mm/min)	Heat input (kJ/mm)	Detail
5083-O	20	220	75	300	80	4.4	Perrett et al. [1]
5083-O	20	120	28	500	50	6.3	Present work
2017-T451	20	240	85	300	120	3.2	Perrett et al. [1]
6082-T651	20	240	65	500	350	1.8	Perrett et al. [1]
7020-T651	20	355	55	200	90	4.2	Perrett et al. [1]
7075-T651	20	280	67	200	80	3.3	Perrett et al. [1]
6061-T6	25.4	–	35.6	480	204	–	Upadhyay and Reynolds [6]
6082-T6	25	–	–	400	200, 300	–	Hamada et al. [7]
2050-T3	19	–	62	280	160	–	Fenoel and Taillard [8]

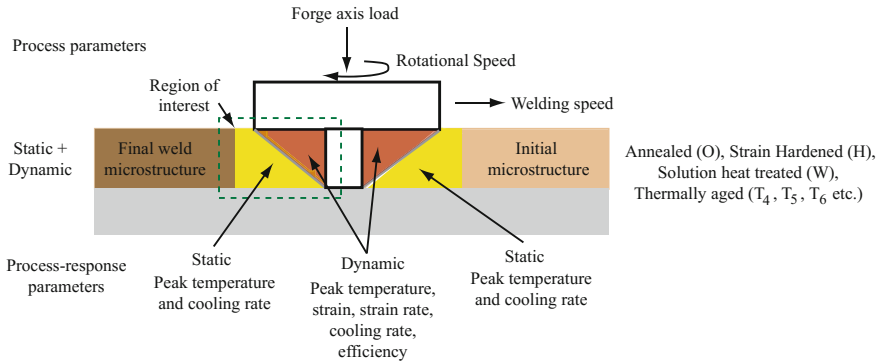


Fig. 1 Schematics showing the **a** heating and deformation phases, **b** thermal boundary conditions, and **c** variation in the hot deformation parameters along thickness direction during FSW

detrimental to the tool life. The presence of such intricate features on the probe surface act as a notch and may lead to tool failure. In addition to the challenges faced on the selection of the process control parameters and tool geometry, the physical interaction of the tool with the workpiece is responsible for the significant variation in the microstructure and mechanical properties in the thickness of the weld. Since the joint properties are highly sensitive to the temperature, the weld thermal management along the thickness of the weld is a key to the success of the FSW of thicker sections. A more detailed understanding can be obtained from the schematic showing the different stages of the static and deformational heating during the FSW (see Fig. 1). During FSW, the overall microstructure development is location sensitive and the effect of the strain, strain rate, cooling rate and thermal cycle creates complexities. The initial microstructure experiences severe deformation conditions due to the higher strain rate and peak temperature at the shoulder/workpiece interface. Both the strain rate and peak temperatures are expected to decrease along the thickness of the weld due to the poor stirring and decrease in the frictional heating at the weld root [9]. The heat loss to the backing plate added another detrimental effect to the plastic flow of the material in the weld root. The practical consequences of this causes the temperature reduction which results in tunnel defects at the weld root. Therefore, a proper weld thermal management is the key to success for the friction stir welding of thicker plates.

To overcome the above challenges in the friction stir welding of thicker aluminium sections, a combined approach of the preheating the workpiece along with the use of a composite backing plate material is adopted. The low diffusivity backing plate covering the whole workpiece has been suggested in the previous works [5, 10]. However, the major drawback of this approach is that it increases the unwanted temperature in the heat affected zones (HAZs), and as a result, may degrade the mechanical properties due to coarsening of the strengthening precipitates or grain size, especially in the precipitation hardened aluminium alloys. Figure 2 shows the overall idea of the present approach for the friction stir welding of thicker aluminium

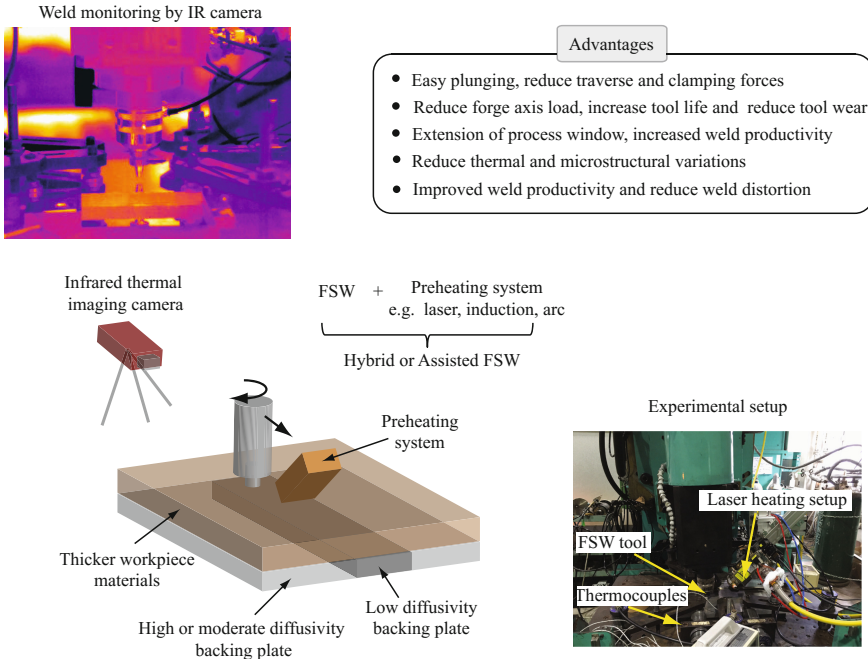


Fig. 2 Overview of the present approach adopted in the present work and its main advantages

sections. The use of a low diffusivity backing plate material in the central region surrounded by the high to moderate diffusivity backing plate material along with the laser preheating system is believed to be an efficient approach for improving the weld productivity and decreasing the requirement of a larger forge axis load. The laser energy used in the present study is to heat the workpiece to an elevated peak temperature in the range of 200–300 °C. At the elevated peak temperatures, the yield stress of the material decreases and hence reduces the larger welding forces. Since this research is at the preliminary stage, the optimized experimental conditions have not yet been obtained. Therefore, the experimental results are not reported in this paper. However, based on this approach, it is believed that not only thicker sections of aluminium alloys but also other thick plates of high strength materials can be friction stir welded using simple and inexpensive welding systems.

Conclusions

A combined approach of preheating the workpiece along with the use of composite backing plates has the potential to lower the need to apply large forces both on the welding tool and the workpiece. The use of simple and inexpensive welding systems

has been made possible by this modification. In addition, a lower rate of tool wear and higher welding speeds are believed to be the major benefits resulting from this approach.

Acknowledgements The authors would like to thank the staffs of the welding workshop of the Joining and Welding Research Institute of Osaka University for their cooperation and support.

References

1. Perrett JG, Martin J, Threadgil PL, Ahmed MMZ (2000) Recent developments in friction stir welding of thick section aluminium alloys. In: Proceedings of 6th World Congress, Al. 2000, Florence. Italy 2007:13–17
2. Sinclair PC, Longhurst WR, Cox CD, Lammlein DH, Strauss AM, Cook GE (2010) Heated friction stir welding: an experimental and theoretical investigation into how preheating influences process forces. *Mater Manuf Process* 25:1283–1291
3. Sun YF, Konishi Y, Kamai M, Fujii H (2013) Microstructure and mechanical properties of S45C steel prepared by laser-assisted friction stir welding. *Mater Des* 47:842–849
4. Sun YF, Shen JM, Morisada Y, Fujii H (2014) Spot friction stir welding of low carbon steel plates preheated by high frequency induction. *Mater Des* 54:450–457
5. Imam M, Racherla V, Biswas K (2015) Effect of backing plate material in friction stir butt and lap welding of 6063-T4 aluminium alloy. *Int J Adv Manuf Technol* 77:2181–2195
6. Upadhyay P, Reynolds A (2014) Effect of backing plate thermal property on friction stir welding of 25-mm-thick AA6061. *Metall Mater Trans A* 45A:2091–2100
7. Hamada AS, Jarvenpaa A, Ahmed MMZ, Jaskari M, Wynne BP, Porter DA, Karjalainen LP (2015) The microstructural evolution of friction stir welded AA6082-T6 aluminum alloy during cyclic deformation. *Mater Sci Eng A* 642:366–376
8. Avettand-Fenoel M-N, Taillard R (2015) Heterogeneity of the nugget microstructure in a thick 2050 Al friction-stirred weld. *Metall Mater Trans A*, 46:300–303
9. Nandan R, DebRoy T, Bhadeshia HKDH (2008) Recent advances in friction-stir welding—process, weldment structure and properties. *Prog Mater Sci* 53(6):980–1023
10. Rosales MJC, Alcantara NG, Santos J, Zettler R (2010) The backing bar role in heat transfer on aluminium alloys friction stir welding. *Mater Sci Forum* 459:636–637

High-Speed FSW Aluminum Alloy 7075 Microstructure and Corrosion Properties

Jingyi Zhang, Piyush Upadhyay, Yuri Hovanski and David P. Field

Abstract High-speed friction stir welding provides an opportunity to enable high-volume aluminum joining, thus lowering the expense of the process. To better understand this important industrial process the properties of the welds must be fully characterized. In this study we examined the microstructures of AA7075 butt welds with welding speeds of 1, 2 and 3 m/min. The welds were also tested for their corrosion resistance in a diluted EXCO solution at room temperature. The welds with higher speeds had a smaller corrosion sensitive area along with smaller HAZs, but the nugget zone became more corrosion susceptible. Their microstructure features were used to explain the non-uniform corrosion behavior across the weld. Both constituent particles and precipitate distribution were altered by the friction stir process and resulted in an overall sensitized weld affected region compared to the base material.

Keywords FSW · AA7075 · Corrosion · Microstructure · EXCO · EBSD · SEM

Introduction

Friction stir welding (FSW) is a relatively new technique which produces high efficiency aluminum alloy joints [1, 2]. The technique is intrinsically free of melting and shielding materials are not generally required, leading to joints with

J. Zhang (✉) · D.P. Field
School of MME, Washington State University, Pullman, WA 99164, USA
e-mail: jingyi.zhang2@wsu.edu

P. Upadhyay
Pacific Northwest National Laboratory, Richland, WA 99354, USA

J. Zhang
Washington State University, Sloan 201, Pullman, WA, USA

Y. Hovanski
Brigham Young University, Provo, UT 84602, USA

less internal stress and smaller/less severe heat affected zones (HAZ) [3–5]. The application of FSW in the aerospace industry has been well accepted and proven to be able to deliver high performance welds [6]. However the introduction of FSW to high throughput fields such as the automobile industry requires some more adjustments and studies to further improve the cost efficiency and product performance stability [7, 8]. In this study we introduced very high welding speeds (1, 2 and 3 m/min) to aluminum alloy 7075 sheets. The joining speeds of meters per minute makes FSW technique comparable to other traditional joining techniques such as laser and fusion welding, hence enabling high volume joining, and further reduces the time and cost to apply FSW. Like any other new technology in the developing process, full analysis of the process design and quality control is necessary before standards can be constructed and used to direct production. In our study, we examined the corrosion performance of high speed welds, and correlated the results to their microstructural features. The base material, aluminum alloy 7075, is an Al–Zn–Mg–Cu type alloy, it provides high strength performance through heavy alloying. The main strengthening mechanism of AA7075 is precipitate hardening and the T6 temper is the peak strength temper. A variety of intermetallic particles (IMPs), including dispersoids, constituent particles, and precipitates can be found in 7075 aluminum. In this paper we will use IMP to refer to constituent particles only. Due to their sizes and growth mechanisms, FSW has different effects on the distribution of constituent particles (IMPs) and precipitates. Both types of particles will be affected in the nugget zone where direct deformation is applied, generating high strain levels and temperature increases, leading to fully recrystallized grains. In the nugget zone the IMPs are physically stirred to be re-distributed around the pin, and possibly also sheared during the process. The precipitates, on the other hand, will likely be dissolved into the matrix during the heating process and re-precipitate in the cooling cycle. Inside the thermomechanically affected zone (TMAZ), the distribution of IMPs will be slightly altered due to the deformation of the material but since relatively small strains are seen in the TMAZ region, the change in IMP density will be very small. Further away from the weld nugget, in the heat affected zone (HAZ) and in the unaffected base material the IMPs should not be affected. However, both TMAZ and HAZ experience a thermal cycle that will overage the T6 tempered base material due to precipitate growth and Ostwald ripening. In this study the change of precipitate state will be qualitatively presented by micro-hardness measurements, no direct measurement or characterization of the precipitate is performed in this work. All types of intermetallic particles present in the matrix will act as corrosion incubation sites because of their electrochemical potential difference from the aluminum matrix [9]. In fact, earlier studies on low speed FSW processed high strength heat-treatable aluminum alloys report an increase of corrosion susceptibility of the TMAZs and HAZs [10, 11].

Table 1 Summary of the welding parameters and processing temperatures

Sample	Weld speed (mm/min)	RPM	Pitch distance (mm)	Temperature (°C)
# 1	1000	1500	0.667	449
# 2	2000	1500	1.333	366
# 5	2900	1950	1.499	386

Experiments

Aluminum alloy 7075-T6 sheets of 2 mm thickness are selected for this study, the work pieces are friction stir processed with bead-on plate procedure using a tool with a tapered pin with 3 flats, and 2 asymmetric threads on the shoulder surface. The diameter of the pin was 4.2 mm and the pin to shoulder diameter ratio is 1:3. The welding direction was along the rolling direction of the work piece. Parameters including welding speed and rotation speed along with the peak temperatures, captured with thermal couples built inside the tool pin during the welding process, are listed in Table 1. All samples were naturally aged for 6 months after the welding process. Cross sections of the welds are sampled 25 mm away from the weld head to make sure they are in the steady temperature and microstructure zone. The samples were mounted in clear epoxy with the cross sections exposed such that the welding direction is coming out of the observing surface, with the advancing side (AS) of weld on the left and the retreating side (RS) on the right. Mechanical polishing with SiC paper were made in consecutive sequence up to 1200 grit and then the specimens were fine polished with diamond paste, followed by a finishing step in a vibro-polisher with 0.05 μ colloidal silica suspension. The as-prepared samples were examined in a field emission SEM with energy dispersive spectroscopy (EDS) to study the morphology, distribution and chemistry of the constituent particles (IMPs) present in the alloy. Electron backscatter diffraction (EBSD) scans were also collected to get micro-texture information. After that the surfaces were cleaned and etched with Weck's reagent (4 g KMnO_4 , 1 g NaOH , in 100 ml water) to show the grain morphology in larger regions. The specimens were then re-polished to expose a fresh surface and immersed in 10% EXCO solution for 18 h for a qualitative overview of the corrosion susceptibility through the cross section of all weld affected volumes.

Results and Discussion

Metallographic Imaging

The optical images of the etched weld cross sections are shown in Fig. 1, along with EBSD scans across the nugget containing the center 1 mm sections of each sample. The etched views show the contour of the nugget zones, with a sharp advancing side (AS) and thermomechanically affected zone boundary and more

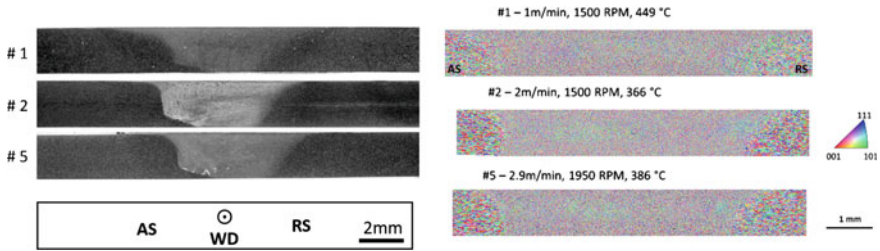


Fig. 1 Overall image showing the microstructure gradient around weld affected regions. *Left* OM image of polished weld cross sections after etched; *Right* large step EBSD scans across the weld with orientation colored by pole direction relative to specimen surface as indicated in the standard triangle

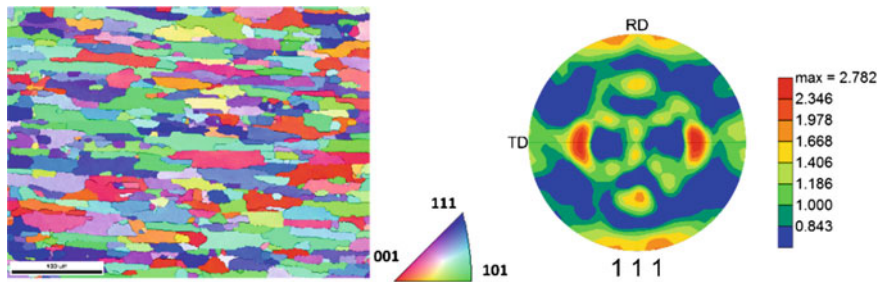


Fig. 2 Orientation map (*left*) and (111) pole figure (*right*) of the base material, cross section view

diffused boundaries on the retreating side (RS) side of the nugget. The overall shape of the weld nugget traces well with the exterior contour of the rotating pin. No onion ring structures were observed in these welds. The EBSD scanning step size of 5 microns used here was large enough for the purpose of creating relatively large area scans to show the texture gradient throughout the near nugget region [12]. The grain size variation from the base material to the inside of the nugget zone can be directly observed in the orientation map. The average grain diameter of the base material is about 10 microns and the average grain diameter of the nugget zones is no larger than 2 μ .

Microstructural Characterization

The microstructure of the base material is shown in Fig. 2, along with the (111) pole figure. The base material has pancake shaped grains and a crystallographic texture typical of rolled aluminum. SEM images of the EBSD-polished surface of the sample show some contrast of the grains and the morphology and distribution of the included intermetallic particles (Fig. 3). The particles in

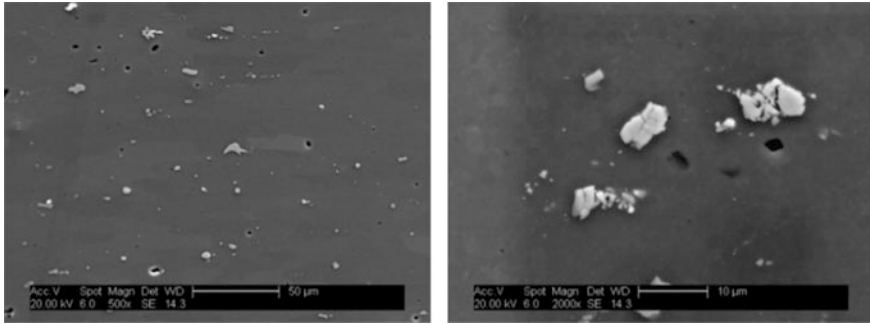


Fig. 3 Typical SEM image of polished surface of base material (*left*) and weld nugget of sample #1 (*right*). The scale bar on the *left* is 50 μ and the one on the *right* is 10 μ

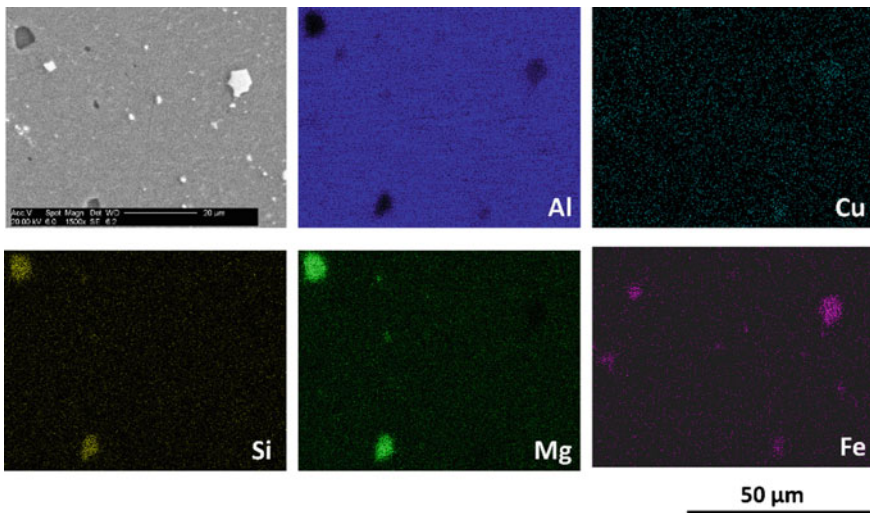


Fig. 4 EDS mapping of base material with second phase particles

AA7075-T6 include $MgSi_2$, $(Fe,Cr)_3SiAl_{12}$, and Al_7Cu_2Fe [13] as confirmed by the EDS mapping in Fig. 4. These particles are generally of higher hardness and are more brittle compared to the matrix. During the stirring process they will break up into smaller pieces and assist in local micro-crack formation. They can also serve as tracing markers. Due to their high stiffness and small size, some of the particles stay undeformed and travel along with the material flow during the process. The composition and chemistry of these particles are well-studied. The iron bearing particles are anodic to the matrix and are targets for selective corrosion incubation sites. These intermetallic particles facilitate the corrosion process and both their density and distribution play important parts in the corrosion resistance of the material [14].

Statistical Characterization of the IMPs

The nugget zones are examined with SEM to measure the stirring process effect on the morphology and distribution of constituent particles. Three different regions are defined in the nugget zone to investigate the inhomogeneous microstructure resulting from the stir: (1) the center portion of a 2 mm² rectangle region with 1 mm along the thickness and 2 mm across the TD is defined as the center zone (C zone), (2) to the left of C zone, a 1 mm wide rectangle that covers from the top to bottom surfaces of the sheets is defined as the near advancing side zone (A zone), and (3) a similar 2 mm by 1 mm region is defined on the right as the near retreating zone (R zone). Illustration of the relative locations of the zones are sketched in Fig. 5, along with representative SEM images in each zone and in the base material (BM). All SEM images are taken with a magnification of 500x and share a common 100 μm scale bar on the top left corner. Twenty images were taken from each region to gather enough area for a statistically reliable determination of the density and distribution of the IMPs. The IMPs in each image were picked out using a grey scale threshold depending on the background of each image. The resulting image is a binary picture recording the location, shape and size of the recognized particles. The binary images are then used to calculate the particle size and distribution. Due to the resolution of the secondary electron images and the noise level, particles too small or that have weak contrast will be disregarded. The results of particle analysis are summarized in Table 2. The advancing side of the nugget (A zone) has the lowest content of IMPs and the retreating side of the nugget (R zone) has the

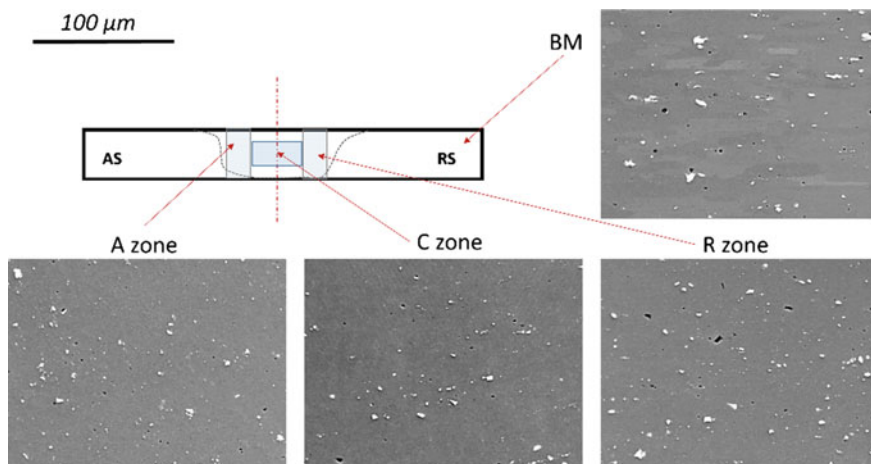


Fig. 5 Illustration of the defined zones for IMPs calculation and representative SE images in each zone. All SE images are 250 μm by 170 μm in size. The A, C, and R zone are all in the nugget zone, directly stirred by the tool pin during FSW, hence have finer, broken pieces of IMPs compared to the unaffected base material

Table 2 Summary of area fraction of IMP in each zone of sample #1 and sample #2

Sample	A zone (%)	C zone (%)	R zone (%)	Base material (%)
#1	0.666	0.788	1.143	1.652
#2	1.095	1.371	1.48	

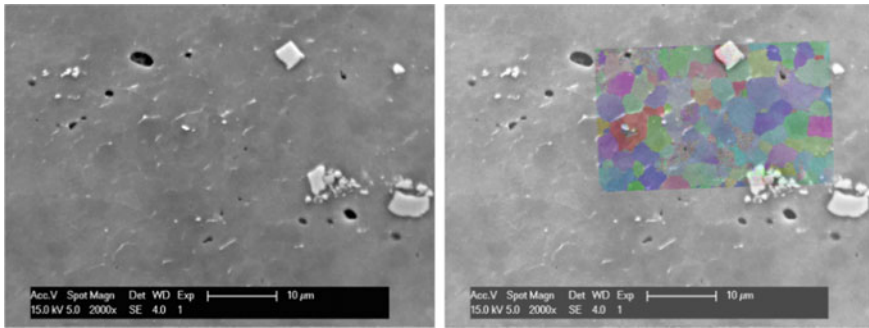


Fig. 6 SE image of broken IMP pieces placed along grain boundaries (*left*) and the same location with an EBSD orientation map overlapping the SE image

highest content. This is a result of the motion of the rotating pin constantly sweeping material from the AS to the RS, and larger IMPs are more likely to get stuck in the RS.

All the regions in nugget zones have smaller area fractions of IMPs than the base metal due to the method used to identify the particles. The small and thin particles are not mapped out or counted in our calculation. Since the nugget zone experienced severe deformation, a lot of particles are broken up into pieces too small to be recognized. At the same time, the grain rotation and material flow flush some small pieces of IMPs in between grain boundaries. Figure 6 is an example taken from sample #1. The left SE image is superimposed with the EBSD map taken from the same location on the right, showing that the small lath shaped IMPs are squeezed between grains and coincide with grain boundaries as seen in the EBSD orientation map. This kind of grain boundary IMP inclusion will not be included in our statistical analysis because the particles are too small and with contrast too low at the magnification we use. Sample #1 is a sample that has a particularly high fraction of these grain boundary IMPs, and this results in an overall lower IMP area fraction in our calculation. All particles entered into the calculation were recorded and the area size probability density histograms are shown in Fig. 7. All regions from the weld nugget have a higher portion of small IMPs than the base material, with the close to AS boundary, A zone, having the highest fraction of smaller IMPs. This is again a result from the heavy deformation in the advancing side of the nugget and that the bigger IMPs tend to get left behind the tool on the retreating side.

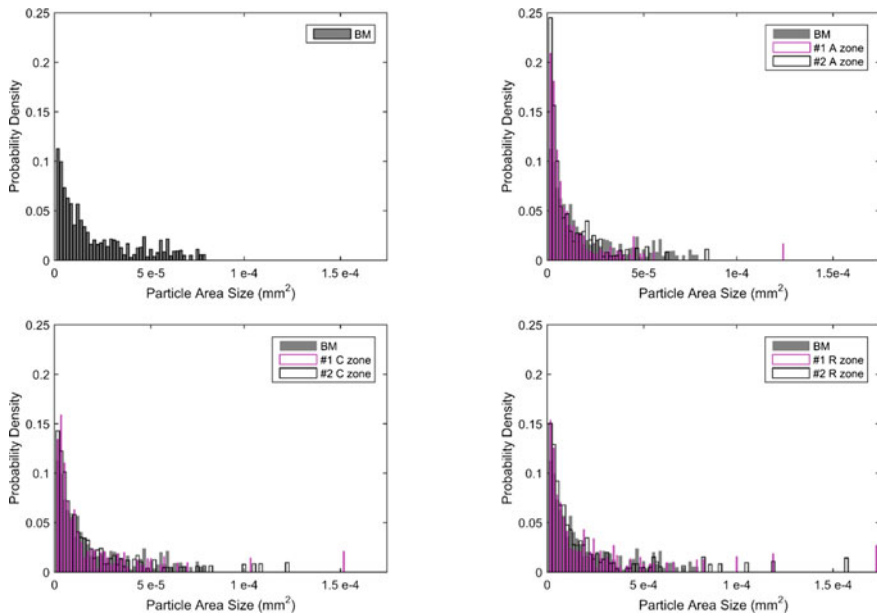


Fig. 7 Probability histogram of the particle area size in each zone. *Top left* base material, *top right* A zone, *bottom left* C zone, *bottom right* R zone

Corrosion Test

Specimens were mounted so that only a 1.5'' wide cross section including all weld affected regions were exposed. All other sides of the piece were covered by epoxy resin. The polished specimens were immersed in 10% diluted EXCO test solution (EXCO formula: 4.0 M of NaCl, 0.5 M of KNO₃ and 0.1 M of HNO₃ [15]) under room temperature (25 °C) for 18 h, the liquid volume to exposed metal surface area ratio was kept to at least the recommended value in ASTM G34 [15]. After 18 h the samples were rinsed in DI water, dried and then cleansed with condensed nitric acid and DI water. Optical microscopy images (Fig. 8 left) of the cleaned surfaces were taken to provide a qualitative view of the corrosion resistance gradient. The heavily corroded (dark) region overlaps with the locations of the TMAZ and HAZs for all samples, suggesting that the thermal cycle accompanied with FSW processing leads to sensitivity to corrosion for the TMAZ and HAZ zones. Close-up examination of the corroded surface in TMAZ and HAZ shows heavy material loss and micro crack formation surrounding the IMPs.

The 2 faster welds (#2 and #5) have smaller HAZ areas but the corrosion effect is more severe as more micro cracks and thicker oxide layers are formed on their HAZs. Another result from the corrosion test is that the slower weld #1 has a

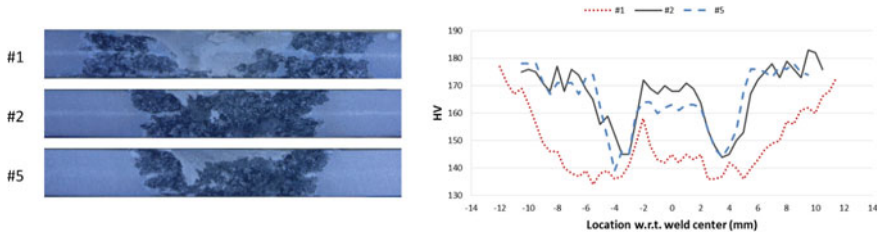


Fig. 8 *Left* optic image of the cross section of the three welds after corrosion test; *Right* the Vickers hardness profile across each weld on the center layer through thickness

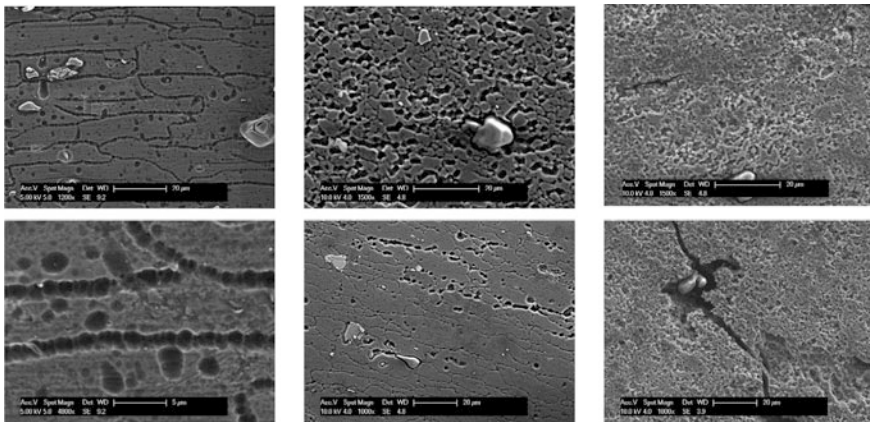


Fig. 9 SE image of the surface after corrosion testing. The *left* two are images of base material at different magnifications. The *center column* are images of sample #1, *top* image is in the nugget zone and *bottom* image in the TMAZ zone. The *left* two are taken from sample #5, *top* is in the nugget zone and *bottom* one is in the TMAZ zone

relatively corrosion free nugget zone, similar to the base material while the other 2 samples show obvious nugget corrosion after the test. This might be a result from the combined effect of grain size and precipitate characteristics. The faster two welds have smaller grain sizes in the nugget, offering more grain boundary fraction and grain boundary precipitate sites for corrosion attack. The three weld nuggets probably have different precipitate types and sizes inside grains as well. The 7xxx series aluminum alloy is a heat-treatable alloy, meaning that most of its high strength comes from precipitate strengthening. Figure 8 right is the hardness profile of center layers of the welds, measured with a standard Vickers hardness test frame using load of 500 g and holding time of 10 s, the spacing between adjacent indent points is 0.5 mm. The fact that the nugget zones of the welds are on different micro hardness levels suggests that different precipitate states are present (Fig. 8 right). The faster two welds also have a relatively clear zone in the nuggets close to their AS. This could be a result from the inhomogeneity of the IMPs spatial distribution.

The AS of nugget zone has mostly very small, crushed IMPs and the overall fraction of IMPs are lower than their RS counterparts. These smaller and less frequent IMPs result in less inhomogeneity and fewer regions of corrosion reaction, resulting in better corrosion resistance. Detailed SE images of the corroded samples are shown in Fig. 9.

The microstructure of the base material after corrosion testing was checked in the SEM (Fig. 9 left column). The grain boundaries and interfaces between IMPs and the matrix were selectively etched. A higher magnification image on the right hand side shows that the grain boundary etching actually consists of small pits associated with the potential difference due to Cu depletion at grain boundaries and precipitate free zones [10]. Some other pits in the middle of grains also suggest that precipitates are the attack spot for selected corrosion environment. The nugget zone and TMAZ of sample #1 (Fig. 9 center column) have similar corrosion results, with mostly circular pits along grain boundaries and gaps between IMPs and the matrix. The higher speed weld #2, however, already shows whole grains being etched away in the nugget zone and micro cracks forming from the IMP sites for both the nugget and TMAZ zones. Further investigation of the precipitates in high speed welds is needed to determine the mechanism of the observed results.

Conclusions

Microstructure of high speed friction stir welded aluminum alloy 7075-T6 sheets were examined before and after corrosion testing. The joints involve a high level of microstructure inhomogeneity, typical for friction stir welds. The size and distribution of intermetallic particles of the nugget zones were analyzed and inhomogeneity of the distributions were found in nugget zones. The higher welding speeds result in larger IMPs and less inhomogeneity of their distributions. The larger IMPs possibly result in higher corrosion rates in the nugget zones of the faster welds. Micro-hardness measurement shows that the higher speed welds have smaller and less severely softened HAZs, their nugget zones also have higher hardness compared to the relatively slower welds. The HAZs of all samples are more susceptible to the corrosion process compared to the base material. With smaller size of HAZs the faster welds have less corrosion sensitive regions. However the nugget zone of the faster welds are also sensitized while the nugget zone of the slower weld keeps a similar performance to the base material, which did not have micro cracks or heavy oxide layer after corrosion testing. In summary, the higher welding speed resulted in smaller HAZs, hence less corrosion sensitive areas, but have more susceptible nugget zones compared to the slower welds.

References

1. Thomas WM, Nicholas ED, Needham JC, Murch MG, Temple-Smith P, Dawes CJ, (1991) Improvements relating to friction welding, US
2. Thomas WM et al (1991) Friction stir butt welding, GB
3. Threadgill PL et al (2009) Friction stir welding of aluminium alloys. *Int Mater Rev* 54(2):49–93
4. Ma ZY (2008) Friction stir processing technology: a review. *Metall Mater Trans A Phys Metall Mater Sci* 39A(3):642–658
5. Mahoney MW et al (1998) Properties of friction-stir-welded 7075 T651 aluminum. *Metall Mater Trans A Phys Metall Mater Sci* 29(7):1955–1964
6. Nandan R, DebRoy T, Bhadeshia HKDH (2008) Recent advances in friction-stir welding - Process, weldment structure and properties. *Prog Mater Sci* 53(6):980–1023
7. Thomas WM, Nicholas ED (1997) Friction stir welding for the transportation industries. *Mater Des* 18(4–6):269–273
8. Hovanski Y et al (2015) High-speed friction-stir welding to enable aluminum tailor-welded blanks. *JOM* 67(5):1045–1053
9. Sukiman NL, Birbilis N, Hughes AE, Mol JMC, Garcia SJ, Zhou X, Thompson GE (2012) Durability and corrosion of aluminium and its alloys: overview, property space, techniques and developments, aluminium alloys—new trends in fabrication and applications, Ahmad PZ (ed)
10. Lumsden JB et al (1999) Intergranular corrosion following friction stir welding of aluminum alloy 7075-T651. *Corrosion* 55(12):1127–1135
11. Pao PS et al (2001) Corrosion-fatigue crack growth in friction stir welded Al 7050. *Scripta Mater* 45(5):605–612
12. Field DP et al Texture effects on corrosion behavior of friction stir welded 7075 aluminum
13. Hatch JE (ed) (1984) Aluminum: properties and Physical Metallurgy. ASM International, p 424
14. (1999) Corrosion of aluminum and aluminum alloys. ASM International
15. ASTM International (2013) Standard test method for exfoliation corrosion susceptibility in 2XXX and 7XXX series aluminum alloys (EXCO Test), p 8

Flow Features in Shoulder Zone During Scroll Tool Friction Stir Welding Thick 6061 Aluminum Plates

David Yan, Xiaoming Wang and Guy Littlefair

Abstract The objective of this present study was to reveal the material flow interaction between the shoulder zone and nugget zone in a thick 6061 aluminum plate during scroll tool friction stir welding. It was observed via microstructural examinations that the scroll tool induces the bulk plasticized material to flow into the advancing side from the retreating side in the shoulder flow zone. This results in a unique flow pattern in the shoulder zone, including, among others, a near-half-onion ring pattern in the transverse section of the weld center. Moreover, a semi-circular pattern accumulated in the longitudinal direction of the bottom portion of the weld zone, but featureless in the top portion of the same weld zone. The obtained flow patterns have also been quantified in relation to the welding parameters to build a database for further and more detailed numerical investigation.

Keywords Friction stir welding • Scroll tool • Shoulder zone flow patterns • 6061 aluminum alloy

D. Yan (✉)

College of Science and Technology, University of Wisconsin-Green Bay,
2420 Nicolet Drive, Green Bay, WI 54311, USA
e-mail: yand@uwgb.edu

X. Wang

School of Engineering Technology, Purdue University, 401 N. Grant Street,
West Lafayette, IN 47907, USA
e-mail: wang1747@purdue.edu

G. Littlefair

School of Engineering, Deakin University, Geelong, VIC 3217, Australia
e-mail: guy.littlefair@deakin.edu.au

© The Minerals, Metals & Materials Society 2017

Y. Hovanski et al. (eds.), *Friction Stir Welding and Processing IX*,

The Minerals, Metals & Materials Series, DOI 10.1007/978-3-319-52383-5_15

Introduction

Friction Stir Welding (FSW) is a relatively new solid-state welding technique and provides an excellent opportunity for joining aluminum alloys. During FSW process, tool geometry and welding conditions directly affect material flow formation and subsequently determine the microstructure and properties of the FSW weld. Therefore, understanding of the material flow in FSW is important as it assists in the process evaluation and welding conditions optimization. Researchers have employed different techniques to investigate the material flow movement and patterns during FSW [1–3].

Donatus et al. [4] recently reviewed the existing material flow theories applied to the FSW process and emphasized that the material flow during FSW is complicated and far from being fully understood and established. Mishra and Ma [5] comprehensively reviewed the FSW process and concluded that during tilted tool FSW, a featureless flow pattern commonly appears within the shoulder zone when sectioning FSW weld parallel to the welding direction. Kumar and Kailas [6] studied the material flow during tilted tool FSW, and found that the featureless flow pattern in the shoulder zone resulted from the bulk flow mode of the shoulder zone material flows. Huang et al. [7] visualized the material flow by copper foil markers during titled tool FSW of 6082 Al alloy and concluded that the pin-driven flow primarily compressed material to the retreating side, whereas the shoulder-driven flow pushed materials from the retreating side to the advancing side and caused banded structure in the advancing side. Chen et al. [3] studied the nugget zone flow formation during tilted tool FSW of 5083 Al alloy and reported that the nugget zone is formed by a shear layer material which detaches in the trailing-retreating location of the tilted tool pin, one layer in each revolution. Layer-to-layer detachments lead to a serial near-semicircular banded structure appearing in the nugget zone of the weld.

According to Rai et al. [8], the scroll tool provides a simple setup to perform FSW by eliminating the tilted tool axis that is commonly used in the tilted tool FSW, and its weld zone material flow formation is still the subject of ongoing research. Donatus et al. [4] studied the material flow behavior during scroll tool FSW of 8 mm thick AA5083/AA6082-Al plates, and reported that the weld zone material is driven by the tool and flows more from the advancing side into the retreating side without mixing. Also, the material flows from the retreating side to the advancing side occurred in the tool shoulder domain only, and the pull is greatest in the transition region between the tool shoulder domain and the tool pin domain. Although a number of weld zone flow patterns have been presented by Donatus et al. [4], Toskey et al. [9] and Tozaki et al. [10] during scroll tool FSW, the exact flow pattern in the shoulder flow zone has not been fully characterized. The objective of this present study was to understand the material flow interaction between the shoulder zone and nugget zone during scroll tool FSW of 6061 aluminum alloy and to reveal its material flow patterns via microstructural examinations.

Experimental Procedures

The materials used in this work were 6061 aluminum (Al–1.0 Mg–0.6Si) rolled thick plates (300 mm × 100 mm × 20 mm). The tool was a non-tilted, one scroll flat shoulder (30 mm diameter) and tapered left-hand-threaded pin (18.8 mm length, 5.0 mm tip diameter and 8° cone angle) tool. All the FSW tests were conducted, employing a TOS Olomouc milling machine under the tool constantly rotating at 250 rpm and travelling at 56 mm/min with the depth of shoulder plunging at 0.4 and 0.6 mm respectively.

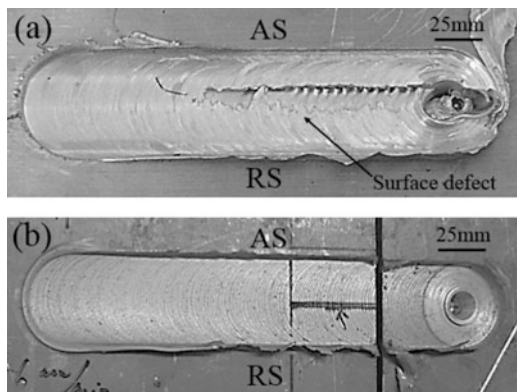
After the welds were made, the samples were sectioned in the both transverse cross section and longitudinal direction (through the welding center line). Standard metallographic practice was followed and Keller's reagent was used for etching. Etched samples were examined via an Olympus-DP70 optical microscope to obtain their microstructures for shoulder zone flow patterns revelation.

Results and Discussions

Post-weld Profile

Figure 1a, b show two post-weld profiles obtained under the tool constantly rotating and travelling at 250 rpm and 56 mm/min for a 250 mm length with a depth of shoulder penetration at 0.4 mm and 0.6 mm respectively. It can be observed from the figures that surface defect appeared on the post-weld produced at the depth of shoulder penetration of 0.4 mm while the defect-free weld was achieved at the depth of 0.6 mm. This indicated that the welding parameter, i.e. the depth of shoulder penetration significantly influences the shoulder zone material flow induction, and subsequently affects the quality of the FSW weld.

Fig. 1 a and b Optical images of post-weld profiles obtained from two FSW welds made under the tool constantly rotating and travelling at 250 rpm and 56 mm/min for a length of 250 mm with a depth of shoulder penetration at a 0.4 mm and b 0.6 mm, showing in (a) a surface defect in the last portion of the weld



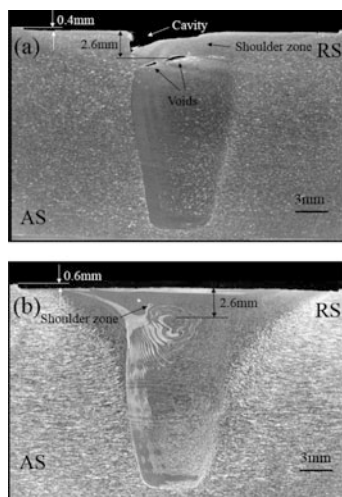
It can also be found from the Fig. 1a that the surface defect occurred at the last 150 mm of the tool travelling whereas the defect-free weld was produced during the first 100 mm of the same welding process. This signified that the supply of the shoulder zone material was unstable under this set of the welding conditions causing an insufficient supply of the material flow at the last section of the welding, but producing a sufficient supply of the material flow at the first portion of the joining process. This phenomenon is interesting enough to be further investigated and will be discussed later.

Flow Pattern in Transverse Cross Section

Figure 2a, b present two micrographs of the transverse cross section of welds obtained by sectioning two post-welds shown in the Fig. 1a, b at the mid position of the weld profiles.

It can be observed from the Fig. 2a that a cavity occurred on the top and two internal voids appeared in the upper weld transverse cross section within the shoulder zone on the advancing side (AS). The formation of the cavity and internal void were considered as a result of the insufficient supply of the shoulder zone material, which agrees with the post-weld profile showing the surface defect in the Fig. 1a. Also, the internal voids found from the figure in the upper weld cross section signified a material flow interaction between the shoulder flow zone and nugget zone. After measuring, the thickness of the shoulder flow zone along the welding center line was approximately 2.6 mm produced under this set of the welding conditions.

Fig. 2 a and b Micrographs of the transverse cross section of the welds obtained under the tool constantly rotating and travelling at 250 rpm and 56 mm/min with a depth of shoulder penetration at a 0.4 mm and b 0.6 mm, showing in (a) a cavity on the top and two internal voids in the upper weld transverse cross section within the shoulder zone on the advancing side (AS), and indicating in (a) and (b) a 2.6 mm thick of the shoulder zone produced under these two sets of welding parameters

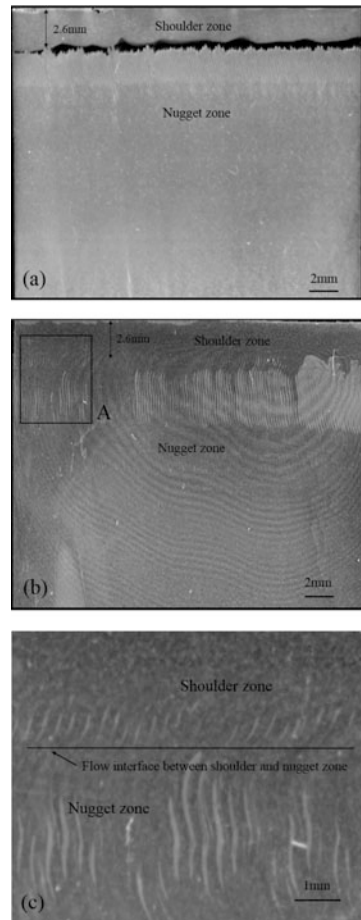


Accordingly, by deploying this estimated 2.6 mm thickness of the shoulder flow zone to examine the Fig. 2b, it can be seen that a near-half-onion ring pattern appeared in the bottom portion of the shoulder flow zone on the both advancing side and retreating side (RS). The appearance of this type of flow pattern in the shoulder zone viewed in the transvers cross section will be discussed in more detail in relation to the flow patterns in the same weld zone viewed in the longitudinal cross direction.

Flow Pattern Along Longitudinal Cross Section

Figure 3a, b illustrate two micrographs of the longitudinal cross section of welds obtained by sectioning the post-welds shown in the Fig. 1a, b through the welding center line, while Fig. 3c presents an enlarged view of the area 'A' indicated in the Fig. 3b.

Fig. 3 a, b and c Micrographs of the longitudinal cross section of the welds obtained under the tool constantly rotating and travelling at 250 rpm and 56 mm/min with a depth of shoulder penetration at a 0.4 mm and b 0.6 mm, showing in (a) a gap between the shoulder zone and nugget zone over the entire weld longitudinal cross section, indicating in (a) and (b) a 2.6 mm thickness of the shoulder zone produced under the current set of welding parameters, and presenting in (c) an enlarged view of the area 'A' of the (b), a semi-circular flow pattern appeared in the *bottom portion* of the shoulder zone but a featureless pattern presented in the *top portion* of the same weld zone



It can be seen from the Fig. 3a that there is a gap between the shoulder zone and nugget zone throughout the entire weld longitudinal cross section. After directly measuring, it was found that the distance between the mid-point of the gap and the top surface of the weld section is around 2.6 mm which is consistent with the shoulder zone thickness approximated from the transverse cross section of the weld shown in the Fig. 2a. Also, a serial near-straight line flow pattern that appeared in the top portion of the nugget zone can be observed from the Fig. 3a which is in agreement with the findings of Donatus et al. [4], Toskey et al. [9] and Tozaki et al. [10] for the flow patterns in the nugget zone produced during scroll tool FSW.

By inspecting the Fig. 3b, it can be noted that a series of discontinuous large-scale vertical curves appeared in the upper portion of the weld longitudinal cross section. Care was taken to locate these patterns in the weld zone, hence, the previously obtained 2.6 mm thickness of the shoulder zone was deployed. Accordingly, it can be seen that the top portion of these serials of discontinuous large-scale vertical curves are, in fact, the flow patterns in the shoulder zone produced by this present scroll tool under the current set of the welding parameters. To interpret the top portion of these flow patterns in relation to the obtained shoulder zone flow patterns in the transverse cross section shown in the Fig. 2b, an enlarged view of the area 'A' indicated in the figure was presented in the Fig. 3c.

It can be observed from the Fig. 3c that there was a flow interaction between the shoulder zone flow and nugget zone flow resulting in a flow interface, subsequently led to the flow pattern shaped like discontinuous vertical curves. As distinguished by a drawn flow interface line in the figure, it can also be seen that a semi-circular flow pattern appeared in the bottom portion of the shoulder flow zone, whereas a featureless pattern appeared in the top portion of the same weld zone.

Concluding Remarks

The material flow interaction between the shoulder zone and nugget zone during FSW of thick 6061 aluminum plates were studied, with the following research findings:

1. The thickness of the shoulder zone along the welding center line was approximately 2.6 mm produced under the present tool, constantly rotating and travelling at 250 rpm and 56 mm/min with the depth of shoulder penetration between 0.4 and 0.6 mm.
2. A unique flow pattern in the bottom portion of the shoulder zone was found in the transverse cross section of the weld center with a near-half-onion ring pattern. Moreover, a semi-circular pattern accumulated in the bottom portion of the shoulder zone along the longitudinal direction of the weld sectioned through the welding center line, but the top portion of the shoulder zone was featureless.

Acknowledgements The authors acknowledge the financial support of The University of Wisconsin-Green Bay Research Council.

References

1. Guerra M, Schmidt C, McClure JC, Murr LE, Nunes AC (2002) Flow patterns during friction stir welding. *Mater Charact* 49(2):95–101. doi:[10.1016/S1044-5803\(02\)00362-5](https://doi.org/10.1016/S1044-5803(02)00362-5)
2. Bhattacharya TK, Das H, Pal TK (2015) Influence of welding parameters on material flow, mechanical property and intermetallic characterization of friction stir welded AA6063 to HCP copper dissimilar butt joint without offset. *Trans Nonferr Met Soc Chin* 25(9):2833–2846. doi:[10.1016/S1003-6326\(15\)63909-7](https://doi.org/10.1016/S1003-6326(15)63909-7)
3. Chen ZW, Pasang T, Qi Y (2008) Shear flow and formation of Nugget zone during friction stir welding of aluminium alloy 5083-O. *Mater Sci Eng A* 474(1–2):312–316. doi:[10.1016/j.msea.2007.05.074](https://doi.org/10.1016/j.msea.2007.05.074)
4. Donatus U, Thompson GE, Zhou X, Wang J, Beamish K (2015) Flow patterns in friction stir welds of AA5083 and AA6082 alloys. *Mater Des* 83:203–213. doi:[10.1016/j.matdes.2015.06.006](https://doi.org/10.1016/j.matdes.2015.06.006)
5. Mishra RS, Ma ZY (2005) Friction stir welding and processing. *Mater Sci Eng R Rep* 50(1–2):1–78. doi:[10.1016/j.mser.2005.07.001](https://doi.org/10.1016/j.mser.2005.07.001)
6. Kumar K, Kailas SV (2008) The role of friction stir welding tool on material flow and weld formation. *Mater Sci Eng, A* 485(1–2):367–374. doi:[10.1016/j.msea.2007.08.013](https://doi.org/10.1016/j.msea.2007.08.013)
7. Huang Y, Wang Y, Wan L, Liu H, Shen J, dos Santos JF, Zhou L, Feng J (2016) Material-flow behavior during friction-stir welding of 6082-T6 aluminum alloy. *Int J Adv Manuf Technol*:1–9. doi:[10.1007/s00170-016-8603-7](https://doi.org/10.1007/s00170-016-8603-7)
8. Rai R, De A, Bhadeshia HKDH, DebRoy T (2011) Review: friction stir welding tools. *Sci Technol Weld Join* 16(4):325–342. doi:[10.1179/1362171811Y.0000000023](https://doi.org/10.1179/1362171811Y.0000000023)
9. Toskey A, Arbogast W, Allen C, Patnaik A (2005) Fabrication of Al box beams using self-reacting and standard fixed pin FSW. In: Jata KV, Mahoney MW, Mishra RS, Lienert TJ (eds) *Friction stir welding and processing III*, vol proceedings of a symposia sic sponsored by the shaping and forming committee of the materials processing and manufacturing division (MPMD) of TMS held at the TMS annual meeting, San Francisco, California, 13–17 Feb 2005, pp 171–178
10. Tozaki Y, Uematsu Y, Tokaji K (2009) Welding structure and tensile-shear properties of friction-stir spot welds joined by scrolled groove shoulder tool without probe in aluminium alloy. *Nihon Kikai Gakkai Ronbunshu, A Hen/Trans Jpn Soc Mech Eng Part A* 75(750): 228–234

Part V
Dissimilar Applications

Joining Dissimilar Material Using Friction Stir Scribe Technique

Piyush Upadhyay, Yuri Hovanski, Blair Carlson, Eric Boettcher,
Robert Ruokolainen and Peter Busuttil

Abstract The ability to effectively join materials with vastly different melting points, like aluminum to steel, and polymer composites to metals, has been one of the roadblocks to realizing multi-material components for lightweighting efforts. The friction stir scribe (FSS) technique is a promising method that produces continuous overlap joints between materials with vastly different melting regimes and high-temperature flow characteristics. FSS uses an offset cutting tool at the tip of the friction stir welding pin to create an in situ mechanical interlock between material interfaces. With investments from the U.S. Department of Energy Vehicle Technologies Office and several automotive manufacturers and suppliers, Pacific Northwest National Laboratory is developing the FSS process and has demonstrated the viability of joining several material combinations. Details of welding trials, unique challenges, and mitigation strategies in different material combinations will be discussed. Joint characterization, including mechanical tests and joint performance, will also be presented.

Keywords Friction stir scribe • Aluminum to steel joining • Friction stir welding • AA6022 • Surfalex 6s • Mild steel • Ultra high strength steel

P. Upadhyay (✉)

Pacific Northwest National Laboratory, 902 Battelle Boulevard, Richland, WA 99354, USA
e-mail: piyush.upadhyay@pnnl.gov

Y. Hovanski

Brigham Young University, Provo, UT 84602, USA

B. Carlson

General Motors Research and Development Laboratory, Warren, MI 48090, USA

E. Boettcher

Honda R&D Americas, Raymond, OH 43067, USA

R. Ruokolainen

FCA US LLC, Auburn Hills, MI 48321, USA

P. Busuttil

Kuka Development Center, Sterling Heights, MI, USA

© The Minerals, Metals & Materials Society 2017

Y. Hovanski et al. (eds.), *Friction Stir Welding and Processing IX*,

The Minerals, Metals & Materials Series, DOI 10.1007/978-3-319-52383-5_16

Background and Introduction

The friction stir scribe (FSS) technique has enabled lap joining of dissimilar materials with very different melting points and vastly different high-temperature material properties [1–4]. A recently invented variant of the friction stir welding (FSW) process, the FSS tool consists of a regular FSW tool with one simple modification: a small cutter (scribe) is added at the tip of the FSW tool pin offset from the tool axis of rotation. Examples of FSS tools and the setup are shown in Fig. 1.

In contrast to typical setups used for conventional FSW of dissimilar systems in lap configuration, materials to be joined are assembled such that the lower-melting-point material is on the top. In FSS, while the regular portion of the FSW tool plastically deforms and “stirs” the lower-melting-point top layer, the scribe makes a small continuous cut on the surface of the higher-melting-point material below. As the tool rotates and travels the machining action of the scribe in concert with FSW in the top layer results in the formation of a mechanical interlocking feature at the material interface. A consistently maintained clearance between the FSS pin and the surface of the bottom sheet ensures that the FSS tool never interacts with the higher-melting-point material (the bottom layer). This aspect—unique to FSS—avoids bulk plastic deformation of the bottom layer. As the bottom layer is only machined rather than being “plowed” through, the propensity for melting and associated defect/void formation typically observed in conventional FSW of dissimilar pairs is greatly diminished in FSS.

An ongoing project at Pacific Northwest National Laboratory (PNNL), in close collaboration with several automotive original equipment manufacturers (OEM)s and a robot supplier, is focused on evaluating and developing this new technique as it applies to joining of aluminum to steel relevant to specific potential automotive

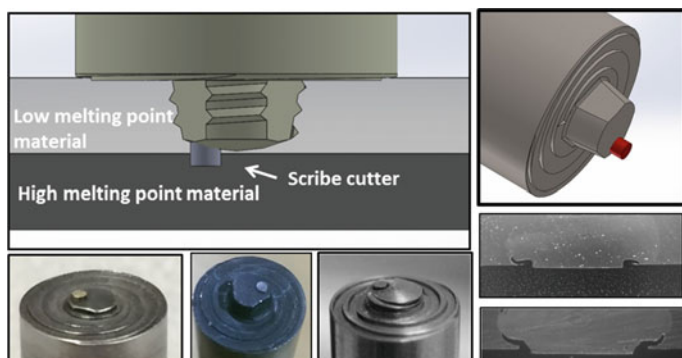


Fig. 1 *Top left* Schematic of friction stir scribe (FSS) welding setup. Note that only the cutting scribe contacts the bottom sheet. The rotating pin has a predetermined clearance from the interface. *Top right* Schematic of FSS tool. *Bottom left* FSS tools. *Bottom right* Transverse cross sections of FSS joints

components. In addition, this technique is also being developed for joining metals to reinforced polymers. Here we present an overview of the process, progress made, and challenges associated with joining a variety of dissimilar material combinations and joint characterizations.

Materials and Experimental Details

FSS welds were made between several combinations of aluminum and steel sheets in lap configuration. The details of materials used and several process control parameters of reported welds are shown in Table 1. Conventional FSW tools as precursors to FSS tools were fabricated from H13 tool steel heat treated to HRC 45. Each of the FSW tools used had a shoulder of 12.7 mm consisting of double scrolls, and a conical pin with three flats. The length of the pin was varied depending upon the thickness of the top layer (See Table 1). A representative example of tool geometry used for a 3 mm thick aluminum-to-steel joint is shown in Fig. 2. Also shown is the schematic of the inserted scribe cutter. The scribe insert, made of W–C–Co, was press fit into a drilled hole offset from the axis of rotation. Subsequently the scribe was ground to the desired length. Joints were produced on a high precision Manufacturing Technology, Inc., gantry-type FSW machine at PNNL using position control. The commanded plunge depth was chosen after some trial and error, such that a satisfactory level of scribe engagement in the steel layer was maintained as well as the clearance between the pin and the steel layer. The FSW system can measure several process responses in real time including tool forces in all three directions, tool torque, and position.

All the welds were ~280 mm long, made with 100 mm × 300 mm flat panel sheets with an overlap of 40 mm.

After welding, the joints were cut transversely into metallographic and lap-shear test specimens using water jet milling. Conventional cutting methods were not used to avoid any deformation of the samples during the cutting process. Select weld

Table 1 Process parameters and material combinations

Pair	Top sheet aluminum	Bottom sheet steel	Pin length/scribe length (mm)	Tool rotation (rpm)	Travel speed (mm/min)	Tool tilt
A	AA6022 (1 mm)	GMW-ST-CR3 (0.7 mm)	0.9/0.42	1950	750	1°
B	Cast Aluminum (3.0 mm)	JAC 270C 45/45 (2 mm)	2.9/0.35	1700	1000	0.5°
C	Surfalex 6s (1.1 mm)	TRIP 590 (1.6 mm)	1.0/0.30	1950	350	0.5°
D	Surfalex 6s (1.1 mm)	Coated Usibor (UHSS) (2 mm)	1.0/0.35	1950	350	0.5°

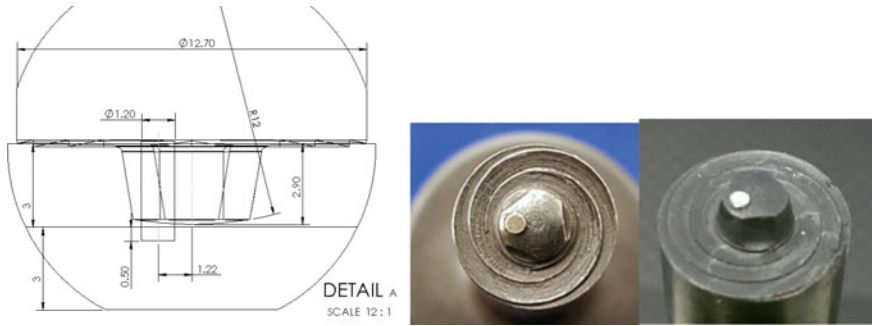


Fig. 2 *Left* Drawing of the FSW tool with scribe insert. *Right* Picture of two scribe tools (W–C–Co) used for welding 1 mm thick AA6022 to 3 mm thick cast aluminum

cross sections were then ground and polished for optical macro/micrographs. A series of unguided lap-shear tensile tests were performed using a universal test frame at the rate of 1.27 mm/min. For each case, several samples from different regions of the joints were tensile tested. Appropriate shims were added to the grips to ensure that samples were aligned during testing and bending stress in the samples was minimized. Since the precise area over which bonding occurs in a FSS lap joint is not known, it is difficult to assign a strength value (load per unit area) to the joint. For this reason, load bearing capacity per unit length of the joint is obtained, by dividing the load at failure by the length of the weld in the test sample.

Results and Discussions

Representative welded panels for four pairs of aluminum–steel combinations (Table 1) are shown in Fig. 3. As is evident from Table 1 and Fig. 3, the steel types shown range from mild steel (200 MPa) to high strength range steel (TRIP 590) to ultra-high strength steel (UHSS, Usibor).

Cross sections that reveal the scribe joint region between two different combinations of aluminum and steel are shown in Fig. 4. The cross sections in the figure were obtained from near the start, middle, and end of the weld, respectively. The FSS process machined out a trough on the surface of the steel layer directly underneath the FSW pin, creating two nominally symmetrical hook-like features embedded on either side of the nugget root of the top aluminum sheet. The area of this trough can be directly linked to the swept radius of the scribe feature, while its depth is dependent upon the length of the scribe and commanded plunge depth (position control) or z-force (force control). For a given joint, the hook features appear to be fairly uniform along the length. This feature is very similar to what was observed in the past for FSS joining of Mg–Zn coated steel [3]. This hook-like



Fig. 3 Representative FSS welded joints made between four different pairs of Aluminum and steel panels. From top left to lower right, the combinations correspond to pairs A, B, C, and D

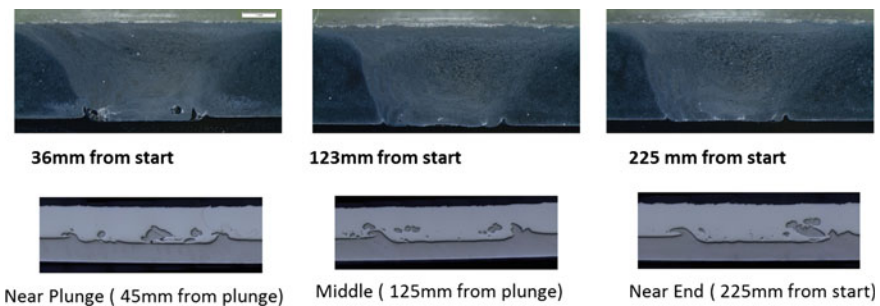


Fig. 4 Transverse weld cross section revealing the FSS joint between mild steel and AA6022 aluminum (*top*) and cast aluminum and steel (*bottom*). The cross sections were obtained from near the start, middle, and end of each 280 mm long joint

interlocking feature can be understood as an in situ, continuous, and permanent rivet-like fastening.

The results of joint lap-shear tests for welds made between AA6022 (1 mm) and mild steel (0.7 mm) (pair A) are shown in Fig. 5. Load per unit weld length is plotted against the measured extension for five different samples obtained from the 280 mm long joint panel. The reference test result obtained for a standard ASTM E8 sample for base mild steel is also shown.

For this material combination, all the tested samples are observed to reach peak load bearing capacity very close to that of the parent mild steel sheet (the weaker of the two base materials). All the tested joints exhibit a large amount of elongation;

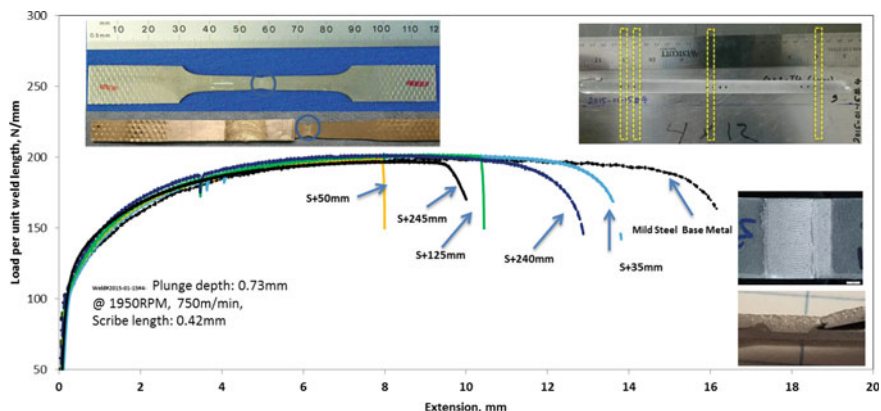


Fig. 5 Load per unit weld length (N/mm) plotted against measured extension for joints made between AA6022 (1 mm) and mild steel (0.7 mm) (pair A). The location relative to weld start for each sample is indicated by $S + x$. *Top left* A fractured E8 tensile sample for MS base metal is shown. A joined sample that fractured away from the weld region is also shown for comparison. The fracture locations are circled. *Bottom right* Fracture path for joints that failed in the weld

nevertheless, there are some variations in measured extension among the samples. These variations can be related to the location and mode of fracture. Two samples, (S + 35) and (S + 240), fractured away from the weld, necking in the base steel, as shown in the inset on the top left. The other three samples fractured in the FSW nugget region. An example of such fracture (top and cross-section views) is shown in the bottom right corner. The fracture appears to have started at the hook-nugget interface and moved toward the aluminum weld crown. It is important to note that direct comparison of elongation cannot be made between the base material tested and the lap-shear specimen. For example, even for joints that failed away from the weld, the elongation values for the joints are lower than that of the base material as more ductile steel is available in the gage length than in the joint, which consists of half aluminum sheet.

Figure 6 shows similar lap-shear test results for joints made with pair B, between cast aluminum (3 mm) and cold rolled steel (2 mm) (JAC 270C). Test results for three samples each from two welded panels are shown. Both the welds were made under identical conditions, but the overlap position of the two material layers was switched to assess effects of advancing- versus retreating-side loading. The retreating-side loaded samples performed slightly better than the advancing-side loaded samples, especially in terms of joint ductility. Nevertheless, a load carrying capacity of ~ 300 N/mm is exceeded in each case. In contrast to pair A shown in Fig. 5, the joint fracture occurred in the weld region for this case. The fracture occurred in the weld region near the hook-nugget boundary, traveling up to the crown along the heat affected zone as seen in cross-section and top views (Fig. 6).

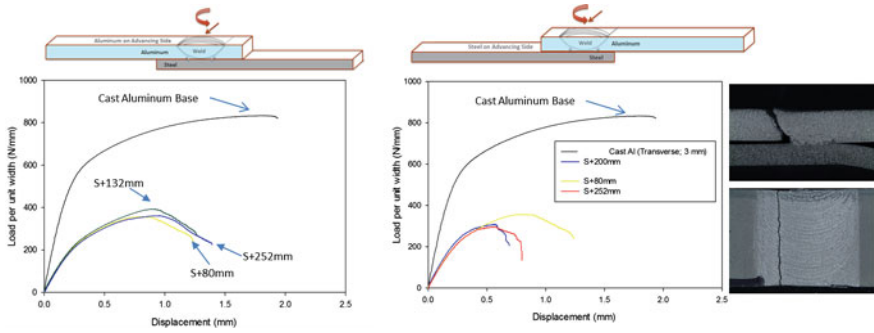


Fig. 6 Load per unit weld length (N/mm) plotted against displacement for joints made between cast aluminum (3 mm) and cold rolled steel (2 mm) (pair B). *Left plot* Results from retreating-side loaded samples. *Right plot* Results from advancing-side loaded samples. *Far right* Typical joint failure for this combination (cross-section and top views)

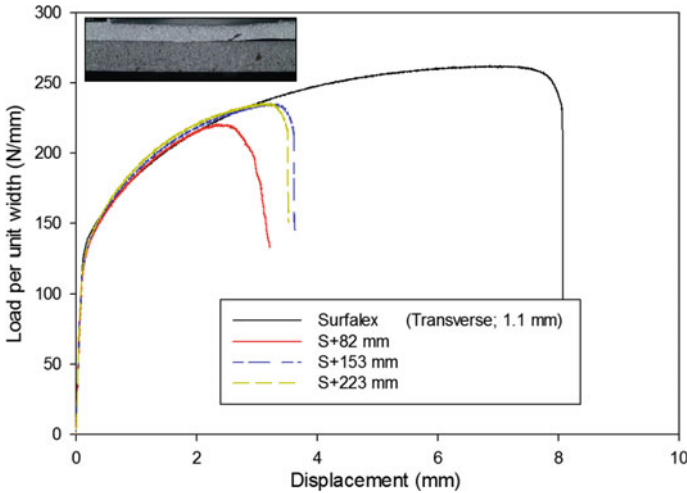


Fig. 7 Load per unit weld length plotted against displacement for FSS joint made between Surfalex 6s and Usibor (pair D)

Finally, Fig. 7 shows a load per unit weld length data set for joints made between Surfalex 6s and press-hardened UHSS Usibor (pair D). As the steel is significantly stronger than the aluminum layer, fracture always occurred in the welded aluminum (inset in Fig. 7) a manner similar to that with pair B. A comparatively minimal amount of the bottom Usibor layer has been machined by the scribe due to its much higher hardness. Nevertheless, a load carrying capacity of ~75% of that of the base Surfalex 6s is observed. A considerable amount of ductility prior to fracture is also noted in the joined sample.

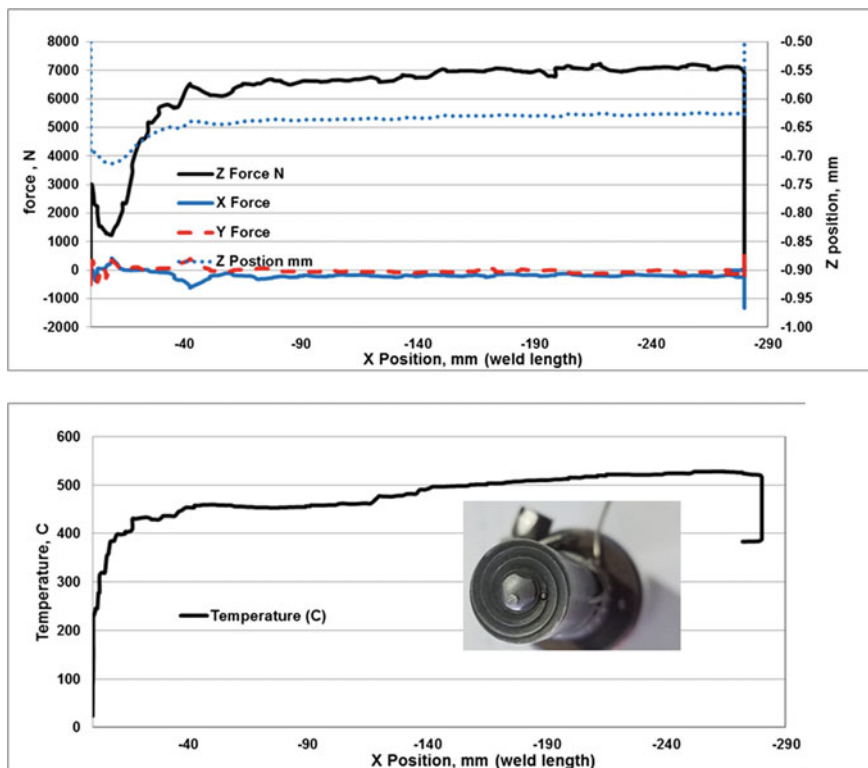


Fig. 8 *Top* Process forces plotted against weld distance. *Bottom* Measured temperature plotted against weld distance. The data set corresponds to pair A. *Inset* Close-up of the tool pin showing TC wire

The top chart of Fig. 8 shows forces experienced by the FSS tool in three directions and recorded plunge depth during welding of AA6022 to mild steel (pair A). The bottom chart of Fig. 8 shows temperature measured by an exposed thermocouple (TC) installed at the surface of the shoulder near the pin edge (see the photo inset in Fig. 8). After the initial tool plunge into the material stack and ramp-up of welding speed to full speed over a length of 50 mm, the lateral x and y forces and forge force (z-direction) experienced by the tool reached a fairly consistent level, indicating a consistent material flow. Process forces qualitatively similar to these have been recorded for all the material sets and will serve as input in designing robotic welders for eventual industrial commercialization.

The temperature measured by the tool rose slowly from around 400 °C at the start of the weld to ~530 °C toward the end of the weld, where the temperature appears to have stabilized. Since the temperature gradient in the nugget region is known to be high, the reported temperature needs to be understood in the context of the concomitant machining process taking place at the interface. As the TC sits very

near the scribe action, the recorded temperature is the result of the combined FSW in aluminum and machining in the bottom-layer steel. For this particular set wherein the aluminum sheet is relatively thin, it will be difficult to resolve the temperature gradient from the top of the crown to the hooking area. Nevertheless, for thicker aluminum sheet, multiple TCs can be added to understand temperature gradients through the thickness during the process.

Summary

FSS technology was successfully applied to join a variety of aluminum and steel alloys relevant to automotive applications in different thickness combinations. The continuous rivet-like in situ mechanical interlocking feature produced during the process results in a viable joint between the two materials. While the hook morphology is fairly consistent along the length of the joint, several joining and tooling parameters can influence its effectiveness.

The lap-shear results from different combinations of aluminum and steel show that joint strength and eventual fracture modes are dependent upon the relative load carrying capacity of the two layers. The quasi-static results discussed for several pairs of aluminum and steel are encouraging. Future effort will be focused on understanding weld characteristics and further characterization, including corrosion and dynamic properties of the joint, as well as expanding the welding window. It is anticipated that this capability of readily joining aluminum to steel will enable new avenues in the use of hybrid structures.

Acknowledgements PNNL is operated by Battelle Memorial Institute for the U.S. Department of Energy under contract DE-AC05-76RL01830. This work was sponsored by W. Joost in association with the U.S. Department of Energy Office of Vehicle Technologies as part of the Lightweight Materials program along with material contribution from participating automotive OEMs: General Motors, Honda R &D Americas, and Fiat Chrysler Automobiles. The authors would like to thank Karl Mattlin, Ram Prasad Prabhakaran, Timothy Roosendaal, and Shelley Carlson for their assistance in material characterization and testing.

References

1. Upadhyay P, Hovanski Y, Fifield L, Simmons K (2015) Friction stir lap welding of aluminum-polymer using scribe technology. In: Friction stir welding and processing VIII proceedings, TMS, Orlando, FL
2. Hovanski Y, Grant GJ, Jana S, Mattlin KF (2013) Friction stir welding tool and process for welding dissimilar materials. U.S. Patent US8434661 B2
3. Jana S, Hovanski Y, Grant GJ (2010) Friction stir lap welding of magnesium alloy to steel: a preliminary investigation. *Metall Mater Trans A* 41(12):3173–3182
4. Jana S, Hovanski Y (2012) Fatigue behavior of magnesium to steel dissimilar friction stir lap joints. *Sci Technol Weld Join* 17(2):141–145

Influence of Stir Flow on Joint Quality During Friction Stir Lap Al-to-Cu Welding

D. Parningotan, M. Tarrant, Z.W. Chen, A. Hilton and T. Pasang

Abstract Discontinuity free interface region of Al-to-Cu lap joints are required for high mechanical strength and low electrical resistance. While discontinuity free Al-to-Cu lap joints are difficult to produce using fusion welding, reviewing the literature, there is insufficient information on how such joints can be made by friction stir lap welding (FSLW). We will first briefly explain how material flow can cause voids, cavities or cracks during FSLW. Then, FSLW experiments are conducted using a tool design coupled with an appropriate positioning so that void-cavity free joints can be obtained. It has been found that speed conditions that cause insufficient downward flow also have resulted in insufficient formation of the interface layer thus in lack of joint. However, conditions that cause excessive downward flow also cause the intermetallic layer to crack. The balance of a mildly downward flow and a moderate growth of the interface layer without cracking will be demonstrated.

Keyword Friction stir lap welding (FSLW)

Introduction

Bimetallic joints, Al-to-Cu in particular, are commonly used in various electrical applications. Such joints divided into non-separable (welded, soldered and glued) and clamped (bolted, screw and wrapped) [1]. It is common knowledge that electric current is basically electrons moving to one place from another. Consequently, for fulfilling the required function, these bimetal joints must continuously be in contact in atomic scale. According to Messler [2], physical gap will always present in mechanical attachment, no matter how tight the joints. Based on this notion,

D. Parningotan (✉) · Z.W. Chen · A. Hilton · T. Pasang
Department of Mechanical Engineering, Auckland University of Technology,
Auckland, New Zealand
e-mail: dparningo@aut.ac.nz

M. Tarrant
National Aluminium Ltd, Auckland, New Zealand

non-separable joints or metallurgical joints is a must. However, high quality dissimilar metal welds are difficult to obtain. Excessive growth of brittle intermetallic always formed in fusion welding [3]. Making it difficult to be used in broader applications.

Various solid state bonding method such as explosion welding and cold roll bonding have commonly been used. However, to produce metallurgical joint, additional procedure (annealing) must be conducted [4, 5]. Friction stir welding is proven to be able to produce a relatively good joints with a layer of intermetallic as the metallurgical joint in Al-to-Fe [6, 7] and Al-to-Ti [8]. In FSLW, material contact as a first step to achieve metallurgical bonding, achieved due to the down flow induced by the rotating threaded pin. This contacted metals, activated by the high frictional temperature, will then react metallurgically to form the metallurgical joint in the form of intermetallic layer. However displaced materials and hooks in the interface region could possibly block the flow creating discontinuity in the form of voids or cavities [9]. In electrical application, this would mean higher resistance.

FSLW Al-to-Cu has been studied extensively. Most of these studies reveal the inevitable formation of intermetallic layer in the interface and the efforts to reduce the excessive growth by varying process parameters and the use of interlayer. In addition, various discontinuities have often revealed in various studies along with how the use of optimal process parameters can overcome them [10–13]. However, no effort on revealing how the thermomechanical mechanism causing this discontinuity formation.

Our preliminary work has revealed two of the discontinuity formation mechanism. First, flow disturbance by Cu particles and Cu flash inward folding creating discontinuity in the form of voids. This problem can be solved by using small penetration towards the bottom plate. Second, in low penetration welding, intermetallic layer cracking in the interface zone. The downward flow induced by the pin thread may partially shear away the growing intermetallic layers. If the following flow failed to re-weld to the sheared zone, discontinuity forms. In order to understand further on the thermomechanical mechanism, a series of experiments were conducted along with the observation and analysis on microstructure, chemical composition and thermal history of FSLW.

Experimental Procedures

FSLW experiments were conducted using a retrofitted milling machine. The top plate was 6 mm thick aluminium 6060-T5 alloy and the bottom plate was 3 mm thick commercially pure copper sheet. Preliminary experiments were conducted using rotational speed (ω) of 1400 rpm and welding speed (v) of 40 mm/min followed with another series of experiments using ω of 500, 710, 1000, and 1400 rpm respectively with same v of 56 mm/min. Normal concave tools were used in the preliminary works and tools with scroll shoulder were used in further experiments. Both were made using heat treated tool steel (H13). The diameter of the shoulder was 25 mm and the threaded pin outside diameter was 8 mm. Pin

penetration depth (d_p) can vary depending on the length of the pin which was adjusted during machining and vertical positioning of the tool during welding. A tilt angle of 2.5° was applied for using normal pins and the tilt angle was zero for using scroll tool.

During welding, temperature of the Al-Cu interface region was measured by placing K-type thermocouple (0.3 mm in diameter) placed in a narrow groove machined in top plate, on the surface that faces the bottom plate. After FSLW experiments, all samples were then cross sectioned, mounted and polished with normal metallographic procedure followed with $0.04 \mu\text{m}$ colloidal silica suspension for final polishing. Samples were examined with optical and scanning electron microscopes (SEM) equipped with energy dispersive spectroscopy (EDS).

Results and Discussion

Various d_p values were used in the preliminary works. The results are shown in Figs. 1 and 2 respectively. For larger d_p values, as shown in Fig. 1, large Cu pieces along with flash curved towards the stir zone, blocking the material flow. As a result, cavities formed in the interface region. Using lower d_p values, close to discontinuity free interface could be achieved. Small Cu particles are present in the stir zone and the flash has curved outward (Fig. 2a). This indicates that there was no blockage in the material flow to the interface during welding. Examination using SEM in Fig. 2b has revealed the common features in FSLW such as mix stir zone (MSZ) and the Al stir zone (SZ). A continuous metallurgical bonding could be achieved in the form of intermetallic layer along in the outermost MSZ. No crack or substantial voids are present in the weld, although there is small local discontinuity.

Another interface with low d_p is shown in Fig. 3. Again, along the interface region close to discontinuity free could be achievable although there is some localized intermetallic cracking. Figure 3 shows that there are $\sim 8 \mu\text{m}$ thick of intermetallic layers formed in the interface. The outer layer is irregular shaped and



Fig. 1 Optical micrographs of FSLW cross section made with normal concave shoulder tool with $d_p \approx 0.6 \text{ mm}$

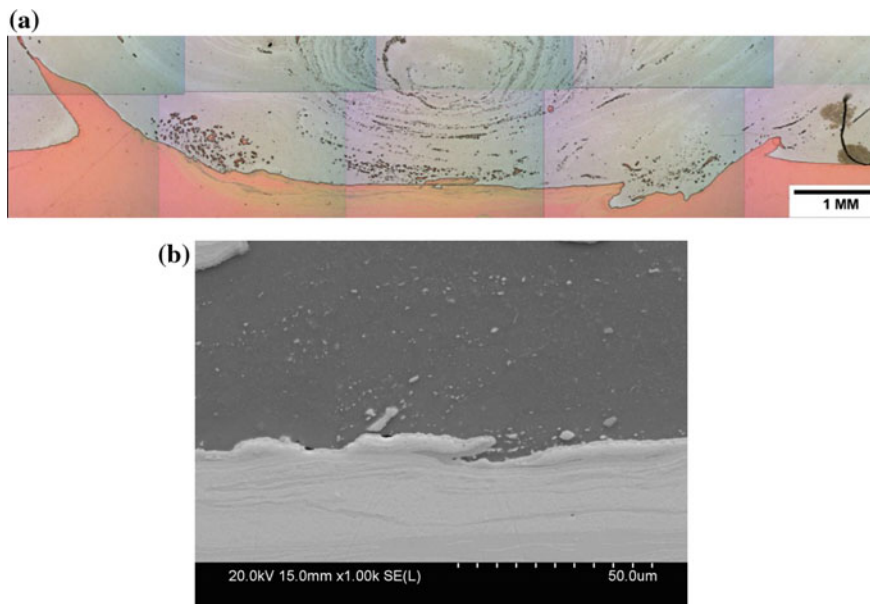


Fig. 2 **a** Optical and **b** SEM micrographs of FSLW cross section made with normal concave shoulder tool with $d_p \approx 0.6$ mm. SEM micrographs showing close to discontinuity free interface

has grown between the Al grains. For more details, shown in Fig. 3b, c that there are blocks of particles “floating” in the SZ, while the layers right at the interface seems to have been cut. On the other hand, Fig. 3d shows cracked and blocky intermetallic. From Chen et al. [14], it is known that material will still flow from RS to AS behind the pin. This continuous Al flow may exert a sufficiently high shear stress to the intermetallic layer, cracking the layer. A cracked layer may be further pushed away by the flow. This may be the reason for the “floating” particles in the SZ. EDS examination showed that this “floating” particles have similar composition with the outer most (adjacent to Al) interfacial intermetallic layer.

Based on the above observations, further experiments were then conducted to study the effect of rotation speed on achieving discontinuity free FSLW interface. In welding with $\omega = 500$ rpm, $v = 56$ mm/min, and $d_p \approx 0.17$ mm, no voids and no big Cu particles are present in the SZ (Fig. 4a). However, higher magnification in Fig. 4b shows that Al is not connected to the reaction zone in the bottom of the pin. There is no intermetallic layer present in the Al side, thus dismissing intermetallic layer brittle fracture. Note that there are some Al left in the bottom zone just above MSZ suggesting that this reaction occurred in the bottom of the pin where Al could slip into the bottom of the pin, mixed with Cu. This mixture will then, with the help of frictional heat, react to form intercalated layers of Al, Cu and intermetallic MSZ. The down flow was probably not able to reach or just slightly grazed the reaction zone, thus having failed to force re-welding. Figure 4c taken from another region of

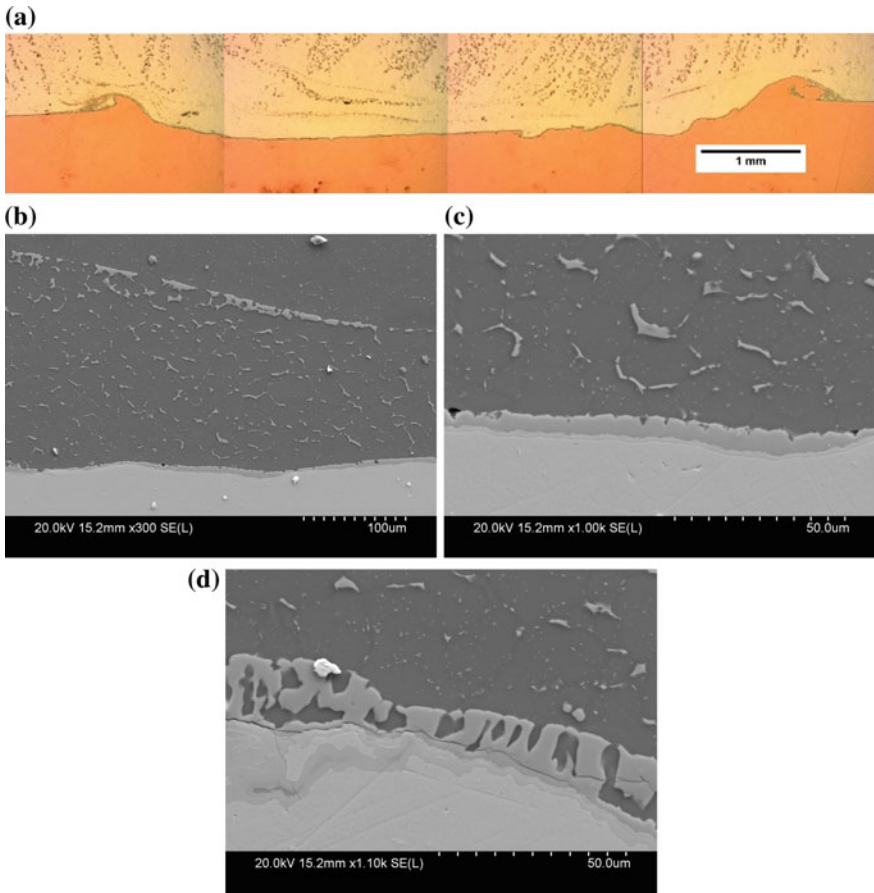


Fig. 3 **a** Optical and SEM micrographs of weld made using normal shoulder tool with $d_p \approx 0.2$ m. **b** Interface with intermetallic layer and “floating” particles in the SZ. **c** Magnification of the intermetallic layer showing cut like interface. **d** Cracked blocky intermetallic layer

the same interface shows a larger gap. Very thin intermetallic layer was formed in the interface. As shown in Fig. 5, similar stir flow and reactions in interface have been observed in weld made with $\omega = 710$ rpm, $v = 56$ mm/min, and $d_p \approx 0.17$ mm.

The next FSLW condition was $\omega = 1000$ rpm, $v = 56$ mm/min, and d_p 0.05 mm. Figure 6a shows that continuous interface could be achieved. SEM examination in Fig. 6b shows typical interface of this weld. There are three layers formed in the interface. Outer and innermost already identified as Al_2Cu and Al_4Cu_9 respectively. The outer most layer was able to extensively grow outward toward Al. This indicates that Al down flow was able to force re-welding, allowing the layer to continue to grow. In some area, the thick intermetallic layer is thick, as

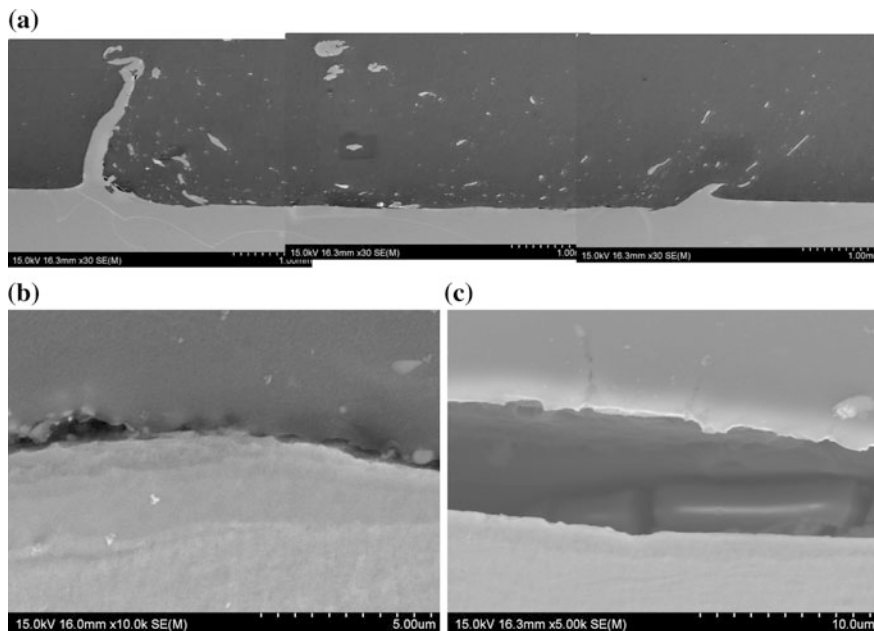


Fig. 4 SEM micrographs of a weld made by using scroll shoulder tool with $\omega = 500$ rpm, $v = 56$ mm/min, and $d_p \approx 0.17$ mm. **a** Interface cross section. **b, c** Al not able to force re-welding to the bottom reaction zone

shown in Fig. 6c. This is the result of the thick MSZ having completely transformed into intermetallic due to excessive frictional heat.

For the weld made using the highest ω value, where $d_p \approx 0.1$ mm, voids are present in SZ (Fig. 7a). Examination in higher magnification in Fig. 7b reveals that the majority of the interface has cracked. The crack has propagated between the Al_2Cu and two inner layer, AlCu in particular. This also in accordance with previous studies [15, 16]. Moreover, Moreno et al. [17] in their study stated that Al_2Cu and AlCu have low interfacial strength as a result of their difference in lattice structure, Al_2Cu being tetragonal and AlCu being monoclinic and orthorhombic. The mechanism of intermetallic layer formation is the same with the previous parameter. However, judging from the crack appearance, it was not caused by the shear flow associated with the down flow. This is because the outer layer seems have at one point grown extensively. It is possible that the layer cracked during sample preparation. During welding, melting has occurred in the SZ as suggested by the presence of eutectic structures in Fig. 7c. Melting could be a reason for voids formation, although in this work this has not been studied further.

Now we examine welding temperature history and relate them to the microstructure features observed above. In this study, v used was 56 mm/min (just under 1 s for the pin to travel for 1 mm). This means one point in a FSLW weldment (in this case, thermocouple hot junction) will be rubbed against the pin bottom for 8 s. As the pin travelled pass the point, the temperature increased and

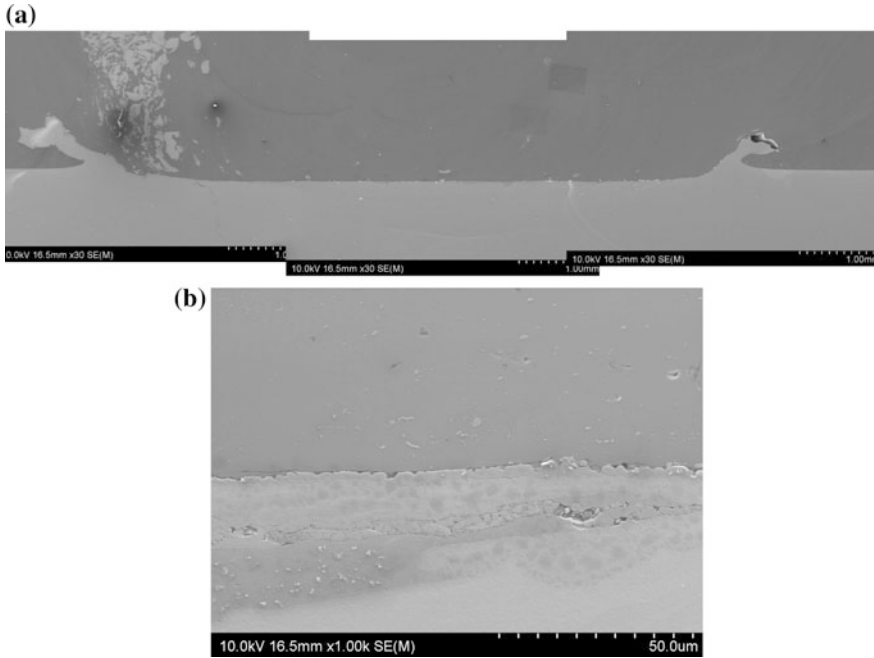


Fig. 5 SEM micrographs of a weld made by using scroll shoulder tool with $\omega = 710$ rpm, $v = 56$ mm/min, and $dp \approx 0.17$ mm. **a** Interface cross section. **b** Al not able to fill in small gaps and force re-welding to the bottom reaction zone

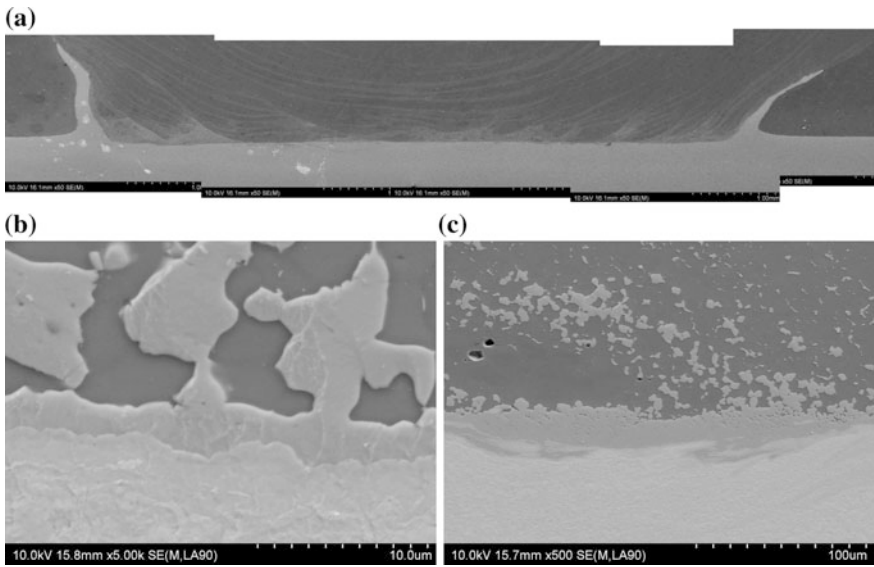


Fig. 6 SEM micrographs of a weld made by using scroll shoulder tool with $\omega = 1000$ rpm, $v = 56$ mm/min, and $dp \approx 0.05$ mm. **a** Interface cross section. **b** Typical interface showing outer layer grows towards the Al SZ. And **c** MSZ turn completely into intermetallic

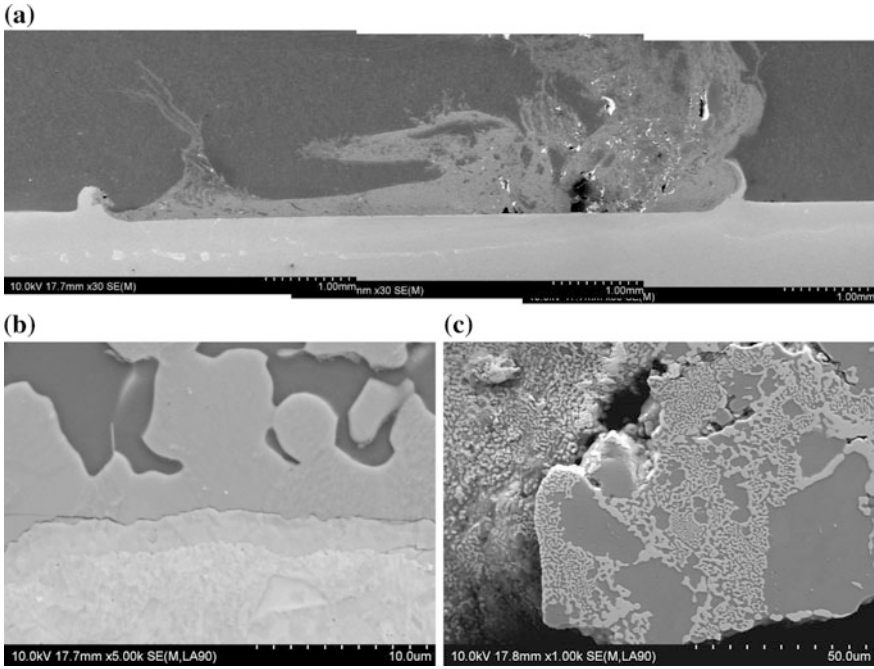


Fig. 7 SEM micrographs of a weld made by using scroll shoulder tool with $\omega = 1400$ rpm, $v = 56$ mm/min, and $dp \approx 0.1$ mm. **a** Interface cross section. **b** Cracked intermetallic layer. And **c** Eutectic microstructure signifies melting

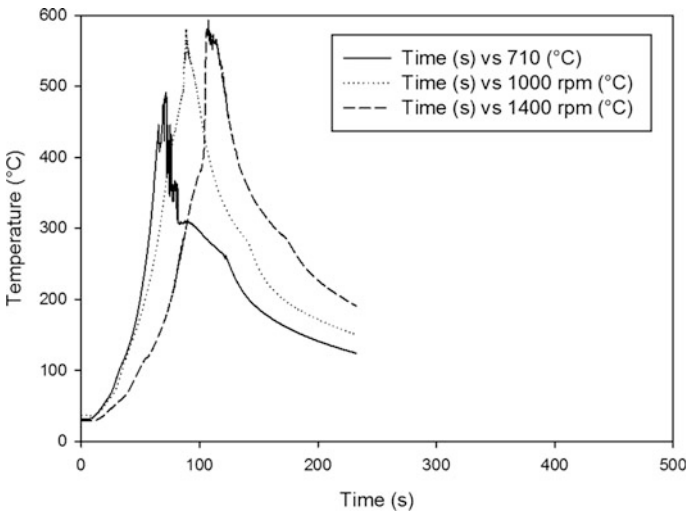


Fig. 8 Temperature history of FSLW

reached the peak right before the pin leaves the point. Temperature peaks for 710, 1000, and 1400 rpm were ~ 490 , 580, and 590 °C respectively (Fig. 8). Temperature record for 500 rpm welding was omitted due to difference in scan frequency. This rise in welding temperature with the increase in ω confirmed the work by Cui et al. [18] who analysed Upadhyay and Reynold's [19] study and formulated:

$$T = T_0 + T_f(1 - e^{-q\omega}) \quad (1)$$

Referring to the phenomenon of stir flow and re-welding, again from Cui et al. [18], with higher temperature the flow stress of the stirred material will have lower flow stress (σ). This relation can be seen in Eq. 2. Furthermore, flow stress of the stirred material will decrease and converge as the temperature increase towards the melting. Which means that as the temperature rises, the stir zone material will be easier to flow downward and to fill spaces. Furthermore, both peak temperature for 1000 and 1400 rpm welding were above Al-Cu eutectic point (480 °C). This means that there is a possibility that the down flow stream in back of the pin for this welding was in a slurry like or even melted condition. The presence of eutectic structure in the stir zone support this theory.

$$\sigma = \alpha^{-1} \sinh^{-1} \left\{ (A^{-1} \varepsilon \exp(Q/RT))^{1/n} \right\} \quad (2)$$

Conclusions

From the preliminary work, it was found that close to discontinuity free interface is achievable in FSLW with low d_p values. However, the excessive down flow could also cause the intermetallic to crack. Experiments using various ω values have revealed that with the increase in ω , Al become easier to flow downward towards the bottom plate. However, the temperature must be high enough to force re-welding. In this study, temperature above eutectic is proven to be effective. However, this condition promotes extensive intermetallic growth, especially Al_2Cu . This thick intermetallic layer could crack due to its brittle nature.

References

1. Braunovic M, Myshkin NK, Konchits VV (2006) Electrical contacts: fundamentals, applications and technology. CRC Press, Boca Raton
2. Robert J, Messler W (2004) Principles of welding: processes, physics, chemistry, and metallurgy. WILEY-VCH Verlag GmbH & Co. KGaA, Weinheim
3. Kah P, Jukka Martikainen MS (2013) Trends in joining dissimilar metals by welding. Appl Mech Mater 440:269–276

4. Chen C-Y, Chen H-L, Hwang W-S (2006) Influence of interfacial structure development on the fracture mechanism and bond strength of aluminum/copper bimetal plate. *Mater Trans* 47 (4):1232–1239
5. Gao Y, Nakata K, Nagatsuka K, Liu FC, Liao J (2015) Interface microstructural control by probe length adjustment in friction stir welding of titanium and steel lap joint. *Mater Des* 65:17–23
6. Chen ZW, Yazdanian S, Littlefair G (2013) Effects of tool positioning on joint interface microstructure and fracture strength of friction stir lap Al-to-steel welds. *J Mater Sci* 48 (6):2624–2634
7. Girard M, Huneau B, Genevois C, Sauvage X, Racineux G (2010) Friction stir diffusion bonding of dissimilar metals. *Sci Technol Weld Join* 15(8):661–665
8. Chen ZW, Yazdanian S (2015) Microstructures in interface region and mechanical behaviours of friction stir lap Al6060 to Ti–6Al–4V welds. *Mater Sci Eng A* 634:37–45
9. Mehta KP, Badheka VJ (2016) Materials and manufacturing processes a review on dissimilar friction stir welding of copper to aluminum: process, properties and variants. *Mater Manuf Process* 31(3):233–254
10. Akbari M, Bahemmat P, Haghpanahi M, Besharati Givi M.-K (2013) Enhancing metallurgical and mechanical properties of friction stir lap welding of Al–Cu using intermediate layer. *Sci Technol Weld Join* 18(6):518–524
11. Bisadi H, Tavakoli A, Tour Sangsaraki M, Tour Sangsaraki K (2012) The influences of rotational and welding speeds on microstructures and mechanical properties of friction stir welded Al5083 and commercially pure copper sheets lap joints. *Mater Des* 43:80–88
12. Firouzdar V, Kou S (2011) Al-to-Cu friction stir lap welding. *Metall Mater Trans A* 43 (1):303–315
13. Saeid T, Abdollah-zadeh A, Sazgari B (2010) Weldability and mechanical properties of dissimilar aluminum–copper lap joints made by friction stir welding. *J Alloys Compd* 490(1–2):652–655
14. Chen ZW, Pasang T, Qi Y (2008) Shear flow and formation of Nugget zone during friction stir welding of aluminium alloy 5083-O. *Mater Sci Eng A* 474(1–2):312–316
15. Xue P, Xiao BL, Ma ZY (2015) Effect of interfacial microstructure evolution on mechanical properties and fracture behavior of friction stir-welded Al-Cu joints. *Metall Mater Trans A* 46 (7):3091–3103
16. Waliach ER, Davies GJ (1977) Mechanical properties of aluminium-copper solid-phase welds. *Met Technol* 4:183–190
17. Moreno D, Garrett J, Embury JD (1999) Technique for rapid characterization of intermetallics and interfaces. *Intermetallics* 7(9):1001–1009
18. Cui S, Chen ZW, Robson JD (2010) A model relating tool torque and its associated power and specific energy to rotation and forward speeds during friction stir welding/processing. *Int J Mach Tools Manuf* 50(12):1023–1030
19. Upadhyay P, Reynolds AP (2010) Effects of thermal boundary conditions in friction stir welded AA7050-T7 sheets. *Mater Sci Eng A* 527(6):1537–1543

A Numerical Simulation for Dissimilar Aluminum Alloys Joined by Friction Stir Welding

Carter Hamilton, Mateusz Kopyściański, Aleksandra Węglowska,
Stanisław Dymek and Adam Pietras

Abstract Dissimilar aluminum alloy sheets of 2017A-T451 and 7075-T651 were friction stir welded. A numerical simulation was developed to visualize the material flow and temperature distribution and to correlate the microstructure with hardness behavior. Due to the flow of surface material into the workpiece thickness, the weld nugget is composed of alternating layers of 7075 and 2017A. These layers have unique temperature histories depending on the material's initial position; therefore, they also have distinctive precipitate distributions. Supersaturated surface material flows into the process zone and forms a core in which GP zones re-precipitate upon cooling. Mid-plane and bottom-plane material flow toward the workpiece surface and encompass the surface material core. Within this region, the weld temperatures overage the equilibrium θ phase in 2017A, decreasing the hardness, and at the same time dissolve the equilibrium η/T phase in the 7075, leading to re-precipitation of GP zones upon cooling and a hardness recovery.

Keywords Friction stir welding · Dissimilar metals · Material flow · Modeling

C. Hamilton (✉)

Department of Mechanical and Manufacturing Engineering,
Miami University College of Engineering and Computing, Oxford, OH, USA
e-mail: hamiltbc@miamioh.edu

M. Kopyściański · S. Dymek

Faculty of Metal Engineering and Industrial Computer Science,
AGH University of Science and Technology, Krakow, Poland
e-mail: mateusz.kopyscianski@gmail.com

S. Dymek

e-mail: gmdymek@cyfronet.pl

A. Węglowska · A. Pietras

Department of the Testing of Materials Weldability
and Welded Construction, Institute of Welding, Gliwice, Poland
e-mail: aleksandra.weglowska@is.gliwice.pl

A. Pietras

e-mail: adam.pietras@is.gliwice.ph

© The Minerals, Metals & Materials Society 2017

Y. Hovanski et al. (eds.), *Friction Stir Welding and Processing IX*,

The Minerals, Metals & Materials Series, DOI 10.1007/978-3-319-52383-5_18

Introduction

The aerospace, automotive and ship-building industries have a critical need to manufacture joints from dissimilar metals in order to produce lightweight and mechanically-sound structures. However, the chemical and mechanical incompatibilities of dissimilar metals can considerably degrade weld quality during traditional fusion welding. In contrast to traditional methods, friction stir welding offers the solution to this welding dilemma, especially for those welds manufactured from aluminum-based alloys joined to other aluminum-based alloys. Though friction stir welding has significantly matured as a manufacturing technology, research and developments efforts have primarily focused on the welding of the same metallic material [1, 2]. DebRoy and Bhadeshia [3] and Murr [4] provide comprehensive literature surveys regarding friction stir welding of dissimilar alloys. The primary difference between the friction stir welding of similar and dissimilar alloys is the discontinuity in properties which promote an asymmetry in heat generation and material flow during welding across the abutting surfaces. Producing high-quality, defect-free joints from dissimilar metals and numerically simulating this process, therefore, remains a major research opportunity to the manufacturing community. The goal of the current research, therefore, is to develop a numerical simulation for the friction stir welding of two dissimilar aluminum alloys, 2017A-T451 and 7075-T651, that correlates the predicted material flow patterns and temperatures to the observed microstructure and experimental hardness behavior.

Experimental Procedure

Friction Stir Welding

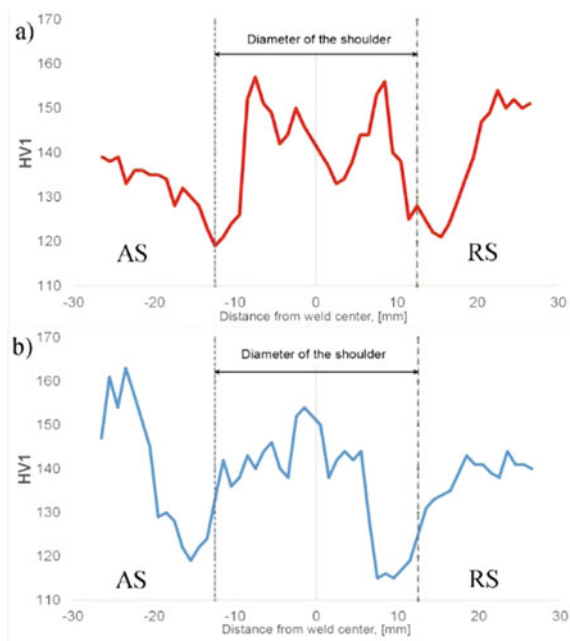
Friction stir welding of 2017A-T451 and 7075-T651 aluminum alloys was performed at the Instytut Spawalnictwa (Polish Welding Centre of Excellence) in Gliwice, Poland utilizing a typical milling machine specifically adapted for the welding trials. The workpieces were in the form of plates 250 mm long, 100 mm wide and 6 mm thick joined in two, distinct butt weld configurations—one with 2017A situated on the advancing side and 7075 on the retreating side and the other with the alloy positions reversed. The FSW tool was made of HS6-5-2 high speed steel with a 24 mm diameter, scrolled shoulder having a 2.5 mm pitch. The pin diameter tapered linearly from 6 mm at the shoulder to 4.5 mm at the tip with an overall height of 5.7 mm. The pin was also threaded with a 3 mm pitch. The tool tilt angle during processing was held constant at 1.5° . The rotational speed, ω , and tool velocity, u_w , were 355 rev min^{-1} and 112 mm min^{-1} , respectively, and the applied force during processing was set to 32.8 kN. Temperatures during welding were experimentally recorded by placing thermocouples on the advancing and retreating sides at 14 and 17 mm from the weld centerline. The temperature profile across the

weld zone was also recorded using a Vigocam v50 Thermal Imaging Camera ($\pm 2\%$ accuracy). St. Węglowski et al. present more details associated with the capabilities of the FSW equipment, such as force and torque measurement in [5].

Microscopy and Hardness

The welds were examined by light microscopy utilizing polarized light, by scanning electron microscopy using back scattered electrons and by chemical analysis utilizing energy dispersive spectroscopy (EDS). The examinations were carried out on sections perpendicular to the welding direction on a Zeiss Axio Imager M1m light microscope and on a high resolution FEI Nova NanoSEM scanning electron microscope equipped with a field emission gun and an EDAX system for chemical analysis. The microstructural studies were supplemented by hardness measurements (Vickers) performed on the same sections as the metallographic examinations. The measurements were made on a Wolpert-Wilson Tukon 2500 apparatus. The Vickers results were used to construct a hardness profile along the line of the mid-thickness plane on the weld cross-section. The applied load was 1 kg, and the distance between test points was 1.0 mm. The hardness profiles of the welds are shown in Fig. 1. The shape of the profiles was similar for both configurations, resembling the W-contour that is typical for all heat treatable aluminum alloys [2]. It should be noted that the hardness profiles were constructed about one month after welding, i.e. after natural aging.

Fig. 1 Hardness profiles along mid-plane for: **a** 7075 on advancing side and 2017A on retreating side, **b** 2017A on the advancing side and 7075 on the retreating side



Model Development

Following the methodology of Hamilton et al. [6], a thermal/flow model was developed with Comsol multi-physics software to simulate the joining of aluminum alloys 2017A and 7075 by friction stir welding. In this simulation, the flow region is sub-divided into two additional regions that represent the unique materials on the retreating and advancing sides. Each flow region, therefore, is characterized by distinct thermal properties, slip factors and viscosities according to which alloy is placed on the advancing or retreating sides. The temperature dependent thermal conductivities, k , and the specific heat capacities, c_p , of the two aluminum work-pieces are taken from [7] for 2017A and from [8] for 7075. The detailed calculation of the viscosity for each aluminum alloy and of the strain rate is presented in [9]. The values of Q , A , α and n used in the viscosity calculations are shown in Table 1 (taken from [10] for 2017A and from [11] for 7075). For the process parameters utilized in this investigation, the maximum effective strain rate is 43.0 s^{-1} .

Originally, Hamilton et al. [6, 12] defined the slip factor based upon the energy per unit length of weld. The authors, however, limited the validity of this factor to energies less than 2000 J/mm . For this investigation, the weld energy was approximately 3000 J/mm , which is outside the range prescribed in [12]. Therefore, the slip factor was redefined based on the welding temperature, T , relative to the solidus temperature, T_s , of each aluminum alloy:

$$\delta = \exp\left(\beta \frac{T}{T_s}\right) \quad (1)$$

where β is a scaling factor. To determine the value of β , the temperature based slip factor was introduced into a prior, calibrated simulation of friction stir welded aluminum 7136-T76 presented in [13]. From this data, the appropriate value for β was found to be $4/7$ and was consistently used in the simulation of all configurations. To verify the redefined slip factor and the subsequent temperature predictions of the simulation, weld temperatures were experimentally recorded by thermocouple placement and thermal imaging camera. Figure 2 plots the thermocouple data (at 14 mm and 17 mm from the centerline on both sides of the weld) and the simulation temperatures for the configuration with 2017A on the advancing side and 7075 on the retreating side. As seen in the figure, the simulation does slightly over-predict the peak temperatures at these thermocouple locations; however, the

Table 1 Material constants for the Sheppard/Wright flow stress equation and Zener-Hollomon parameter [10, 11]

Material constant	Value		Units
	2017	7075	
Q	159898	129000	J mol^{-1}
A	3.30×10^{11}	1.03×10^9	s^{-1}
α	0.0160	0.0141	MPa^{-1}
n	5.33	5.41	n/a

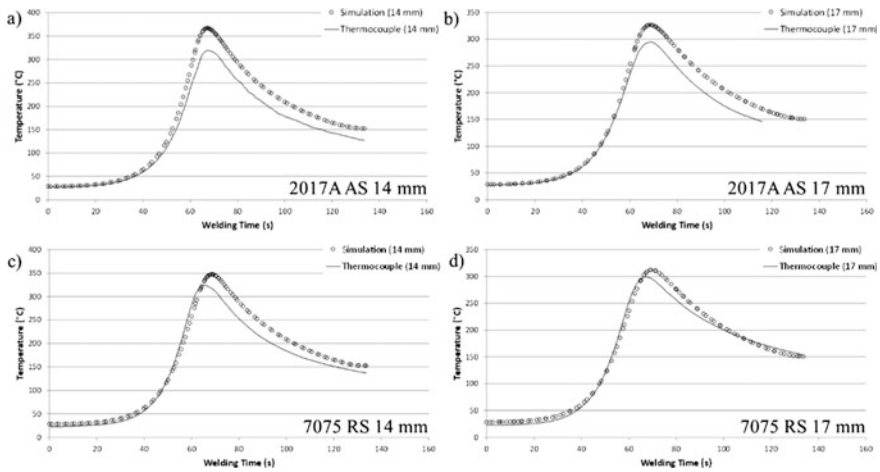


Fig. 2 Thermocouple data and simulation temperatures for: **a** 2017A advancing side at 14 mm, **b** 2017A advancing side at 17 mm, **c** 7075 retreating side at 14 mm, **d** 7075 retreating side at 17 mm

simulation is in good agreement with the experimental time-temperature profiles, particularly on the retreating side of the weld. For this configuration, the thermal camera also recorded the temperature within the weld zone at 3 mm behind the tool as 622 K (349 °C) compared with 636 K (363 °C) predicted by the simulation at this same location. Similar agreement between the thermocouple data and the simulation temperatures are achieved for the configuration with 7075 on the advancing side and 2017A on the retreating side. For this configuration, the thermal camera recorded the weld zone temperature as 630 K (357 °C) compared with 637 K (364 °C) predicted by the simulation.

Discussion

Material Flow Behavior

Optical micrographs of the two weld configurations are shown in Fig. 3. For each of the alloy configurations the microstructure is composed of interleaving bands of material from each alloy, thus revealing their flow patterns around the tool during welding. Material from the advancing side predominantly occupies the central part of the nugget with a smaller portion of material from the retreating side also appearing. EDS mapping for the distributions of the primary alloying elements, i.e. Zn, Mg and Cu, shows that copper dominates the optically “darker” bands, while zinc and magnesium enrich the optically “brighter” bands. Therefore, the dark bands in the images correspond to 2017A, and the bright bands correspond to the

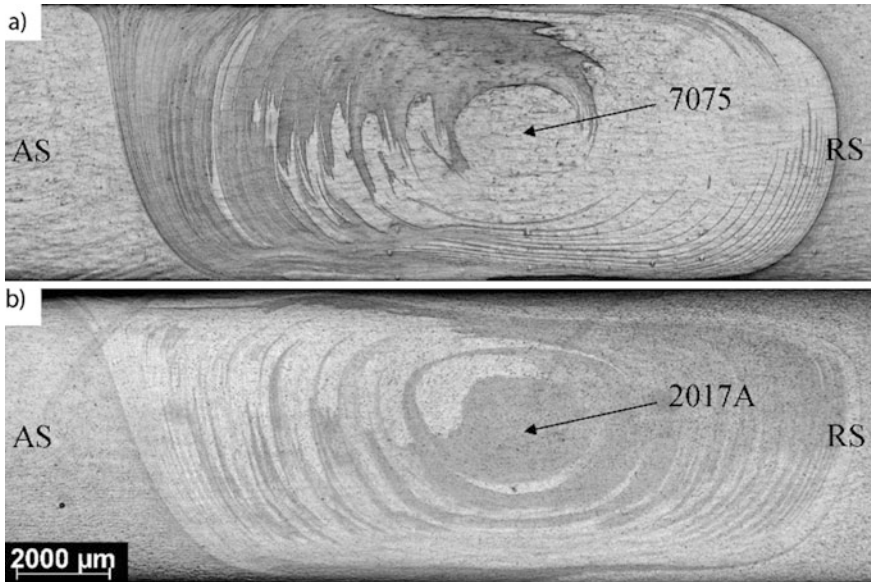


Fig. 3 Weld microstructures for: **a** 7075 on the advancing side and 2017A on the retreating side **b** 2017A on the advancing side and 7075 on the retreating side

7075 alloy. The bands exhibit different grain sizes and different densities of the second phase particles—2017A displays a larger grain size than 7075, and 7075 displays a higher density of intermetallic particles than 2017A. The distribution of misorientation angles between grains strictly corresponds to a MacKenzie plot, indicating that grains are randomly oriented and recrystallized in the stir zone irrespective of the alloy type.

Figure 4a from the simulation presents the material flow behavior of surface “tracers” from the advancing and retreating sides during friction stir welding for each welding configuration. The tracers are released from a position ahead of the tool on either side of the weld centerline at several time intervals. The black tracers represent aluminum 7075 and the gray tracers represent aluminum 2017A. For both weld configurations, materials tracers from either side of the weld are initially swept toward the retreating side with the scroll of the tool shoulder directing their flow toward the tool center. Ultimately, under the influence of the tool pin, the surface tracers flow down into the material thickness adjacent to the pin. As observed in the figure, advancing and retreating side surface material is “pulled” into the workpiece with some advancing side material even flowing the entire pin length into the thickness. The majority of surface material that is introduced into the workpiece, however, rotates around the pin and remains within a zone that extends to ~ 5 mm on either side of the centerline.

Figure 4b shows the flow behavior of tracers initially located at the mid-plane thickness ($z = 3$ mm). With 7075 on the advancing side and 2017A on the

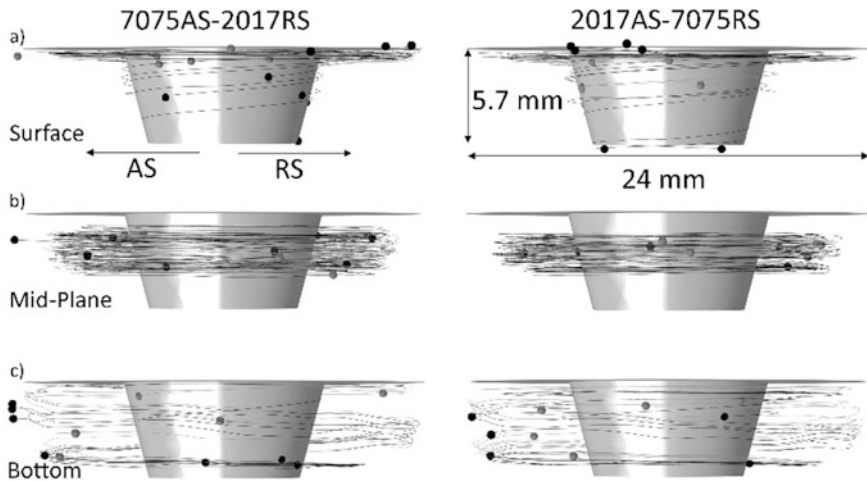


Fig. 4 Material flow patterns during FSW (2017A—gray tracer and 7075—black tracer): **a** surface, **b** mid-plane, **c** bottom plane

retreating side, the tracers follow the tool rotation, but flow up toward the workpiece surface as they rotate. This flow region begins at approximately 6 mm from the centerline and extends out to 11 mm, essentially surrounding the surface material zone described above. Given the downward flow of surface material into the workpiece thickness, a complementary upward flow of material surrounding it is not surprising. Reynolds [14] also noted a downward motion of surface material on the advancing side coupled with the vertical rise of material from the bottom surface of the retreating side within the pin diameter. Such flow behavior gives rise to the alternating layers of 7075 and 2017A within the process zone as seen in the micrograph of Fig. 3. The same flow behavior is noted when 2017A is placed on the advancing side and 7075 is placed on the retreating side; however, the flow region is slightly larger, beginning at 5 mm from the centerline and extending out to 11 mm.

Materials tracers initially located at the bottom plane of the workpiece thickness ($z = 5$ mm) also reveal a strong upward flow to the workpiece surface where material is “recaptured” by the tool shoulder and then pulled back into the workpiece thickness by the pin. Figure 4c demonstrates this flow behavior for each configuration of the 7075 and 2017A friction stir welding. The material flow will significantly impact the final microstructure of the weld nugget and, therefore, its hardness profile. The nugget is ultimately composed of regions of 7075 and 2017A with unique temperature histories depending on the material’s initial location within the joint cross-section. Depending on the magnitude of these temperatures in relation to the precipitate transformation temperatures of 7075 and 2017A, distinctive precipitate distributions develop across the weld nugget, influencing the hardness profile and mechanical properties.

Temperature Distribution and Influence on Hardness

Figure 5a again presents the material flow behavior of surface material tracers for each welding configuration (2017A—gray tracer and 7075—black tracer), but now with color shading added to indicate the temperature history. For both configurations, surface tracers under the shoulder can reach temperatures in excess of 713 K (440 °C), temperatures near the solution heat treat temperatures of either alloy (2017A is solution heat treated at approximately 773 K (500 °C) and 7075 is solution heat treated at approximately 753 K (480 °C) [15, 16]). Surface material, therefore, becomes supersaturated before it is introduced into the material thickness by the action of the shoulder and tool. Due to the material flow, this region of supersaturated 2017A and 7075 in the nugget extends ~ 5 mm to either side of the weld centerline. Upon cooling after welding, re-precipitation of fine GP zones occurs in both alloys. The precipitation response is stronger in 2017A, than 7075, due to the natural aging behavior of 2017A. As the GP zones form, there is a corresponding increase in hardness for this region, as seen in Fig. 1a, b. Within this zone, a local maximum of just over 150 HV is realized, but there are also sharp, local hardness peaks throughout. This behavior may be associated with the unique hardness character of the individual 2017A and 7075 layers as similarly noted by Khodir and Shibayanagi [17] in the welding of 2024 and 7075.

As previously discussed, material initially at the mid-plane level envelops the surface material core during friction stir welding, extending on either side of the weld from approximately 5 mm from the centerline to 11 mm. Figure 5b presents the temperature history associated with this region, indicating that temperatures range from ~ 643 K (~ 370 °C) to ~ 703 K (~ 430 °C). DSC curves reveal that the

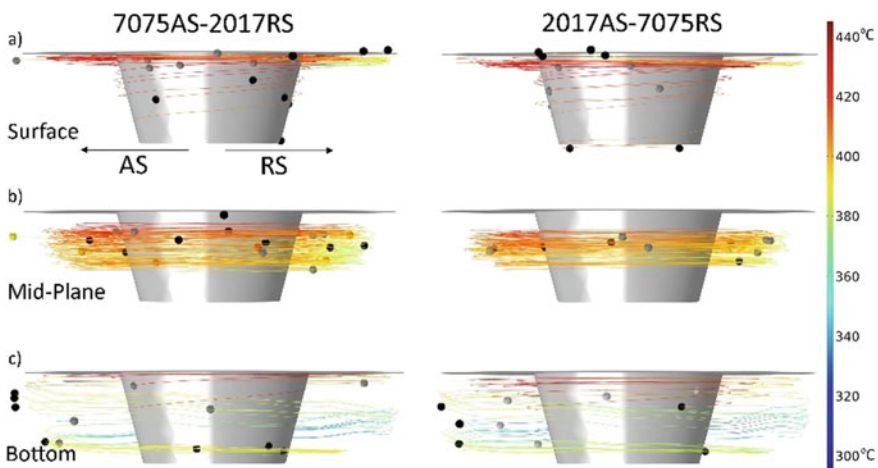


Fig. 5 Flow and temperature behavior of material tracers during FSW (2017A—gray tracer and 7075—black tracer): **a** surface, **b** mid-plane, **c** bottom plane

equilibrium θ phase in 2017A begins dissolving at ~ 573 K (~ 300 °C) and reaches complete dissolution at ~ 773 K (~ 500 °C). In 7075, the equilibrium η/T phase begins dissolving at ~ 523 K (~ 250 °C) and reaches complete dissolution at ~ 753 K (~ 480 °C). This region, therefore, is primarily composed of 7075 that is supersaturated and 2017A that contains overaged θ precipitates. Upon cooling, GP zones form in the 7075, resulting in a hardness recovery similar to that of the weld core, while in 2017A the equilibrium phase is retained, giving a much lower hardness than the core. This is consistent with the hardness profiles presented in Fig. 1a, b. The core hardness (~ 140 HV) is essentially retained from the weld centerline to a distance equivalent to the tool radius (12 mm) on the 7075 side of the weld, whereas on the 2017A side of the weld, the core hardness drops at approximately 8 mm from the centerline, reaching a minimum (~ 115 HV) at a distance equal to or just less than the tool radius, i.e. 12 mm.

Material located toward the bottom of the workpiece thickness contributes to both of the weld regions described above. Figure 5c presents the thermal history for material tracers initially located at the bottom plane of the workpiece. As the tracers flow upward, the material temperature increases. Some bottom plane material remains within the workpiece thickness, flowing with the mid-plane material and reaching equivalent temperatures. Some bottom plane material reaches the surface where it is heated to temperatures in excess of 713 K (440 °C) before being reintroduced into the workpiece thickness, but remaining within the weld core formed by the surface material.

Outside the weld zone, in the heat affected zone, between 12 and 20 mm from the weld centerline on either side of the weld, the process temperatures (from the simulation) are between ~ 563 K (~ 290 °C) and ~ 683 K (~ 410 °C). In this area, the equilibrium phase in 7075 is significantly overaged. The equilibrium phase of 2017A is also overaged, but not to the same extent as it is in the weld zone and not to the same degree as the overaging in 7075. Hence, on the 7075 side of the weld, the minimum hardness (~ 120 HV) occurs at approximately 15 mm from the centerline, just outside of the weld zone, while on the 2017A side of the weld the hardness is already increasing toward the baseline value (~ 140 HV) at this same distance from the weld centerline.

Conclusions

A numerical simulation of friction stir welding was developed to analyze the joining of dissimilar aluminum alloys 2017A-T451 and 7075-T651 and to correlate the temperature distribution and material flow with the microstructure and hardness behavior. Surface material from both alloy workpieces, primarily from the advancing side, is pulled into the material thickness during welding, forming a core (~ 5 mm radius) around the pin diameter. Material temperatures within the core exceed 713 K (440 °C), such that supersaturation occurs in both alloys during welding, and fine GP zones re-precipitate upon cooling. Surrounding this core

(beginning at ~6 mm from the weld centerline and extending to ~11 mm) is mid-plane and bottom-plane material that flows upward during welding, giving rise to the alternating layers of 2017A and 7075 within the weld microstructure. Temperatures in this region generally promote dissolution of the equilibrium η/T phase in the 7075, but overaging of the θ phase in 2017A. As such, the hardness decreases from the core on the 2017A side of the weld, but remains effectively constant on the 7075 side of the weld where re-precipitation of GP zones occur. The upward flow of material in the process zone is sufficient that some bottom-plane material flows to surface where it is “recaptured” by the tool shoulder ultimately flowing back into the workpiece thickness.

Acknowledgements This work was supported by Polish National Science Center, grant No. 2013/11/B/ST8/04409.

References

1. Uday MB, Ahmad Fauzi MN, Zuhailawati H, Ismail AB (2010) Advances in friction welding process: a review. *Sci Technol Weld Join* 15:534–558
2. Threadgill PL, Leonard AJ, Shercliff HR, Withers PJ (2009) Friction stir welding of aluminium alloys. *Int Mater Rev* 54:49–93
3. DebRoy T, Bhadeshia HKDH (2010) Friction stir welding of dissimilar alloys—a perspective. *Sci Technol Weld Join* 15:266–270
4. Murr LE (2010) A review of FSW research on dissimilar metal and alloy systems. *J Mater Eng Perform* 19:1071–1089
5. St. Węglowski M, Pietras A, Dymek S, Hamilton C (2012) Characterization of friction modified processing—a novel tool for enhancing surface properties in cast aluminium alloys. *Key Eng Mater* 504–506:1231–1236
6. Hamilton C, Kopyściański M, Senkov O, Dymek S (2013) A coupled thermal/material flow model of friction stir welding applied to Sc-modified aluminum alloys. *Metall Mater Trans A* 44:1730–1740
7. Serajzadeh S, Ranjbar Motlagh S, Mirbagher SMH, Akhgar JM (2015) Deformation behavior of AA2017-SiCp in warm and hot deformation regions. *Mater Des* 67:318–323
8. Colegrove PA, Shercliff HR (2003) Experimental and numerical analysis of aluminum alloy 7075-T7351 friction stir welds. *Sci Technol Weld Join* 8:360–368
9. Hamilton C, St. Węglowski M, Dymek S (2015) A simulation of friction-stir processing for temperature and material flow. *Metall Mater Trans B* 46:1409–1418
10. Bailey JA, Haas SL, Shah MK (1972) Effect of strain-rate and temperature on the resistance to torsional deformation of several aluminum alloys. *Int J Mech Sci* 14:735–754
11. Colegrove PA, Shercliff HR, Zettler R (2007) Model for predicting heat generation and temperature in friction stir welding from material properties. *Sci Technol Weld Join* 12:284–297
12. Hamilton C, Sommers A, Dymek S (2009) A thermal model of friction stir welding applied to Sc-modified Al-Zn-Mg-Cu alloy extrusions. *Int J Mach Tool Manuf* 49:230–238
13. Kalembe I, Hamilton C, Dymek S (2014) Natural aging in friction stir welded 7136-T76 aluminum alloy. *Mater Des* 60:295–301
14. Reynolds AP (2000) Visualization of material flow in autogenous friction stir welds. *Sci Technol Weld Join* 5:120–124

15. Hartel M, Wagner S, Frint P, Wagner M (2014) Effects of particle reinforcement and ECAP on the precipitation kinetics of an Al-Cu alloy. *IOP Conf Ser Mater Sci Eng* 63:1–10
16. Lloyd DJ, Chaturvedi MC (1982) A calorimetric study of aluminum alloy AA-7075. *J Mater Sci* 17:1819–1824
17. Khodir SA, Shibayanagi T (2007) Microstructure and mechanical properties of friction stir welded AA2024-T3 Aluminum Alloy. *Mater Trans* 48:1928–1937

Realization of Ultrasound Enhanced Friction Stir Welded Al/Mg- and Al/Steel-Joints: Process and Robustness, Mechanical and Corrosion Properties

Marco Thomä, Guntram Wagner, Benjamin Straß, Christian Conrad, Bernd Wolter, Sigrid Benfer and Wolfram Fürbeth

Abstract As an innovative hybrid joining process ultrasound enhanced friction stir welding (USE-FSW) was successfully applied on Al/Mg-joints and offers a beneficial impact on the resulting microstructure and mechanical properties. Whereas in conventional FSW of Al to Mg continuous band-shaped intermetallic layers of Al_3Mg_2 and $\text{Mg}_{17}\text{Al}_{12}$ are always present, the formation of these layers can be influenced positively by the ultrasound energy that is transferred into the stirred zone in USE-FSW. In this case, the intermetallic phases are spread over the complete nugget zone. Consequently, the tensile strength increases about 25% and the fatigue strength rises by up to 3.5 times. Based on this USE-FSW was investigated with regard to possible advantages for Al/steel-hybrid-joints. Preliminary investigations have shown significant differences in the microstructure of

M. Thomä (✉) · G. Wagner
Chemnitz University of Technology, Chemnitz, Germany
e-mail: marco.thomae@mb.tu-chemnitz.de

G. Wagner
e-mail: guntram.wagner@mb.tu-chemnitz.de

B. Straß · C. Conrad · B. Wolter
Fraunhofer Institute for Nondestructive Testing IZFP Saarbrücken,
Saarbrücken, Germany
e-mail: benjamin.strass@izfp.fraunhofer.de

C. Conrad
e-mail: Christian.conrad@izfp.fraunhofer.de

B. Wolter
e-mail: bernd.wolter@izfp.fraunhofer.de

S. Benfer · W. Fürbeth
DECHEMA-Forschungsinstitut, Frankfurt, Germany
e-mail: benfer@dechema.de

W. Fürbeth
e-mail: fuerbeth@dechema.de

ultrasound enhanced and non-ultrasound enhanced EN AW-6061/DC04-joints. While conventional FSW led to hooks and larger particles of steel in the aluminum, USE-FSW-joints show remarkably smaller and more homogenous distributed steel particles in the nugget. Beside mechanical investigations, non-destructive examinations and corrosion tests were carried out.

Keywords Friction stir welding • Ultrasound enhancement • Dissimilar metals • Nondestructive testing • Corrosion

Motivation

In times of high-performance materials like carbon- or glass-fiber reinforced polymers also well-known metals as aluminum, steel and magnesium are still in the focus of scientific research. The interest lies amongst other things in the combination of these materials, because hybrid-joints of dissimilar metals offer a wide range of applications for different industrial sectors. Beside conventional joining methods like fusion welding or brazing the process of friction stir welding established itself as a very promising alternative. The relative low process temperature results in a decreased amount of brittle intermetallic phases compared to fusion welded joints of dissimilar metals [1]. This altered microstructure could be detected for the combination of Al/Mg-hybrid-joints [2, 3]. But even the noticeably reduced temperature of the FSW-process cannot avoid the formation of intermetallics completely. Therefore the USE-FSW was developed and successfully applied on joints of aluminum and magnesium alloys [2]. While conventional Al/Mg-FSW-joints showed two continuous intermetallic layers, the USE-FSW-joints revealed only one continuous layer. This advantageous influence on the stirred zone during USE-FSW has also been subject of investigations on the joining of aluminum and steel. The significantly different melting points cause some additional challenges compared to Al/Mg [4]. First investigations also showed a remarkably difference in the microstructure of the Al/steel-joints between ultrasound enhanced and non-enhanced welds. The following paper will describe the influence of ultrasound enhancement for Al/Mg-FSW-joints on the resulting microstructure as well as on the mechanical and corrosion properties and will furthermore display comparative investigations on Al/steel-joints.

Experimental Procedure

Straß et al. used AZ80 (MgAl₁₈Zn) and EN AC-48000 (AlSi₁₂CuNiMg) in the die-casted condition for their investigations. In comparison to that DC04 (1.0338) and the wrought alloy EN AW-6061 (AlMg₁SiCu) were used for the latest welding tests. A plate geometry with dimensions of 280 mm length, 100 mm width and

3.3 mm (Al/Mg) respectively 3 mm (Al/steel) thickness was chosen and welded in a butt-weld configuration. Therefore a universal machining center DMU80T from Deckel Maho was modified to fix the sheet metals with a pneumatic clamping and run the welding tests force-controlled (Fig. 1a) [2].

A tool made of hot-work steel 1.2344 (X40CrMoV51) with a shoulder diameter of 16 mm, a probe length of 3.1 mm for Al/Mg respectively 2.8 mm for Al/steel and a metric thread M4.5 was used for the FSW (Fig. 1b) with a side tilt angle of 2° [2]. Additionally to this set up an ultrasonic seam module from Schunk Sonosystems got integrated in the FSW-system. The USE-FSW set up is depicted in Fig. 2 [2].

The seam module works with a resonant frequency of 20 kHz, a generator power maximum of 3000 W and an amplitude of up to 35 μm . It runs synchronously and parallel to the FSW-tool controlled by LabVIEW. For Al/Mg-USE-FSW-joints an optimized work distance of 95 mm between sonotrode and faying surface was calculated. The transfer of the ultrasound energy takes place in the aluminum sheet located on the advancing side [2]. First Al/steel-USE-FSW-joints were produced by transferring the ultrasound on the advancing side as well; this time located in DC04 and using the same work distance. Furthermore, a 2.55 mm lateral offset of the FSW-tool axis into EN AW-6061 was used.

For the investigation of the corrosion properties electrochemical measurements were carried out in the way described by Benfer et al. [5]. To enable measurements on different areas of the joints a three electrode setup within a mini cell (measurement area 0.071 cm^2) was used. The investigated joint-samples were used as working electrodes, a platinum electrode as counter electrode and a standard calomel electrode [+246 mV versus normal hydrogen electrode (NHE)] as reference electrode. The recorded values were converted against the NHE. A Zahner IM 6 measurement unit was used for the open circuit potential (OCP) measurements and the potentiodynamic polarization measurements. The OCP was recorded for 60 min prior to the potentiodynamic experiment. The resulting curves were started at -0.1 V relative to the OCP (E_{OC}) and recorded up to $+0.5$ V relative to E_{OC} with a scan rate of 1 mV/s. All electrochemical measurements have been done in 0.5 molar NaCl solution [5].

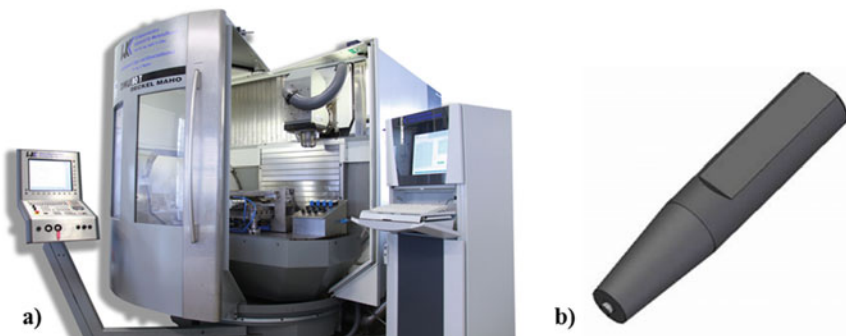


Fig. 1 a Machining center DMU80T, b 3D-model of a FSW-tool [2]

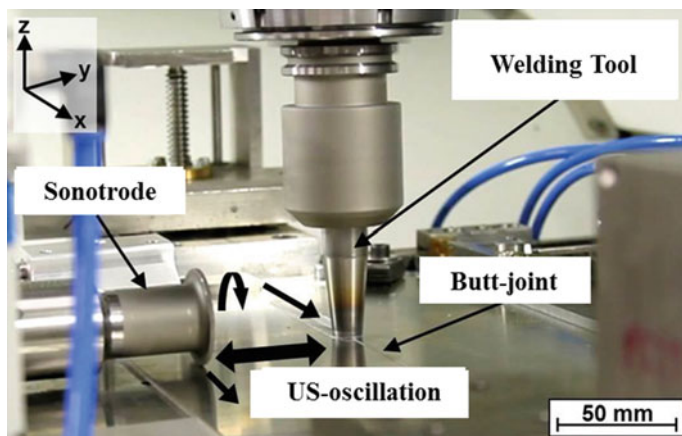


Fig. 2 USE-FSW set up [2]

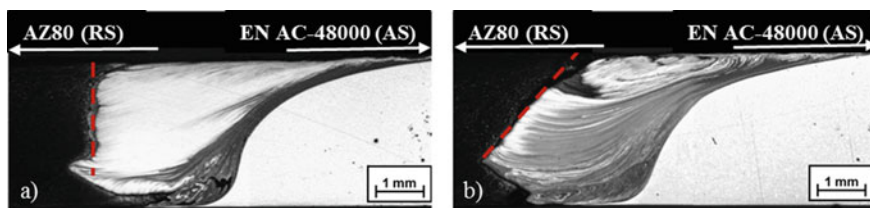


Fig. 3 Cross-section images of a Al/Mg-FSW and b Al/Mg-USE-FSW [2]

Results and Discussion

To investigate the influence of ultrasound during Friction Stir Welding light-microscopic cross-section images were investigated by Straß et al. as a first step to compare EN AC-48000/AZ80-FSW-joints and EN AC-48000/AZ80-USE-FSW-joints (Fig. 3) [2].

The difference of the USE-FSW-process is obvious regarding the microstructure of the joints and the shape of the stirred zone as well. Figure 3a shows the conventional FSW-nugget with its nearly perpendicular interface between stirred zone and AZ80, whereas Fig. 3b depicts a significantly flatter interface Mg/nugget [2]. Furthermore, the ultrasound enhancement strongly intensifies the stirring of the joining-partners in the nugget. This fact was already observed by other researchers [6]. Scanning electron microscopy (SEM) formed a next step in microstructural investigations by using the higher resolution for more detailed knowledge about the stirred zone. Two intermetallic phases (IM-phases) could be detected at the interface nugget/AZ80 with the shape of continuous layers. Even Klag et al. reported this in their studies about similar Al/Mg-FSW-joints [3]. EDX-spot-measurements

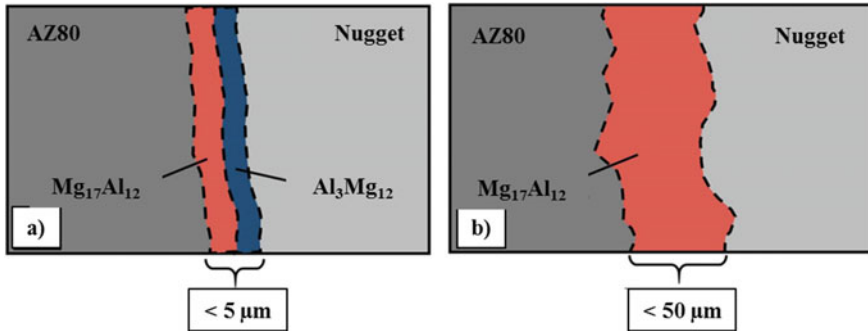


Fig. 4 Scheme of the interface Mg/nugget for a FSW and b USE-FSW [2]

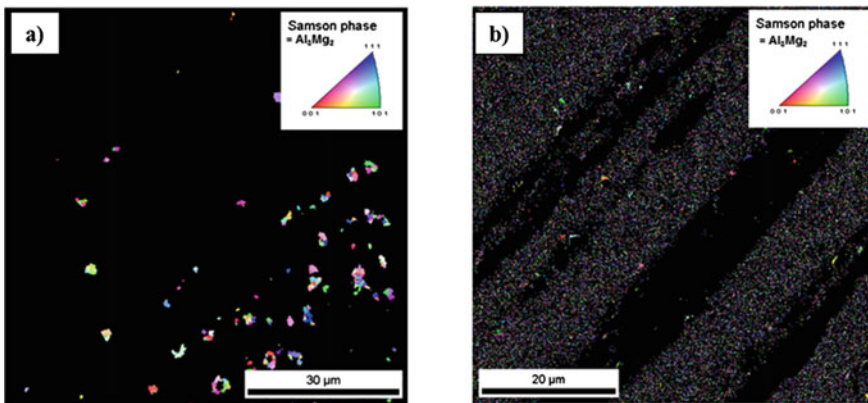


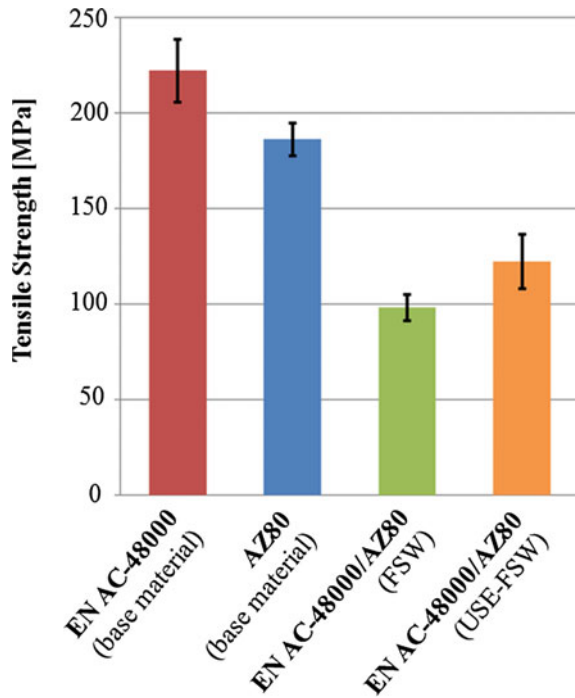
Fig. 5 EBSD-analysis of Al_3Mg_2 in the nugget-area: a FSW and b USE-FSW [2]

identified the layers as the brittle intermetallics $Mg_{17}Al_{12}$ and Al_3Mg_2 . IM-phases like them weaken the FSW-joints concerning their mechanical properties. By running USE-FSW for the EN AC-48000/AZ80-joints only one intermetallic phase occurs continuously (Fig. 4).

Due to this effect it can be assumed that the ultrasound cracks the aluminum rich Al_3Mg_2 after its formation and then disperses it over the nugget [2]. EBSD-mappings of the stirred zone help to achieve a better understanding of this behavior (Fig. 5).

The varying distribution of the Al_3Mg_2 -phase for the non-ultrasound-enhanced (Fig. 5a) and the ultrasound-enhanced condition (Fig. 5b) is visible in this EBSD pictures. The significant larger intermetallic phase particles are randomly arranged for FSW. In comparison to that, USE-FSW led to much smaller intermetallics of Al_3Mg_2 , which are dispersed more homogenous over the whole nugget. The research of Park [6] agrees with this result.

Fig. 6 Achieved tensile strengths of EN AC-48000, AZ80, FSW-joints and USE-FSW-joints [2]



A next step in the studies of the effect of ultrasound enhancement of FSW for Al/Mg-joints were monotonic and cyclic investigations. In Fig. 6 the different values of the tensile strengths are depicted for aluminum alloy, magnesium alloy and FSW- and USE-FSW-joints.

The Al/Mg-FSW-joints achieve an average tensile strength of 98 MPa. This value corresponds to half the strength of the weaker joining partner AZ80. EN AC-48000/AZ80-joints with ultrasound enhancement reach higher values of about 122 MPa, which corresponds to an increase of 25%. The reason for this behavior lies in the modified distribution of the brittle intermetallic phases of Al_3Mg_2 . The fine dispersed morphology has a less negative impact on the specimen than the continuous layer, who acts as a large impurity.

Another focus in the characterization of the welded aluminum and magnesium materials was on fatigue tests. Therefore, S/N-curves were created (Fig. 7), which show clearly higher lifetimes at the same stress level for Al/Mg-USE-FSW-joints.

This behavior can also be explained by the lower proportion of the continuous layer shaped aluminum-rich IM-phase at the interface Mg/nugget, which acts as a preferred location of fatigue failure due to its brittle character. In this case the lifetime of USE-FSW-joints can be enhanced by the factor 3.5 [2].

In addition to the destructive tests, nondestructive examinations (NDT) using EMAT (Electromagnetic Acoustic Transducer) technology and X-ray radiography

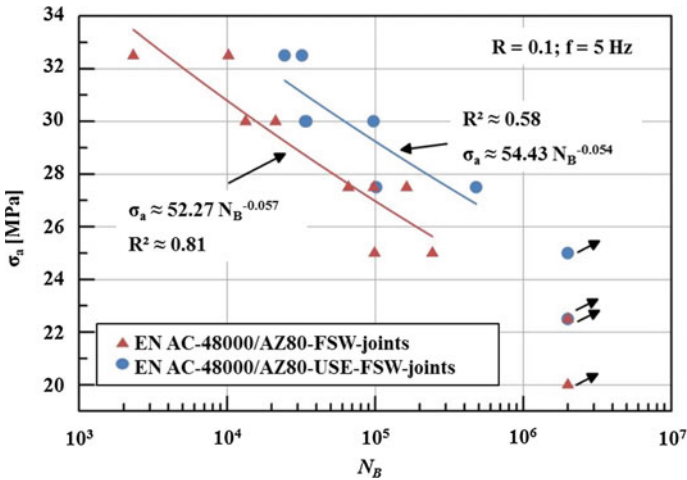


Fig. 7 S/N-curves for EN AC-48000/AZ80-FSW-joints and EN AC-48000/AZ80-USE-FSW-joints [2]

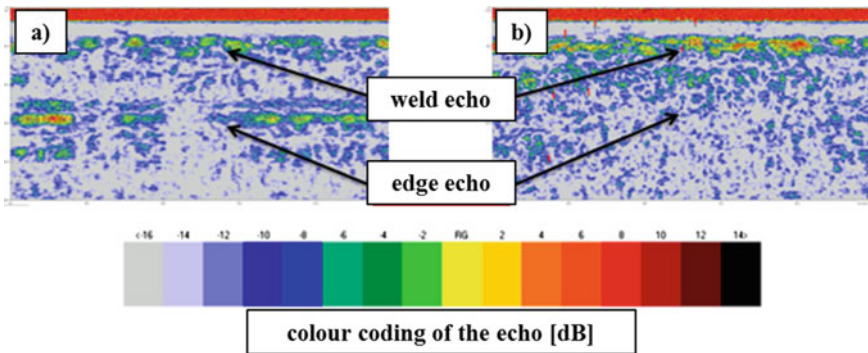


Fig. 8 EMAT measurements at a flawless FSW-weld (a) and at a flawed weld (b) [2]

were carried out to prove their capability of detecting irregularities in the welds. Figure 8 depicts the results of the EMAT measurements.

Whereas sound joints (Fig. 8a) exhibit echo signals of the welding area and the edge of the metal sheet at low intensities, the intensity of the EMAT signal increases at the locations where irregularities are present (Fig. 8b).

Investigations by X-ray radiography reveal significant differences between FSW- and USE-FSW-joints (Fig. 9).

The high quality of the welds is visible for both conditions. In each case, only one irregularity occurs in the stirred zone, which can be attributed to the mold for the die-casting process of the base material sheets. In the aluminum several pores are present due to the manufacturing process of these sheets. For USE-FSW the

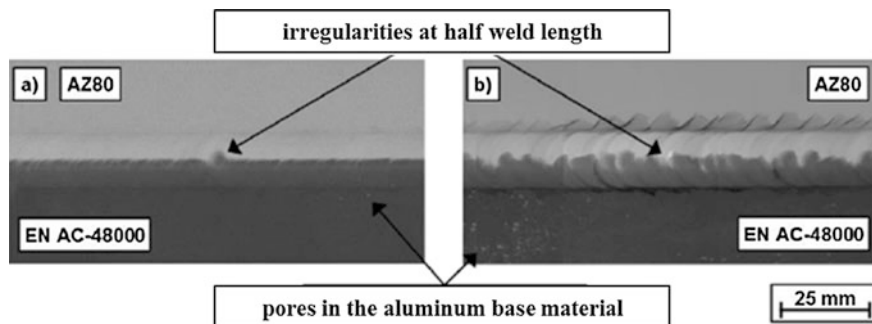


Fig. 9 Comparative X-ray radiography of an EN AC-48000/AZ80-FSW-joint (a) and an EN AC-48000/AZ80-USE-FSW-joint (b) [2]

intensified stirring of the nugget, which was already described before, is clearly apparent.

To provide a comprehensive characterization for joints of dissimilar metals corrosion investigations need to be carried out as well. Benfer et al. studied the corrosion behavior of Al/Mg-joints with and without ultrasound enhancement for EN AC-48000 and AZ80 [5]. Therefore, they investigated the integral corrosion properties with the electrochemical mini cell for the two welding conditions (Fig. 10).

For the conventional FSW-joints (Fig. 10a) the OCP of the stirred zone lies between the two base materials aluminum and magnesium showing a continuous increase during the time of measurement. This is characteristic for the formation of a passive layer and is in contrast to the trend for both base materials. They reach their constant values of about -0.44 V (EN AC-48000) and -1.3 V (AZ80) after 10 min. The potential difference of 0.9 V prove the significant more ignoble corrosion behavior for the magnesium alloy. Regarding the transition area between nugget and aluminum a similar, but slightly more positive (-0.64 V) trend for the OCP- curve is visible compared to that for the nugget. The OCP for the transition of nugget/AZ80 achieves a constant value after several min of about -1.17 V and is close to that of the magnesium alloy. Comparing investigations for USE-FSW-joints were also carried out and depicted in the diagram Fig. 10b [5]. The values of the base materials are not influenced by the ultrasound as expected. The stirred zone and the interface nugget/EN AC-48000 show similar curves as for the conventional welded joints. Furthermore, there exist areas in the transition area between stirred zone and aluminum alloy, which differ from this behavior. This can be explained with the increased amount of AZ80 due to the increased stirring of the nugget-zone.

Following the 1h immersion test potentiodynamic polarization measurements on varying positions of FSW- and USE-FSW-joints were performed by Benfer et al. (Figure 11).

In Fig. 11a the aluminum alloy EN AC-48000 exhibits a free corrosion potential of about -0.4 V and shows a small passive range and pitting potential of -0.35 to

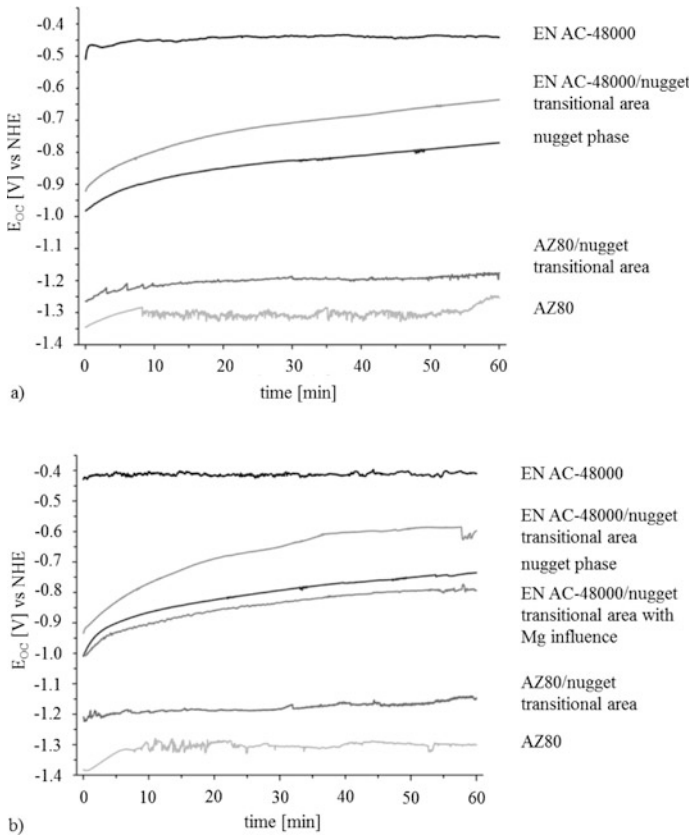


Fig. 10 Open circuit potential measurements at varying positions for **a** FSW and **b** USE-FSW joint in 0.5 molar NaCl solution [5]

-0.25 V depending on the measurement location. Furthermore, the current density lies below $1 \mu\text{A}/\text{cm}^2$ and therefore indicates a low corrosion rate. Compared to aluminum the free corrosion potential of AZ80 is about 1 V lower and the current density is clearly higher (about $20 \mu\text{A}/\text{cm}^2$) at the same time. Regarding the curve of the stirred zone a wide passive range can be observed as well as a pitting potential of -0.34 V . Despite the relatively low free corrosion potential of -0.8 V the pitting potential of the nugget fits well to that one of EN AC-48000. Also the transition zone between aluminum and stirred zone shows such a passive range. Comparing these curves with that of an USE-FSW-Al/Mg-joint (Fig. 11b) it is noticeably that the described passive range is clearly more pronounced for the conventional FSW. As mentioned before even for these investigations the measurement position has an impact on the resulting curves, which can be evidenced by two different trends for the curves of the transition area between the aluminum alloy and the nugget. On one side a current density potential curve with a free corrosion

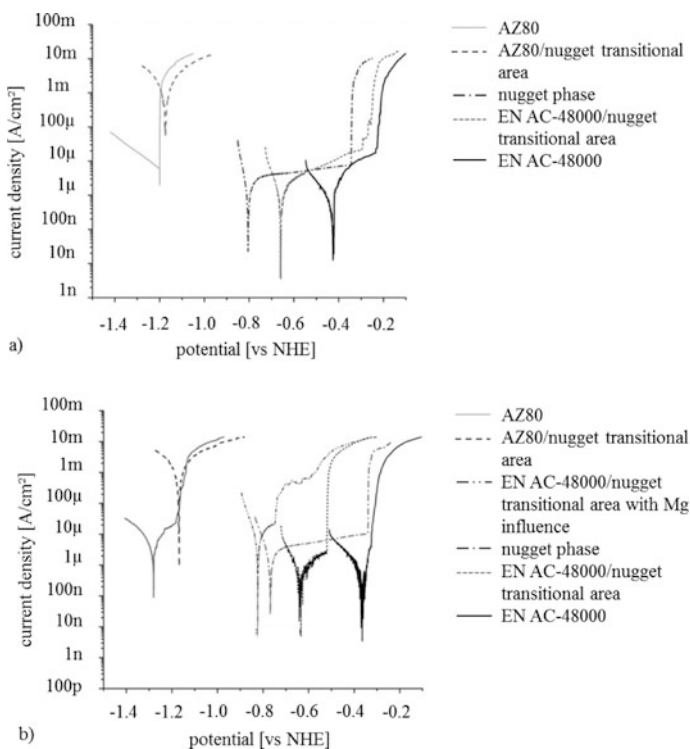


Fig. 11 Potentiodynamic polarization curves measured at varying positions of **a** FSW- and **b** USE-FSW-joints [5]

potential between -0.7 to -0.6 V can be determined, showing a low current density comparable to the values of EN AC-48000. This type of curve is equal to that for FSW-joints. On the other side a second curve occurs for ultrasound enhanced FSW, which reaches a free corrosion potential of -0.83 V and is more negative than that of the stirred zone. For this case higher current densities and thus higher corrosion rates were measured. This fact can again be explained with the locally increased amount of Mg through the improved stirring of the nugget by the ultrasound. The largest increase of current density is detected for the transition between stirred zone and AZ80 as well as for FSW and USE-FSW joints. Beside the fact that the free corrosion potential is close to that of the base alloy of magnesium, the current density is strongly increased by a factor of about 100 and therefore reaches a value of about 1 mA/cm^2 . Microscopic investigations of the measurement area after the polarization experiment show that the nugget seems to be without any corrosive attack, whereas the magnesium part exhibits a strong dissolution. This can be regarded as a typical example for galvanic corrosion where the electrochemical nobler partner (this time the stirred zone) is protected on the expense of the AZ80, which acts as sacrificial anode [5].

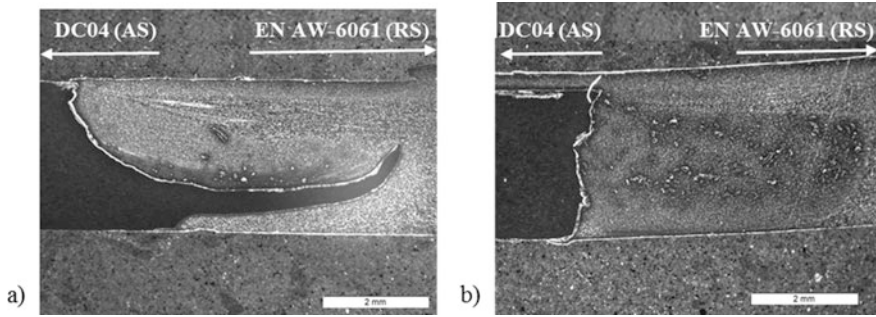


Fig. 12 Cross section images of **a** Al/steel-FSW and **b** Al/steel-USE-FSW

Basing on the positive effects of USE-FSW detected for Al/Mg-joints first investigations on Al/steel-joints were carried out with regard on the influence of additional ultrasound. Comparing the light-microscopic cross section images of an EN AW-6061/DC04-FSW-joint and an –USE-FSW-joint obvious differences are visible (Fig. 12).

For conventional welded joints large steel particles and occasional hooks could be identified in the stirred zone (Fig. 12a). Whereas the ultrasound enhanced Al/steel-joints show a different structure of the nugget (Fig. 12b). The interface is rather perpendicular and a more intensified stirring of the stirred zone can be proved, what leads to the assumption that the ultrasound in principal has the same effect on the welding area of Al/steel-joints as on Al/Mg-joints.

Further investigations of the nugget under the different welding conditions reveal in SEM-pictures two diverse types of particles. Beside steel particles surrounded by a cover of an intermetallic shell, also particles consisting of fine striped intermetallic layers, who are also surrounded by a cover of different intermetallics can be found (Fig. 13).

The depicted layer in the stirred zone of a FSW-Al/steel-joint has a partial surrounding shell of two slightly different phases (Fig. 13a). Through EDX spot measurements the phases could be identified as Fe_2Al_5 (phase 1) and FeAl_3 (phase 2). Figure 13b shows the fine layer shaped structure of the particle. Regarding the thinness of the shells only an EDX average analysis of the particle can be carried out with the available SEM. Thereby a larger amount of about 83% steel and only about 17% of aluminum was detected.

In the nugget of the USE-FSW-joints only nearly pure steel particles completely surrounded by a shell of intermetallic phase can be found (Fig. 14). The cover can be identified via spot measurements as an aluminum-rich FeAl_3 -phase (detail position 1). EDX spot measurements at position 2 in the detail of Fig. 14 prove that the particles contains 98% of steel.

In SEM images of the interface of Al/steel-FSW joints also the striped intermetallic phases can be detected (Fig. 15). EDX spot measurements at the red marked point in the enlarged detail in Fig. 15 reveal that the aluminum rich phase Fe_2Al_5 can be found beside other phases.

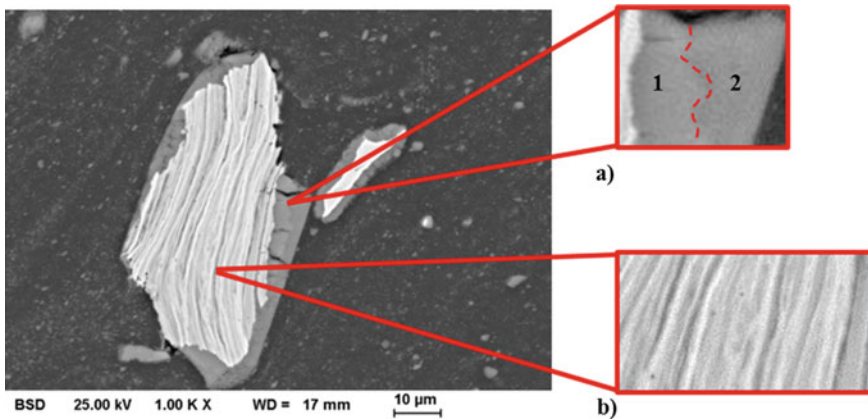


Fig. 13 Particle consisting of fine striped intermetallic phases: **a** detail with surrounding cover, **b** detailed image of the layer structure of the particle center

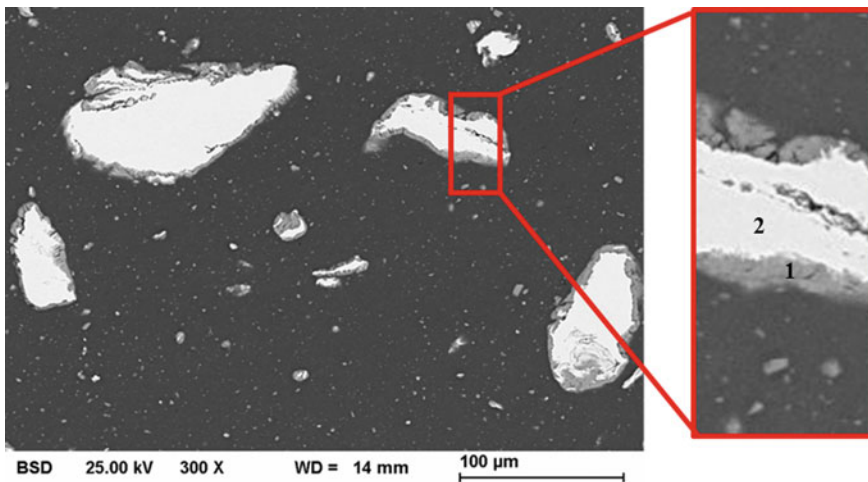


Fig. 14 Steel particles in the stirred zone of USE-FSW-Al/steel-joint and detail of a particle

The microscopic investigations have shown that ultrasound enhances the stirring of the stirred zone for Al/steel-joints as well as for Al/Mg, reduces hooks, and minimizes the size of particles in the welding zone. Furthermore, different particles with covers consisting of the aluminum-rich Fe_2Al_5 - and FeAl_3 -phases can be identified for conventional Al/steel-FSW joints, whereas USE-FSW-joints showed only steel particles with one surrounding shell of FeAl_3 in the nugget. The interface Al/steel possesses also a differing morphology. For FSW-EN AW-6061/DC04-joints

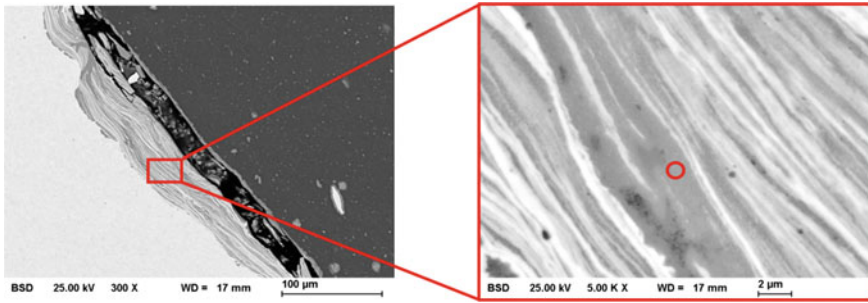


Fig. 15 SEM image of the interface Al/steel with layer shaped intermetallic phases

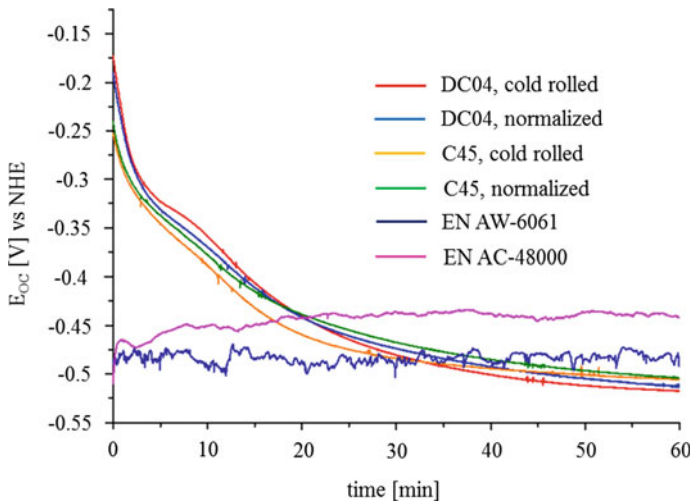


Fig. 16 Open circuit potential measurements at different base materials in 0.5 molar NaCl solution

the transition area shows fine layered intermetallic phases. In contrast to that, ultrasound enhanced welds contains a considerable lower proportion of IM-phases.

First corrosion investigations on the base materials for the upcoming USE-FSW-joints were carried out with OCP and potentiodynamic polarization measurements. Beside the two aluminum wrought and cast alloys two different heat treatment conditions for each of the steel partners were investigated regarding their corrosion behavior. Figure 16 shows the OCP measurements for the steels and the aluminum alloys.

Both aluminum alloys reach constant OCP values after a few min. After 60 min the die casted alloy EN AC-48000 exhibits a value of -0.44 V which is about 50 mV less negative than that of the wrought alloy EN AW-6061 (-0.49 V). The steel samples show a different behavior. Their OCP values decrease continuously

during the whole time of the measurement from a range between -0.18 and -0.25 V to a value of about -0.51 V independent of their heat treatment condition. The slopes of the OCP curves of the steel samples indicate that even after 60 min the values have not reached a constant level. Longer OCP measurements (4 h) have shown that the further decline is very low (about 10–20 mV) and nearly constant values were reached after 2 h. The final OCP values of the steel samples are a little bit more negative than the values of the aluminum alloys. With about 0.1 V the resulting OCP difference between the steels and the aluminum alloys is much smaller than that between magnesium and aluminum alloys (about 1 V, s. Fig. 10). Therefore, a lower risk of contact corrosion at the interface Al/steel is expected.

Figure 17 shows the potentiodynamic polarization curves of the base materials.

In accordance with the OCP measurements the potentiodynamic polarization curves for the steels show that the heat treatment has no influence on the corrosion properties. The curves are nearly identical with a current density at E_{OC} of about $2 \mu\text{A}/\text{cm}^2$.

For the steel samples the current density in the anodic range increases continuously—no passive range or pitting potential is observed. In contrast, both aluminum alloys show clear pitting potentials. With -0.43 V the pitting potential of the wrought alloy EN AW-6061 is significantly more negative than that of the die casted alloy EN AC-48000 (-0.2 V), which shows a broader passive range. The current density at E_{OC} is lower in case of the wrought alloy EN AW-6061 but as the pitting potential is near the E_{OC} a small shift in the anodic direction leads to an increase of several orders of magnitude and therefore to an increased corrosion.

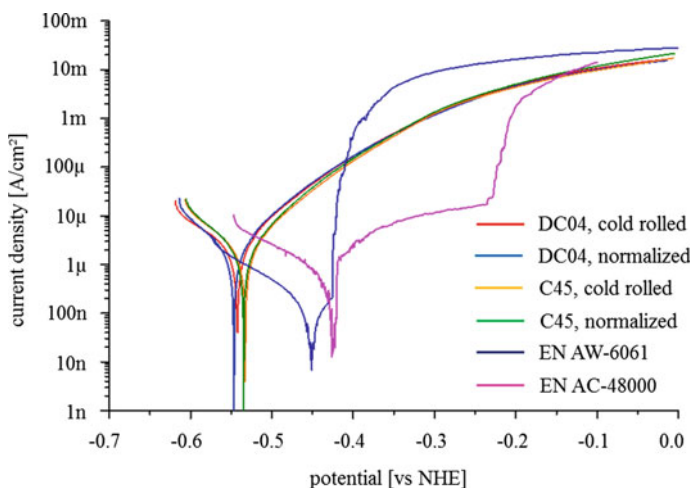


Fig. 17 Potentiodynamic polarization curves of aluminum and steel base material for (USE-) FSW-joints

Summary

The innovative hybrid joining process of ultrasound enhanced friction stir welding was applied on Al/Mg- and Al/steel-joints. Afterwards microscopic and corrosion investigations were carried out regarding the influence of the additionally introduced ultrasound. For the EN AC-48000/AZ80-joints a positive impact of the ultrasound enhancement can be detected in the welding area characterized by a more intensified stirring of the stirred zone, as well as the reduction of continuous intermetallic layers at the interface AZ80/nugget. Based on this promising results the mechanical properties were investigated by monotonic tensile tests and high cycle fatigue tests. In both cases the achieved results got improved by USE-FSW. The tensile strength of an Al/Mg-joint with ultrasound enhancement increased about 25% compared to conventional FSW and the fatigue life time got improved by a factor of 3.5. Additional nondestructive test methods were applied regarding their suitability for post-process detection of irregularities in the welding area. Thereby the EMAT (Electromagnetic Acoustic Transducer) technology and the X-ray radiography proved themselves to be able to identify flawed welds with high accuracy. Electrochemical corrosion investigations were carried out and led to the conclusion that the intensified stirring of the stirred zone promotes a more intensified corrosive attack at the transition zone nugget/EN AC-48000. This can be explained by an increased amount of magnesium in this area. For the first investigations on USE-FSW-Al/steel-joints the microstructure showed also a more intensive stirring of the stirred zone as it was detected for aluminum and magnesium welds. The ultrasound enhancement lead to smaller steel particle sizes and reduces hooks. Furthermore in FSW-joints existing intermetallic particles with a double layer shell can not be observed in samples with ultrasound enhancement. Moreover, steel particles in USE-FSW-joints only had one surrounding shell consisting of the intermetallic phase FeAl_3 . In addition, the interface Al/steel showed another structure. Only the transition area of FSW-joints contains a high amount of fine layered intermetallic phases. These investigations lead to the conclusion that ultrasound has a high impact on the resulting microstructure of the welds. It can be assumed that larger intermetallic phases first get destroyed by the ultrasound and then spread over the nugget. The effect the mechanical properties of the joints in detail will be a central question of the ongoing examinations. Regarding the corrosion behavior of the FSW- and USE-FSW-Al/steel-joints more investigations with integral and space-resolved electrochemical measurements will be carried out. Also, additional nondestructive measurements will be conducted for the Al/steel welds to ensure high quality of the joints and to improve the process.

Acknowledgements We would like to thank the “German Research Foundation (DFG)” for the support of the present work as a part of the Priority Program 1640 “Joining by Plastic Deformation”.

References

1. Khaled T (2005) An outsider looks at Friction Stir Welding. Federal Aviation Administration, Lakewood
2. Straß B (2015) Ultraschallunterstütztes Rührreißschweißen von Al/Mg-Verbunden: Prozessanalyse, mikrostruktureller, mechanischer und korrosiver Eigenschaftsvergleich. Dissertation TU Kaiserslautern
3. Klag O (2013) Mikrostruktur, mechanische Eigenschaften und Korrosionsverhalten rührreibgeschweißter AZ91/AZ91- und AZ91/AlMg3Mn-Verbunde. Dissertation TU Kaiserslautern
4. Reinhold B, Blücher D, Korte M (2013) Herausforderungen an Füge- und Oberflächentechnik für zukünftige Leichtbaukonstruktionen im Automobilbau—Challenge of joining and surface technologies for light weight constructions in automobile applications. *Materialwiss Werkstofftech* 44:58–69
5. Benfer S, Straß B, Wagner G, Fürbeth W (2016) Manufacturing and corrosion properties of ultrasound supported friction stir welded Al/Mg-hybrid joints. *Surf Interface Anal* 48(8): 843–852. doi:[10.1002/sia.5871](https://doi.org/10.1002/sia.5871)
6. Park K (2009) Development and analysis of ultrasonic assisted friction stir welding process. Dissertation, Department for Mechanical Engineering, University of Michigan

Part VI
Industrial Applications

Friction Stir Welding Process Development of AA7075 for Hot Stamping Applications

François Nadeau and Nia R. Harrison

Abstract In order to compete with advanced high strength steels (AHSS) such as dual-phase (DP) or temperature induced plasticity (TRIP) in structural parts, some automotive manufacturers are looking to introduce high strength aluminum alloys that have high peak-aged mechanical properties like AA7075. Formability of these high strength aluminum alloys is possible through hot stamping. Hot stamping refers to simultaneously forming and quenching a blank that is initially at an elevated temperature. Material efficiency can be obtained by using tailor welded blank sections which could lead to weight reductions between 10 and 12%. Friction stir welding (FSW), as a solid-state welding process, has already been proven suitable without hot cracking issues when welding AA7075. However, abnormal grain growth (AGG) issues arise when post-weld operations at high temperature are required such as solution heat treatment or hot stamping operations. This paper details the development of FSW process parameters which will be adapted to hot stamping to effectively join tailor welded AA7075 blanks.

Keywords Friction stir welding • Hot stamping • Tailor welded blanks • AA7075

F. Nadeau (✉)
National Research Council of Canada (NRC), Ottawa, Canada
e-mail: francois.nadeau@cnrc-nrc.gc.ca

N.R. Harrison
Ford Motor Company, Dearborn, USA
e-mail: nharri31@ford.com

Introduction

One key to viable vehicle light-weighting is the incorporation of aluminum over heavier materials. In recent years, hot stamping of aluminum has gained ground because it allows for increased formability of high strength aluminum alloys. When hot stamping, a pre-heated blank is formed at high temperature (i.e. 480 °C) and simultaneously quenched into a cold die. Researchers at Ford Motor Company have demonstrated the feasibility of hot stamping a B-pillar outer panel from AA7075 sheet [1]. High strength aluminum alloys such as AA7075 are widely used in the aerospace industry due to its high specific mass. Within the automotive industry, this alloy could serve as a strong competitor to advanced high strength steels (AHSS) such as dual-phase (DP) or temperature induced plasticity (TRIP) in structural parts. Additional material efficiency is possible by using tailor welded blank (TWB) sections instead of a uniform thickness sheet for a hot stamped part like a B-pillar.

A tailor welded blank is one approach for weight savings as it allows for a decrease in sheet thickness at specific sections which can lead to weight reduction between 10 and 12% in aluminum structural parts. Autogenous laser welding is widely used for steel parts and, at a lesser extent, on aluminum with Al–Mg (5xxx) and Al–Mg–Si (6xxx) series alloys. Although productivity is improved by using laser welding (6–12 m/min), weld defects such as weld concavity, remain a constant challenge for aluminum tailor welded blanks [2]. In addition, AA7075 is susceptible to hot cracking for fusion welding processes and is considered non-weldable [3, 4]. Friction stir welding (FSW), as a solid-state welding process, has been proven suitable without hot cracking issues for welding AA7075 in the aerospace industry [5, 6]. This welding process, when applied to tailor welded blanks, is slower than laser welding but shows relatively high cadency (≥ 3 m/min) in thin sheets (≤ 2.0 mm) and good surface appearance [7]. Despite the fact that FSW is a very interesting technique to join tailor welded blanks prior to cold forming, abnormal grain growth (AGG) issues arise when post-weld operations at high temperature are required such as solution heat treatment, superplastic forming or hot stamping operations [8–11].

The present paper relates the development of FSW process parameters that successfully join tailor welded AA7075 blanks which will be later be evaluated under hot stamping conditions. The FSW process operational windows in addition to post-weld mechanical properties are investigated for two tool shoulder designs as a function of the revolutionary pitch.

Experimental Procedure

FSW experiments were conducted using 1.6–2.0 mm AA7075-T6 tailored blank coupons of 100 mm wide \times 300 mm long in the transverse direction using an MTS I-Stir PDS gantry type equipment as shown in Fig. 1.



Fig. 1 Friction stir weld experiments on 1.6–2.0 mm AA7075 tailored blank coupons using a MTS I-Stir PDS gantry type equipment

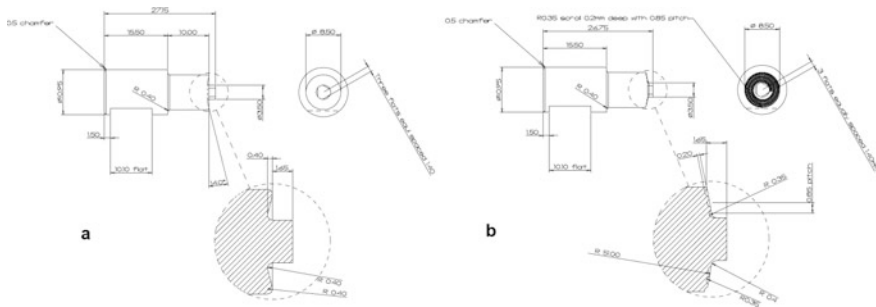


Fig. 2 FSW pin tool designs and dimensions, **a** cup shoulder design, **b** scroll-convex shoulder design

The welds were done in position control first and then in force control; which is more representative of a production environment. Two (2) different shoulder designs were tested, i.e. cup and scroll-convex. Shoulder design changes the friction between the tool and the AA7075-T6 top sheet which is a possible contributor to sub-surface microstructures differences. In all cases, the shoulder diameter was kept constant at 8.5 mm, the pin length constant at 1.55 mm as well as a constant pin design which was a Triflat without any threads. A schematic of the tool designs are shown in Fig. 2.

A design of experiments has been assessed covering a wide range of process parameters as shown in Tables 1 and 2. The specific energy (E_s), which represents the heat generated per unit length, has been approximated using the relationship below and assuming a FSW process efficiency of 0.9 [12, 13]:

$$E_s \approx 0.9 * (M * \omega) / v$$

where:

E_s Specific energy (J/mm)

M Process torque (N-m)

ω Rotational speed (RPM)

v Travel speed (m/min)

As a qualification procedure, each weld condition was initially subjected to a non-destructive evaluation (NDE) using an immersed bath ultrasound (30 MHz focalized probe) which could detect volumetric defects up to 100 μm in size as shown in Fig. 3 [14, 15]. If no defect was observed, qualified welds were subject to a destructive evaluation which included: (1) root bend test, (1) micrograph and (3) tensile tests. The root bend test, shown in Fig. 4, bends the tailored blank coupon of 100 mm (w) \times 300 mm (l) using a 13 mm diameter mandrel. This test allowed for the initial insight into internal defect susceptibility and lack of

Table 1 Design of experiments on principal process parameters for cup shoulder design

FSW shoulder design	Rotational speed	Travel speed	Side angle	Travel angle	Torque	Specific energy	Process condition #
	RPM	m/min	°	°	N-m	J/mm	
Cup shoulder	2000	0.25	1.5	1.5	2.5	180.0	1
	1750				2.0	126.0	2
	1500				2.4	129.6	3
	1250				5.0	225.0	4
	1000				9.0	324.0	5
	750				10.7	288.9	16
	1750	0.50			8.0	252.0	17
	1500				9.8	263.3	18
	500				14.3	128.7	19
	2000	1.00			4.3	77.4	6
	1750				4.5	70.9	7
	1500				5.0	67.5	8
	1250				8.0	90.0	9
	1000				10.0	90.0	10
	2000	2.00			6.7	60.3	11
1750	7.0		55.1	12			
1500	7.3		49.3	13			
1250	10.0		56.3	14			
1000	14.0		63.0	15			

Table 2 Design of experiments on principal process parameters for convex-scroll shoulder design

FSW shoulder design	Rotational speed	Travel speed	Side angle	Travel angle	Torque	Specific energy	Process condition #
	RPM	m/min	°	°	N-m	J/mm	
Convex-scroll shoulder	2000	0.25	1.5	0.5	5.6	403.2	1
	1750				5.0	315.0	2
	1500				4.5	243.0	3
	1250				8.0	360.0	4
	1000				10.3	370.8	5
	750				12.4	334.8	18
	1500	0.50			4.7	126.9	16
	1250				7.0	157.5	17
	1000				10.5	189.0	19
	2000	1.00			5.5	108.0	6
	1750				6.0	118.1	7
	1500				7.5	121.5	8
	1250				9.0	126.0	9
	1000				11.2	103.5	10
	2000	2.00			5.6	50.4	11
	1750				7.0	55.1	12
	1500				7.8	52.7	13
	1250				10.0	56.3	14
	1000				13.5	60.8	15

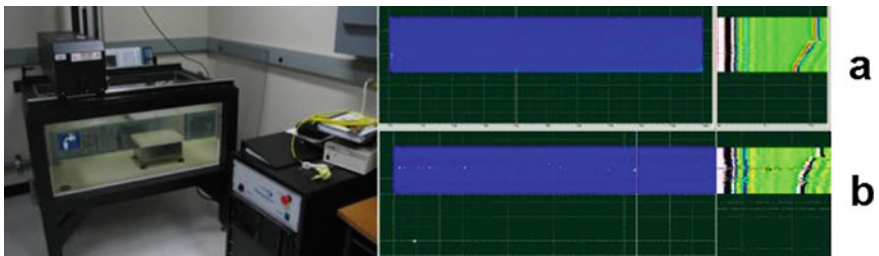


Fig. 3 Non-destructive evaluation of friction stir tailer welds using immersed bath ultrasounds with a 30 MHz focalized probe, **a** sound weld, **b** weld showing sporadic volumetric defects in center

penetration. Room temperature tensile tests were performed in accordance to ASTM E8 standards using strain control up to $\approx 1.4\%$ elongation and displacement control from 1.4% elongation to fracture. The tensile test setup is shown in Fig. 5.

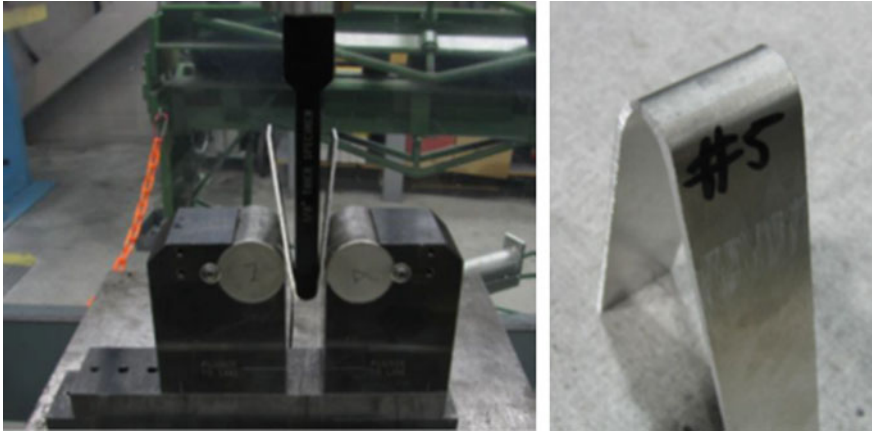
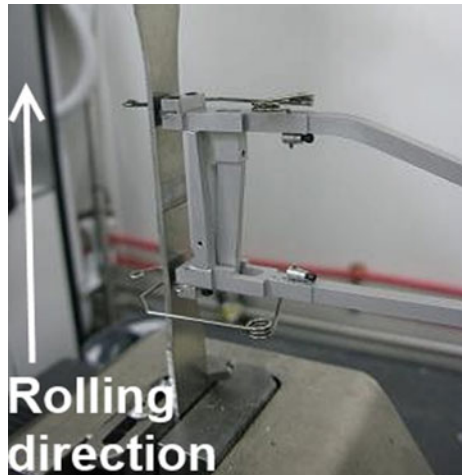


Fig. 4 Test fixture for root bend weld test (left) and bend coupon (right)

Fig. 5 Tensile test setup



Results

Weld Evaluation

The operational window relative to cup shoulder design is presented in Fig. 6 based on the NDE and root bend test performance. High rotational speed (>1500 RPM) appeared to be an unfavorable parameter as it can produce local incipient melting in the sub-surface area. When using a smaller shoulder diameter (8.5 mm) high rotational speed also appeared to be unfavorable because the solvus is much lower for the AA7075 aluminum alloy (477 °C) compared to 6xxx or 5xxx aluminum

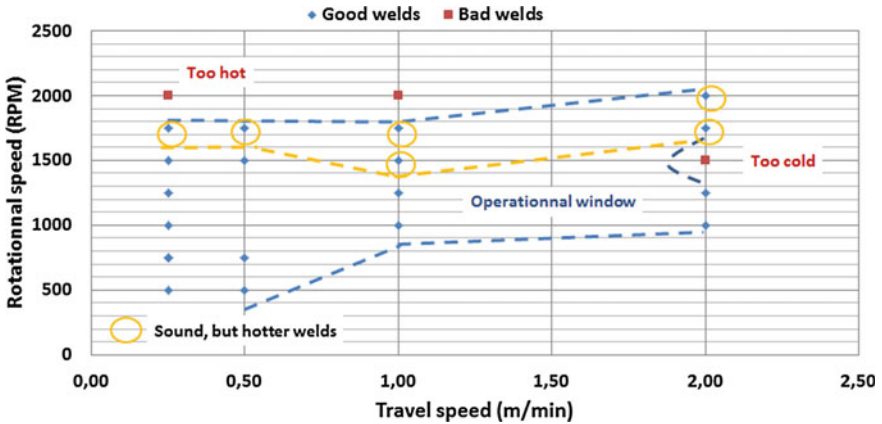


Fig. 6 Process window for the cup shoulder design

Condition	Micrograph	Comments
1750RPM, 0.25m/min		OK condition - but seems hot due to nugget collapse
1000RPM, 0.25m/min		Good condition
1750RPM, 0.5m/min		OK condition - but lack of full penetration

Fig. 7 Examples of weld micrographs for the cup shoulder design

alloys (~580 °C). Examples of a good weld and the observed weld issues are shown in Fig. 7. In general, the process windows were fairly large and similar for both shoulder designs. The operational window relative to scroll-convex shoulder design is shown in Fig. 8 based on the NDE and root bend test performance. Examples of good weld and observed weld issues are shown in Fig. 9.

When directly comparing the two designs, the scroll-convex shoulder design created larger flash on the advancing side in comparison to the cup shoulder design due to the aggressive scroll-convex depth (0.5 mm) used in this study; see Fig. 10. A less aggressive scroll-convex depth should reduce the weld flash.

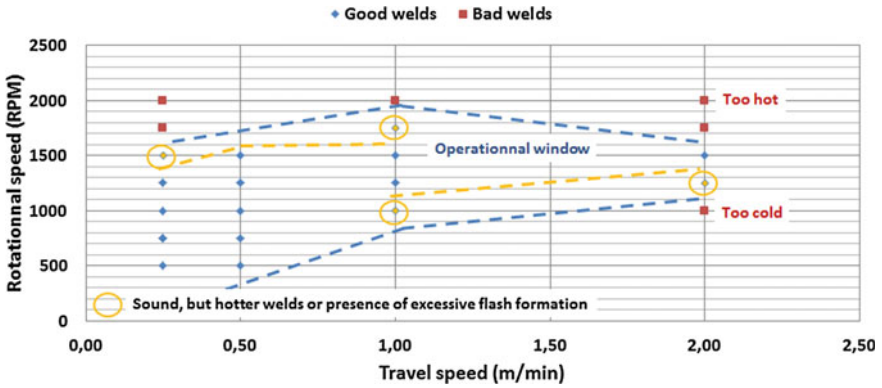


Fig. 8 Process window for scroll-convex shoulder design

Condition	Micrograph	Comments
1500RPM, 0.25m/min		Large sheet thinning on 2.0mm sheet
1000RPM, 0.25m/min		Good condition
1000RPM, 1.0m/min		Good condition- but high flash
1000RPM, 0.5m/min		Good condition - but lack of full penetration

Fig. 9 Examples of weld micrographs for the scroll-convex shoulder design

Although some FSW conditions showed a hotter weld with near nugget collapse, no major microstructural defects were observed for the given weld conditions. Additionally, there did not appear to be flash issues using the cup shoulder design as found with the scroll-convex design.

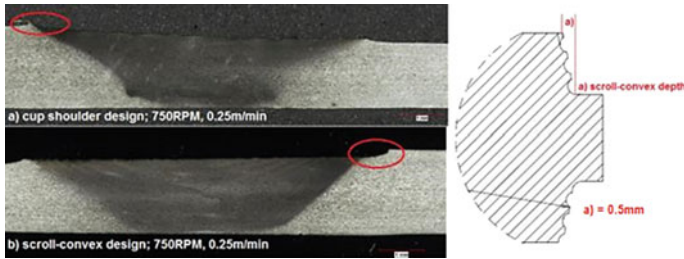


Fig. 10 Penetration depth on advancing side comparing both shoulder designs for given process parameters: 750 RPM, 0.25 m/min (Keller's etchant)

Mechanical Properties

The as-welded mechanical properties after a 7-day natural aging period under tensile testing were recorded for the process conditions that passed the NDE and bending test using a MTS electromechanical test machine (Fig. 11). The mechanical properties were very high for every condition using a scroll-convex shoulder design; reaching between 83% and 87% of ultimate tensile strength joint efficiency when compared to the base material. The mechanical properties using the cup shoulder design were still high but slightly lower than the scroll-convex design; reaching between 77% and 87% of the ultimate tensile strength. The yield strength appeared to be slightly higher using the scroll-convex design versus the cup design; 368–400 MPa compared to 338–393 MPa, respectively. However, condition #19 (500 RPM, 0.5 m/min) using the cup shoulder design, showed much higher yield strength compared to any other weld conditions (i.e. 454 MPa). This weld condition was the only one with a rotational speed as low as 500 RPM and only occurred when using the cup shoulder design. It is expected that the scroll-convex shoulder should have a similar or better mechanical performance. This condition was determined based on grain size analysis but is not covered in this paper. The tensile tests fractured in various locations depending on the process parameters is shown in Fig. 12. No direct relationship has been observed relatively to the specific energy or the revolutionary pitch as a function of the tensile test fractured zone.

On the other hand, a comparison can be made regarding the yield strength as a function of the revolutionary pitch which is an approximation of the heat input (Fig. 13). As expected, the yield strength increased as the revolutionary pitch increased due to a lower heat input, thus a lower coarsening of the precipitates found in the thermo-mechanical and heat affected zones of AA7075. However, this behavior was observed up to a revolutionary pitch of 0.65 using the scroll-convex shoulder design and thereafter decreased. This trend was not seen using the cup shoulder design as the yield strength slowly increased for every revolutionary pitch

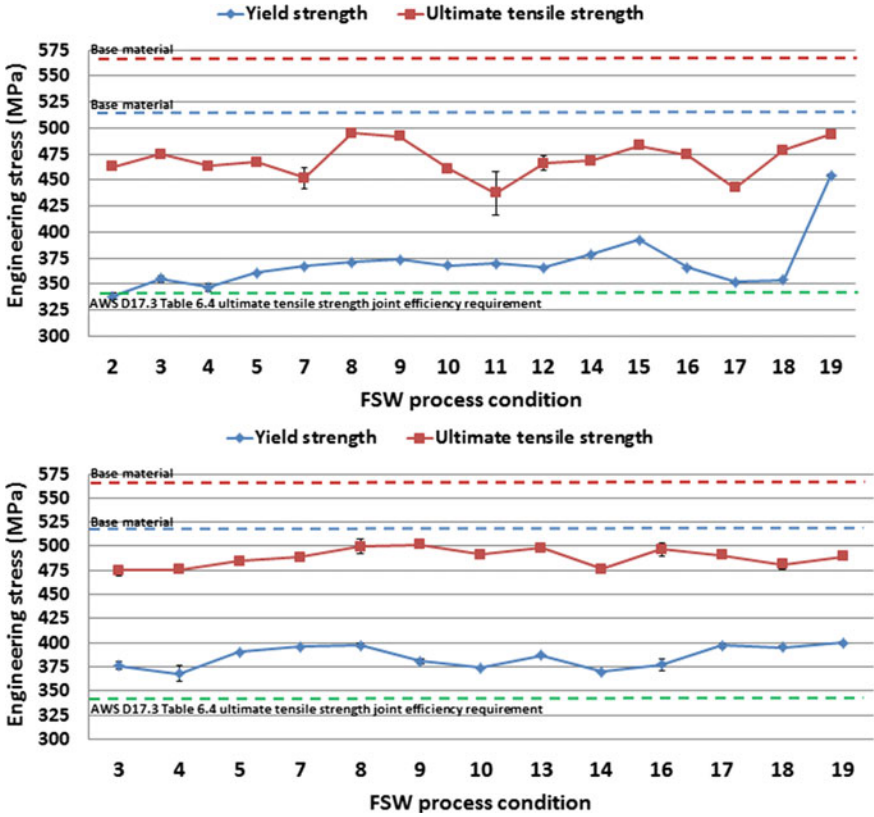


Fig. 11 Mechanical properties for the cup shoulder (top) scroll-convex shoulder (bottom) designs

evaluated. When the rotational speed was kept at its lowest value (500 RPM), the yield strength increased drastically, reaching 454 MPa even when the revolutionary pitch was at an intermediate level (1.0). To conclude, the optimal mechanical performance on tailor welded AA7075 blanks was obtained using low rotational speeds (500 RPM).

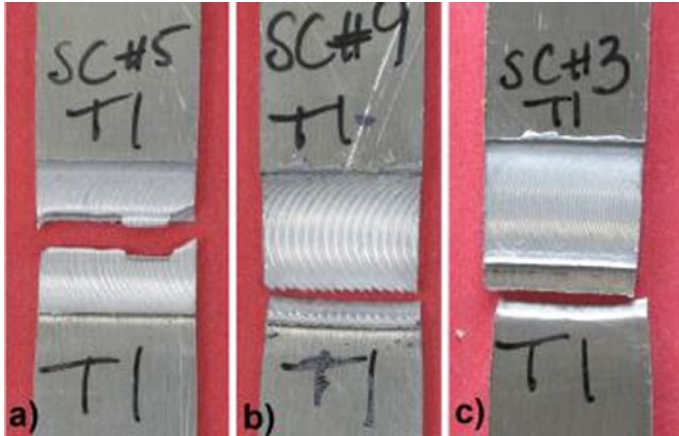


Fig. 12 Tensile tests fractured in various locations, **a** nugget zone, **b** thermomechanical heat affected zone (TMAZ) on retreating side, **c** heat affected zone (HAZ)

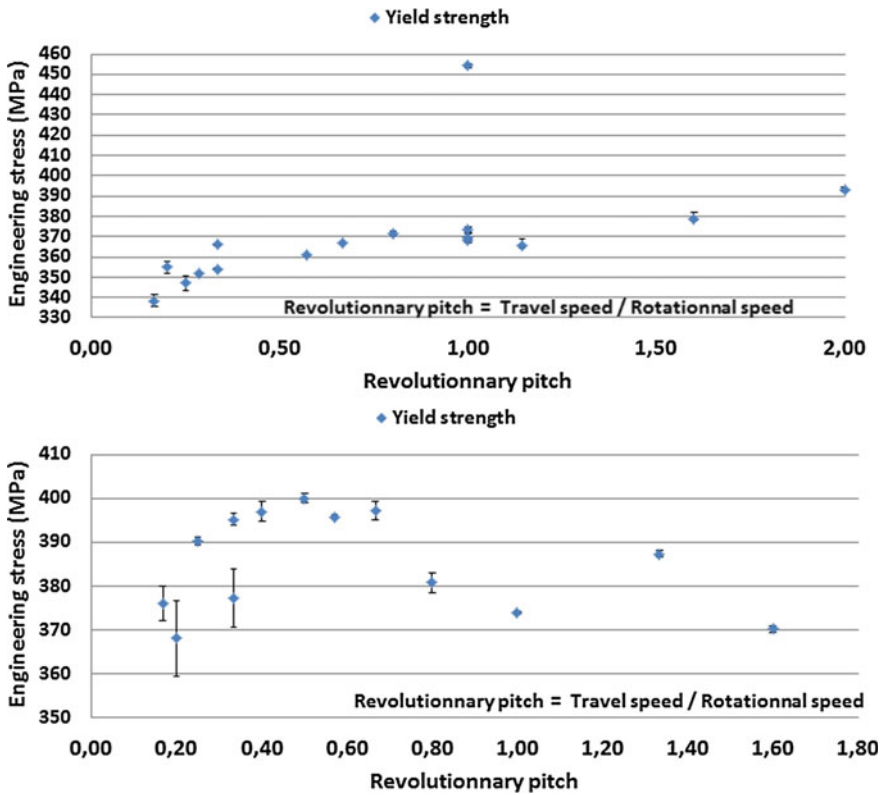


Fig. 13 Yield strength as a function of the revolutionary pitch for the cup shoulder (top) scroll-convex shoulder (bottom) designs

Conclusion

This work investigated the development of FSW procedures and process parameters that would successfully join tailor welded AA7075 blanks which will be evaluated under hot stamping conditions in the future. Process parameters windows have been defined for both shoulder tool feature (scroll-convex and cup designs). While travel speeds of 2.0 m/min were obtained, AA7075 in a TWB configuration (1.6/2.0 mm) did not generally tolerate high rotational speed (≥ 1500 RPM) independent of the travel speed. FSW of TWB 7075-T6 using 8.5 mm cup shoulder diameter showed an overall better surface finish when compared to the scroll-convex design. Larger flash was observed toward the thicker sheet (2.0 mm) for certain conditions when using the scroll-convex shoulder design possibly due to an aggressive scroll-convex depth. The overall mechanical properties, yield and ultimate tensile strength, were slightly better using the scroll-convex shoulder design compared to the cup design in the as-welded and naturally aged condition. However, the peak yield strength was obtained when the rotational speed was kept at its lowest value (500 RPM). Based on the results obtained, 16 (out of 19) of the cup shoulder conditions and 13 (out of 19) of the scroll convex conditions will be further explored with respect to abnormal grain growth (AGG) using a simulated hot stamping thermal cycle. In addition, elevated tensile performance of the optimum parameters of this study and thermal stability will be evaluated.

References

1. Harrison N, Luckey S (2014) Hot stamping of a B-pillar outer from high strength aluminum sheet AA7075. *SAE Int J Mater Manuf* 7(3):567–573
2. Hovanski Y et al (2014) Comparing laser welding technologies with friction stir welding for production of aluminum tailor-welded blanks. *SAE Int J Mater Manuf* 7(3):537–544
3. Cheng CM et al (2005) Hot cracking of welds on heat treatable aluminum alloys. *Sci Technol Weld Joining* 10(3):344–352
4. Pujari KS, Patil DV (2013) A review on GTAW technique for high strength aluminum alloys (AA 7xxx Series). *Int J Eng Res Technol* 2(8):2477–2490
5. Tavares SMO (2011) Design and advanced manufacturing of aircraft structures using friction stir welding. PhD thesis, University of Porto, 1–91
6. Khaled T (2005) An outsider look at friction stir welding. Report #: ANM-112N-05-06, Federal Aviation Administration
7. Nadeau F (2015) Developments in friction stir and spot welding: tailored blanks & al/steel joining techniques. Paper presented at the 11th global automotive lightweight materials, Detroit, Michigan, 14 Apr 2015, p 8
8. Nadeau F, Larouche D, Gougeon P (2013) Abnormal grain growth in friction stir welds subjected to hot forming applications: A AA5083 microstructural case study. In: 12th international conference on aluminum
9. Smith CB et al (2010) Friction stir processing of commercial grade marine alloys to enable superplastic forming. *Key Eng Mater* 433:141–151
10. Shibayanagi T, Naka M (2007) Control of grain size and texture in al alloys utilizing friction stir processing. *Mater Sci Forum* 539–543:3769–3774

11. Chen PS, Russell C (2012) Mitigating abnormal grain growth for friction stir welded Al-Li 2195 spun formed domes. In: 9th international symposium on friction stir welding, pp 490–508
12. Cui S, Chen ZW, Robson JD (2010) A model related tool torque and its associated power and specific energy to rotation and forward speeds during friction stir welding/welding/processing. *Int J Mach Tools Manuf* 50:1023–1030
13. Kalya P et al (2007) Specific energy and temperature mechanistic models for friction stir processing of Al-F357. In: Proceedings of the 2007 minerals, metals, and materials society annual meeting, pp 113–125
14. Mandache C et al (2012) Non-destructive detection of lack of penetration defects in friction stir welds. *Sci Technol Weld Joining* 0(0):1–9
15. Levesque D et al (2008) Assessment of friction stir welds with non-destructive methods. In: Proceedings of the 47th conference of metallurgists

A Novel Approach for Joining EN AW 1050 Stranded Wire and EN CW 004A Contact Elements by Friction Stir Spot Bonding

Anna Regensburg, René Schürer, Jan Ansgar Gerken,
Helmut Steinberg and Jean Pierre Bergmann

Abstract The increasing demand for comfort and safety features leads to a rising amount of electronic components in modern vehicles. As a consequence, copper is increasingly substituted by aluminum, which raises the challenges for conventional joining technologies especially for stranded wire connections. In this case, the use of aluminum leads to larger cable cross sections in order to obtain constant electrical properties, which limits the applicability of technologies like crimping and ultrasonic welding. Therefore, a new friction based process was developed, which enables the joining of EN AW 1050 59 mm² stranded wire to EN CW 004A contact elements by friction stir spot bonding. By positioning the strand in line to the tool axis and into a cap-like contact element, this process enables joining the end face of the strand to the contact element without excessive cable deformation, so that the energy transport can take place throughout the whole cable cross section.

Keywords Friction stir spot joining • Dissimilar joints • Stranded wire • Ultrasonic welding • Electrical contacts • Eutectic reaction

Introduction

In the current discussion of environmental topics, reducing the emission of CO₂ is one of the most important subjects. Currently, public and private road traffic is depending to more than 90% on fossil energy and leads to approx. 20% of the total CO₂ emissions in Germany [1]. To reduce the emissions, the producers put the lightweight construction of the cars into focus of the technological development.

A. Regensburg (✉) · R. Schürer · J.A. Gerken · J.P. Bergmann
Department of Production Technology, Technische Universität Ilmenau,
Gustav-Kirchhoff-Platz 2a, 98693 Ilmenau, Germany
e-mail: anna.regensburg@tu-ilmenau.de; info.fertigungstechnik@tu-ilmenau.de

H. Steinberg
Nexans Autoelectric GmbH, Vohenstraußer Straße 20, 92685 Floß, Germany
e-mail: hsteinberg@autoelectric.de

On the other hand, the government pushes the automotive industry to raise the market share of electric cars. In 2009 the German government published the aim to get one million electric cars on the road. Considering lightweight design methods, not only the car body but also the electrical system of the car becomes a point of interest for such approaches.

Especially, the continuously increasing demand for comfort and safety features leads to up to 4000 cables with an overall length of 6 km and a weight of 60 kg in modern cars [2]. A reduction of the weight of the cables can be achieved by substituting copper with suitable lightweight materials like aluminum.

To maintain the initial electrical conductivity, the diameter of aluminum conductors has to be increased by about 20% [3], but due to its lower density, this substitution still achieves a weight reduction of up to 50%. However, the use of aluminum leads to several challenges because of the different material characteristics. For the connection between the conductor and the battery, a copper contact element, a so-called terminal, which connects to the battery by force locked connections, is fixed to the conductor. For terminals, the use of aluminum leads to decreasing contact pressure and therefore to a reduction of contact area due to the creeping behavior of aluminum. For this reason, terminals are made out of copper, which leads to numerous dissimilar material joints in the electrical system. These material combinations need to be joined with a suitable technology.

The crimping process is used mainly for cross sections smaller than 6 mm². Due to the low cost and short cycle time of the crimping process, billions of contacts are joined yearly by this process. Nowadays, usually copper strands are used for signal cables [3]. To reduce the weight and space of cables with small cross sections between 0.35 and 0.50 mm², pure copper is rather substituted by copper alloys with higher tensile or bending strength like CuMg0.2 and CuSn0.3. Cables with cross sections between 0.75 and 10 mm² have the biggest share of the weight incorporated in the wiring system. Mostly, copper is used for these cross sections, but a substitution by aluminum can lead to weight reductions up to 48% [4]. For bigger cables with cross sections of 10–120 mm², the substitution of copper with aluminum can obtain much more significant results. In order to use this benefit, established joining technology have to be evaluated again regarding the adjusted requirements and if needed substituted by innovative approaches. An especially important factor to be considered is the reduced cross conductivity between the single aluminum wires because of the oxide coating. This must be taken into account for crimping procedures. Furthermore, in case of dissimilar connections, a suitable sealing needs to be used to avoid electrochemical corrosion. Consequently, this leads to the need of significant higher crimping forces and a preparatory treatment. The wires need to be totally free of oils and other production residues.

Using welding techniques, especially for materials combinations with low solubility in the solid state like Al-Cu, a high heat input during joining can promote the formation of intermetallic compounds (IMCs). These compounds usually exhibit a complex lattice structure, leading them to be brittle and much less electrically conductive than the base materials. This highly affects the long term performance of joints under thermal or mechanical load [4]. In order to minimize IMC formation

during welding, significantly elevated temperatures over an increased period of time have to be avoided. However, for obtaining a sufficient adhesion and bond quality at all, a certain amount of diffusion over the interface is required. According to the Arrhenius law and for otherwise constant boundary conditions, these mechanisms can either be accelerated by increased temperature T or decreased activation energy Q .

$$D = D_0 \cdot e^{-\frac{Q}{R \cdot T}} \quad (1)$$

The activation energy can be highly influenced by subjecting the material to plastic deformation, thus inducing strain hardening and increasing the dislocation density. When solid state joining processes are applied, the combination of plastic deformation and elevated temperature, e.g. caused by frictional heating, promotes dynamic recrystallization. This simultaneous presence of strain hardening and recrystallization leads to a fine grained microstructure within the weld. Using this approach, welds with outstanding bond strength can be obtained without triggering excessive IMC formation.

In the past decades, ultrasonic metal welding (USMW) has been well established for producing joints for electrical applications. For aluminum cables it is used to pre-compact the strands of cross sections between 2.5 mm^2 up to 6 mm^2 prior to the crimping process [4]. This improves the conductivity between the single wires towards the crimp contact. For cross sections up to 200 mm^2 , the Al strands and the Cu contact elements can be welded directly within one process step, without pre-compaction. In this case, the welding tool, the so called sonotrode, applies a force towards the top package of wires and feeds the oscillation energy into the stranded package. Due to relative movement and frictionally induced heating, the oxide coating will break up and the wires will experience plastic deformation.

However, due to the initially only low compacted cable, the friction energy brought into the upper part of the strand, decreases with higher welding depth. At the actual connection between terminal and cable, the energy for plastic deformation can be diminished compared to that at the contact face to the sonotrode. Figure 1 shows the maximum deformation rate near the contact zone to the sonotrode. Due to the effect of “acoustic softening”, the wires are subjected to severe plastic deformation. Damping effects within and between the single strands reduce the vibration energy with increasing distance to the sonotrode. Depending to the process setting, this leads to a reduced interface being firmly bonded, compared to the actual contact area of the sonotrode.

Using the USMW-process for joining, the terminal is connected radially to the strand. In Fig. 2, the difference between a radial and an axial connected terminal is shown schematically. In a radial bonded terminal all the current has to flow through the wires directly connected to the copper. If the connection between one wire and the terminal is not sufficient, the resistance of the total bond is increased compared to an axial bonding with one defective wire.

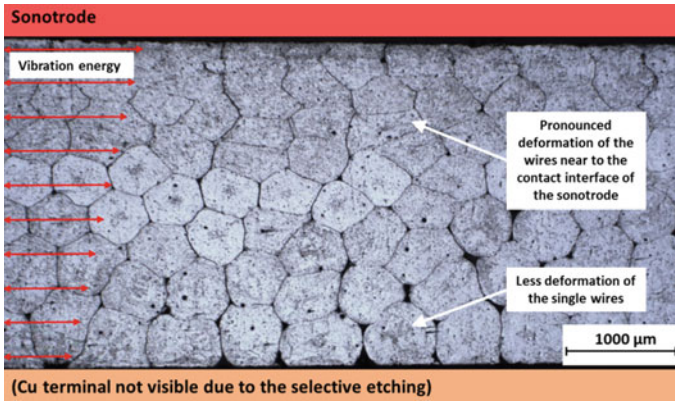


Fig. 1 Decreasing deformation rate with higher welding depth

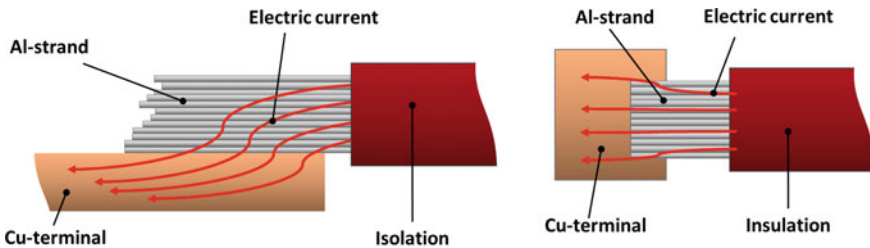


Fig. 2 Electric current flow into radial (left) and axial (right) terminals

So, in the macroscopic view, the geometrical arrangement is a very important aspect to be considered. In the microscopic point of view, also the thickness of the intermetallic compounds (IMCs) between aluminum and copper influences the quality of the bonding. In comparison to the pure metals, these intermetallic compounds show a brittle characteristic and a reduced conductivity as shown in Table 1.

Table 1 Selected material properties of intermetallic phases of Cu and Al [5]

Phase	Chem. composition	Cu [wt%]	Al [wt%]	Hardness [kg/mm ²]	ρ [$\mu\Omega$ cm]	D_0 [cm ² /s]
Cu	Cu	100	0	42	1.75	–
λ_2	Cu ₂ Al	80	20	35	14.2	3.2×10^{-2}
δ	Cu ₃ Al ₂	78	22	180	13.4	2.6×10^{-1}
ζ_2	Cu ₄ Al ₃	75	25	624	12.2	2.7×10^6
η_2	CuAl	70	30	648	11.4	1.7×10^{-6}
θ	CuAl ₂	55	45	413	8.0	9.1×10^{-3}
Al	Al	0	100	38	2.9	–

The formation of intermetallic compounds is caused by high temperatures either during the production process or due to the operation during the lifecycle of the product. Severe formation of intermetallic compounds between aluminum and copper can increase the electrical resistance of the bonding depending on the morphology of the interface. This leads to an increased operational temperature, which again encourages the growth of the IMC-layer. This chain reaction will continue until the bonding fails, either due to the brittle material properties or due to a thermal overload due to the increased electric resistance. To prevent locally increased temperatures by a high current density, an axial mounted terminal would represent an opportunity compared to a radial mounted one (See Fig. 2).

Therefore, the objective of this examination is to create a direct bond of an Al cable and an axial mounted Cu contact element and avoid the brittle intermetallic compounds by creating a low melting eutectic phase between the dissimilar joining partners. For this welding task, a friction stir spot welding process (FSSW) is applied.

Experimental Setup

To obtain an axial bonding between the Cu contact element and an aluminum cable with a cross section of 59 mm^2 , a specially designed cap with a wall thickness of 1.5 mm is used. The stripped cable is inserted into the cap and fixated by a crimping process. As shown in the schematic illustration in Fig. 3a, the Cu contact element is being finally bonded with an axial friction-stir-spot-bonding operation on a milling machine Hermle UWF-1000.

The experiments are carried out with and without precompaction by a TIG process. In the first experiments, the strands were joined to the Cu caps without precompaction. This crimping process is used to prevent the wires from being pushed out of the cap. In Fig. 4, selected results of the experiments are shown. As can be seen, there is no direct correlation between the rotational speed of the tool or the dwell time and the separation forces of the cap. But with a higher plunge speed, also the process force rises, what leads to lower separation forces of the cable. An explanation for this behavior is the displacement of the wires prior to the formation of the eutectic interlayer. To ensure the formation of the targeted eutectic layer, the plunge speed was reduced. This leads to an increased processing time and therefore to a decreased rate of deformation. By doing so, the single wires got firmly bonded to the cap which is shown by a significantly increased separation force. But through the slightly uneven cutting surface of the wires, a uniform contact face during the bonding process between all the wires and the cap cannot be ensured. Accordingly, the reliable cross section of the cable is reduced what leads to a relatively low separation force of 2000 N. However, the failure of the wires still takes place outside of the bonding zone within the wires.

In order to connect all the wires in the middle of the cable, in a further step, the wires were preprocessed by an arc welding process, then inserted and crimped into

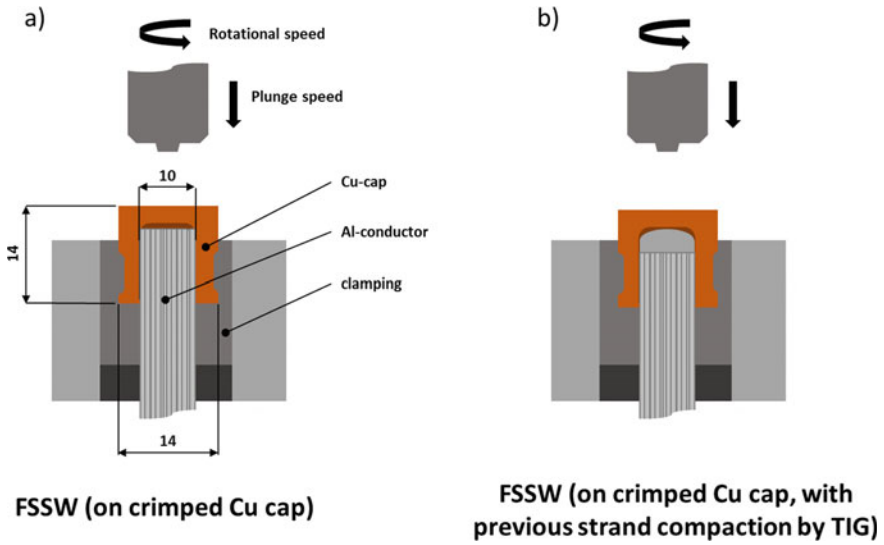


Fig. 3 FSSW of copper caps and aluminum wires with different pretreatments. **a** Bonding of Al-cable and Cu-contact-element. **b** Using previously compacted strands

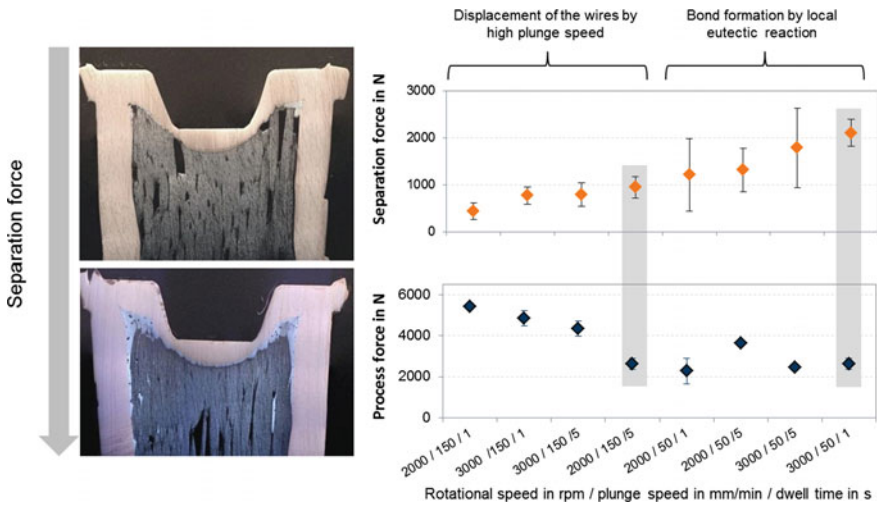


Fig. 4 Separation forces without pre-compacting the wires

the cap. This also breaks up the usually formed oxide layer at the interfaces of the single wires. Using a tungsten inert gas welding (TIG) process for the bonding, the used electric current and the welding time are two important parameters. In Fig. 5 the influence of the different parameters is shown. It is apparent, that with increasing welding current the amount of molten material is increased and a

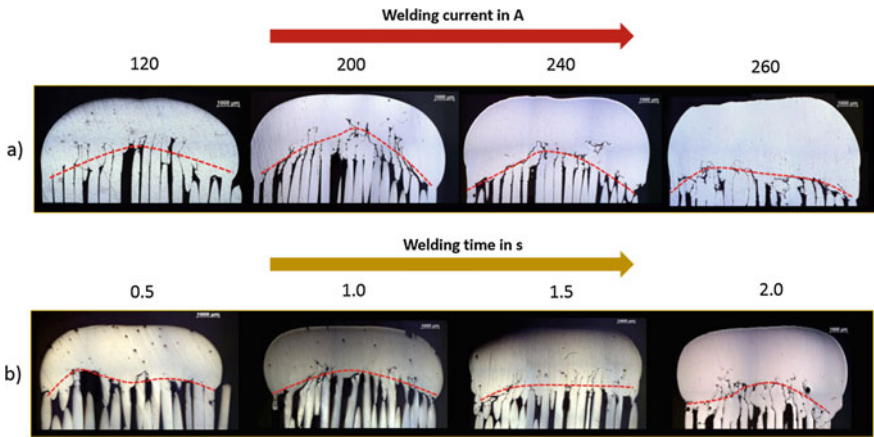


Fig. 5 TIG-process. a Increasing welding at 2 s process time. b Increasing welding time at 260A

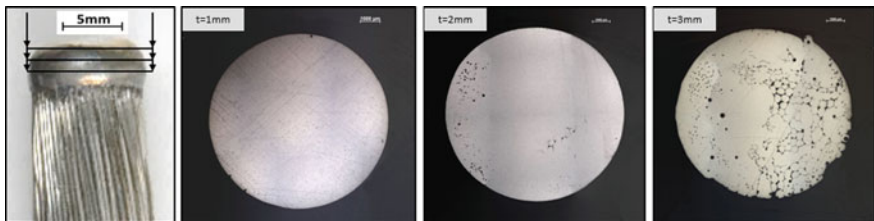


Fig. 6 Horizontal cuts through the molten wires, each with a distance of 1 mm

sufficient bonding of the wires is created. The pictures also reveal, that with short welding times a lot of pores remain within the molten area. Increasing the welding time to 2 s, the molten area is formed most homogeneously.

As shown in Fig. 6, the TIG-process also leads to an evenly distributed melting range, so the molten cable endings can easily be fitted into the cylindrical caps. As shown in Fig. 7, the heat effected zone is also minimized and leads to a recrystallization of the aluminum only of a few mm along the wires, so the temperature-sensitive isolation out of PVC is not harmed.

Using the TIG-process to melt the cable endings together, a solid element of aluminum is formed. To obtain best separation forces, the crimping process is not performed where this massive element is located, but right under the element at a distance of 5 mm to the end of the cap. This leads to an interlocking effect between the aluminum and the copper and the best starting conditions for the FSSW-process.



Fig. 7 Cross section of the melt area (260A, 2 s process time, etched electrolytically)

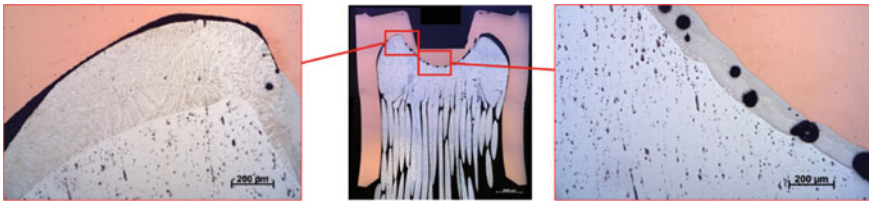


Fig. 8 Increased heat input using a tool with a pin and the resulting pores

Applying the initial process setup with a tool with a pin leads to a highly increased heat development with an insufficient connection between aluminum and copper due to severe melt layer and pore formation as shown in Fig. 8.

Hence a tool with a diameter of 9.5 mm without a pin was used for further experiments. This leads to a reduced heat development within the cap. Parametric studies show a small process window for a well formed eutectic material. As long as the frictional energy and the degree of deformation of the cap is not sufficient, the eutectic layer is less than 10 μm in diameter as shown in Fig. 9a. A slight change of the parameters as shown in Table 2 leads to a well-established eutectic interlayer with a thickness of approximately 100 μm (See Fig. 9b) and reached comparatively high separation force values of up to 2733 N in average. However, if a nickel plating is used in the cap, the reaction between Al and Cu is completely avoided, as the Ni interlayer is not damaged by the process induced deformation (See Fig. 9c).

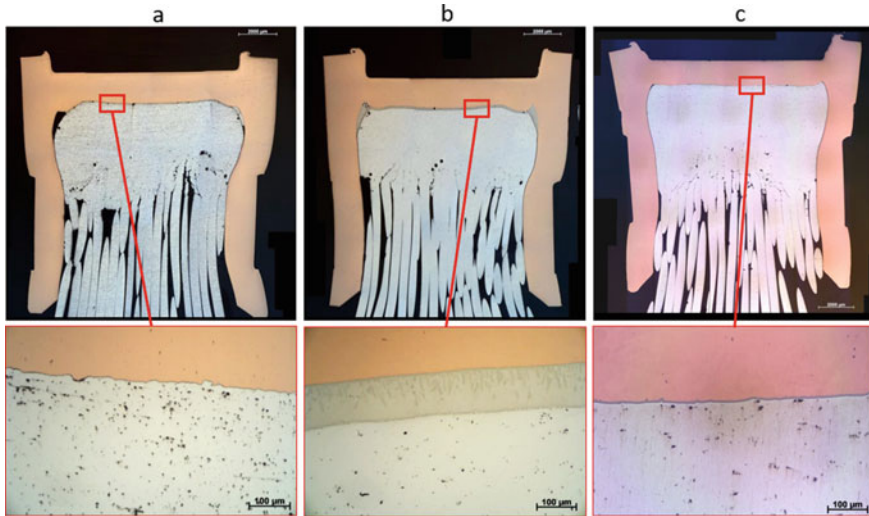


Fig. 9 Cu-terminal welded to Al-cable with FSSW. **a** Thin layer between CU-cap and aluminum cable. **b** Eutectic layer with a 100 μm thickness. **c** Cap coated with nickel

Table 2 Process parameters for joining process with precompaction

Sample	Rotational speed (rpm)	Plunge feed rate (mm/s)	Plunge depth (mm)	Dwell time (s)
Figure 7	3000	50	0.5	3
Figure 8a	2000	50	1.5	3
Figure 8b	3000	50	1.8	2
Figure 8c	3000	50	1.5	2

Conclusion

In this investigation, CW004A copper contact elements and a AW1070A aluminum cable were joined axially by a friction stir spot bonding process in order to consider the current requirements on stranded wire joints for automotive applications. To avoid single wires being pushed out of the contact element during the bonding process, the cable was first crimped within the cap. Considering the first results, the strand end face was than precompacted by a TIG process. This leads to a form fit and firmly bonded connection also exhibiting the formation of a continuous eutectic interlayer at the Al-Cu interface. Using a Ni plating at this interface, the formation of intermetallic compounds or an eutectic layer at the Al-Cu interface during the process could be avoided completely. However, relatively high separation forces compared to the conventional joining process could still be obtained. In summary the results show a high potential regarding future applications with e.g. even higher

cable cross sections and increased requirement on the bond between the single wires and the respective contact element.

Acknowledgements The authors gratefully acknowledge the support of Nexans autoelectric GmbH for this research.

References

1. Emissionsberichterstattung der Bundesrepublik Deutschland 2010. Umweltbundesamt. Dessau
2. Ernst M, Heuermann M (2014) Die wichtigsten Bordnetz-Trends, Elektronik automotive Sonderausgabe Bordnetz
3. Hentschel W (2012) Ressourceneffiziente Lösungen Best-Practice AUTO-KABEL. Ressourceneffizienz-kongress, Karlsruhe
4. Aurich T (2016) Das Netz hält, http://www.autokon.de/home/-/article/33673047/42082131/Das-Netz-h%C3%A4lt/art_co_INSTANCE_0000/maximized/
5. Braunovic M, Konchits VV, Myshkin, NK (2007) Electrical contacts, fundamentals, applications and technology. CRC Press

Joining Al 6061 to ZE41A Mg Alloy by Friction Stir Welding Using a Cold Spray Transition Joint

Todd R. Curtis, Victor K. Champagne III, Michael K. West,
Reza Rokni and Christian A. Widener

Abstract The joining of highly dissimilar metals such as aluminum and magnesium has proven to be a difficult challenge using most of the technologies available today. This paper presents a novel method to join dissimilar materials using a combination of two advanced metals processing technologies, friction stir welding (FSW) and cold spray. By utilizing both technologies the strengths of each can be employed, while at the same time mitigating otherwise disqualifying aspects if used alone. In this study, cast ZE41A-T5 magnesium was joined to wrought 6061 aluminum. The joint was accomplished by first cold spraying a 6061 transition zone onto the magnesium alloy, followed by FSW of a 6061 plate to the cold sprayed 6061 zone. Utilizing this method, the formation of detrimentally thick intermetallic layer between the aluminum and magnesium was avoided, providing a resultant joint which matched the strength of the magnesium cast alloy. Detailed materials characterization by electron and optical microscopy, along with mechanical test results is presented. Comparisons to conventional joining techniques and potential applications of this technique is discussed.

Keywords Friction stir welding • Cold spray • Transition joint • Dissimilar metal joining

T.R. Curtis (✉) · M.K. West · C.A. Widener
Arbegas Materials Processing and Joining Laboratory,
South Dakota School of Mines and Technology, Rapid City, SD, USA
e-mail: todd.curtis@sdsmt.edu

V.K. Champagne III
Mechanical Engineering, University of Massachusetts, Amherst, MA, USA

R. Rokni
University of Southern California, Los Angeles, CA, USA

Introduction

There are numerous methods which have been employed to join aluminum and magnesium such as diffusion [1, 2], friction stir welding [3], magnetic pulsed arc welding [4], laser welding [5, 6], TIG welding [7], electron beam welding [8], and resistance spot welding [9]; however, none of the methods have yielded excellent results. Due to the high chemical affinity between aluminum (Al) and magnesium (Mg) alloys, the resulting welds form an intermetallic layer at the dissimilar metal interface, which is significantly lower strength and more brittle than either the Mg or Al alloys. Because the reaction occurs so quickly and so ubiquitously across a wide range of joining techniques, it has been concluded that the formation of a large number of Mg/Al intermetallic compounds is largely unavoidable. As a result, there have been limited direct applications for welded Al/Mg joints. Cold Metal Transfer (CMT) dissimilar Al/Mg welding attempts have been reported [10], but have resulted in poor mechanical properties and also brittle fracture of the intermetallic layer at the dissimilar interface. The addition of a zinc alloy interlayer between Mg and Al during the diffusion bonding process has been found to significantly improve the microstructure of the bond zone at the interface, but deleterious intermetallics are still formed in the bond region [1]. Somasekharan and Murr [11] fabricated numerous welds from Mg alloys and the 6061-T6 Al alloy using friction-stir welding (FSW) with better results in that the formation of a large number of Mg/Al intermetallic compounds were avoided but not altogether eliminated. In another study by Tomaa et al., the microstructure of the interface layer between Al (4043) and Mg (RZ5) joined by CMT was found to contain high concentrations of Al–Mg intermetallics (Al_3Mg_2 and $Al_{12}Mg_{17}$) [12].

The Cold Spray Process

Cold spray is a low temperature thermal spray process that uses primarily kinetic energy rather than thermal energy to form a coating or near net shape deposition on a wide range of substrates. The process can deposit metallic particles or combinations of metallic and non-metallic particles and consolidate them by means of ballistic impingement upon a suitable substrate [13–15]. The particles utilized can be from commercially available powder sources and typically range in size from 5 to 50 μm . The powders are then typically accelerated to from 500 to 1,400 m/s when injected into a high pressure, pre-heated gas stream and accelerated through a converging-diverging De Laval nozzle. The pressurized gas is expanded to supersonic velocities, approximately Mach 3, with an accompanying decrease in pressure and temperature [16–18]. The particles, initially carried by a separate gas stream, are injected into the nozzle either prior to the throat of the nozzle or downstream of the throat. The particles are subsequently accelerated by the main nozzle gas flow and impacted onto a substrate after exiting the nozzle.

Upon impact, the solid particles deform and create a bond with the substrate [19, 20]. The bonds are comprised of both mechanical interlocking, as well as metallurgical bonding by dynamic recrystallization at high shear strain boundaries. As the process continues, particles continue to impact the substrate and form bonds with the consolidated material resulting in a uniform deposit with very little porosity and high bond strength. The term ‘cold spray’ has been used to describe this process due to the relatively low temperatures (100–400 °C) of the expanded gas stream that exits the nozzle, but more importantly because of low rate of heating caused in the material substrate. The temperature of the gas stream is set below the melting point of the particulate material during cold spray, and the resultant consolidated material is formed in the solid state, which yields some unique material properties. The low temperatures associated with the cold spray process are desirable, especially when it comes to joining dissimilar metals that have low melting points, such as aluminum to magnesium, materials which are sensitive to heating and oxygen uptake such as titanium, or when nanostructured powders are used as feedstock. Because the process is occurring at low temperatures and very short durations, the risk of grain growth and phase transformation is minimal or nonexistent, as is the formation of a heat affected zone (HAZ). Additionally, particle oxidation is avoided as are high tensile stresses that occur during thermal contraction from the liquid to solid phase, most often associated with welding techniques. The stresses which do occur are generally low by comparison to traditional welding and are compressive rather than tensile, but nevertheless may not be negligible for very thin substrates or complex stress states. Because of all of these advantages, cold spray has been successfully developed for a broad range of applications. In particular, the US Army Research Laboratory (ARL) has helped to develop this technology for numerous repair solutions to aging and legacy weapon systems across the DoD, with fielded solutions in the Army, Navy, and Air Force [21]. The technology is now at a Technology Readiness Level (TRL) of 9, and is increasing being looked at for repair applications and as a new manufacturing process for cost savings and increased performance in multiple industries.

Importance of Joining Dissimilar Materials

The ability to join dissimilar metals is a significant challenge for many industries, including the automotive and aerospace industries. The need for joining Al, Ti, and Mg is to take advantage of the weight savings and subsequent energy efficiency in the automobile industry and the requirement for chemical plants and cryogenic applications [22]. The automotive industry’s target is to reduce car weight by taking out aluminum and steel components and replacing them with magnesium parts resulting in a weight reduction of 15% by 2020 in order to increase fuel efficiency by 9–12% [23]. Dissimilar welding of aluminum (Al) and magnesium (Mg) alloys would achieve weight reduction and high efficiency of production by allowing the mixed use of both Mg and Al alloys where the best combination of performance,

cost, and weight savings can be achieved. For example, car parts that are being switched out for magnesium parts are shock mounts that are attached to aluminum or steel frame rails and cross members which have been used on an aluminum subframe. Cold spray offers a solution to the joining challenges of these two materials and has been tested and approved for aerospace applications through the US Army Research Laboratory in conjunction with the U.S. Army Aviation and Missile Research Development and Engineering Center (AMRDEC) and Original Equipment Manufacturers (OEM's). In addition to joining dissimilar metals, in the form of conventional sheet, plate or bar stock, there is a need to build-up dissimilar materials in more complex shapes to form tabs, flanges, protrusions or even near-net parts. Cold spray can achieve these additional criteria.

Experimental Procedure

Cold Spray Processing

Prior to cold spray, the surfaces of the ZE41A-T5 magnesium substrates were cleaned using a 60 grit aluminum oxide in an abrasive Port-A-Blast sandblast system (*Lindberg Products Co., Long Beach, CA*) applied by hand, followed by an ethanol solvent rinse. The blast media was sprayed at a pressure of 6.9 bar at a 45-degree angle and a stand-off distance of 100–150 mm from the part. A cold spray layer of 6061 Al was then deposited onto the edge of the magnesium plate to a depth of approximately 1 cm in order to enable it to be joined to the 6061 aluminum plate. The 6061 Al layer was produced using commercially available gas-atomized 6061 Al powder (*Valimet, Stockton, CA*). The specified particle size cut was -325 mesh which corresponds to a maximum particle size of approximately 44 μm and an average of 18 μm measured using a Horiba LA-910 laser diffraction particle size analyzer (*Horiba Scientific, Wyomissing, PA*). A VRC Gen III high pressure cold spray system (*VRC Metal Systems, Rapid City, SD*) was used and helium was chosen as the process gas to achieve high impact velocities between incident particles. The pressure and temperature of helium were maintained at 2.8 MPa and 400 °C, respectively. Deposition took place using a nozzle stand-off distance of 25 mm, 90° deposition angle, medium powder feed rate (12 g min⁻¹), and a high nozzle traveling speed (600 mm s⁻¹). The total deposition thickness of ~ 8.5 mm was achieved in this study. Figure 1 shows several pictures of the samples in preparation and the planned layout for incorporating cold spray and FSW. Figure 1a shows a sample of ZE41A-Mg that has been coated on its edge with a CS layer of 6061 Al. Two additional plates were placed next to the sample to help ensure that the buildup met the required dimensions. A second set of plates was also produced by United Technologies Research Center (UTRC) using the same parameters, but with an enhanced 6-axis path plan performed by an articulated robot, which did not require side plate supports to fully build up on the edge, and

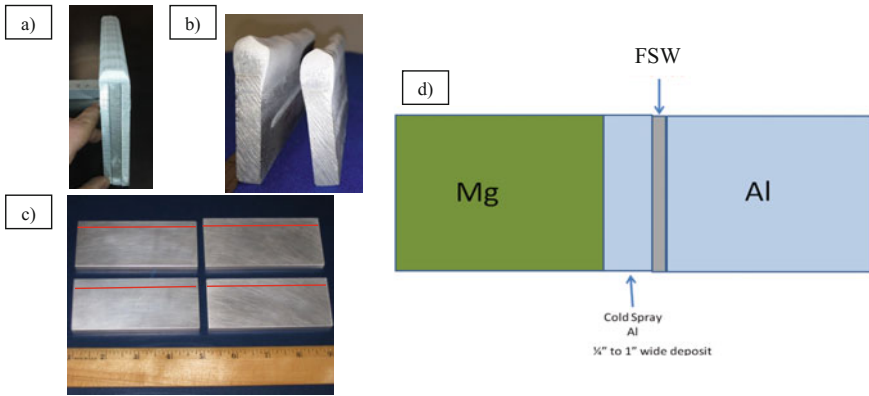


Fig. 1 Shows how the samples were prepared to enable cast ZE41A Mg to be joined to wrought 6061 Al by a combination of the cold spray process and friction-stir welding. **a** Samples of cast ZE41A-Mg coated on one edge with 6061 Al cold spray at SDSM&T, **b** samples produced at UTRC, **c** Finished machined samples of cast ZE41A-Mg coated with 6061 Al cold spray (*Red lines* denote the Al/Mg interface), and **d** the welding schematic

proved to be a superior method for building up the edges (Fig. 1b). The samples were approximately 100 mm long, 50 mm wide and 6.3 mm thick and then final machined flat and parallel to the original magnesium plate surfaces (Fig. 1c). After the cold spray layer was applied, the FSW process was used to join the materials together (Fig. 1d).

Friction Stir Welding

Friction Stir-welding was chosen to join a piece of cast ZE41A Magnesium with a cold sprayed Al 6061 transition joint zone to a plate of wrought 6061 Al, allowing a similar alloy weld to be formed between the two plates. The purpose of the cold spray transitional material was to mitigate the formation of a deleterious inter-metallic layer at the dissimilar metal interface. The 100 mm aluminum 6061 plates were welded to the cold sprayed 6061 pieces of cast ZE41A Magnesium using an MTS Istir 10 friction stir welding system (*PaR Systems, Shoreview, MN*). The process parameters of the tool were 800 RPM, 254 mm/min., 1° Lead Angle and a 3.81 mm/min. plunge rate. The two plates to be joined were initially machined to 6.35 mm thickness. A two-piece adjustable pin tool was used for the welding with a 10.8 mm diameter concave H13 tool steel shoulder, a 10° tapered pin with 3 flats, and a MP159 adjustable pin set to a 3.3 mm pin length. Figure 2 shows the FSW pin tool, set up, and completed joint of the cast ZE41A Mg with 6061 Al cold spray transition joint to wrought 6061 Al.

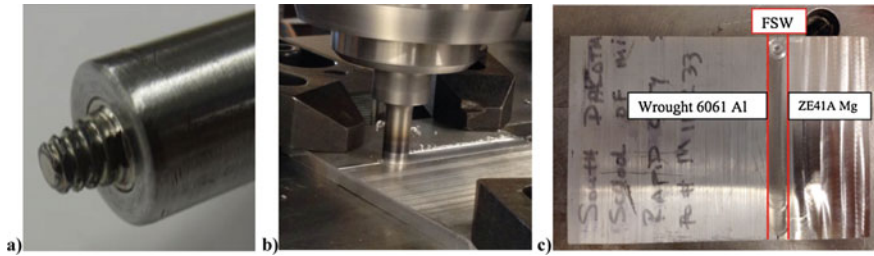


Fig. 2 a FSW tool, b In process FSW and c Completed FSW joining of cast ZE41A Mg with cold spray transition joint to wrought 6061 Al

Microstructural Analysis Procedure

The microstructural features of the samples in the study were evaluated per ASTM E3-11 procedures using optical microscopy and a Zeiss SUPRA 40 scanning electron microscope (*Zeiss, Oberkochen, Germany*) operated at 15 kV. Cross-sections of the samples were taken utilizing a LECO cut-off saw. The samples were sectioned in a way to have the interface in the middle of the samples and then prepared by standard metallographic techniques. 25 mm diameter metallographic samples were mounted in Bakelite and prepared incorporating a series of grinding steps starting at 180 grit and finishing with 2400 grit. Final polishing was accomplished using 3 μm diamond paste followed by 0.25 μm diamond paste and completed using a 0.05 μm colloidal silica suspension, followed by etching with Keller's reagent. Transmission electron micrographs (TEM) were obtained by utilizing a JEM-2100 LaB6 TEM microscope (*JEOL USA, Peabody, MA*) equipped with EDS analysis operating at 200 kV. Thin discs of 3 mm diameter were excised from the deposition/substrate in a way to the interface in the middle of final samples, and then polished, dimpled, and ion milled for 5 h.

Microhardness Testing Procedure

Vicker's microhardness measurements were performed on the CS/FSW samples per ASTM E92. A microhardness traverse (collected from a substrate/coating cross-section) was conducted whereby measurements were obtained with a fixed spacing of 300 μm , traveling across the center of the weldment from the Mg substrate through the CS/Mg substrate interface, to the surface of the CS layer and across the FSW area and into the wrought 6061 Al. The position of the indentation relative to the various regions was measured using optical microscopy in conjunction with image analysis. Vickers hardness testing was performed using a 500 g load.

Mechanical Test Procedures

The Triple Lug Shear Test method was used to study the adhesive shear behavior of the cold spray buttered edge, where 6061 Al was cold sprayed onto ZE41A-T5 magnesium. Triple Lug procedure methodology is prescribed in military specification, MIL-J-24445A. A deposit with a thickness of greater than 0.125 inches is applied onto the ZE41A-T5 magnesium by the cold spray process. Three rectangular-shaped 'lugs' are machined from the 6061 Al cold spray weld. The lugs are then sheared from the test specimen using a compressive load frame set-up. Only one lug is sheared from the specimen at a time. Failure stress is reported based on the load at failure and the surface area of the lug. Control specimens milled from single pieces of cast magnesium were included in the matrix to establish a baseline for comparison. The specimens were tested in shear in a MTS 810 22-kip universal tensile testing machine (*MTS Systems Corporation, Eden Prairie, MN*) under displacement control at constant cross-head speed of 1 mm/min. The applied load was measured continuously with a 25 kN load cell. The force required to shear off the coating and the coating/substrate attachment area allows the calculation of the shear strength of the bond.

Tensile testing was performed per ASTM E-8 procedures using sub-size tensile specimens. A total of 8 tensile bars were cut from actual deposits of CS 6061 Al, in order to test both the strength of the cold spray deposit and its response to heat treatment, 2 samples per condition. Samples were machined to final thickness and then waterjet machined from the sample blocks, followed by sanding with 1200 grit sand paper to remove burrs and any nicks or appreciable surface roughness from the machining process. Results reported are the average of the two samples. Another nine sub-size specimens were machined from within the approximately 100 mm wide FSW to cold spray specimens in order to test the mechanical properties across the joint in the as-welded and as-sprayed condition, 3 from SDSM&T cold sprayed coupons and 6 from UTRC sprayed coupons.

Results

Microstructural Examination of Cold Spray Deposits

As shown in Fig. 3, the cold spray deposit exhibited very low porosity (<0.5%), and in fact appears to be more uniform and defect free than the cast ZE41A-T5 Mg. The interface is highly textured, which both creates a higher degree of interlocking and is evidence of the extreme deformation of the interface taking place with the first layer of cold spray particles. Neither the optical or SEM images revealed any evidence of intermetallic formation. Very close inspection under a TEM microscope, however, revealed two distinct bands at the Al cold spray to Mg alloy interface. The EDS detector was used to analyze the exact composition of these

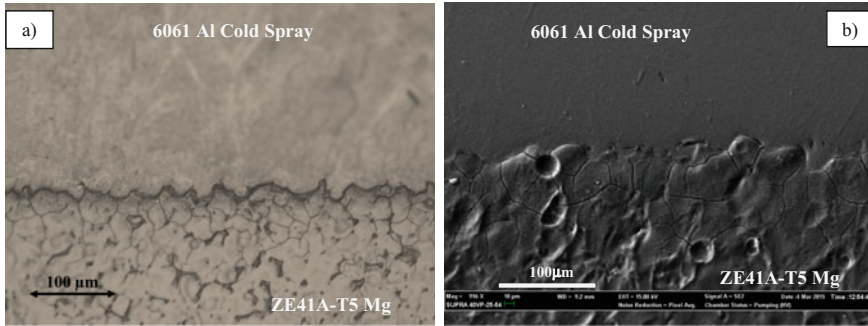


Fig. 3 a Optical image of etched microstructure of Al 6061CS deposited onto ZE41A-T5 Mg and b Scanning electron microscope image of the CS/Mg interface

Table 1 TEM EDS Analysis of Suspected Intermetallic Layer at the CS Interface

Spectrum	Mg	Al	Remaining elements	Total
Al coating	1.59	98.20	0.21	100.00
Region I	39.91	50.66	9.43	100.00
Region II	52.98	32.59	14.42	100.00
Mg substrate	93.63	1.47	4.90	100.00

regions. The results are presented in Table 1. As was expected, region I has more Al with about 40% Mg and region II contains more Mg (~53% Mg). These results are in full agreement with the literature and they represent γ phase (39.23–39.27 at. % Mg) close to the Al deposition, and the β phase (51.97–55.41 at. % Mg) close to the Mg substrate. The total thickness of the intermetallic layer across the visible interface was observed to range from 200 nm to 2 μm , but was typically just over 1 μm thick (Fig. 4).

Microstructural Examination of the FSW Samples

The most significant question for the microstructural investigation was to determine whether or not friction stir welding directly adjacent to the cold spray interface would cause either (1) delamination, or (2) significant growth of an intermetallic layer between the Al 6061 cold spray and the cast ZE41A-T5 Mg. Neither were observed in the samples. Figure 5 shows a cross section of the weld in the as-polished and etched condition respectively as observed optically confirming that there were not any induced failures at the CS/Mg interface or a thickened intermetallic layer. The cold spray material served as the transitional material allowing the two dissimilar metals to be joined without the formation of a deleteriously thick intermetallic zone or other undesirable microstructural features. The welded area



Fig. 4 TEM image at Al 6061 CS to ZE41A-T5 Mg interface, showing two intermetallic regions, Region I (*white arrow*) and Region II (*black arrow*)



Fig. 5 Cross-section in the as-polished and etched condition showing the cast ZE41A Mg with the cold spray 6061 Al transition zone and FSW weld zone transitioning into the wrought 6061 Al (*left to right*)

was free from voids and joint line oxide remnants, showing excellent consolidation. While both alloys in the weld zone were technically the same (6061 Al), the clear differences in microstructure were retained throughout the welding process and remain clearly visible even though they have been thoroughly mixed and reached

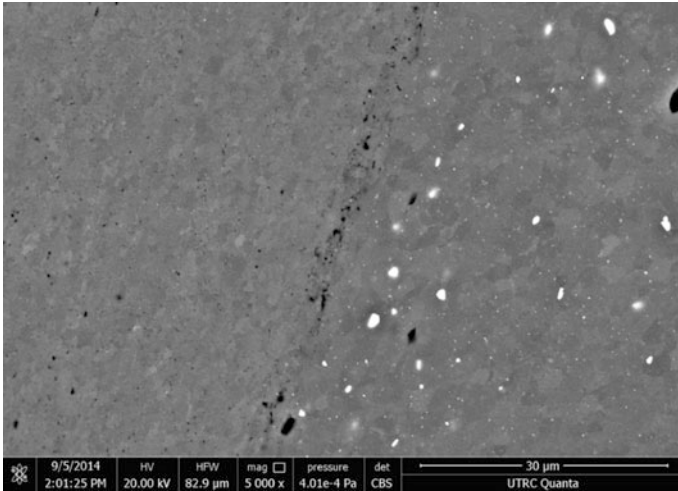


Fig. 6 SEM of the FSW joint within the nugget zone at a banded interface line

near solution temperatures. An SEM image from the nugget region is shown in Fig. 6. The grain refinement is clearly visible across the sample with grain sizes ranging from 1 to 4 μm .

Microhardness Testing

Vicker’s microhardness measurements were performed on the CS/FSW samples. Measurements were taken across the various zones of the weldment, as shown in Fig. 7. The results show the typical hardness plot for friction stir welded materials,

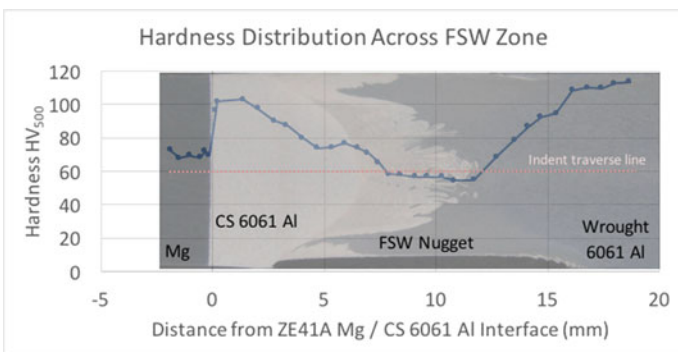


Fig. 7 Microhardness traverse across the Mg substrate and CS/FSW into the 6061 Al

and cover the complete transition from base metal hardness to cold spray and FSW induced hardness gradients. The hardness across the nugget was lower than both that of the cold spray 6061 Al as well as the wrought 6061 Al due to the solutionizing effect on the 6061 alloying elements in the nugget zone, which was expected. Another interesting note, is that a heat affected zone (HAZ) was not observed in the ZE41A Mg base material as a result of the cold spray process or the subsequent FSW process, which was far enough away from the weld zone that it was not softened by it.

Triple Lug Shear Testing

All of the 6061 Al cold spray lugs showed very high adhesion on the magnesium alloys. The average adhesive strength of the 6061 Al cold spray lugs on ZE41A-T5 Mg was about 152 MPa and actually exceeded the average shear strength of the base line ZE41A-T5 Mg samples, which were 117 MPa. The 6061 Al cold spray lugs on the ZE41A-T5 broke off by fracturing material well beneath the Al/Mg interface, as shown in Fig. 8. This substantiates the claim that a structural weld is possible between ZE41A-T5 Mg and Al 6061 utilizing the cold spray process alone, since the failures were occurring in the magnesium substrate and not at the interface. This positive result also confirms that in contrast to conventional joining methods, the Al/Mg interface produced by cold spray, while it does form an intermetallic layer up to 2 μm , it does not produce a deleterious effect at that thickness.

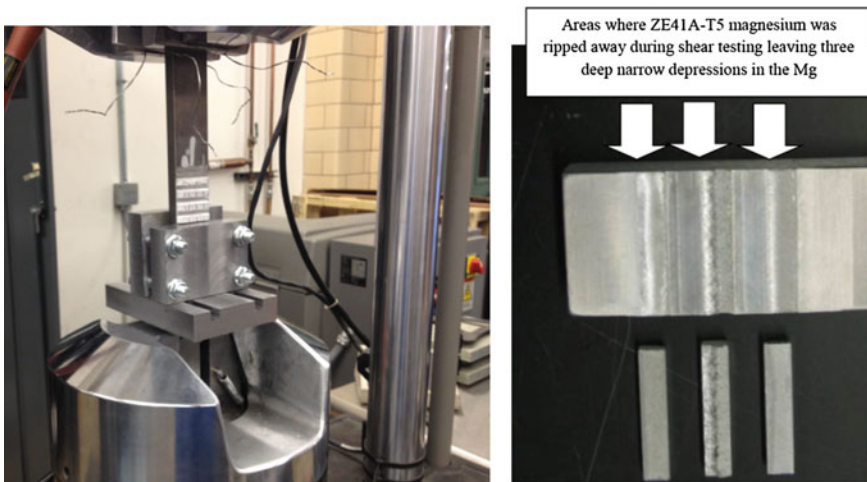


Fig. 8 Triple Lug Shear test setup (*left*), and tested coupon after cold spray, but without FSW (*right*)

Tension Testing

Tensile test samples were extracted from an un-welded block of cold spray deposition of Al 6061 (Fig. 9) to evaluate its tensile strength prior to friction stir welding. Samples extracted from this block were found to have very high tensile strengths, up to 340 MPa, in the as-cold sprayed condition, as shown in Table 2. The Yield Strength (YS) and the Ultimate Tensile Strength (UTS) of the cold spray 6061 Al actually exceeds the properties of wrought 6061-T6 [24]. The primary strengthening mechanism is the work hardening that occurs during particle impact and consolidation in the solid state. The elongation at failure (%EL) is 5%, which actually exceeds that of the ZE41A-T5 Mg and is comparable with other cast magnesium alloys. Additionally, post cold spray heat treatments (HT) were investigated to determine if they would strengthen the deposit or improve its ductility. The samples were subsequently heat treated to a T4 and T6 condition, as well as a full anneal. As heat treatment times and temperatures increased, both the UTS and YS decreased but provided corresponding significant increases in ductility, matching values typical of wrought 6061. Both the as-deposited and post spray heat treated data indicate that there is potential for utilizing cold spray to

Fig. 9 Cold spray deposition block for extracting ASTM E-8 sub-size tensile specimens for properties evaluation of cold spray material strength

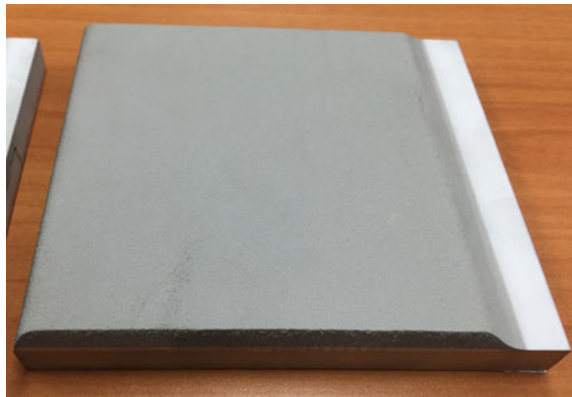
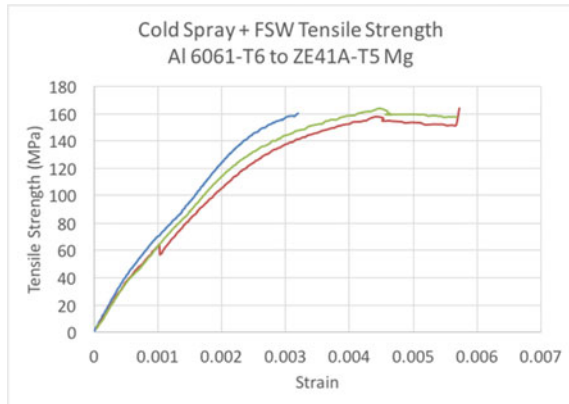


Table 2 Tension test results of cold spray 6061 Al compared to wrought 6061 Al

Material	Source	UTS (MPa)	YS (MPa)	%EL
ZE41A-T5 Mg	AMS4439	205	140	3.5
CS 6061 – As sprayed	[24]	340	293	5
CS 6061 + T6 HT	[24]	290	241	10
CS 6061 + T4 HT	[24]	207	110	18
CS 6061 + annealed HT	[24]	124	55	25
FSW Joint with CS	Figure 10	163 ± 2.0	159 ± 1.3	0.3
FSW Joint with CS	[24]	193 ± 6.4	184 ± 10.9	0.35

Fig. 10 Tension results from FSW of Al 6061 cold spray on ZE41A-T5 Mg specimens



serves as a suitable transition material when joining ZE41A-T5 Mg to 6061-T6 Al by FSW.

When combined with friction stir welding it was possible to test the material perpendicular to the cold spray layer and FSW zone, which tests both the strength of the weld zone and the cold spray bond to the magnesium. In this study, tensile strengths across the weld joint and cold spray interface were found to average 163 MPa, as shown in Fig. 10 and Table 2. These strengths were nearly 100 MPa higher than reported by fusion based processes, such as using the MIG welding process at 64 MPa [25], and about 30% higher than similar materials reported using friction stir welding at 127 MPa [26]. In second set of cold spray samples produced at UTRC and welded at SDSM&T, even higher tensile strengths were observed, up to 193 MPa, based on a total of 6 samples. This was attributed to an improvement in the motion and path planning using a 6-axis robot as opposed to the simpler 3-axis path plan executed at SDSM&T. Failures occurred at the Al 6061 cold spray to ZE41A interface for all samples, except one UTRC sample which actually failed in the weld zone of the FSW joint in the Al 6061 nugget zone and achieved 4.7% elongation with the change in failure mode.

Discussion

A transition joint of aluminum cold sprayed for the purpose of making a dissimilar metal joint to magnesium has been successfully demonstrated. This combination of materials was chosen because of their widespread applicability across several sectors of industry and throughout the U.S. Department of Defense. In this study, a cold spray layer of 6061 Al was deposited onto the edge of cast ZE41A-T5 magnesium plate to form a material transition zone that was later joined to wrought 6061 Al by the FSW process. The purpose of the cold spray transitional material is to mitigate the formation of a deleterious intermetallic layer at the dissimilar metal

interface that commonly forms with most other joining methods. Intermetallics between these two materials unavoidably form in any metallurgical joining process, but when the process is performed rapidly at lower temperatures it can be prevented from growing thick enough to significantly affect mechanical properties, as seen in this study, where an intermetallic layer of less than $2\mu\text{m}$ does not appear to affect the static strength of the joint. It was demonstrated that the cold spray process does not induce any significant intermetallic formation when Al is deposited on Mg, but just as importantly, it was demonstrated that the heat from friction stir welding adjacent to the interface does not cause significant growth of the intermetallic layer. Through this investigation it was shown that if the weld zone is at least as far removed from the cold spray interface as shown here (10 mm in this case) then intermetallic growth can be avoided. It was also shown that the strength of the cold spray to magnesium bond can approach or exceed the strength of the cast ZE41A alloys itself in shear, and it can exceed the joining strength of other methods which produce thicker intermetallic layers. The novel aspect of the concept to join dissimilar materials by the cold spray process included the cold spray material joint design, which is the key element to enable the joining of dissimilar materials that, prior to this work, had never been achieved with any degree of structural integrity because of numerous limitations, of which the primary, is the high thermal input associated with conventional welding techniques and the subsequent formation of deleterious intermetallics. Additionally, other factors that prohibit the use of conventional welding techniques include; the formation of tensile residual stresses due to the contraction of a weld melt pool and restrictions on the types of materials that can be joined because of chemical incompatibility. Shear strength testing of the 6061 Al cold spray transitional material deposited onto the ZE41A Mg showed that the interface could be stronger than the Mg in some loading scenarios. Further analysis of the strength of the cold spray 6061 Al transitional material revealed that it had a greater ultimate tensile strength and ductility than the ZE41A Mg to which it was deposited onto.

Conclusions

This work represents a novel way of joining dissimilar alloys such as magnesium and aluminum while maintaining very high joint strengths. It also demonstrates how complex solutions can be created using multiple materials processing technologies to provide a robust solution. The principle conclusions of this work are as follows:

- The results of this work represent a viable and high strength method to join dissimilar materials, specifically, wrought 6061 Al alloy to cast ZE41A Mg, by a combination of the high pressure cold spray process (CS) and friction-stir welding (FSW).

- Materials characterization and analysis of results showed conclusively that high pressure cold spray can be used to join aerospace and automotive alloys of Mg and Al. The CS joint had higher shear strength than the base Mg and exceptional tensile and hardness properties.
- No heat affected zone formed in the AZ41A Mg material due to cold spray or the remote FSW joint.
- Cold spray can be used to deposit material of exceptionally high tensile strengths with some ductility, or through modest heat treatment cycles can greatly enhance the ductility, if some tensile strength can be sacrificed.

References

1. Zhao LM, Zhang ZD (2008) Effect of Zn alloy interlayer on interface microstructure and strength of diffusion-bonded Mg-Al joints. *Scripta Mater* 58:283–286
2. Peng L, Yajiang L, Haoran G, Juan W (2005) A study of phase constitution near the interface of Mg/Al vacuum diffusion bonding. *Mater Lett* 59(16):2001–2005
3. Kostka A, Coelho RS, Dos Santos J, Pyzalla AR (2009) Microstructure of friction stir welding of aluminium alloy to magnesium alloy. *Scripta Mater* 60(11):953–956
4. Ben-Artzy A, Sternb A, Frage N, Shribman V, Sadot O (2010) Wave formation mechanism in magnetic pulse welding. *Int J Impact Eng* 37:397–404
5. Liu Liming, Hongyang Wang (2011) Microstructure and properties analysis of laser welding and laser weld bonding Mg to Al joints. *Metall Mater Trans A* 42(4):1044–1050
6. Borrisutthekul R, Miyashita Y, Mutoh Y (2005) Dissimilar material laser welding between magnesium alloy AZ31B and aluminum alloy A5052-O. *Sci Technol Adv Mater* 6:199–204
7. Peng Liu, Yajiang Li, Haoran Geng, Juan Wang (2007) Microstructure characteristics in TIG welded joint of Mg/Al dissimilar materials. *Mater Lett* 61:1288–1291
8. Ben-Artzy A, Munitz A, Kohn G, Bronfin B, Shtechman A (2002) Joining of light hybrid constructions made of magnesium and aluminum alloys. *Magnes Technol* 295–302
9. Tomiharu O (2004) Resistance welding of aluminum alloy to dissimilar metals. *J Light Metal Weld Constr* 42:2–15
10. Shang J et al (2012) Microstructure characteristics and mechanical properties of cold metal transfer welding Mg/Al dissimilar metals. *Mater Des* 34:559–565
11. Somasekharan AC, Murr LE (2004) Microstructures in friction-stir welded dissimilar Mg Alloys and Mg alloys to 6061-T6 aluminum alloy. *Mater Charact* 52:49–64
12. Tomaa C, Cicalaa E, Sallamandb P, Greveyb D (2012) CMT Joining of aluminum magnesium alloys in a statistical experiment. In: *Metal 2012, 21st international conference on metallurgy and materials*, 23–25 May, Hotel Voronez I, Brno, Czech Republic, EU
13. Papyrin A (2001) Cold spray technology. *Adv Mater Process* 49
14. Van Steenkiste TH (1999) Kinetic spray coatings. *Surf Coat Technol* 111:62
15. Rokni MR, Widener CA, Champagne VK (2014) Microstructural evolution of 6061 aluminum gas-atomized powder and high-pressure cold-sprayed deposition. *J Therm Spray Technol* 23(3):514–524
16. Dykhuisen R, Smith M (1998) Gas dynamic principles of cold spray. *J Therm Spray Technol* 7(2):205
17. Kosarev VF, Klinkov SV, Alkhimov AP, Papyrin AN (2003) On some aspects of gas dynamic principles of cold spray process. *J Therm Spray Technol* 12(2):265
18. Grujicic M, Zhao CL, Tong C, DeRosset WS, Helfrich D (2004) Analysis of the impact velocity of powder particles in the cold-gas dynamic-spray process. *Mater Sci Eng A* 368:222

19. Dykhuizen RC, Smith MF, Gilmore DL, Neiser RA, Jiang X, Sampath S (1999) Impact of high velocity cold spray particles. *J Therm Spray Technol* 8(4):559
20. Grujicic M, Saylor JR, Beasley DE, Derosset WS, Helfritch D (2003) Computational analysis of the interfacial bonding between feed-powder particles and the substrate in the cold-gas dynamic-spray process. *Appl Surf Sci* 219:211
21. Champagne V (ed) (2007) *The cold spray materials deposition process: fundamentals and applications*. Woodhead Publishing Limited, Abington Hall, Abington, Cambridge CB21 6AH, England, p 57
22. Walsh Michael P (2000) Motor vehicle pollution control. *Platin Met Rev* 44(1):22–29
23. Gould J. Automakers look to solid state welding of dissimilar metals. *Fastening/Joining/Assembly Supplement*, 09.13.04
24. Nardi A. Cold spray test report, United Technologies Research Center, (UTRC), East Hartford, CT
25. Zhang HT, Song JQ (2011) Microstructural evolution of aluminum/magnesium lap joints welded using MIG process with zinc foil as an interlayer. *Mater Lett* 65(21):3292–3294
26. Venkateswaran P, Reynolds AP (2012) Factors affecting the properties of friction stir welds between aluminum and magnesium alloys. *Mater Sci Eng A* 545:26–37

Refill Friction Stir Spot Joining for Aerospace Aluminum Alloys

**Enkhsaikhan Boldsaikhan, Shintaro Fukada, Mitsuo Fujimoto,
Kenichi Kamimuki, Hideki Okada, Brent Duncan, Phuonghanh Bui,
Michael Yeshiambel, Brian Brown and Alan Handyside**

Abstract Refill Friction Stir Spot Joining (RFSJ) developed by Kawasaki Heavy Industries (KHI) is a derivative technology of friction stir spot welding for joining aerospace aluminum alloys. The aerospace aluminum alloys were previously considered not weldable using conventional fusion welding methods. RFSJ does not consume any filler materials so that no additional weight is introduced to the assembly. As the solid-to-liquid phase transition is not involved in RFSJ in general, there is no lack of fusion or material deterioration caused by liquefaction and solidification. Unlike the conventional friction stir spot welding, RFSJ produces a spot joint with a perfectly flush surface finish without a key/exit hole. KHI has advanced the original friction stir spot welding concept and developed a robotic system that is capable of producing refill friction stir spot joints. The goal of this study is to demonstrate process parameter optimization of RFSJ for baseline aerospace aluminum alloys.

Keywords Refill friction stir spot joining · Aerospace aluminum alloys · Robotic spot welding

Introduction

Refill Friction Stir Spot Joining (RFSJ) is a variant of Friction Stir Spot Welding (FSSW), which has been developed by Kawasaki Heavy Industries (KHI) [1, 2]. It produces lap joints between sheet metals, preferably aluminum alloys, without using a filler or foreign material. As the solid-to-liquid phase transition is not

E. Boldsaikhan (✉) · B. Duncan · P. Bui · M. Yeshiambel · B. Brown · A. Handyside
Wichita State University, Wichita, USA
e-mail: enkhsaikhan.boldsaikhan@wichita.edu

S. Fukada · M. Fujimoto
Corporate Technology Division, Kawasaki Heavy Industries, Tokyo, Japan

K. Kamimuki · H. Okada
Aerospace Division, Kawasaki Heavy Industries, Tokyo, Japan

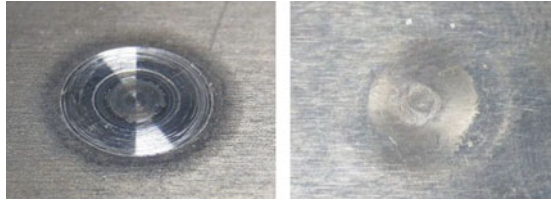


Fig. 1 Perspective views of top, *left image*, and bottom, *right image*, of refill spot joint in its as-welded condition

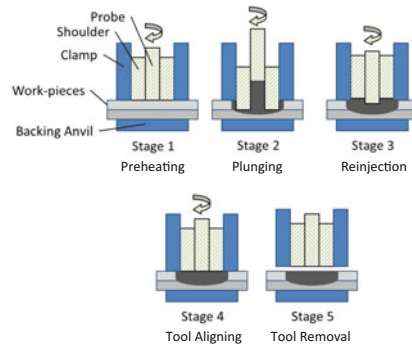


Fig. 2 Robot with RFSJ end effector, *left*, and the RFSJ process stages, *right*

involved in RFSJ in general, there is no lack of fusion or material deterioration caused by liquefaction and solidification. KHI has advanced the basic FSSW technology to produce spot welds with a perfectly flush surface finish without an exit or key hole in the work-piece (Fig. 1). A similar refill FSSW technique was developed by GKSS-GmbH [3].

The Kawasaki RFSJ system implemented in this study is shown in Fig. 2. It uses a wear-resistant weld tool with a retractable probe and a shoulder that are contained inside a cylindrical clamp (Fig. 2). The probe and shoulder components move in the reverse directions to capture and re-inject the plasticized material displaced by the plunging part of the tool. During the welding process, the rotating weld tool plunges into the work-piece and causes mechanical friction and deformation within the stir zone. The mechanical friction and deformation produce heat in the stir zone so that the stir-zone metal becomes softer and more plastic to stir. The work-pieces are securely gripped between the stationary clamp tip and the backing anvil during the welding process. The entire process time from tool touch down to tool removal takes about 2–3 s. RFSJ developed by KHI consists of 5 stages as illustrated in Fig. 2.

Stage 1: The first stage involves work-piece clamping and preheating. The work-pieces are firmly clamped between the backing anvil and the clamp tip before

the rotating tool touches down the work-piece surface. Then, the rotating weld tool touches down and resides on top of the work-piece surface for a certain period of time to frictionally preheat the material.

Stage 2: In the second stage, either of the shoulder-plunging process or the probe-plunging process can be held. During the shoulder-plunging process, the shoulder plunges into the work-piece and the probe retracts and opens up a cavity to accommodate the material displaced by the shoulder. The probe-plunging process is the other way around. When the probe plunges into the work-piece, the shoulder retracts and opens up a cavity to accommodate the material displaced by the probe. In each of these two cases, when the targeted plunge depth is approached, the weld tool may dwell in that position for a certain period of time. Note that the shoulder-plunging process requires a higher plunge force. However, the shoulder-plunging process stirs more volume of material and can produce stronger joints [2]. In this study, the shoulder-plunging process was employed in Stage 2.

Stage 3: In the third stage, the rotating probe and the shoulder move in the reverse directions and re-inject the captured material back into the stir zone. Furthermore, to improve the flushness of the surface, the probe and the shoulder may keep moving in the reverse directions until they slightly exceed their aligned position [2].

Stage 4: In the fourth stage, the probe and the shoulder are aligned with each other right on top of the work-piece surface to establish the final flush surface finish.

Stage 5: In the fifth stage, the weld tool and the clamp are removed from the work-piece.

The goal of this study is to demonstrate an RFSJ-process development method for aerospace aluminum alloys using the Design-of-Experiments approach. The presented results include mechanical and metallurgical properties of refill spot joints along with statistical analysis and discussion.

Experimental Condition

No industry specification was used for the mechanical tests performed in this study. The material combination consists of 1.27-mm-thick (0.050 in.) AA7075-T6 as the top sheet and 1.6-mm-thick (0.063 in.) AA2024-T3 as the bottom sheet. They are high strength aluminum alloys mostly used for making metallic structures of aircraft. AA7075-T6 is used for making stiffeners and AA2024-T3 is used for making aircraft skins. Only the bare aluminum alloys were employed in this study. The mechanical properties of the alloys are presented in Table 1.

The probe, the shoulder, and the clamp tip of the RFSJ tool had diameters of 3.25, 6, and 16 mm, respectively. The RFSJ process took place on the top sheet side, which is AA7075-T6. The shoulder-plunging method was employed in the refill spot joints.

The design of experiments (DoE) was a 3^2 full factorial design that is presented in Table 2. The factors of DoE were the plunge depth and the spindle speed of the

Table 1 Nominal mechanical properties of AA7075-T6 and AA2024-T3

	AA7075-T6	AA2024-T3
Hardness value, vickers	175	137
Ultimate tensile strength	572 MPa	483 MPa
Tensile yield strength	503 MPa	345 MPa
Elongation, diameter 12.7 mm (0.5 in.)	11%	18%

Table 2 DoE runs

Run	Plunge depth, mm	Spindle speed, rpm
1	1.27	1200
2	1.27	1500
3	1.27	1800
4	1.47	1200
5	1.47	1500
6	1.47	1800
7	1.67	1200
8	1.67	1500
9	1.67	1800

RFSJ tool. Two response variables were identified for the DoE analysis. They were the ultimate shear load and the ultimate tension load. To characterize the response variables, each DoE run produced a straight lap-shear coupon and a cross-tension coupon. The coupon configurations are shown in Fig. 3. The ultimate shear load was identified through the unguided static lap-shear test shown in Fig. 4. The pull rate of the static lap-shear test was 1.27 mm/min (0.05 in./min). The ultimate tension load was identified through the static cross-tension test shown in Fig. 5. The pull rate of the static cross-tension test was 12.7 mm/min (0.5 in./min). The DoE results were analyzed using the Statgraphics[®] software.

During the unguided lap-shear testing, the lap-shear coupons were deformed as illustrated in Fig. 4. The coupon deformation was caused by the asymmetric pull loads exerted in the lap-shear directions of the joint. The deformation and the asymmetric pull loads induced the minor tension loads and the major shear loads on the joint.

During the cross-tension testing, the pull loads were exerted in the perpendicular directions of the faying surface to split the top and bottom sheets as shown in Fig. 5. Those pull loads caused intense deformation in the cross coupon and induced tension and shear loads on the lap joint.

The ultimate loads were measured in the pull load direction in either of the two aforementioned static tests. The tension and shear loads on the joint contributed to the formation of different joint failures.

Generally, a refill spot joint may exhibit one or a combination of the following mechanical failures.

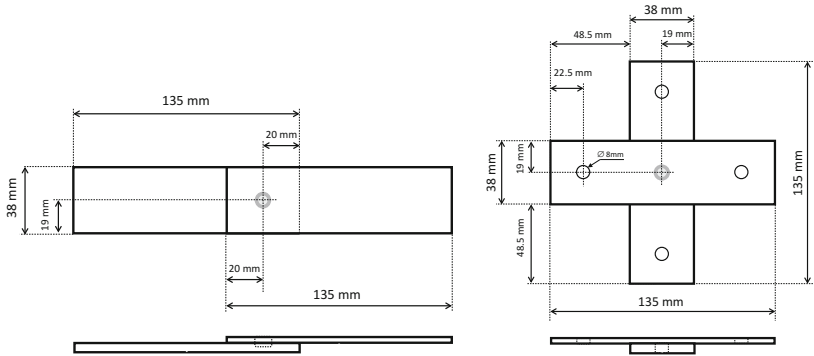


Fig. 3 Straight lap-shear coupon configuration, left, and cross-tension coupon configuration, right

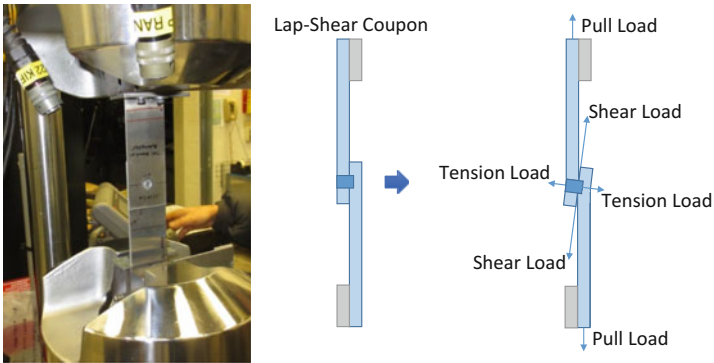
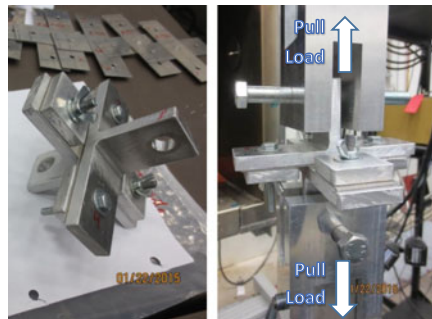


Fig. 4 Static lap-shear test setup, left, and the coupon deformation caused by the asymmetric pull loads, right

Fig. 5 Cross tension test setup



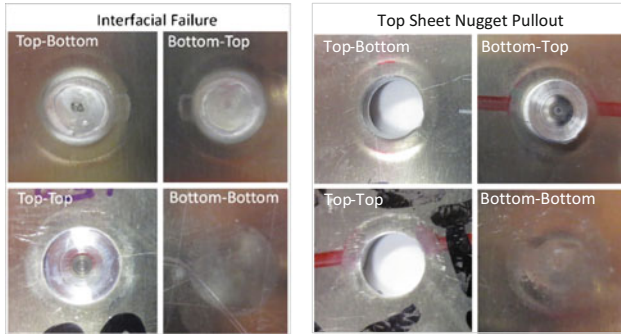


Fig. 6 Interfacial failure, *left*, and *top* sheet nugget pullout failure, *right*. In each figure, the first column shows the *top* sheet surfaces and the second column shows the *bottom* sheet surfaces

- **Interfacial Failure (IF):** The Interfacial Failure (IF) is a failure that the refill spot joint breaks right through the interface between the top and bottom sheets. In some literatures, IF is also called a shear failure. Usually, an insufficient plunge depth induces a smaller and weaker joint that exhibits IF. However, a sufficient plunge depth may also produce IF when the parent metal thicknesses are relatively larger than the joint size. The images of IF are in Fig. 6. Note that RFSJ is performed on the top sheet side.
- **Top Sheet Nugget Pullout (TSNP) and Bottom Sheet Nugget Pullout (BSNP):** The Top Sheet Nugget Pullout (TSNP) is a failure that the weld nugget is pulled out of the top sheet (Fig. 6). Likewise, if the weld nugget is pulled out of the bottom sheet, it is called the Bottom Sheet Nugget Pullout (BSNP). Usually, the TSNP and BSNP failures are observed around the weld nugget. Note that the weld nugget is the main stir zone, where the plastic deformation is heavily involved during RFSJ.

Results and Discussion

A 3^2 full factorial design (3 levels and 2 factors) was implemented in this study. The plunge depth and the spindle speed were the DoE factors of the experiments. The DoE response variables were characterized by unguided lap-shear tests and guided cross-tension tests. 2nd-order models were fitted to estimate the response surfaces for the ultimate shear load and the ultimate tension load. The Analysis of Variance (ANOVA) was performed on the DoE results using the Statgraphics[®] software. The R-squared statistic of ANOVA for the ultimate shear load was 80% and the estimated standard error (standard deviation) was 314.506 N. The R-squared statistic of ANOVA for the ultimate tension load was 90% and the estimated standard error (standard deviation) was 173.563 N. Note that the R-Squared statistic indicates that

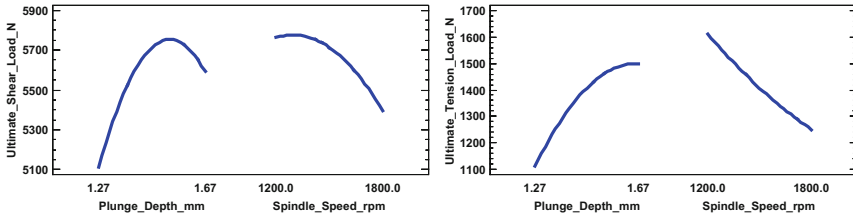


Fig. 7 Main effects plots for the ultimate shear load, *left*, and the ultimate tension load, *right*

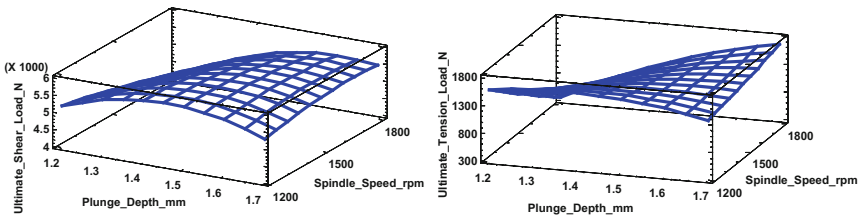


Fig. 8 Estimated response surfaces for the ultimate shear load, *left*, and the ultimate tension load, *right*

the model as fitted explains the percentage of the variability in the response variable. For instance, the R-squared statistic of 100% means the response surface model perfectly fits the observed data points.

The main effects plots and the response surfaces are presented in Figs. 7 and 8. The plunge depth had strong positive effects on the ultimate shear load and the ultimate tension load, which means deeper plunge depths produced stronger joints. However, deeper plunge depths may require relatively high process forces depending on tool-material combinations. So, some deeper plunge depths cannot be achieved for certain tool-material combinations because of the rated payload capacity of the RFSJ system.

The spindle speed had noticeable negative effects on the ultimate shear and tension loads. In other words, lower spindle speeds produced higher ultimate loads. This is intuitive as a higher spindle speed of the RFSJ tool may introduce an excess heat input to the work-piece and may degrade microstructural and mechanical properties of the joint. So, lower spindle speeds were preferred. However, too low spindle speeds may not be able to produce the required heat input to plasticize and soften the work-piece material. This lack of heat input may lead to volumetric defects in the joint or, in the worst case, failures in the RFSJ tool.

Only IF and/or TSNP were exhibited by the straight/cross single-spot coupons of the DoE runs. Based on the observations, IF was associated with shallower plunge depths and higher spindle speeds of the weld tool. TSNP was associated with deeper plunge depths and lower spindle speeds of the weld tool. Therefore, it is assumed that stronger welds exhibit TSNP and weaker welds exhibit IF according

Fig. 9 Failure modes and ultimate loads of DoE coupons

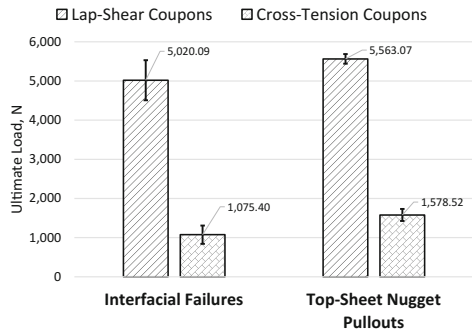
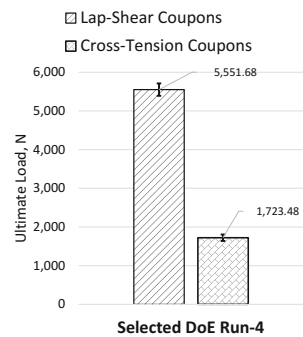


Fig. 10 Selected DoE-run coupons



to the main effects plots shown in Fig. 7. In fact, this assumption is in a good agreement with the Fig. 9 data estimated from the DoE test results.

After the process development experiments, DoE Run-4 in Table 2 was selected for further mechanical and metallurgical evaluations. This selection was based on the response surface analysis, the refill joint appearances, and the weld tool performances. Further evaluations for the selected DoE run included static lap-shear and cross-tension tests, cross-sectional metallography, and micro-hardness tests.

Three straight coupons and three cross coupons were produced using the DoE-Run-4 parameters and tested. Their static test results are presented in Fig. 10. All of the coupons consistently exhibited TSNP. The average ultimate shear load of the lap-shear coupons was 5,551.68 N and the average ultimate tension load of the cross coupons was 1723.48 N.

A cross-sectional specimen shown in Fig. 11 was generated from a lap-shear coupon of the selected DoE run to inspect a cross-section of the entire weld nugget and the material flow pattern. As the parent metals are dissimilar, the intermixing flow pattern can be easily seen in the weld nugget cross-section. In Fig. 11, the top sheet with a lighter color is AA7075-T6 and the bottom sheet with a darker color is AA2024-T3. RFSJ took place on the top sheet side. The weld nugget is about 6 mm wide, which is the diameter of the weld tool. The tool plunge depth was 1.47 mm. The weld cross-section in Fig. 11 indicates that the bond between the top and

Fig. 11 Cross-section of selected DoE-Run-4 weld

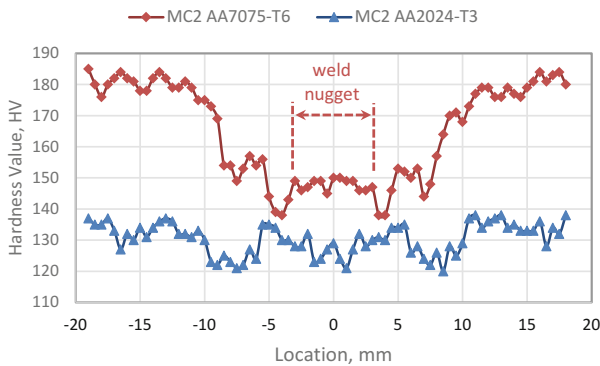
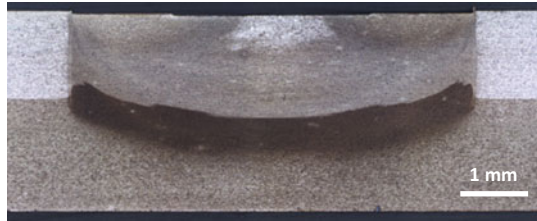


Fig. 12 Microhardness map of refill spot joint produced by the selected DoE run. The hardness measurements were taken from the mid-plane lines of the *top* and *bottom* sheets. The weld nugget is about 6 mm wide. The weld center is at the origin

bottom sheets was fully consolidated and free from porosity or volumetric defects. Also, the top and bottom surfaces appear flawlessly flat.

The Vickers microhardness test was performed on the cross-sectional specimen using a diamond indenter along with a 0.5 kg load. The hardness measurements were taken from the mid-plane lines of the top sheet and the bottom sheet of the weld cross-section. The spacing between two adjacent indents was 0.5 mm. The hardness map is presented in Fig. 12. The average hardness values (HV) of the top-sheet weld nugget was about 148 HV. In Fig. 12, the top-sheet heat-affected zone extends up to ± 15 mm from the weld center based on the gradients in the hardness values. Because of the Hall-Petch relationship [4], the hardness values right outside the weld nugget are lower than the hardness values of the weld nugget. In addition, two localized HV bumps were noticed in the top-sheet heat-affected zone in the vicinity of ± 6 mm. Perhaps these HV bumps were caused by the stationary clamp tip as their locations were right below the clamp tip so that the clamp tip might have absorbed some heat during the welding process and accelerated the cooling rate in those locations. Note that the top and bottom surface areas of the specimen were exposed to the air during the welding process except the areas

gripped between the weld tool and the backing anvil. On the other hand, the hardness values of the bottom sheet were barely affected by the welding process. In the future, thorough microhardness measurements should be carried out for the entire weld nugget and the heat-affected zone of refill spot joints.

Summary

A 3^2 full factorial design was implemented in the DoE experiments. The plunge depth and the spindle speed were the DoE factors of the experiments. The DoE response variables were characterized by unguided lap-shear tests and guided cross-tension tests. The plunge depth had strong positive effects on the ultimate shear load and the ultimate tension load, which means deeper plunge depths produced stronger joints. The spindle speed had noticeable negative effects on the ultimate shear and tension loads. In other words, lower spindle speeds produced higher ultimate loads. Also, stronger welds mostly exhibited TSNP and weaker welds exclusively exhibited IF. The refill spot joints produced by the selected/optimized DoE run were fully consolidated and free from porosity or volumetric defects. The microhardness measurements revealed only partial hardness patterns of the refill spot joint so that further measurements will be necessary for the entire weld nugget and the heat-affected zone of refill spot joints.

Acknowledgements The funding support was provided by Kawasaki Heavy Industries, Ltd, through Center for Friction Stir Processing (CFSP).

References

1. Okada H, Kamimuki K, Fujimoto M (2013) Application study of refill FSSW for aerospace industry. In: Proceedings of friction stir welding and processing symposium VII, TMS
2. Okada H, Kamimuki K, Fujimoto M (2013) Assembly study of refill FSSW. SAE Int J Aerosp 6(1):299–304. doi:[10.4271/2013-01-2310](https://doi.org/10.4271/2013-01-2310)
3. Schilling C, dos Santos J (2002) Patent No. US 6722556 B2
4. Jata KV, Semiatin SL (2000) Continuous dynamic recrystallization during friction stir welding of high strength aluminum alloys. Scripta Mater 43:743–749

Part VII
Control and Simulation

Depth and Temperature Control During Friction Stir Welding of 5 cm Thick Copper Canisters

Lars Cederqvist, Olof Garpinger and Isak Nielsen

Abstract Depth control is needed to repeatedly produce welds with minimum flash formation and hook defect, which disturb the temperature control and reduce the corrosion barrier, respectively. The need for depth control is mainly caused by different manufacturing techniques and heat treatments of the lids and tubes that lead to varying properties. The depth is measured using four different sensors; a laser sensor, two linear variable differential transformers (LVDT), and an axial position sensor. The actual depth is estimated from measurements of the shoulder footprint, and can then be compared with the depth sensors. The depth controller uses the axial force to manipulate the shoulder depth during the first two weld sequences. Thirteen welds were carried out in three different lids/rings (twelve short and one full circumferential) with an active depth controller. The laser sensor was used as feedback signal to the controller, and the desired shoulder depth was set to 2.2 mm. For comparison, eighteen short welds (also in three different lids/rings) were performed without any depth control. For the thirteen welds with active depth control, the shoulder depth measured by the laser sensor varied between 2.19 and 2.40 mm (0.21 mm span) at a point two degrees into the joint line, i.e. with a maximum control error of 0.20 mm. The shoulder footprint depth ranged between 2.52–2.86 mm (0.34 mm span). For the eighteen uncontrolled welds, the laser varied between 1.74 and 2.49 mm (0.75 mm span). The corresponding span for the footprint depth was 0.60 mm. Furthermore, macro samples from the thirteen depth controlled welds showed no signs of hook defect nor of joint line remains. The flash formations from the same welds were also small (0–1 mm). It was concluded that

L. Cederqvist (✉)
SKB, Oskarshamn, Sweden
e-mail: lars.cederqvist@skb.se

O. Garpinger
Alten Sverige AB, Lund, Sweden

I. Nielsen
IAN Control AB, Linköping, Sweden

the LVDT sensor placed in the lid is best suited for feedback to the depth controller, partly because it is best at modelling the shoulder footprint depth out of the four depth sensors, but also since it does not suffer from extensive measurement noise like the laser sensor.

Keywords Friction stir welding • Copper • Automatic control

Background

The Swedish Nuclear Fuel and Waste Management Company (SKB) will join at least 12,000 lids and bottoms to the extruded 5 cm thick copper tubes containing Sweden's nuclear waste using FSW. Similarly, Posiva Oy will also use FSW to seal its copper tubes containing Finland's nuclear waste. Unlike most FSW applications where straight welds are made on flat plates, the welding procedure to seal copper canisters requires variable power input throughout the weld cycle to keep the probe temperature within the process window. This is due to variable thermal boundary conditions throughout the different sequences in the weld cycle (see Fig. 1).

By using a cascaded loop that determines the power requirement, the controller will not be dependent on repeatability in the power, and the lagtime in the temperature will not be critical. Due to fast-changing thermal boundary conditions, a feedforward of power was designed to further improve controller performance. The cascade controller result in a probe temperature within ± 5 °C of the desired value (845 °C) during full circumferential welds compared with a process window of 60 °C [1].

In addition to the cascade temperature control, the depth also needs to be controlled mainly because different manufacturing techniques and heat treatments of the lids and tubes leads to varying properties and hence, varying depth.

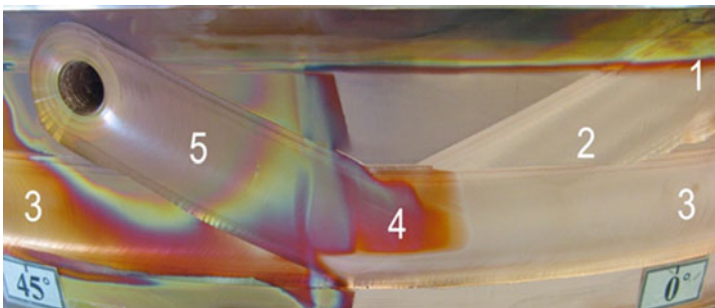


Fig. 1 Sequences in a weld cycle: 1. Start, 2. Downward, 3. Joint line, 4. Overlap, 5. Parking

Depth Control

In this article, the depth will be defined as the extent to which the convex shoulder penetrates the copper surface, and called the shoulder depth. It should be noted that the convex part of the shoulder used has a depth of 3 mm. By adding the probe length to the shoulder depth, one can calculate the total depth of the tool penetration. Currently a probe length of 51 mm is standard (tested in an earlier study to be optimal to minimize the hook defect or remain) but most probes are usually used in more than one weld, and experience have shown that the probe length will decrease with approximately 0.1–0.3 mm/weld (for short welds).

There are two important factors associated with the depth, which makes it important to control throughout the weld:

1. To maximize the corrosion barrier by minimizing the hook defect or remaining joint line.
2. To avoid large torque disturbances caused by flash formation at the overlap sequence.

An ideal weld has little to no flash (see Fig. 1), and the probe tip just barely reaches the vertical joint line (see Fig. 2a). If a weld is too shallow, it results in a joint line remain (see Fig. 2b), which decreases the corrosion barrier. Deep welds, on the other hand, lead to extensive flash (see Fig. 3) and leave a hook defect (see Fig. 2c), which also decrease the corrosion barrier. Flash during the downward sequence typically leads to a quick torque decrease (disturbance) at the overlap sequence. Such a disturbance usually reduces the measured shoulder temperatures, but not the controlled probe temperature. Since the temperature controller reacts to the torque disturbance, by increasing the tool rotation rate, this results in a probe temperature increase of roughly 5–10 °C. It is thus desired to get as little flash formation as possible during the downward sequence and the beginning of the joint line sequence.

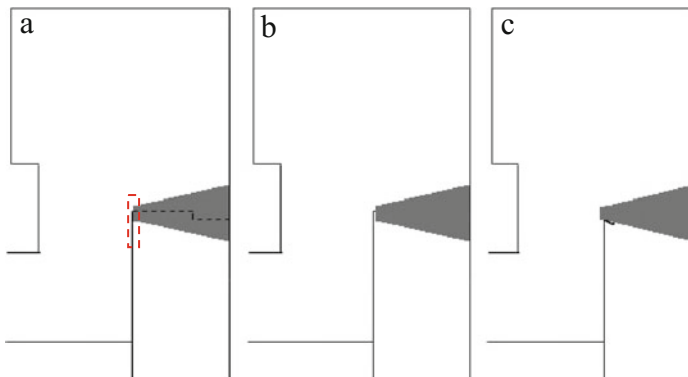


Fig. 2 **a** Ideal weld where the probe tip just reaches the *vertical* joint line. **b** Shallow weld that leaves a remain of the (*horizontal*) joint line. **c** Deep weld that leads to hook defect

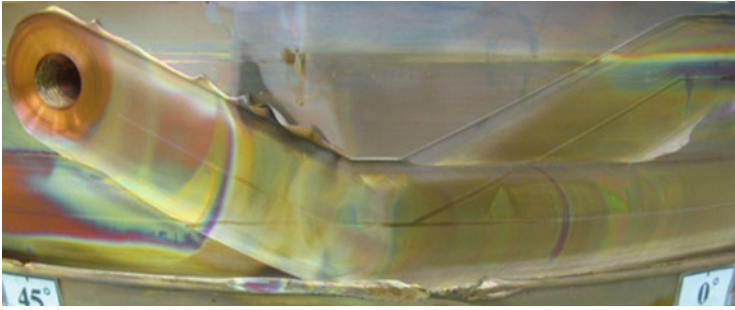


Fig. 3 Weld with extensive flash during joint line and parking sequences

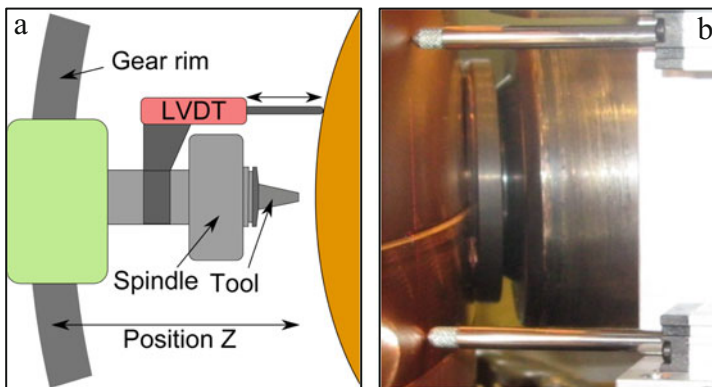


Fig. 4 **a** overview of the depth sensor configuration. **b** the two LVDT sensors and the laser beam during the joint line sequence

Depth Sensors

There are currently four depth sensors attached to the FSW machine:

1. Z-axis position sensor
2. Laser sensor
3. Two linear variable differential transformer (LVDT) sensors.

The z-axis sensor measures the position of the tool in relation to the gear rim that the z-axis is attached to, see Fig. 4a. This is the most commonly used measure of FSW depth, but it also comes with a number of shortcomings, especially for canister sealing; canister eccentricity, z-axis deflection, thermal expansion of canister and variations in the gear rim shape. These different sources of misinformation in the z-axis signal make it very difficult to use for depth control purposes [3]. For this reason, three other depth sensors were installed in early 2015.

A laser sensor is mounted 13.1° ahead of the tool (in the x-direction) and at the same vertical height (y-direction) as the tool. It measures the distance to the copper using several beams and averaging is used to derive the actual value. The laser signal is calibrated against the z-axis position signal, before the tool has touched the canister. The main drawbacks with the laser sensor are that it partly captures the joint between the lid and the tube and sometimes have an increased magnitude of its measurement noise.

Two LVDT sensors (LVDT1 and LVDT2) are mounted 13.1° ahead of the tool (in the x-direction), see Fig. 4b. LVDT1 is positioned 32.5 mm above the tool centre (in the y-direction), and LVDT2 32.5 mm below the tool centre. LVDT1 thus measures depth with respect to the lid during the whole weld. LVDT2, on the other hand, measures depth with respect to the tube during the joint line sequence, and with respect to the lid for the rest of the weld. Both LVDT-signals are calibrated against the z-axis signal, before the tool has touched the canister.

The laser and LVDT sensors lack several of the disadvantages associated with the z-axis sensor. They are, however, still sensitive to the difference in thermal expansion to the tool position, since they cannot be placed directly at the tool. This difference is currently neglected, assuming repeatability between welds, and future work will show whether or not this is a valid assumption.

Depth Measurements

It is difficult to measure the actual depth, even if the canister is cut up into macro samples (presented in the Results chapter). The weld nugget is larger than the probe, and its size also depends on the welding temperature (although this might be negligible since the welds are temperature controlled).

An easier way to estimate the depth is by measuring the shoulder footprint. The convex shoulder geometry is known, so the shoulder depth can be calculated from measurements of the shoulder footprint width. It is the best estimation of the true shoulder depth currently available and will thus be used for comparison with the different sensors, to evaluate their practical use as feedback signals in the depth controller. The shoulder footprints were measured two degrees (18 mm) into the joint line sequence, where the footprint is more easily measured than during the downward sequence.

The Depth Controller

The depth controller implemented uses the axial force reference as its control signal. The minimum and maximum limits of this reference were set to 82 and 89 kN respectively, during the verification welds (derived from an earlier study [2] that shows that lower force increases the risk of cavities). Investigating simulations of

the controlled process, it was concluded that the performance improvement from a PID controller (rather than a PI) does not motivate the added complexity of such a controller [3]. Hence, it was decided to use a PI controller to regulate the depth and tuning of the PI controller was performed using the model-based optimization approach presented in [4]. This tuning method selects the best performing PI controller (in terms of minimizing the integrated absolute control error), while keeping stability within user-defined margins. The currently used controller is tuned to have large stability margins, rather than high performance.

The depth controller can use either of the LVDT1, LVDT2, laser, or z-axis sensors. During the verification welds the laser sensor was used with a shoulder depth reference value of 2.2 mm (derived from previous study to achieve a large shoulder footprint width but without flash or cavities). At the moment, the depth controller is only active during the start and downward sequences and 20 s into the joint line sequence. It is assumed that the depth keeps fairly constant during the joint line sequence, and that it is the start and downward sequences that are the most important when it comes to setting the depth of the full weld. The objective of the depth controller is therefore to achieve the desired shoulder depth at the point where the joint line is reached. Hence, tracking the desired shoulder depth during the initial part of the downward sequence is not as high priority as reaching the desired depth at the joint line. It should be noted that the depth controller most probably also will be active during the parking sequence, but this is not included in this paper.

Results

The depth controller was verified during 13 separate weld cycles in lids and tubes with different material properties (due to different manufacturing techniques). Pilot hole forming has been performed identically for all welds, using the same drill hole size and depth and then forming the drill hole with the same probe. Measuring the maximum axial force needed to perform the forming thus provides a consistent measure of the lid hardness. The first lid (weld ID's 604–609) had an average maximum force of 97.5 kN, and is thus slightly harder than the second lid (weld ID's 610–615), which had an average maximum force of 95.3 kN. These two lids were thus much harder than the last lid (weld ID 640), which had an average maximum force of 72.4 kN.

Weld data from welds 604–615 and 640 (2° into the joint line sequence) are collected in Table 1, together with mean values, maximum deviation, and standard deviation. LVDT1 data from weld 614 was rejected because of a sensor failure. It is still unclear what caused this error. The last column shows the laser signal as the set axial force was reached during the plunge sequence (i.e. the shoulder is not in contact therefore the negative depth values).

Table 1 Data from the depth controller verification welds 2° into the joint line sequence. Fp. is an abbreviation for foot-print. All data in millimetres

Weld ID	Fp. width	Fp. depth	Laser	LVDT1	LVDT2	Laser, plunge
604	67.8	2.73	2.39	2.24	2.43	-4.21
605	68.9	2.86	2.23	2.07	2.21	-4.34
606	68.1	2.76	2.23	2.05	2.23	-4.11
607	67.1	2.64	2.30	2.11	2.20	-4.02
608	66.1	2.52	2.23	2.14	2.37	-4.13
609	67.4	2.68	2.24	2.01	2.12	-4.18
610	67.6	2.70	2.36	2.17	2.64	-3.86
611	67.4	2.68	2.40	2.22	2.54	-3.92
612	67.1	2.64	2.37	2.21	2.34	-3.89
613	66.9	2.62	2.36	2.27	2.23	-3.81
614	66.5	2.57	2.22	-	2.04	-4.02
615	66.5	2.57	2.21	2.04	2.23	-3.68
640	-	-	2.19	2.05	2.19	-1.21
Mean:	67.3	2.66	2.29	2.13	2.29	-3.80
Max. dev:	2.8	0.34	0.21	0.26	0.60	3.13
St. dev:	0.7	0.09	0.08	0.09	0.17	0.77

Figure 5a–c show how the depth sensor measurements (except LVDT2) varied for the first 400 s of the thirteen verification welds (counted from the beginning of the start sequence). The start of the joint line sequences are marked by black squares in the figures. The data was smoothed to make the plots less cluttered. Figure 5d shows the control signal from each weld, i.e. the axial force reference during first 400 s of the thirteen welds.

Figure 5a shows the thirteen laser signals. At a point 2° into the joint line sequence, the laser signal values are larger than the reference of 2.2 mm in almost all of the welds, and although the welds are made in lids of different hardness, it is clear from Table 1 that the controller manages to maintain a maximal control error of only 0.2 mm for all welds. In Fig. 5d it can be seen that a lot of the welds end up with a saturated axial force, thus constraining what the controller can possibly carry out.

Although the shoulder depth varied more than 3.1 mm between cycles during the plunge sequence (see Table 1), the depth controller was able to achieve the desired shoulder depth of 2.2 mm for both these cycles as the joint line was reached, and the standard deviation for all cycles at this location was 0.1 mm.

Figure 5b show the same measurement signals for LVDT1. At the point 2° into the joint line sequence, LVDT1 varies slightly more than the laser (0.26 mm compared to 0.21 mm). It can be seen that the LVDT1 signal is the smoothest of the four sensor signals (even before the smoothing is applied). For example, it does not suffer from the kind of noise that can be present in the laser signal.

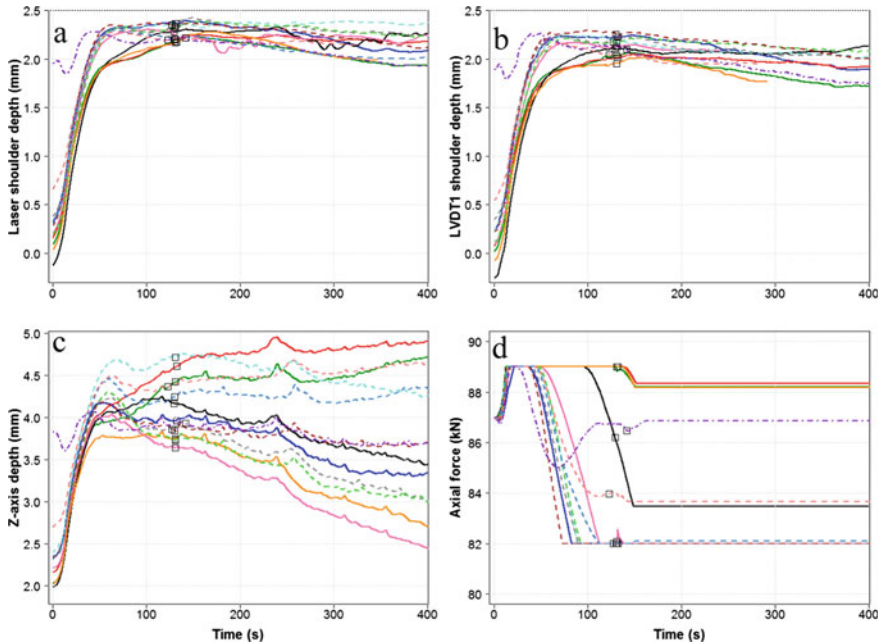


Fig. 5 **a** Laser depths during the 13 verification welds. **b** LVDT1 depths during the 13 verification welds. **c** Z-axis position depths during the 13 verification welds. **d** Axial force reference during the 13 verification welds

Figure 5c shows the z-axis signals, which varies a lot even though both static and force induced gear rim deflection were compensated for. This sensor is obviously unsuitable for use in the depth controller.

Next, the depth controlled welds are compared to welds without any active depth control, which will give an indication of the benefits of the depth controller. The additional weld data (see Table 2) will also make it easier to see how well the different depth sensors can model the shoulder footprint depth.

The 18 welds were made in three different lids and tubes. Using the maximum pilot hole forming force as a measure of hardness, the average of the lids were: 80.6 kN (welds 616–621), 91.7 kN (welds 622–627), and 103.4 kN (welds 628–633). Comparing these hardness values to those for depth controlled welds (with means 97.5 kN, 95.3 kN and 72.4 kN respectively), it is obvious that weld 640 was made in the softest lid out of the six, welds 616–621 in a soft lid, welds 622–627 in a medium hard lid, welds 604–609 and 610–615 in hard lids, while welds 628–633 were made in the lid that was the hardest.

It can be seen from Table 2 that lid hardness affects the depth at the beginning of the start sequence. At a point 2° into the joint line sequence, it seems like the hardness has less to do with both laser and footprint depth. That is, welds that are shallow during the dwell sequence will have a greater depth increase during the

Table 2 Data from the 18 welds without active depth control, 2° into the joint line sequence. All data in millimetres

Weld ID	Fp. width	Fp. depth	Laser	LVDT1	LVDT2
616	69.5	2.94	2.06	2.24	2.10
617	69.0	2.87	2.19	2.12	1.99
618	68.0	2.75	2.11	2.03	1.97
619	67.0	2.64	1.98	1.85	1.88
620	68.5	2.81	2.29	2.14	2.15
621	69.5	2.94	2.40	2.33	2.24
622	66.0	2.51	1.93	1.75	2.15
623	65.0	2.40	1.83	1.64	2.02
624	66.0	2.51	1.74	1.55	1.81
625	67.5	2.69	1.94	1.78	1.95
626	68.0	2.75	2.16	2.02	2.09
627	69.0	2.87	2.30	2.22	2.03
628	67.5	2.69	2.38	2.38	2.39
629	66.0	2.51	1.87	1.68	2.08
630	65.0	2.40	1.97	1.73	2.18
631	64.5	2.34	1.99	1.78	2.08
632	67.5	2.69	2.35	2.11	2.40
633	68.0	2.75	2.49	2.36	2.40
Mean:	67.3	2.67	2.11	1.98	2.11
Max dev:	5.0	0.60	0.75	0.83	0.59
St. dev:	1.6	0.19	0.22	0.27	0.17

start and downward sequences. Further-more, welds with active depth control have a lot lower variation than those without control. For the thirteen welds with active depth control, the shoulder depth measured by the laser sensor varied between 2.19 and 2.40 mm (0.21 mm span) at the point 2° into the joint line sequence, i.e. with a maximum control error of 0.20 mm. The shoulder footprint depth ranged between 2.52–2.86 mm (0.34 mm span). For the eighteen uncontrolled welds, the laser varied between 1.74 and 2.49 mm (0.75 mm span). The corresponding span for the footprint depth was a 0.60 mm difference. The uncontrolled welds were, on the other hand, greater in numbers.

Next, it will be seen how well the different depth sensors can model the actual depth. For this purpose, the depth sensors (except the z-axis) has been used to model the shoulder footprint depth (2° into the joint line sequence) as estimated from the shoulder footprint width (see Tables 1 and 2). Figure 6a, b shows plots of footprint depth versus laser and LVDT1. The crosses show the welds with depth control, that obviously do not have enough variation to provide a decent model in most cases. Together with the uncontrolled welds (in circles), however, it is possible to derive much more reliable models. Linear regression models with one variable were derived (minimum least squares modeling in the programming language R), and have been plotted with blue dashed lines in the figures. Their

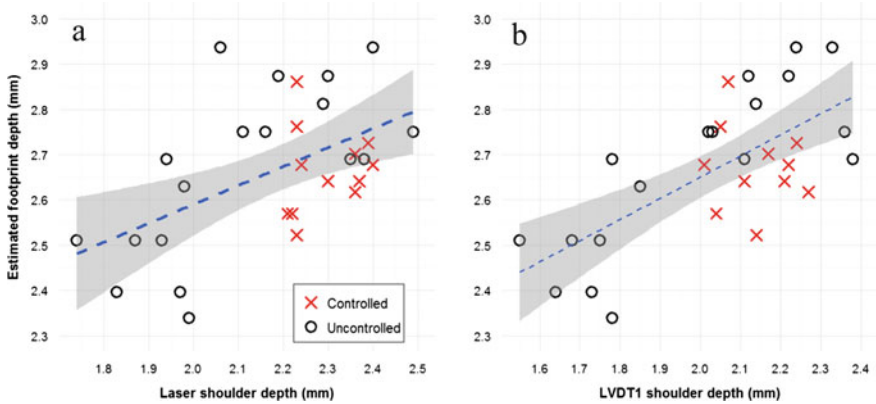


Fig. 6 **a** Linear regression of footprint depth using the laser as predictor. The linear model (Eq. 1) is marked with a dashed line, with its 95% confidence interval shadowed. **b** Linear regression of footprint depth using the LVDT1 as predictor

Table 3 F-statistics and R² statistics for the seven linear regression models

Model:	Laser	LVDT1	LVDT2
F-statistic	11.1	23.2	0.39
R ² statistic	0.28	0.46	0.014

respective 95% confidence intervals are marked with grey regions. This gave the following models (in mm):

$$\text{Footprint Depth} = 0.42 \cdot \text{Laser} + 1.75, \tag{1}$$

$$\text{Footprint Depth} = 0.47 \cdot \text{LVDT1} + 1.72, \tag{2}$$

$$\text{Footprint Depth} = 0.094 \cdot \text{LVDT2} + 2.46, \tag{3}$$

Table 3 summarizes measures of the models (on training data) that indicate both how significant the model relationships are, as well as how accurately the models describe the footprint depth. The F-statistic [5] can be derived to measure the significance of the hypothesis that there is a relationship between the variables. An F-statistic value much larger than 1 indicate a high probability that a relationship exist. The accuracy of the model can be assessed using the R² statistic [5], which takes on a value between 0 and 1. It has the nice interpretation that it explains how much of the predicted variable variance that is explained by the model. A model with its R² statistic close to 1 will thus explain almost all variability and the relationship is therefore strong. On the other hand, a model with an R² statistic close to 0 explains very little of the outcome variability.

The F-statistics in Table 3 show that there seem to be valid relationships in all cases except for LVDT2 model (Eq. 3), which also has a very low R² statistic. Out

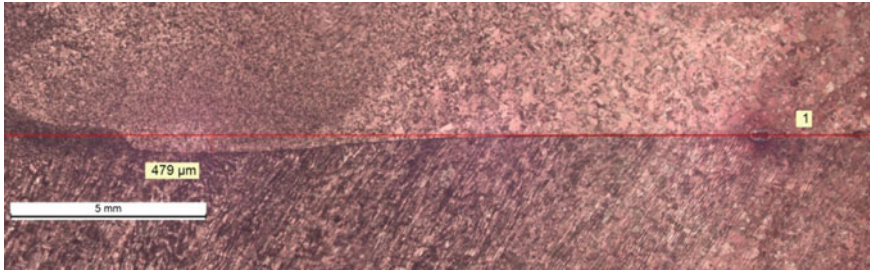


Fig. 7 Macro sample from weld 604. See *dashed box* in Fig. 2a that is rotated 90° counter clockwise

of the three shoulder depth sensors, LVDT1 seems to give the best predictions of the footprint depth. Taking this, as well as the laser measurement noise into account, it seems reasonable to use the LVDT1 sensor as the controller feedback signal. The laser signal can be used as a back-up in case of an LVDT1 sensor failure (like in weld 614).

It should be noted that the shoulder (outside diameter) temperature measured also correlated well with the actual footprint depth, but this is not included in this paper as it needs to be further investigated.

Two macro samples were collected from each weld 604–615, one based on indication from non-destructive testing (NDT) report and one random, and 18 samples from the full weld (9 based on NDT and 9 random). There was no visible hook defect reported and no joint line remains. In addition, there was no visible hook defect reported in 14 macro samples from the full circumferential weld 640. So overall, the results were very satisfying. Examples of the macro samples are presented in Fig. 7. Instead of hook defect, it can be noted in Fig. 7 that the vertical joint has been pressed inwards (maximum 0.479 mm in weld 604, with range of maximum 0.2–1.1 mm for all welds) in all welds.

Conclusions

In this paper, a combined approach for controlling temperature and depth is presented. The proposed method was evaluated using 13 welds with active depth control, and 18 welds without depth control. During the development and evaluation of the control approach, the following findings were made:

1. The welds with active depth control had much less depth variation than the welds without any depth control. For the laser sensor and footprint depth, the controlled welds spanned 0.21 mm and 0.34 mm, respectively (at a point 2° into the joint line). The corresponding measures for the uncontrolled welds were 0.75 mm and 0.60 mm, respectively.

2. The laser and LVDT1 sensors can be used to predict the shoulder depth in terms of the estimated footprint depth. The LVDT2 sensor only has a very weak relation (if any) with the footprint depth. The model given by the LVDT1 sensor has the lowest prediction error range of ± 0.20 mm.
3. It is suggested that the LVDT1 sensor is used as feedback signal in the depth controller. Besides being the most accurate sensor when it comes to predicting the shoulder footprint depth, it does not suffer from measurement noise like the laser signal does.
4. Lids with different hardness affect the depth, especially during the plunge sequence. As expected, harder lids give shallower welds. At a point 2° into the joint line, the effect of lid hardness is smaller.
5. The verification welds used a reference depth of 2.2 mm (laser sensor feedback to the controller). The macro samples showed that this was a reasonable reference, since none of the them had any visible signs of neither hook defect nor joint line remains. The length of the probe varied between 50.6–51.1 mm over these welds, which suggests that the depth reference has a relatively wide range that is acceptable. However, additional welds in lids made from various manufacturing techniques are needed to ensure that welds without hook defect can be produced repeatedly.
6. The fact that the axial force reference saturates in most welds suggests that this is a difficult process to control. So far, however, the current strategy seems to be sufficient to avoid hook defect and remains. If future welds would show it is necessary to control the depth more accurately, e.g. for softer lids, it seems reasonable to try depth control also during the plunge sequence.

References

1. Cederqvist L, Garpinger O, Cervin A, Nielsen I (2015) Improved temperature and depth control during FSW of copper canisters using feedforward compensation. In: Proceedings of friction stir welding and processing VIII, Orlando, USA
2. Cederqvist L, Garpinger O, Nielsen I (2012) Control of temperature, power input and tool depth during FSW of copper canisters. In: Proceedings of 9th international symposium on friction stir welding, Huntsville, USA
3. Nielsen I (2012) Modeling and control of friction stir welding in 5 cm thick copper canisters. Master thesis LiTH-ISY-EX-12/4567-SE, Department of Automatic Control, Linköping University, Sweden
4. Garpinger O, Häggglund T (2008) A software tool for robust PID design. In: Proceedings of 17th IFAC world congress. Seoul, South Korea
5. James G, Witten D, Hastie T, Tibshirani R (2013) An introduction to statistical learning. Springer, New York

Predicting Lap Shear Strength for Friction Stir Scribe Joining of Dissimilar Materials

Erin Iesulauro Barker, Piyush Upadhyay, Yuri Hovanski and Xin Sun

Abstract Friction stir scribe technology has been developed to join materials with vastly different properties, most importantly different melting regimes. Specifically lighter, lower temperature materials such as aluminum or magnesium can be joined to higher temperature materials such as steel and titanium. The scribe portion of the modified friction stir welding pin tool creates in situ mechanical interlocks at the material interface. This mechanical interlocking, or hook-like interface morphology, has shown promising joint strength. However, this morphology can vary along a weld length and is sensitive to joining and tooling parameters. The current work seeks to determine the sensitivity of joint strength to the morphology of the hook interface and predict joint strength based on key morphology parameters. Key morphology features of the hooks extracted from joined samples are varied to quantify their impact on simulated lap shear strength. Predictable joint strength is key to wide spread use of this technique.

Keyword Friction stir scribe joining

E.I. Barker (✉) · P. Upadhyay · X. Sun
Pacific Northwest National Laboratory; 902 Battelle Boulevard,
Richland, WA 99352, USA
e-mail: erin.barker@pnl.gov

P. Upadhyay
e-mail: piyush.upadhyay@pnnl.gov

X. Sun
e-mail: xin.sun@pnnl.gov

Y. Hovanski
Manufacturing Engineering Technology, Brigham Young University;
265P CTB, Provo, UT 84602, USA
e-mail: yuri.hovanski@byu.edu

Introduction

The effort to increase fuel efficiency continues to drive research for light-weighting vehicles. Avenues of interest have included developing next generation materials that deliver strength and ductility at reduced weights, such as advanced high-strength steels, magnesium, and aluminum. In addition, combining dissimilar materials is also being pursued. Optimizing the strength and weight of a component can involve utilizing multiple materials. However, this also means joining dissimilar materials to each other. Employing conventional joining techniques on dissimilar materials is often problematic and costly. Large differences in thermal conductivity and melting temperatures make traditional techniques such as fusion welding problematic [1].

Friction Stir Scribe Welding can be a viable option for joining dissimilar combinations such as aluminum to steel [2–6]. Friction Stir Scribe (FSS), a variation of Friction Stir Welding where a scribe is inserted into the pin tip, was developed at Pacific Northwest National Laboratory [7]. The FSS process has been previously describe. The focus of the current work is to model the resulting morphology of the lap joint to determine the impact on joint strength.

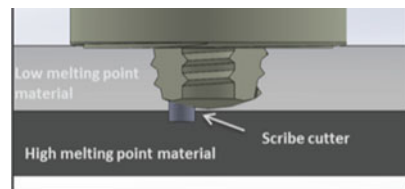
Friction Stir Scribe Process

FSS enables joining materials with extremely different melting points by creating a rivet like fastening between the materials using a modified friction stir welding pin [7]. Figure 1 shows a schematic of the FSS tool plunged into a lap joint configuration.

The FSS tool is a typical FSW tool with a cutter scribe attaches offset from the axis of rotation. The tool is positioned such that only the scribe penetrates into the lower material. The scribe acts to create a rivet-like mechanically interlocking feature between the dissimilar materials. This unique feature prevents bulk plastic deformation of the high melting point material to avoid melting and void formation when joining materials with significantly different melting points.

Figure 2 illustrates the motion of the FSS tool across the plates and the material configuration currently under consideration. The top sheet was 1.0 mm thick 6022-T4 Aluminum while the bottom sheet was 0.7 mm thick low carbon

Fig. 1 Schematic of friction stir scribe tool plunged into dissimilar material lap joint



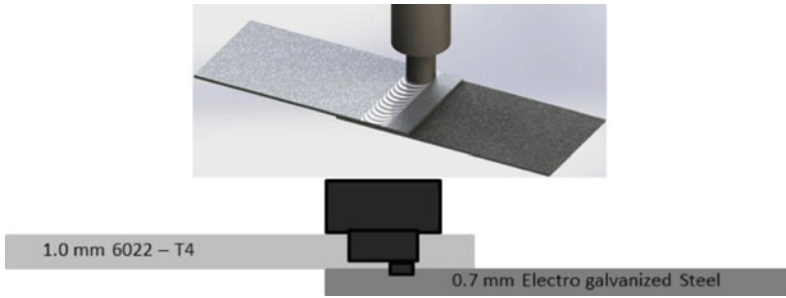


Fig. 2 Lap weld configuration

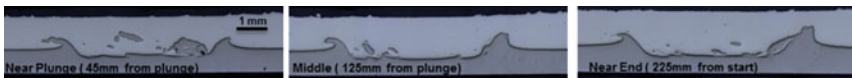


Fig. 3 Representative FSS joint cross-sections between aluminum and steel

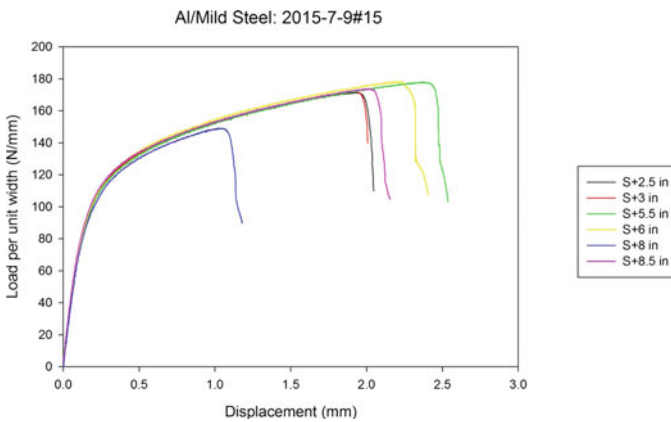


Fig. 4 Lap shear strength results for multiple welds

galvanized steel with a 1 inch overlap. The weld was made in the center of the overlapping section. An example of the resulting joint interface is shown in Fig. 3.

After welding, lap shear tensile tests were conducted on 38 mm wide samples sectioned from the welded panels using abrasive waterjet cutting. Lap shear tests were conducted at room temperature and using a crosshead displacement speed of 2.5 mm/min. Averaged results are shown in Fig. 4. For easy comparison with other tests and simulation results, the load values shown were normalized by the width of the test specimen, or length of the weld through the specimen.

FSS Lap Joint Modeling

Variation in the morphology of the joint interface is observed along the length of a given weld as well as between welds made using different combinations of plunge depth, rotational speed, and translational speed. The goal of the current work is to determine the impact of joint interface morphology on lap shear strength. If an ideal morphology can be determined this will help guide the choices FSS welding parameters.

Figure 5a shows an example FSS lap joint interface. As discussed above, the top plate is 1.0 mm thick 6022-T4 Aluminum and the bottom plate is 0.7 mm low carbon galvanized steel. Figure 5b, c shows the 2D geometry and finite element mesh generated in LS-DYNA based of the joint interface seen in Fig. 5a. The top plate is described in three sections. First, the base material which is unaffected by the welding process is shown in red. Second, the heat affect zone (HAZ) which experiences a thermal gradient due to the welding process but is not plastically deformed is shown in green. Finally, the thermo-mechanically affect zone, or nugget, which is heated and plastically deformed, is shown in yellow. The lower steel plate is shown in blue. Each region is modeled using the LS-DYNA piecewise linear plasticity material model. The yield stress is varied for the different regions of the aluminum plate. Material parameters used are shown in Table 1.

The finite element mesh for each region is generated separately. This results in duplicate nodes along the interfaces. A perfect interface is assumed between regions of the aluminum plate as well as in the region directly affected by the FSS process. Therefore, the nodes from both sides of these interfaces, highlighted in Fig. 5c,

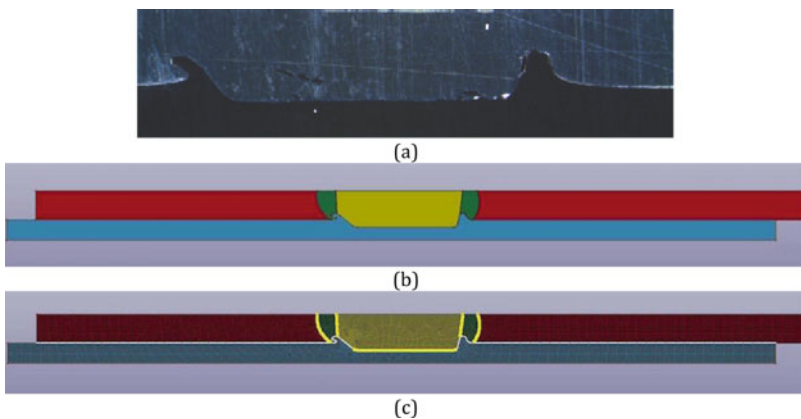


Fig. 5 Example joint interface and resulting finite element geometry and mesh. **a** Close up of the FSS joint. **b** Lap joint model geometry. The *top* Al plate consists of base material (*red*), the nugget (*yellow*), and HAZ (*green*). The *bottom* plate is mild steel (*blue*). **c** Highlighted nodes are merged to create perfectly bonded interfaces between regions of the same material as well as the stir zone between the two plates

Table 1 Material properties

Material	E (GPa)	ρ	ν	σ_{yld} (MPa)
6022-T4 Al base	93.9	2.7e-9	0.35	147
Nugget				140
HAZ				132
Low carbon steel	254.0	7.8e-9	0.30	140



Fig. 6 Overlay of various hook geometries investigated

were merged. Along the rest of the overlapping regions the meshes for the top and bottom plate remain separate to allow sliding and separation during loading. A penalty contact model is used along the interface of both hooks to prevent crossing of the hooks through the aluminum plate. The boundary conditions consisted of fixing the left end of the bottom steel plate and applying a 5 mm displacement to the right end of the top aluminum plate.

As seen in Fig. 3, the morphology of the interface varies not only from weld to weld, but along the length of a given weld. The height of the hook changes as well as the length of the flattened portion of the hook. To determine the impact of the interface morphology on the lap joint strength, the height and width of the left hook was varied. Various hook geometries investigated are overlaid on the initial model geometry in Fig. 6. Two wider hook geometries as well as a narrower hook were generated. Two shorter hook geometries were also created for the original and narrower widths.

Results

Simulations were conducted for each hook morphology. Figure 7 shows the resulting load vs. displacement curves as well. The base morphology generated from a physical sample is shown in black. The variation in the models is limited to the changes to the hook morphology shown in Fig. 6. For comparison, a sample experimentally load vs displacement curve from Fig. 4 is shown as the black dashed line.

The yield stress and tensile strength are comparable to the experimental results shown in Fig. 4 but in general higher than the experiments. The final failure elongation of the models is below the range seen experimentally. The minor changes to the left hook morphology results in a large variation in final

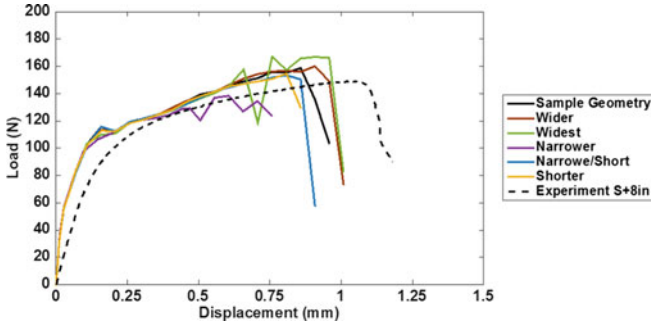


Fig. 7 Load versus displacement curves for each hook morphology modeled

displacement. The current results indicate that the wider hook morphology increases joint strength while the shorter and narrower morphologies decrease the resulting strength.

While the variation in hook morphology did result in variation in the ultimate strength of the lap joints, it did not vary the failure location. Each model failed near the interface between the nugget and HAZ regions of the aluminum plate. This indicates the microstructural changes due to the welding process and resulting material property changes are important to the joint strength and ductility. Therefore, the location of the region boundaries and the variation in properties must be captured to accurately model the strength of the resulting joint.

Conclusions

The FSS welding technique has been successfully used to lap join dissimilar materials. Welding parameters such as plunge depth, rotation speed, and translation speed can influence the hook morphology observed at the joint interface. Computational models of representative joint morphologies were conducted as well as several analyses with modified hook morphologies.

Preliminary results indicate that hook morphology does impact the joint strength but not the failure location. The current work limited the morphology variation to the hook on the advancing side of the pin. Future work will expand to include the morphology of the retreating side hook as well as the presence of isolated chunks of the bottom plate material within the nugget region of the top plate. These preliminary results have also shown that properly characterizing the extent of the nugget and HAZ and the variation in material properties in the top plate are critical to predicting failure location. Additional characterization of the lap joint using micro-indentation is currently being conducted. The resulting micro-hardness also indicates material property variation in the bottom plate in the region disturbed by

the scribe. Future simulation will investigate the impact of the property variation in the bottom plate on strength and failure location.

Acknowledgements Pacific Northwest National Laboratory is operated by Battelle Memorial Institute for the US Department of Energy under Contract No. DE-AC05-76RL01830. This work was funded by the Department of Energy Vehicle Technologies Office.

References

1. Shi SW, Mulligan S (1999) TWI Bull 2007
2. Chen Y et al (2008) Mater Sci Technol 24(1):33–39
3. Elrefaey A et al (2005) J Mater Eng Perform 14(1):10–17
4. Movahedi M et al (2012) Sci Technol Weld Join 17(2):162–167
5. Wei Y et al (2013) J Mater Eng Perform 22(10):3005–3013 (2013)
6. Xiong J et al (2012) Sci Technol Weld Join 17(3):196–201
7. Hovanski Y et al (2001)

Simultaneous Independent Control of Tool Axial Force and Temperature in Friction Stir Processing

Ken Ross, Glenn Grant, Jens Darsell and David Catalini

Abstract Maintaining consistent tool depth relative to the part surface is a critical requirement for many friction stir processing (FSP) applications. Force control is often used with the goal of obtaining a constant weld depth. When force control is used, if weld temperature decreases, flow stress increases and the tool is pushed up. If weld temperature increases, flow stress decreases and the tool dives. These variations in tool depth and weld temperature cause various types of weld defects. Robust temperature control for FSP maintains a commanded temperature through control of the spindle axis only. Robust temperature control and force control are completely decoupled in control logic and machine motion. This results in stable temperature, force and tool depth despite the presence of geometric and thermal disturbances. Performance of this control method is presented for various weld paths and alloy systems.

Keywords Friction stir • Temperature control • Force control • Process control

Introduction

Control of tool position relative to the part surface has been a challenge in FSP since its inception. In the early days of FSP, the FSP community adopted two approaches to controlling tool depth. The first approach is to control weld position based on encoder feedback on motors driving tool axial motion. Some early FSP machines lacked rigidity and their control systems didn't correct for machine deflection during FSP. This resulted in significant error between commanded and actual depth. Some early FSP researchers discovered that on their machines they could get more constant weld depth using force control. When force control is used,

K. Ross (✉) · G. Grant · J. Darsell · D. Catalini
Pacific Northwest National Laboratory, 902 Battelle Blvd, Richland, WA, USA
e-mail: kenneth.ross@pnl.gov

© The Minerals, Metals & Materials Society 2017
Y. Hovanski et al. (eds.), *Friction Stir Welding and Processing IX*,
The Minerals, Metals & Materials Series, DOI 10.1007/978-3-319-52383-5_26

if weld temperature decreases, flow stress increases and the tool is pushed up. If weld temperature increases, flow stress decreases and the tool drives.

Using either position control or force control, process engineers typically run iterative experiments to develop a parameter set, or program, where commanded force or depth, spindle speed and traverse speed are defined values for each position throughout the weld. The objective was to define the weld parameter set to compensate for repeatable changes in welding conditions to produce a sound weld.

Non-repeatable changes in welding conditions such as variations in: part to part geometry or chemistry, clamp force, how parts sit within fixtures or clamps and changing thermal boundary conditions are process disturbances that can produce weld defects. Methods of dealing with process disturbances are required to expand FSP to applications with complex contours, changing thermal boundary conditions, lower geometric and material chemistry tolerances.

An example of a process with varying thermal boundary conditions is the sealing of copper canisters by the Swedish Nuclear Fuel and Waste Management Co. (SKB). While developing a friction stir welding (FSW) solution for sealing copper canisters, SKB and collaborators determined that temperature control was required to ensure weld quality. In 2008 Cederqvist et al. [1] presented a cascade control methodology where a faster inner loop controls weld power and a slower outer loop modulates the weld power set point to achieve a desired tool temperature.

SKB has also developed a decentralized temperature and shoulder depth control solution for their FSW machine, in which depth measurements are fed back to a PID controller [2]. The depth controller then manipulates the set point to an axial force controller in order to achieve the target depth.

Results presented and discussed in the remainder of this paper use a cascade control temperature regulator. It differs from SKB's approach in that the inner loop controls power through torque modulation as described by Ross and Sorensen [3]. Applications presented using PCBN tools to weld steel acquire temperature data from thermocouples in the locking collar of the FSW tool pressed against the PCBN insert [4]. Non-ferrous applications presented have thermocouples placed in through holes such that they contact plasticized material. This instrumentation technique can produce a fast temperature response and was first reported by Fehrenbacher et al. [5].

Process control during the plunge and initial traverse are beyond the scope of this paper. Control during plunge and initial traverse of the applications described in the remainder of the document will be presented in future publications.

Copper Rotors

PNNL and the General Motors R&D Center are using FSP to join copper components in the rotor and stator assemblies of induction-based electric motors to increase motor efficiency [6]. The application of FSP overcomes some of the manufacturing challenges in current motor fabrication methods and may help to



Fig. 1 Copper rotor “as welded” using FSP with simultaneous temperature and force control

achieve the goals of lower manufacturing cost and higher power density needed in current and next generation electric vehicles.

FSP is used to weld copper shorting bars to copper end caps. An “as welded” copper rotor assembly is shown in Fig. 1. The weld ramped from 0 to 250 mm/min in the first 25° of welding and continued at that speed traversing the entire weld path in 86 s. Temperature control resulted in large power input at the beginning of the weld to overcome heat flow into the cold copper end cap. As the thermal capacitance of the end cap began to saturate, power was reduced until the exit tab was reached. If a constant spindle speed is used, temperature continually increases throughout the weld. These trends are seen in Fig. 2.

Simultaneous force and temperature control was used to promote a more automated, more self-adjusting and robust weld. Anticipated process disturbances in high volume production of this part include: lack of parallelism (between the FSP machine, rotary turntable, fixtures and rotor assembly), part to part geometric or material chemistry variation and changes in thermal boundary conditions during a weld or throughout a production shift.

Force control and temperature control proved useful in rejecting process disturbances caused by variations in length of shorting bars and variations in how shorting bars were positioned within the assembly. Without the use of this control scheme weld depth and temperature varied with length and positioning of shorting bars. With force control and temperature control, the process self-adjusted and produced a uniform weld within the part and from part to part. Micrographs showing uniformity of the weld along the weld path are shown in Fig. 3.

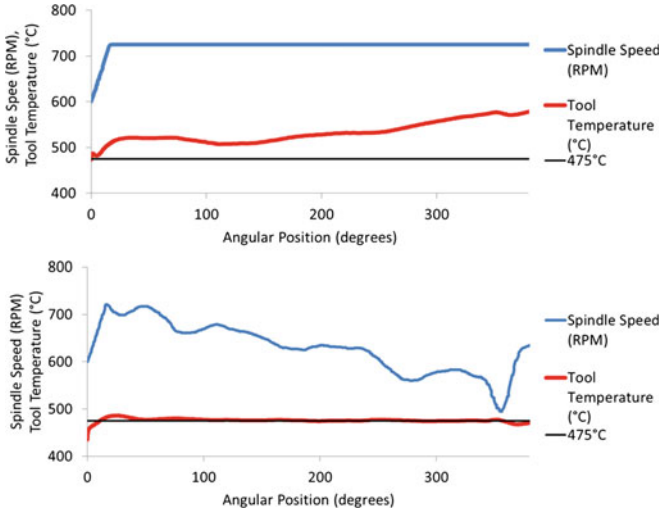


Fig. 2 Comparison of temperature and spindle speed response in FSP of copper rotors; *(top)* Temperature response in constant spindle speed weld, *(bottom)* spindle speed response in constant temperature weld

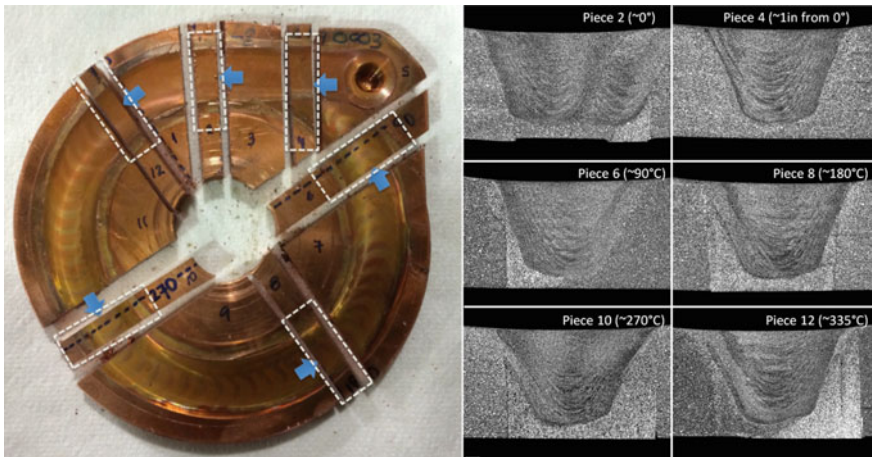


Fig. 3 Micrographs of cross sections taken along the weld path of a copper end cap welded with simultaneous temperature and force control; *(left)* copper end cap, *(right)* micrographs taken along weld path

Thick Section Sensitized 304

The Nuclear Regulatory Commission has identified chloride-induced stress corrosion cracking (CISCC) of austenitic stainless steel dry cask storage systems (DCSS) as an area of great concern. Sutton et al. [7] investigated the use of Friction Stir Processing (FSP) to repair laboratory-generated stress corrosion cracking (SCC) in representative 25.4 mm thick stainless steel 304 coupons (Fig. 4).

All crack repair welds were run at 38.1 mm/min, 55.6 kN tool axial force, 0° spindle tilt, with Megastir Q70 tools. PNNL’s robust temperature control algorithms were used to hold the weld at a temperature of 850 °C ± 2 °C, Fig. 5. Argon shielding and a liquid cooled tool holder were used for all welds. Additional information on FSP process development is given by Ross et al. [8].

The combined use of temperature control and force control resulted in a well controlled weld. Figure 4, shows that size, shape and features of the stir zone appear to be similar across the raster pattern. Dotted parallel lines were added to show that combined force and temperature control resulted in the uniform weld depth throughout the weld path.

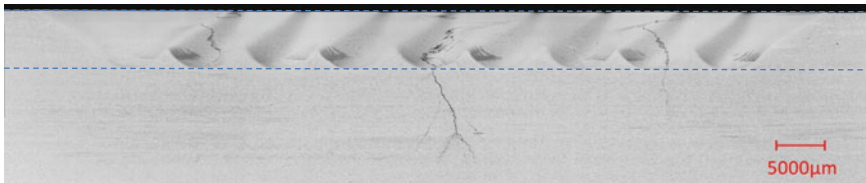


Fig. 4 Micrograph of FSP to seal cracks in lab generated stress corrosion cracked coupon

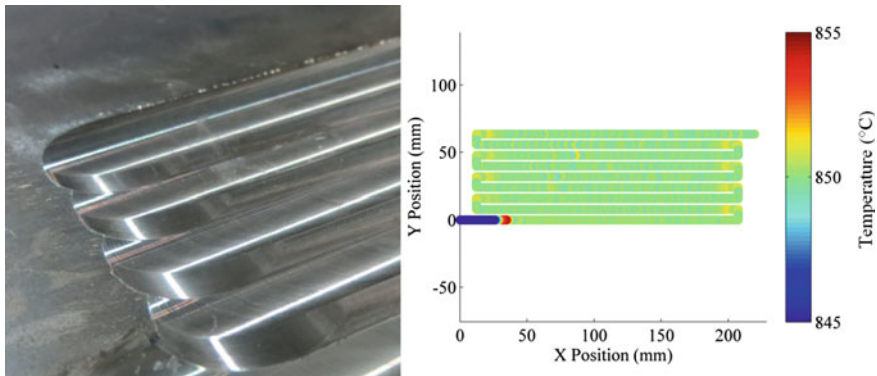


Fig. 5 FSP raster pattern used to heal SCC coupon; (left) Photo of surface finish for FSP region, (right) Temperature profile for FSP path

The stir zone on the far right hand side of Fig. 4 is traversing into the page with the advancing side on the right and the retreating side on the left of the stir zone. The second stir zone from the right is traversing out of the page with the advancing side on the left and the retreating side on the right of the stir zone. The pattern continues across the entire rastered area. All areas inside the stir zones are fully consolidated. Dark areas are areas of preferential etching due to corrosion products in the cracks dispersed within the processed region.

Results presented demonstrate that SCC repair and sensitization remediation of DCSS canisters via FSP is feasible. Liquid penetrant inspection, ultrasonic inspection and destructive metallographic analysis show that: Crack growth does not occur during FSP repair operations, cracks of a depth less than that of the stir zone are fully consolidated by FSP repair; cracks extending deeper than the stir zone are dimensionally stable and successfully embedded within the test coupon during FSP repair.

FSP using tool temperature and tool axial force control resulted in a stable and uniform stir zone across a large multi-pass raster pattern, sealing 3 cracks in fully consolidated processed regions.

High Speed FSP in Thin Sheet Aluminum

As FSP of thin section aluminum is gaining acceptance in the transportation industry, companies are pushing for faster welding speeds and increasingly complicated geometries. In 2014 Ross [9] presented the use of temperature control for welding complex contours in a 2D plane at continually increasing speeds. Using similar methods, simultaneous temperature control and force control were demonstrated at 3,000 mm/min in 2014 [10]. On a separate occasion, a high speed demonstration weld was developed on a prototypical part in thin section aluminum containing 3D complex contours. This work performed by Rose [11] in 2014 using force control and power control [3] to achieve traverse speeds that varied from 3,000 to 6,000 mm/min in the prototypical part. This control scheme required power set points to be adjusted along the weld path to produce defect free welds. Power control resulted in a weld that was less sensitive to thermal and geometric disturbances than running in RPM control with force control. This suggests temperature control is feasible for speeds above 3,000 mm/min in complex contours.

Conclusions

Running force control and temperature control results in stable temperature, force and tool depth despite the presence of geometric and thermal disturbances. This control scheme produced a robust FSP process for: fabrication of copper rotors, sealing cracks in thick, sensitized stainless steel and enables expansion of FSP to

previously unattainable weld speeds and geometries in thin section aluminum. If implemented correctly, it can be intuitive to use and dramatically reduce process development time for new applications.

Use of simultaneous temperature control and force control can drive higher speeds and accommodate lower part tolerances, increasing the value proposition of FSP for high volume manufacturers. It also provides process robustness and repeatability required for high risk application such as fabrication and repair of nuclear canisters.

References

1. Cederqvist L, Bolmsjö G, Sorensen C (2008) Adaptive control of novel welding process to seal canisters containing Sweden's nuclear waste using PID algorithms. In: Proceedings of the 18th international conference on flexible automation and intelligent manufacturing, University of Skövde, Sweden
2. Cederqvist L, Garpinger O, Cervin A, Nielsen I (2015) Improved temperature and depth control during FSW of copper canisters using feedforward compensation. In: Friction stir welding and processing VIII
3. Ross KA, Sorensen CD (2013) Paradigm shift in control of the spindle axis. In: Friction stir welding and processing VII, San Antonio, TX
4. MegaStir, Operation manual for PCBN friction stir welding tools. http://www.slb.com/services/megastir/products/~media/Images/megastir/files/equip_req.ashx
5. Fehrenbacher A, Cole EG, Zinn MR, Ferrier NJ, Duffie NA, Pfefferkorn FE (2011) Towards process control of friction stir welding for different aluminum alloys. In: Friction stir welding and processing VI, San Diego, California, USA
6. Grant G, Catalini D, Ross K(2016) Novel manufacturing technologies for high power induction and permanent magnet electric motors. In: DOE vehicle technologies program annual merit review and peer evaluation meeting
7. Sutton B, Ross K, Grant G, Cannell G, Frederick G, Couch R (2017) Friction stir processing of degraded austenitic stainless steel nuclear fuel dry cask storage system canisters. In: Friction stir weld and processing IX, San Diego
8. Ross K, Sutton B, Grant G, Cannell G, Frederick G, Couch R (2017) Development of friction stir processing for repair of nuclear dry cask storage system canisters. In: Friction stir welding and processing IX, San Diego, CA
9. Ross K (2014) Temperature control in friction stir welding for industrial and research applications. In: 10th international symposium on friction stir welding, Beijing, China. <http://www.fswsymposium.co.uk/previous-symposia/pdf-download/>
10. Hofferbert D (2016) Interviewee, President, bond technologies [Interview]. 10 Nov 2016
11. Rose S (2016) Interviewee, Welding engineer, Boeing research and technology. [Interview]. 10 Nov 2016

Process Force Reduction During Robotic Friction Stir Welding of Aluminum Alloys with Reduced Tool Aspect Ratios

Anna Regensburg, Michael Grätzel, René Schürer, Michael Hasieber and Jean Pierre Bergmann

Abstract Friction Stir Welding has increasingly been gaining relevance for joining nonferrous metals, especially aluminum alloys. However, when considering FSW as an alternative for conventional processes, some characteristics of FSW like high process forces and clamping requirements still represent drawbacks regarding accessibility and work piece loading capacity. The tendency towards lightweight design and more complex components amplifies this challenge. Therefore, the objective of this investigation is to evaluate the scaling effects during FSW with reduced tool diameters at adjusted process parameters, in order to keep the shear stress conditions in the shear layer constant and hence counteract the compromised mechanical loadability of the scaled tools. The experiments in this investigation are carried out for EN AW 5754 H12 with a material thickness of 2 mm. The results demonstrate the potential to decrease the axial force by reducing the material volume displaced by the pin and hence reduce the load on the workpiece and the required spindle torque.

Keywords Friction stir welding · Aluminum alloys · Process forces · Scaling effects

Introduction

Within the last decade, Friction Stir Welding (FSW) has increasingly been gaining relevance for joining nonferrous metals, especially aluminum alloys. Possible applications range from the aerospace and automotive sector up to manufacturing electrical components. The operation principle of this technology is based on a rotating tool which plasticizes the material by a friction-induced heat input. The process offers numerous advantages like relatively high weld strength and e.g. the

A. Regensburg (✉) · M. Grätzel · R. Schürer · M. Hasieber · J.P. Bergmann
Department of Production Technology, Technische Universität Ilmenau,
Gustav-Kirchhoff-Platz 2a, 98693 Ilmenau, Germany
e-mail: anna.regensburg@tu-ilmenau.de; info.fertigungstechnik@tu-ilmenau.de

© The Minerals, Metals & Materials Society 2017
Y. Hovanski et al. (eds.), *Friction Stir Welding and Processing IX*,
The Minerals, Metals & Materials Series, DOI 10.1007/978-3-319-52383-5_27

ability to produce dissimilar joints. Other positive aspects are the high environmental compatibility and that no filler material or shielding gas is required.

Still, FSW is not taken into account during the product development process in proportion to its potential. Mostly, it rather represents an alternative, when other joining technologies do not prove suitable, e.g. due to material related challenges. At that point, the joint design is usually completed and e.g. aimed for an arc welding process, so that typical characteristics of the FSW process like high process forces, clamping requirements and relatively high seam widths represent drawbacks considering accessibility and work piece loading capacity. The tendency towards lightweight design and more complex or functionalised components also amplifies this challenge. Moreover the tool design for FSW is carried out rather empirically. Though various tool designs and welding parameters are documented in the literature, it still lacks profound investigations on the effect of the tool design on the process force and the resultant potentials for reducing them.

Therefore, the objective of this investigation is to evaluate the tool and force related scaling effects during FSW of aluminum alloys. In order to set up the experimental procedure and be able to derive the respective correlations, the following considerations have to be regarded (See Fig. 1) [1–3]:

- The process forces are caused by the material resistance of the volume, which is displaced by the tool during plunging and tool travel.
- The resistance of the material can be described by the flow stress, which is mostly dependent on rotational speed and friction (at otherwise constant parameters).
- The flow stress is mainly influenced by temperature and degree/speed of deformation.
- The speed of deformation is influenced by the relative movement between the tool/work piece interface, where the material is transported around the pin, hence approximately indicated by the circumferential speed at the pin and shoulder. Therefore reducing the tool diameter at constant rotational speed does not provide constant boundary conditions, as the flow stress increases and causes high shear stress on the pin.

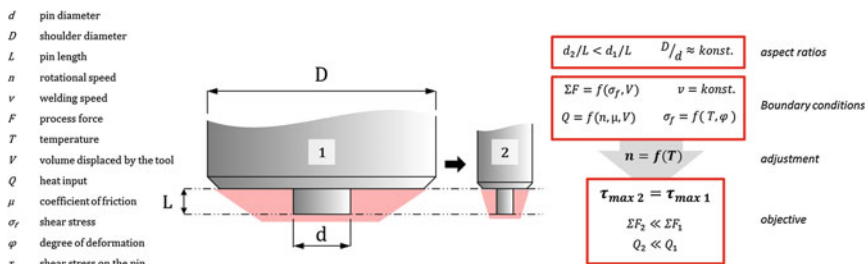


Fig. 1 Schematic illustration of the approach for reducing the tool aspect ratios

- The reduction of the pin and shoulder diameter leads to reduced process forces and heat input, as less material has to be displaced and plasticised. However this can only be applied if the flow stress in the shear layer around the tool and hence the load on the tool is kept approximately constant by adjusting the rotational speed.

In summary of these considerations, the plasticizing of the material determines to what extent the deformation, extrusion and displacement of material around the tool pin takes place. In this context, the tool geometry has a significant influence. On the one hand it represents the actual material volume that is displaced during plunging, leaving cavities that has to be refilled during tool travel. On the other hand, it determines the contact area between the workpiece and the tool and therefore influences the friction based mechanisms. Some investigations have already been carried out on this subject [4, 5], showing that e.g. the required total torque increases with increasing shoulder diameter and increasing welding speed. Furthermore, the axial force F_z is observed to be most significantly influenced by the tool diameter.

Apart from the dependence of the axial force on the tool design, the forces acting opposite and perpendicularly to the welding direction represent especially critical factors for the load on the tool. As the tip of pin processes relatively cold material due to the maximum distance of this location to the tool shoulder, a bending moment is caused, which can lead to a typical failure behavior by shearing of the pin at the transition to the shoulder [6] at high peak loads.

Experimental Procedure

In order to display the effect of the tool geometry on the FSW process, the experiments were carried out by using conventional tool aspect ratios for welding 2 mm thick EN AW-5754 H12 sheets. The chemical composition is shown in Table 1.

The process parameters, especially rotational speed and axial force, were varied to illustrate their effect on the joint properties and also promote the appearance of typical FSW defects. Subsequently the actual scaling was performed by reducing the shoulder and pin diameters in steps of 10% (See Fig. 2) and investigating the respective requirements for parameter adjustment by applying different rotational

Table 1 Chemical composition of aluminum alloy EN AW-5754 H12 according to DIN EN 573-3

Element	Si	Fe	Cu	Mn	Mg	Cr	Zn	Ti
Min. %	0.3	0.1	–	–	0.35	–	–	–
Max. %	0.6	0.3	0.1	0.1	0.6	0.05	0.15	0.1

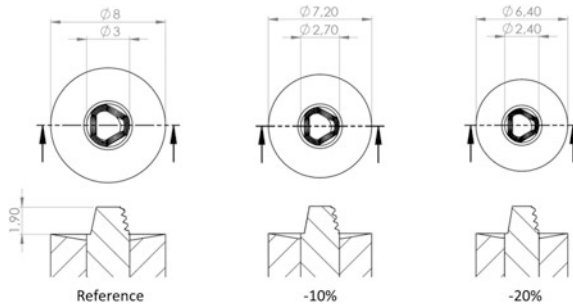


Fig. 2 Comparison of the applied tools for the reference geometry and for a diameter reduction of 10 and 20%



Fig. 3 Robotic FSW system and clamping setup

speeds and axial forces. Therefore the joints were characterized by visual inspection, metallography and tensile testing. The experiments were carried out 3 times for each parameter set.

The experiments were carried out on a robotic FSW system by Grenzebach Maschinenbau GmbH with a KUKA KR500 heavy duty robot (See Fig. 3). This setup provides an axial force of up to 10 kN and a maximum rotational speed of up to 14.000 rpm. The resultant spindle torque was recorded by incorporating a contact free, strain gauge based torque and axial force measurement system by Artis, which is able to record torques ranging from 2 to 60 Nm. In addition to that, the lateral forces F_x and F_y were recorded by a piezoelectric based multi-component dynamometer type 9255C by Kistler.

The pin length was adjusted to 90% of the material thickness in order to provide full penetration depth. The rotational speed was varied in a range from 1500 rpm till up to 6500 rpm, while the welding speed was kept constant at 1000 mm/min and the tilt angle at 2° .

Results and Discussion

In order to enable a comparability of the results for the scaled tools, the rotational speed was adjusted towards a constant relative movement at the interface and therefore, the circumferential speed was set as the relevant process parameter. The conversion of the values is shown in Fig. 4.

Figure 5 shows the resultant spindle torque and tensile strength regarding different circumferential speeds for joints produced with the reference tools (See Fig. 2). At low circumferential speeds of 0.3 and 0.4 m/s, the material is not plasticized and transported sufficiently, leading to typical wormhole defects as can be observed in Fig. 6. Above these values, defect free welds are produced, all of them exhibiting tensile strength values of more than 90% compared to the base material. At higher circumferential speed, the spindle torque reaches an area of saturation at more than 0.7 m/s, which represents a rotational speed between 4500 rpm and 5500 rpm for the reference geometry. This effect is assumed to be caused by a reduction of the coefficient of friction due to local melting and change in the stick-slip-condition.

Fig. 4 Conversion of the rotational speed for the reference and scaled geometries

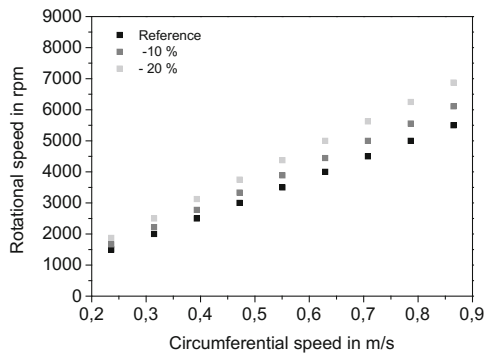
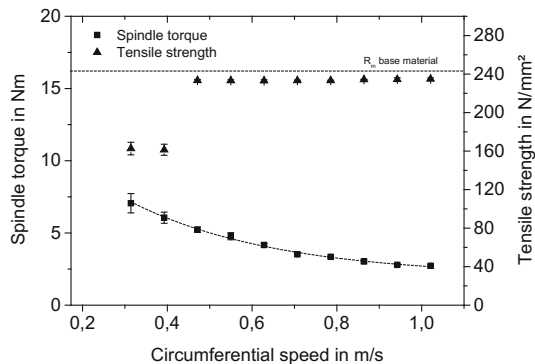


Fig. 5 Resultant spindle torque and tensile strength of for different circumferential speeds (Axial force: 3 kN)



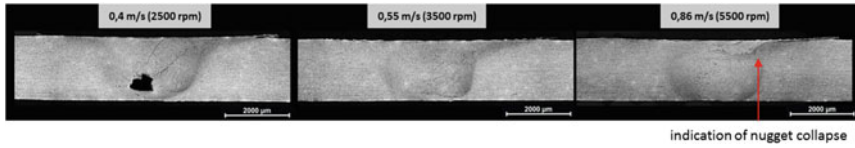


Fig. 6 Cross sections of welds produced with the reference geometry at different circumferential/rotational speeds (Axial force: 3000 N)

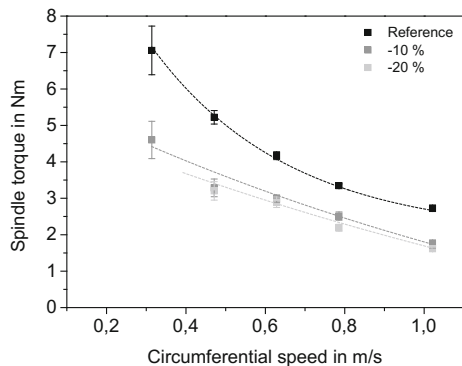
In summary however, the spindle torque can be reduced by up to 60% over the varying speed range, which is contributed to the following effects. In general, the increase of the rotational speed leads to an increase of the relative movement at the interface between tool and work piece and hence also of the friction and deformation induced heat input. Consequently, the shear stress in the shear layer is reduced and the plastic deformation and extrusion of the material around the tool is facilitated, leading to a reduced spindle torque at constant axial force. Looking at this effect from another side, the axial force could also be reduced for higher rotational speeds. The limits of this reduction have to be considered in further investigations.

Further effects can be observed in the cross sections. As the rotational speed increases, the nugget size becomes wider. However, indications of nugget collapse can be observed for higher circumferential speeds, though they do not show an effect on the resultant tensile strength.

In a further step, the pin diameters were reduced by 10 and 20%. The shoulder size was reduced in the same dimension, in order to adjust the heat input gradient over the weld depth and to still provide sufficient contact face to keep the plasticized material within the cavity.

Furthermore, the force values were also adjusted by considering the pressure applied by the projected area of the tool during plunging at a given axial force, which is approx. 60 N/mm². Consequently, the experiments for the 10 and 20% reduced tool dimensions were carried out with a reduced axial force of 2430 and 1920 N. The resultant spindle torques in comparison to the reference experiments are shown in Fig. 7.

Fig. 7 Comparison of the spindle torque for different circumferential speed, tool profiles and between the reference and the 10 and 20% reduced tool geometry



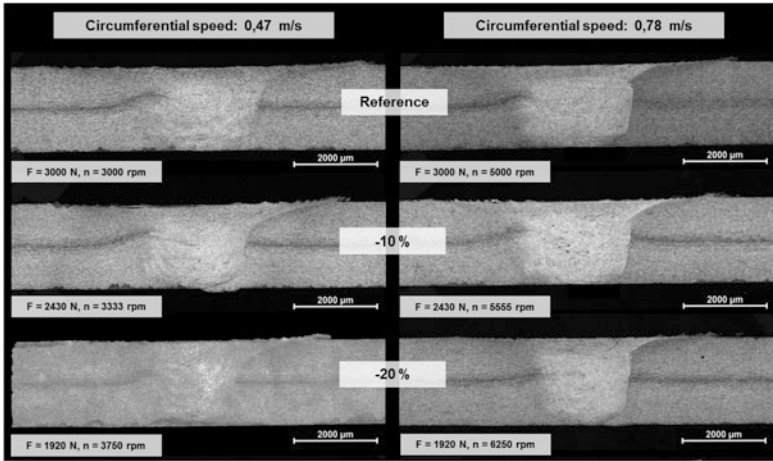


Fig. 8 Cross sections of welds produced with different tool diameters and different circumferential speeds (axial pressure: 60 N/mm²)

Firstly, the torque values for the scaled tools are generally lower and show a similar dependency on the circumferential speed like the reference welds with a decrease in spindle torque of up to 60% for a –10% and up to 50% for a –20% considered range, respectively. This is contributed to the decreased volume of material, which has to be plasticized and transported around the tool.

Figure 8 shows the cross sections of welds produced with the different tool diameters and at two circumferential speeds, where defect free welds could be produced for each combination. In contrast to the cross sections of the reference welds, the size of the welds produced with the scaled geometries shows a significant decrease in nugget size, while still producing defect free welds at the adjusted parameters with a force reduction of up to 40%. At the same time, a tensile strength of over 90% of the base material could still be obtained for defect free welds as shown in Fig. 9.

Figure 10 shows the axial and lateral process forces for the geometries with a scaling of 0–20% and two different circumferential speeds, at which defect free welds were produced. While the axial forces were set as described before, the lateral forces were measured and revealed values of about 10–19% of the axial force for F_x and about 4–5% for F_y , respectively. However, a decrease in the lateral forces could only be observed for the higher circumferential speed of 0.78 m/s which represents rotational speeds between 5000 rpm and 6250 rpm depending on the respective tool diameters. For these values, the force acting opposite to the traverse motion of the tool F_x could be reduced by up to 25%, while the force acting perpendicular to the traverse motion F_y decreased by up to 46%.

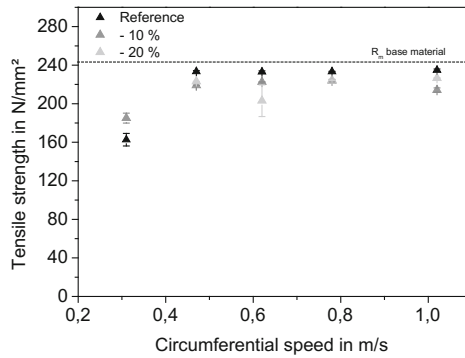


Fig. 9 Tensile strength of welds produced with different circumferential speeds and tool diameters (axial pressure: 60 N/mm²)

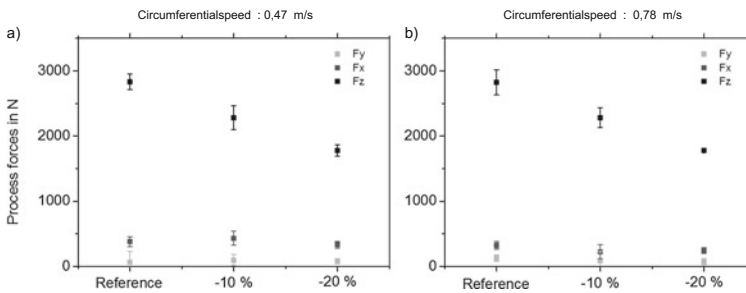


Fig. 10 Process forces of reference and scaled tool geometries for a circumferential speed of 0.47 and 0.78 m/s

Conclusion

In order to reduce the required axial force and spindle torque for welding 2 mm thick EN AW-5754 H12 sheets, the diameter of the applied tools were reduced by 10 and 20% and the occurring scaling effects were analyzed by varying the circumferential speed and adjusting the applied axial forces considering the reduced tool diameters. The results show a significant influence of the circumferential speed on the required spindle torque, which can be decreased by more than 60% at high speed values. However, by reducing the tool diameters, the torque values could be decreased even further by up to 40%. At the same time, a reduction of the weld width and nugget size was obtained, while the penetration depth and the tensile strength of the defect free welds could be kept constant. Regarding the lateral forces, a significant force reduction could only be obtained for the higher circumferential speed. Summarizing the effects, defect free welds with high tensile strength values could be produced at 36% reduced axial force and up to 46% lateral

force. Further investigations will focus on the transferring the results to different aluminum alloys and sheet thicknesses.

Acknowledgements The IGF Project No. 18.843 B of the research association „Schweißen und verwandte Verfahren e.V.“ of the DVS, Aachener Straße 172, 40223 Düsseldorf was, on the basis of a resolution of the German Bundestag, promoted by the Federal Ministry for Economic Affairs and Energy via AiF within the framework of the program for the promotion of joint industrial research and development (IGF). The authors thank all the participants for the funding and the support.

References

1. Mishra RS (2014) Friction stir welding and processing: science and engineering. Springer, Cham, p 18 ff. ISBN: 978-3-319-07042-1; doi:[10.1007/978-3-319-07043-8](https://doi.org/10.1007/978-3-319-07043-8)
2. Hamilton C, Dymek S, Sommers A (2008) A thermal model of friction stir welding in aluminum alloys. *Int J Mach Tools Manuf* 48:1120–1130
3. Rai R, De A, Bhadeshia HKDH, DebRoy T (2011) Review: friction stir welding tools. *Sci Technol Welding Join* 16:325–342
4. Arora A, DebRoy T (2011) Toward optimum friction stir welding tool shoulder diameter. *Scripta Mater* 64:9–12
5. Kumar R, Singh K, Pandey S (2012) Process forces and heat input as function of process parameters in AA5083 friction stir welds. *Trans Nonferrous Metals Soc China* 22:288–298
6. Sorensen CD, Stahl AL (2007) Experimental measurements of load distributions on friction stir weld pin tools. *Metallurg Mater Trans B* 38:451–459

Part VIII
Poster Session

Friction Stir Processing of 2507 Super Duplex Stainless Steel: Microstructure and Corrosion Behaviour

M.K. Mishra, G. Gunasekaran, A.G. Rao, B.P. Kashyap
and N. Prabhu

Abstract Friction stir processing (FSP) has been shown to be effective in the microstructural modification. In this study, 2507 super duplex stainless steel was subjected to multipass FSP and the processed samples were investigated. Refinement in grain size of both ferrite and austenite was observed in the stir zone of the processed samples. Increased number of passes led to further reduction in grain size. Anodic polarization studies in 3.5 wt% NaCl solution showed that the processed samples possessed improved corrosion resistance. The Mott-Schottky analysis confirmed that the charge carrier density in the passive oxide layer is decreased with decreasing grain size.

Keywords FSP • Potentiodynamic polarization • Donor/acceptor density

M.K. Mishra (✉) · B.P. Kashyap · N. Prabhu
Department of Metallurgical Engineering and Materials Science,
Indian Institute of Technology Bombay, Mumbai 400076, India
e-mail: manjeshkumar.mishra@gmail.com

B.P. Kashyap
e-mail: bpk@iitb.ac.in

N. Prabhu
e-mail: nprabhu@iitb.ac.in

G. Gunasekaran · A.G. Rao
Naval Materials Research Laboratory, Shil-Badlapur Road,
Ambernath 421506, India
e-mail: gunanmrl@gmail.com

A.G. Rao
e-mail: gouravdrdo@gmail.com

Introduction

Super duplex stainless steel (SDSS) belongs to family of duplex stainless steel having a two phase microstructure viz. ferrite and austenite [1]. A good combination of properties is obtained with the microstructure containing ferrite and austenite in the ratio of 1:1. Because of their attractive combination of mechanical properties as well as corrosion resistance (pitting resistance equivalent number >40) they are extensively used in nuclear reactors, oil and gas industries [2].

It is well established that in Fe–Cr alloys, corrosion resistance improves with decrease in grain size [3]. There are several techniques to refine the grain size such as thermomechanical controlled processing, equal channel angular pressing, friction stir processing (FSP) etc. [4]. FSP is a solid state processing technique based on the principles of friction stir welding (FSW). In this technique, a specially designed rotating tool is plunged into the work piece and traversed in the direction of interest. Initially, FSP/FSW was focused for comparatively soft material such as aluminium, magnesium alloy etc. [5, 6]. However, due to recent advancement of equipment, instrumentation and tools FSP/FSW of high strength materials is now become possible.

Experimental Procedures

The chemical composition of 2507 super duplex stainless steel is given in Table 1. A 100 kN FSP machine was used for the processing. FSP tool was made of lanthanated tungsten (W-La₂O₃) with a shoulder diameter, pin length and diameter of 25, 6 and 8 mm respectively. In order to avoid the surface oxidation, Ar gas was introduced around the tool. FSP was conducted with a tool rotation and traverse speed of 600 rpm and of 50 mm/min respectively. After one pass, samples are cooled to room temperature and subsequently, one more 100% overlapping pass was carried out over first pass referred to here after as two-pass sample. The FSP machine and processed samples are shown in Fig. 1. Electron back scattered diffraction (EBSD) study was carried out using FEI Novo 200. Samples for EBSD were ground with successively finer grades of emery paper and polished with 1 μm diamond paste. Samples were then electropolished using Struers Electropol-5. The electrolyte was a mixture of methanol and perchloric acid in the ratio of 80:20 and the electropolishing was carried out at 18 V for 20 s at a temperature of –5 °C.

Table 1 Chemical composition of the 2507 SDSS sample

Elements	C	S	P	Mn	Si	Cr	Ni	Mo	Cu	N	Fe
wt%	0.016	0.003	0.023	0.72	0.25	25.20	6.9	3.79	0.19	0.26	Balance

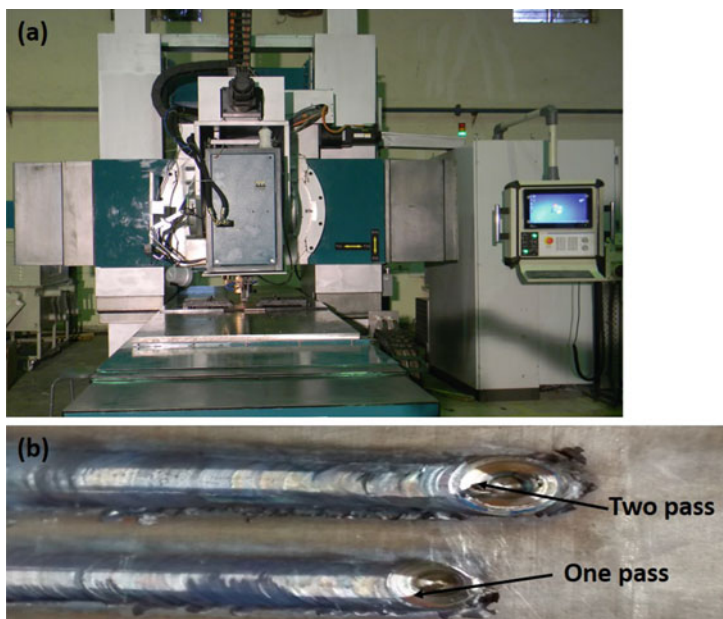


Fig. 1 The photographs show the **a** FSP machine used and **b** the processed samples (one and two pass)

For the electrochemical study, specimens of dimensions $10 \text{ mm} \times 4 \text{ mm}$ were machined from the base metal (2507 SDSS), stir zone (SZ) of one-pass and SZ of two-pass samples. These samples were soldered to copper wire (on unexposed face) to maintain electrical conductivity with sample and mounted in resin. Samples were ground with emery paper up to 2500# and then polishing were carried out with $1 \mu\text{m}$ diamond paste. A three-electrode flat cell setup, consisting of working electrode (base metal, SZ of one-pass and SZ of two-pass), a platinum mesh as the counter electrode and a standard calomel electrode (SCE) as the reference electrode, was used for all the electrochemical measurements. The electrolyte used for the electrochemical measurement was 3.5 wt% NaCl solution. All the electrochemical measurements were carried out on a computer controlled Auto lab Potentiostat PGSTAT30 with GPES and FRA2 (4.9 version) module software. In order to check the repeatability of results, measurements were conducted on three samples, each from the base metal, SZ of one-pass sample and SZ of two-pass sample. Potentiodynamic polarization tests were carried out using a scan rate of 0.167 mV/s . The capacitance measurements based on Mott-Schottky (M-S) theory was carried out at an applied potential range of -300 to 100 mV vs SCE at a frequency of 1 kHz and perturbing AC amplitude of 10 mV .

Results and Discussion

Microstructural Characterization

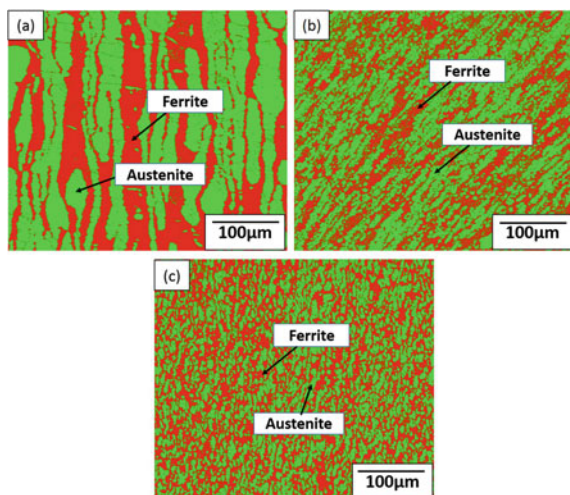
Figure 2 shows that EBSD phase map of the base metal, SZ of one pass and SZ of two pass samples. It can be seen that base metal contains elongated grains of ferrite and austenite. The grains size is considerably reduced in SZ of one pass sample. Further, grain size is reduced with increasing the number of passes. The refinement of grain size in the SZ is attributed to the dynamic recrystallization [7]. It is believed that restoration process in ferrite and austenite is dynamic recovery and dynamic recrystallization respectively [8]. Santos et al. [9] suggested that under the severe deformation of duplex stainless steel, a shift in restoration mechanism of ferrite from dynamic recovery to continuous dynamic recrystallization may occur.

Potentiodynamic Polarization Measurements

In order to study the electrochemical behaviour, polarization study was carried out. Figure 3 shows the potentiodynamic polarization plots for base metal, one pass and two pass samples. The anodic and cathodic Tafel slopes increase with FSP passes, indicating reduction in the rates of anodic and cathodic reactions. A maximum corrosion current density is observed for the base metal and a minimum for the two pass sample. Further, the potentiodynamic polarization curves clearly show that FSP leads to lower passive current density.

From the potentiodynamic results, it appears that grain refinement (more fraction of grain boundaries) obtained during FSP provides better conditions for forming the

Fig. 2 EBSD phase map **a** base metal, **b** SZ of one pass and **c** SZ of two pass



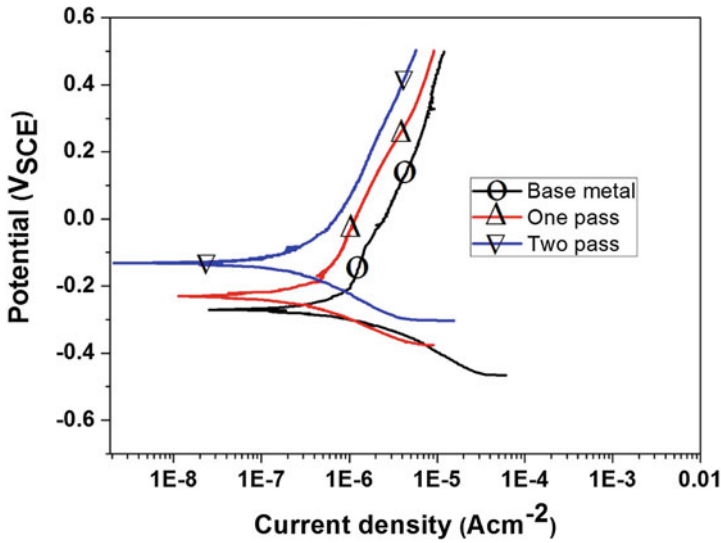


Fig. 3 Potentiodynamic polarisation plots of base metal and its FSPed samples in 3.5 wt% NaCl at 25 ± 2 °C

passive films. Few researchers have suggested that grain boundary acts as a high diffusivity path (grain boundaries) for diffusion of chromium which leads to faster growth kinetics of passive film and also Cr enrichment of the passive film [3, 10]. However, Gupta et al. [11] have reported that faster diffusion of Cr through bulk and grain boundary is not possible due to a very low value of diffusivity at room temperature. The reported values of diffusion coefficient of Cr in BCC Fe at room temperature through bulk and grain boundary are 9.4×10^{-48} m²/s and 4.1×10^{-40} m²/s respectively. These low values of diffusion coefficient at room temperature may not be a probable reason for enrichment of Cr in the passive film and hence for significant improvement in corrosion resistance. These contradictory views could be reconciled as follows. According to the theory of passivity of stainless steel, selective dissolution of Fe occurs while Cr forms a stable oxide layer. It is believe that finer grain sample surface are more reactive resulting in enhancement of Fe dissolution and the Cr oxide formation and hence better passivation behaviour. However, further work needs to be done to support this hypothesis.

Capacitance Measurement

Mott-schottky theory has been used extensively in the literature for the characterization of the semiconducting property of the passive film formed on the metal surface. According to the M-S theory, the space charge capacitance (C) for n-type

and p-type semiconductor is given by Eqs. (1) and (2) assuming that the capacitance of the Helmholtz layer could be neglected [3],

For n-type semiconductor,

$$\frac{1}{C^2} = \frac{2}{e\epsilon_r\epsilon_0N_D} \left[E - \varphi_{fb} - \frac{kT}{e} \right] \tag{1}$$

For p-type semiconductor,

$$\frac{1}{C^2} = - \frac{2}{e\epsilon_r\epsilon_0N_A} \left[E - \varphi_{fb} - \frac{kT}{e} \right] \tag{2}$$

where N_D is the donor density for n-type semiconductor, N_A is the acceptor density for p-type semiconductor, E is the applied potential, φ_{fb} is flat-band potential, k is Boltzmann constant ($1.38 \times 10^{-23} \text{ J K}^{-1}$), e is electron charge ($1.6 \times 10^{-19} \text{ C}$), ϵ_r is the dielectric constant of the passive film (usually taken as 15.6) [10], ϵ_0 is the vacuum permittivity ($8.85 \times 10^{-14} \text{ F cm}^{-1}$), and T is absolute temperature. M-S plots (C^{-2} vs E) for passive films formed on base metal, one-pass and two-pass samples, measured at 1 kHz in 3.5 wt % NaCl solution at 25 °C, are given in Fig. 4. The donor/acceptor densities calculated from Eqs. (1) and (2) for base metal and its FSPed samples in 3.5 wt% NaCl are shown in Fig. 5. It can be seen that donor/acceptor densities are affected by the grain size. Literature shows that donor/acceptor act as defect and any increase in its density leads to less protection of the passive film [12]. The donor/acceptor density decreased in samples processed

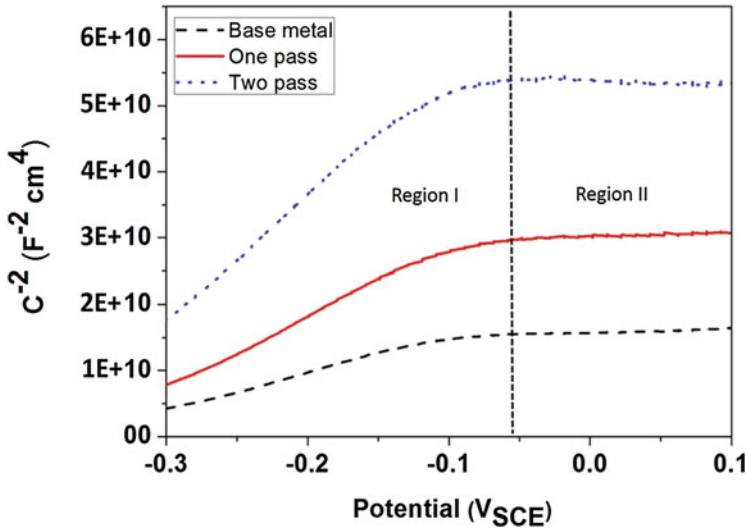


Fig. 4 Mott-Schottky curves for base metal and its FSPed samples in 3.5 wt % NaCl solution at $25 \pm 2 \text{ }^\circ\text{C}$

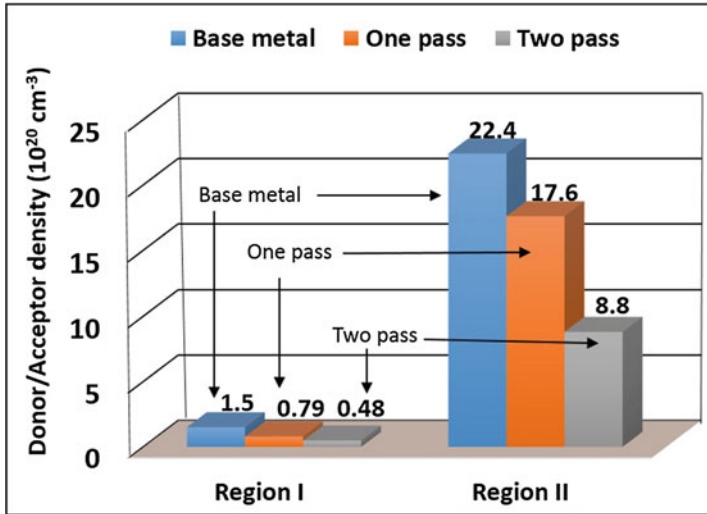


Fig. 5 Variation in donor/acceptor densities of base metal and its FSPed samples in 3.5 wt% NaCl at 25 ± 2 °C

through increased number of FSP passes indicates that passive film formed on the base metal is highly defective. Hence the above result suggests that performing FSP on base metal lowers the defects in the passive film formed on the surface resulting in the compact passive film formation and improved corrosion resistance.

Conclusions

FSP significantly refines the grain size of both ferrite and austenite in SZ through dynamic recrystallization. Based on the potentiodynamic polarization studies, corrosion and passive current density for the FSPed samples were found to lower than the base metal. Mott-Schottky analysis confirmed that oxide film formed on the FSPed samples are less defective resulting in improved corrosion resistance than the base metal.

References

1. Byun S, Kang N, Lee T, Ahn S, Lee HW, Chang W, Cho K (2012) Kinetics of Cr/ Mo-rich precipitates formation for 25Cr-6.9Ni-3.8Mo-0.3 N super duplex stainless steel. *Met Mater Int* 18:201–207
2. Deng B, Jiang Y, Gong J, Zhong C, Gao J, Li J (2008) Critical pitting and repassivation temperatures for duplex stainless steel in chloride solutions. *Electrochim Acta* 53:5220–5225

3. Fattah-alhosseini A, Vafaeian S (2015) Comparison of electrochemical behavior between coarse-grained and fine-grained AISI 430 ferritic stainless steel by Mott-Schottky analysis and EIS measurements. *J. Alloys Compd.* 639:301–307
4. Kashyap BP (2014) Enhancement of flow properties by grain refinement and other structural modification. *Procedia Eng* 86:18–26
5. Ma ZY, Mishra RS, Mahoney MW, Grimes R (2003) High strain rate superplasticity in friction stir processed Al-Mg-Zr alloy. *Mater Sci Eng A* 351:148–153
6. Ma ZY, Mishra RS, Mahoney MW (2002) Superplastic deformation behaviour of friction stir processed 7075Al alloy. *Acta Mater* 50:4419–4430
7. Sato YS, Nelson TW, Sterling CJ, Steel RJ, Pettersson CO (2005) Microstructure and mechanical properties of friction stir welded SAF 2507 super duplex stainless steel. *Mater Sci Eng A* 397:376–384
8. Duprez L, Cooman BC, Akdut N (2002) Flow stress and ductility of duplex stainless steel during high-temperature torsion deformation. *Metall Mater Trans A* 33:1931–1938
9. Santos TFA, Lopez EAT, Fonseca EB, Ramirez AJ (2016) Friction stir welding of duplex and superduplex stainless steels and some aspects of microstructural characterization and mechanical performance. *Mater Res* 19:117–131
10. Sarlak H, Atapour M, Esmailzadeh M (2015) Corrosion behavior of friction stir welded lean duplex stainless steel. *Mater Des* 66:209–216
11. Gupta RK, Raman RKS, Koch CC (2012) Electrochemical characteristics of nano and microcrystalline Fe–Cr alloys. *J Mater Sci* 47:6118–6124
12. Wang L, Kang B, Gao N, Du X, Jia L, Sun J (2014) Corrosion behaviour of austenitic stainless steel as a function of methanol concentration for direct methanol fuel cell bipolar plate. *J Power Sources* 253:332–341

Effect of Heat Treatment on Friction-Stir-Processed Nanodispersed AA7075 and 2024 Al Alloys

I. El-Mahallawi, M.M.Z. Ahmed, A.A. Mahdy,
A.M.M. Abdelmotagaly, W. Hoziefa and M. Refat

Abstract Friction stir processing (FSP) is gaining wide recognition in producing surfaces with high hardness and enhanced properties for light weight transportation application and armored vehicles. This work compares the effect of T6 peak-aging heat treatment on the toughness properties and the aging precipitation behavior of friction stir processed and nanodispersed AA2024 and AA7075 alloys. Plates of aluminum alloy AA7075-O with and without the addition of alumina nano-particles (Al_2O_3) of average size ~ 40 nm were FSP. The AA2024 nanodispersed alloys were prepared by casting, then were FSP. Combining nanodispersion and friction stir processing with peak-aged condition has shown to be an effective route in enhancing the elongation % of AA2024 alloy to double that of the T6 peak aged condition, and improving the impact toughness of AA7075 by 35% compared to the peak aged condition. The presence of nanodispersions affects the precipitation

I. El-Mahallawi (✉)

Faculty of Engineering, Department of Metallurgy and Materials Engineering,
Cairo University, Giza 12316, Egypt
e-mail: ielmahallawi@Bue.edu.eg

M.M.Z. Ahmed

Suez and Sinai Metallurgical and Materials Research Center of Scientific,
Excellence (SSMMR-CSE), Suez University, Suez, Egypt

A.A. Mahdy · W. Hoziefa

Faculty of Engineering, Department of Metallurgy, Mining & Petroleum Engineering,
Al-Azhar University, Cairo 11884 Egypt

M.M.Z. Ahmed · M. Refat

Faculty of Engineering, Department of Mechanical Engineering,
The British University in Egypt, El-Shorouk City 11837, Egypt

A.M.M. Abdelmotagaly

Centre for Advanced Materials, The British University in Egypt,
El-Shorouk City 11837, Egypt

M. Refat

Mechanical Engineering Department, Polytechnic School,
University of Girona, Campus Montilivi s/n, 17071 Girona, Spain

© The Minerals, Metals & Materials Society 2017

Y. Hovanski et al. (eds.), *Friction Stir Welding and Processing IX*,

The Minerals, Metals & Materials Series, DOI 10.1007/978-3-319-52383-5_29

behavior of both AA2024 and AA7075 in peak aged condition, where the precipitates attach themselves to the nanoparticles and spinel type precipitates form resulting de-acceleration of the aging process.

Keywords Nano-surface composite • Friction stir processing • AA7075 • AA2024

Introduction

High strength to weight ratio and absence of ductile to brittle transition temperature has placed aluminum alloys as the major structural material for aircraft construction for the past 60 years [1, 2]. Aluminum based alloys are divided into two categories wrought alloys, and casting alloys. Both categories may be either: heat-treatable alloys (gain their strength by alloying but depend upon solution heat treatment and age hardening (precipitation hardening)), or non-heat-treatable alloys (derive their strength by alloying (e.g. increasing content of Mg) or from work hardening (usually by cold rolling)) [3]. The series of 2xxx and 7xxx aluminum alloys are used in various civil and military industries. Both alloys are recognized for their significant developed strength in the T6 aged condition, however, some of their applications are limited by their relatively low ductility and impact toughness, respectively, as their increase in strength is usually on the expense of their ductility or toughness. When copper is primarily added with small amounts of magnesium, manganese, iron or silicon, the 2xxx alloys gain their strength through the formation of the following intermetallic phases: Super saturated solid solution (ssss) \rightarrow GP zones \rightarrow θ'' \rightarrow θ' \rightarrow θ . These intermediate phases are formed during ageing. GP zone (Guiner Priston) have thickness about 5–10 nm. Initially a single layered hard GP zone of about 5–10 nm thickness is formed, than a multilayered metastable intermediate compound θ'' is formed. As ageing continues θ' is formed from θ'' , but the hardness slightly decreases. After prolonged ageing the equilibrium phase (θ phase) is formed and the hardness further decreases [4]. The 7xxx alloys gain their strength through the formation of complex precipitation of GP zones and (η) (semi-coherent $MgZn_2$) phase (coherent in some lattices and incoherent in others) [5]. This is achieved by solution treatment and controlled aging. These phases are stable in the temperature range of 20–120 °C and 120–250 °C, respectively [6].

Nowadays, additional manufacturing and material design technologies are known to develop increased strength without harming ductility or toughness. Among these technologies are semisolid casting, friction stir processing and nanodispersion. Though heat treatment is always an additional metallurgical process aiming at enhancing the properties of cast or welded parts, the current state of art shows that subsequent heat treatment of heat treatable Al alloys, following nanodispersion and/or friction stir processing, may cause a range of effects between deteriorating and enhancing the final mechanical properties of the manufactured parts [7–17]. The review of literature shows that the effect of heat treatment on the

friction stir processed and the nanodispersed Al heat treatable alloys is still under debate. The aim of this work is to compare the effect of T6 heat treatment following friction stir processing on two important Al heat treatable nanodispersed alloys, which are namely 2024 and 7075 alloys and to correlate these changes with the aging precipitation behavior of these alloys.

Experimental Work

In this work friction stir processed work pieces were prepared from nanodispersed AA7075-O plates and AA2024 semisolid cast nanodispersed billets. FSP experiments were performed using a FSW machine of 22 kW power with 3000 rpm max rotation rate, 1000 mm/min max traverse speed, and 100 kN vertical force. This was followed by subjecting both materials to peak aging conditions. Conventional metallurgical characterization tools were used thereafter.

Preparation of Samples of 2024

The Al 2024 FSP pieces were prepared from commercial wrought billets of the chemical composition shown in Table 1. Cast samples were prepared by compo casting, where after melting and degassing the melt was brought down from 700 °C to the semi-solid state (590–605 °C) and hence 1 wt% 50 nm Al₂O₃ nano-particles were added simultaneously with mechanical stirring for 5 min at 800 rpm. The cast billets were then subjected to FSP, using a pin made from H13 heat-treated steel of 55 HRC hardness, 7 mm probe diameter, 7 mm probe length and 25 mm diameter shoulder. The FSP conditions used where: 400 rpm with linear speed of 20 mm/min. Full details of the work piece preparation is given elsewhere [18, 19]. The 2024 FSP samples where then solution treated at 500 °C for 3 h followed by water quenching. The solution treated samples were artificially aged at 190 °C for 12 h. The heat treatment (T6), of the AA2024/Al₂O₃ composite was carried out once before and another after FSP to evaluate its effect on the ageing precipitates.

Table 1 Chemical composition of commercial wrought AA2024

Composition (wt%)	Cu	Mg	Mn	Fe	Si	Zn	Cr	Al
2024	4.39	1.26	0.57	0.50	0.50	0.25	0.10	Bal.
7075	1.259	2.224	0.021	0.176	0.054	5.178	0.149	Bal.

Preparation of Samples of 7075

Aluminum alloy AA7075-O plates (of the chemical analysis shown in Table 1) were used in the O temper (annealed) condition (64HV). Al_2O_3 nanoparticles with average size of 40 nm were used for reinforcement. Work pieces were prepared with a length of 200 mm and width of 75 mm. A groove (4.5 mm deep and 2 mm wide) was machined through the surface of the AA7075 along the whole length of the piece. Al_2O_3 nanoparticles were packed into the groove after closing the sides of the groove to prevent escaping of the nanoparticles during FSP. A probeless tool made from H13 heat treated tool steel of dimensions of 6.2 mm probe diameter, 5.3 mm probe length and 19 mm diameter shoulder was used for top closing of the groove at the same FSP parameters used. The FSP conditions used where: constant traverse speed of 40 mm/min, rotation rate 500 rpm and tool tilt angle was set at 3°. The plate was subjected to 4 passes based on results found by previous work by the authors [20]. The FSP tool rotation direction was reversed every each pass. After FSP the material of O temper condition was subjected to T6 temper heat treatment by solution treatment at 515 °C and water quenching followed by artificial ageing at 120 °C for 12, 24, 36, 48 and 60 h.

Microstructural Examination

A number of material characterization tests were carried out including optical micrography and scanning electron microscopy investigations. After FSP and heat treatment, samples from each condition were cut (perpendicular to the processing direction) and prepared for metallographic examination according to the standard preparation methods. The samples were examined using Olympus optical microscopy. After etching using diluted Keller's reagent of chemical composition (190 ml distilled water, 3 ml HNO_3 , 5 ml HCL and 2 ml HF) for 30 s. Samples coated by gold sputter coater (SPI-module) were examined under X-ray micro-analyzer (Module Oxford 6587 INCA x-sight) attached to SEM (JEOL-JSM-5500 LV) by using high vacuum mode at 20 kV after gold coating.

Mechanical Testing

Hardness, micro-hardness measurements, impact toughness and tensile tests were used in this study. The micro-hardness tests were made on a Vickers micro-hardness testing machine where a number of at least 20 readings were taken at 1 mm intervals, using load of 1 kg for 15 s dwell time through the whole processed zone. The impact toughness testing was done on a JB-W500 Impact Testing Machine, using a 15 kg Pendulum, on notch-less specimens of 10 × 10 × 60 mm dimensions.

Results and Discussion

Mechanical Properties of AA2024

The Average UTS of the cast and friction stir processed samples are shown in Fig. 1, and the elongation percentages are shown in Fig. 2. The cast samples have UTS of 197 MPa and 217 MPa for AA2024 without and with nanodispersion, respectively. The elongation % of AA2024 and AA2024/Al₂O₃ nanocomposite show that the nano reinforced AA2024 has higher elongation percentage compared to AA2024. After friction stir processing, the FSPed samples showed higher UTS values for both AA2024 and AA2024/Al₂O₃ which was 212 MPa and 247 MPa, respectively as shown from Fig. 1. However, the elongation % also increased to be 4% for AA2024 and 8% for AA2024/Al₂O₃. FSP caused a slight increase in UTS (7% for the monolithic alloy and 15% for the nanodispersed alloy), whereas the elongation % almost doubled after FSP. The heat-treated samples showed even higher UTS values as shown in Fig. 1 for the monolithic alloy as the UTS increased from 212 to 230 MPa, but the elongation percentage remained at about 4.2%. Friction stir processing for the T6-AA2024/Al₂O₃ heat-treated samples (before FSP) showed a dramatic drop in UTS to about (155 MPa), this decrease in UTS value was associated with cracking of the base metal. When FSP was conducted on solution treated AA2024/Al₂O₃, followed by T6 heat treatment, a higher UTS value of 259 MPa was reported. The elongation % of this sample reached 10%.

The average Vickers hardness values of the cast and friction stir processed samples are shown in Fig. 3. The hardness values of the FSPed AA2024 and FSPed AA2024/Al₂O₃ were 114.7 and 118.5 HV, versus as cast reported values of 94 HV and 77.5 HV, respectively. The hardness values of the heat-treated cast sample T6-AA2024/Al₂O₃ before and after FSP remained the same. The highest hardness value was reported for the sample, which was solution-treated, then friction stir processed followed by artificial ageing T6, where the hardness reached 128 HV.

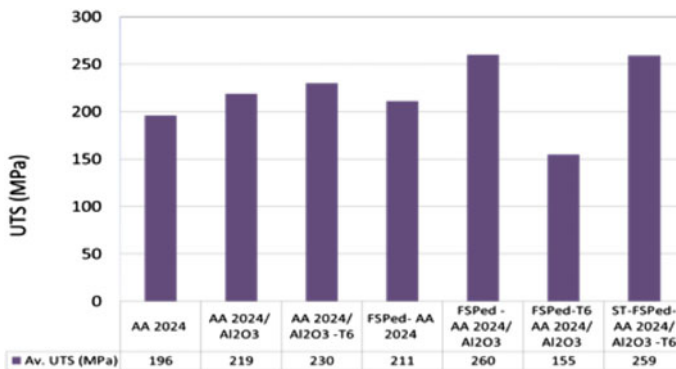


Fig. 1 Average UTS in (MPa) for AA2024 samples

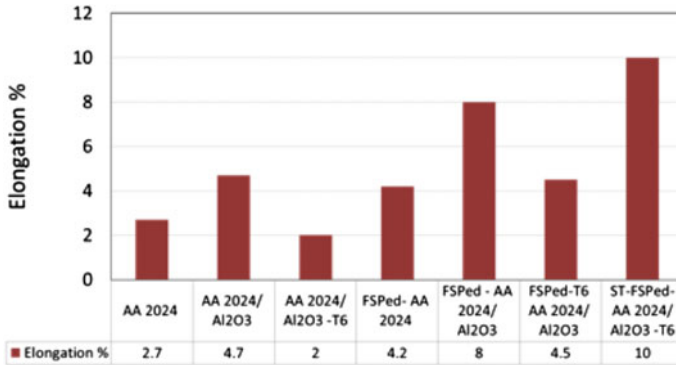


Fig. 2 Elongation % for AA2024 samples

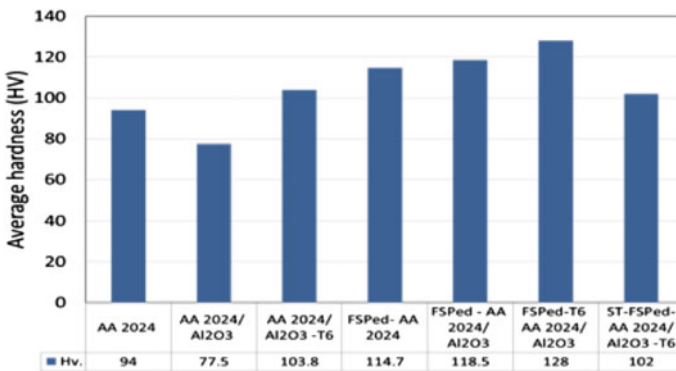


Fig. 3 Average hardness (HV) for AA2024 samples

The results reveal a very interesting observation, which is that, both FSP samples of AA2024/Al₂O₃ with and without T6 heat treatment showed an UTS of 260 MPa, but the T6 heat treated sample (after FSP) showed an increase in elongation % from 8 to 10% accompanied with a slight drop in hardness from 119 to 102 HV.

Mechanical Properties of AA7075

It can be seen from Fig. 4 that for the AA7075 alloy, the average hardness in the nugget zone was 120 HV after 4 passes FSP for the material without nanodispersion and 140 HV for the material with nanodispersion after solution treatment. Aging for 12, 24, 36 and 48 h caused further increase in the average hardness to 177, 200, 214 and 210 HV for the material without nanodispersion, respectively.

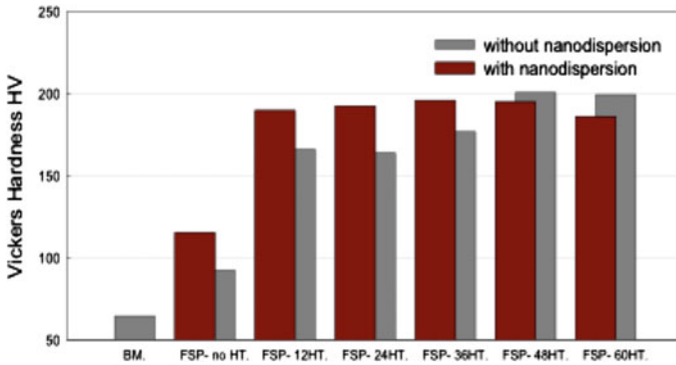


Fig. 4 Average hardness values for AA7075 before and after heat treatment

Also, aging for the same period of time caused an increase in hardness to 195, 202, 199 and 175 HV, respectively for the material with nanodispersion. It can be observed from Fig. 4 that the addition of nanoparticles during FSP results in an increase in the hardness of the NZ. However, after heat treatment (solution treatment at 515 °C for 1.5 h and age hardening at 120 °C for different times) very slight difference observed in the hardness between the two cases, with and without nano particle additions. This suggests that adding nanoparticles during FSP will tend to conceal or suppress the effect of heat treatment, probably due to the formation of different type of precipitates. The increase in hardness with aging time continues till 48 h, after which the hardness decreases for both without and with nanodispersion cases. At 48 h the hardness of the nanodispersed material is less than the monolithic (without nanodispersion) material.

Charpy impact notch-less samples were prepared perpendicular to the nugget zone such that the FSP zone is in the middle, in order to evaluate the pure material effect of microstructure alone without introducing a notch effect. The specimens were hit on the FSP zone perpendicular to the nugget. Figure 5 shows the change in impact toughness for all samples. It can be seen that generally the monolithic samples without nanodispersion had higher impact toughness (154–180 J), compared to those with nanoparticles and aged for the same time (103–134 J). This is explained by the effect of the groove (as the nanoparticles-containing samples were prepared by embedding the nanoparticles in a groove), and this groove produced a notch effect on the specimens. The highest impact toughness was obtained for both with and without nanodispersion after 48 h aging. Figure 5 also shows that the maximum toughness was obtained for both the monolithic and nanodispersed alloys after aging for 48 h: 134 and 181 J, respectively. This is associated with the highest hardness values (Fig. 4), also shown for this condition. After 60 h aging, a drop in the impact toughness occurred. However, the hardness of the monolithic alloy did not show similar drop. The optimized hardness-impact toughness was achieved for

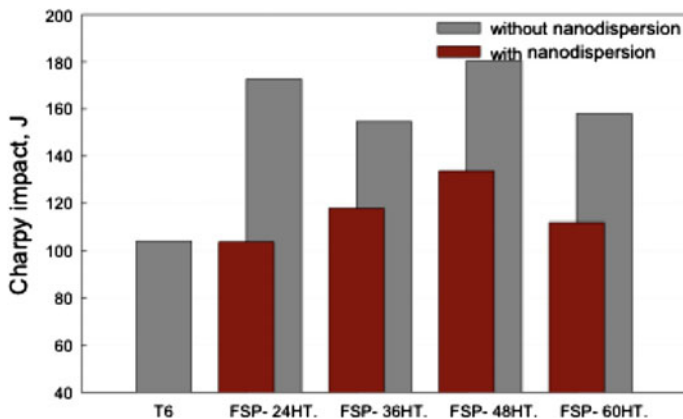


Fig. 5 Impact toughness for all ageing conditions for AA7075 samples with and without nanodispersion

the 48 h. alloy for both with (198 HV–134 J) and without (213 HV–181 J) nanodispersed conditions. Though the FSPed alloy without nanodispersion showed higher values of both hardness and impact toughness, the nanodispersed alloy exhibited features of ductile fracture of the surface.

Microstructure Characterization of T6 Heat Treated FSP AA2024 Alloy

Figure 6 shows the dispersion of precipitates around the globular grains of AA2024/ Al_2O_3 . The homogeneous distribution of the Al_2O_3 particles around the grain boundaries is shown from the lower magnification images, Fig. 6a and c. Al_2O_3 reacts with many divalent transition metal oxides to form aluminates, which are isostructural with spinels of composition Al_2O_3 and MgO [7]. Spinel forms by (1) the reaction of Al_2O_3 and MgO produced from direct oxidation of Mg in the melt, or (2) the reduction of Al_2O_3 in the particles by Mg, or (3) preferential formation of fine Al_2O_3 from oxidation of the melt. Whatever the mechanism is, a large thermodynamic driving force exists for spinel formation, which increases with increase in Mg content. Precipitates were found in the voids or in the cavity structure and they were reduced in size but not eliminated by FSP. The Al_2O_3 particles morphology was detected in several voids as shown in Fig. 6a. Figure 6a and b show the nanoparticles distribution in the as-cast condition, with many nanoparticles agglomerating in clusters. Nanoparticles clustering increases levels of local stress and provides crack nucleation sites and low energy propagation routes [21]. The severe deformation of the aluminum matrix after friction stir processing shown in Fig. 6c and d decreases the porosity content, which creates stronger bonding

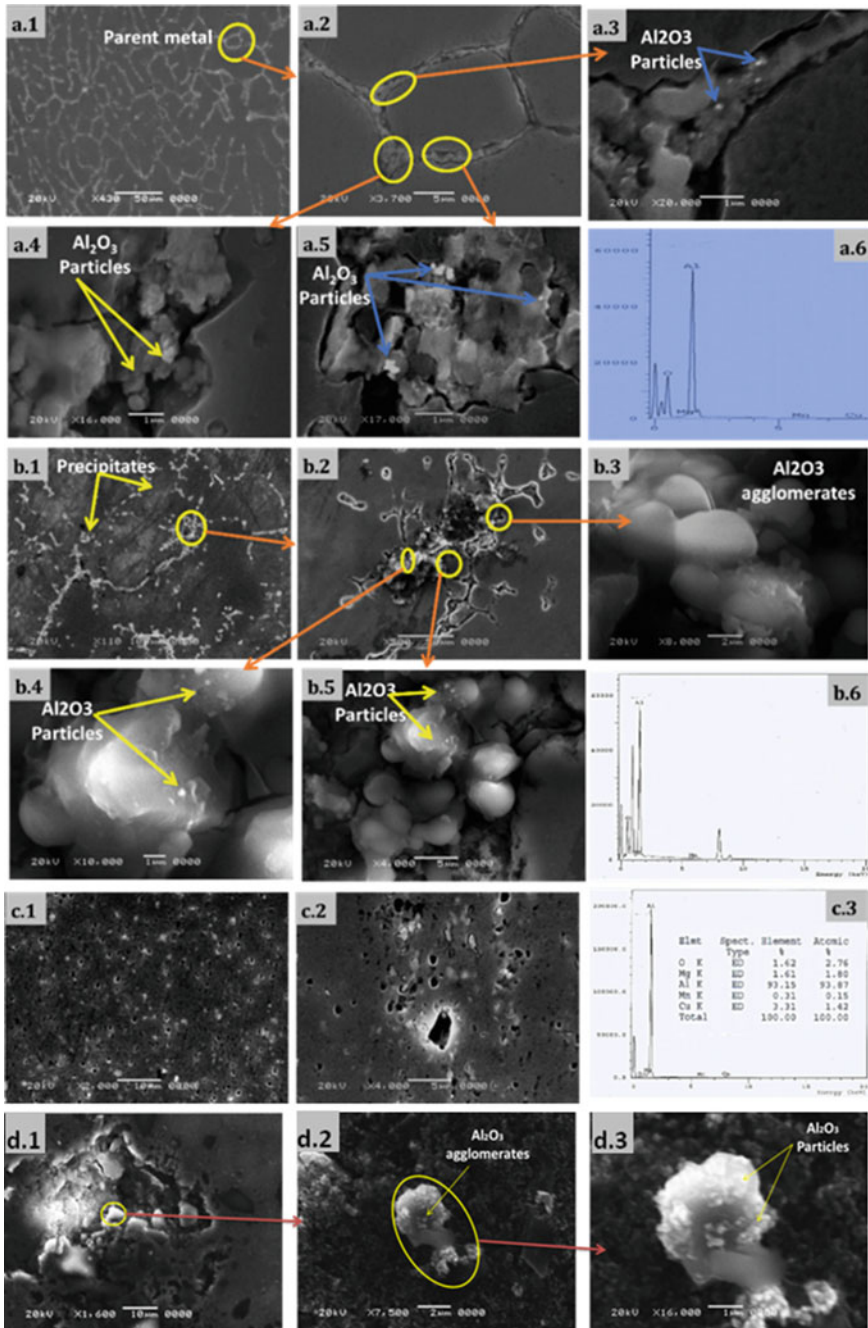


Fig. 6 a SEM Micrographs of (a) Cast AA2024/Al₂O₃ showing grain boundary precipitation of Al₂O₃, b heat treated cast AA2024/Al₂O₃, (solution treated at 500 °C for 3 h, then quenched followed by ageing at 190 °C for 12 h) show clusters of precipitates and CuO in the treated sample, c FSPed AA2024 nugget zone (400 rpm, 20 mm/min), d FSPed AA2024/Al₂O₃ nugget zone (400 rpm, 20 mm/min)

between the aluminum layers, imparting higher strength and elongation to the processed materials. The increase in elongation % age after FSP and T6 heat treatment is attributed to the refining of grain size induced by FSP, reducing the clustering of nanoparticles as a result of FSP and to the formation of modified precipitates attached to the nanoparticles.

The precipitation can be explained as follows: after solution treatment, whilst most of the non-equilibrium second phase (Cu Al_2) and (Cu Mg Al_2) of the matrix has dissolved, a thin ring of (Cu) is left around the Al_2O_3 particles as shown in Fig. 6b. Thermodynamically, the formation of CuAl_2O_4 spinel or CuO will be hindered by the presence of Mg, which would preferentially form a magnesium spinel, MgAl_2O_4 , or MgO. Further, during ageing Cu Al_2O_4 becomes unstable and decomposes into CuO and Al_2O_3 . However, the more stable $\text{Mg Al}_2\text{O}_4$ could envelope the Cu spinel, preventing outward diffusion of copper [22]. Thus, the concentration of Cu in the matrix in the AA2024 A1 alloy will affect the precipitation process. This reduction in Cu concentration might be the reason for the deaccelerated ageing of the composite.

Microstructure Characterization of T6 Heat Treated FSP AA7075 Alloy

It can be revealed from the lower magnification Fig. 7a that the dispersion of the alumina nanoparticles is less homogeneous than the case of the AA2024 alloy. This is attributed to the manufacturing method in both cases, where the nanoparticles were added during casting in the first case, and during friction stir processing in the second case. However, similar evidence was obtained on the fracture surface of the AA7075 to the AA2024, where alumina particles were identified attached to the precipitates of CuZnMg, Fig. 7b–d. The increased toughness after FSP was studied by the authors at a previous stage [23] and was explained to be a result of the high angle grain boundaries developing in the recrystallized grains in the nugget zone. The holding at the aging temperatures for 48 h caused the strain hardened low angle grain boundaries to develop into the high angle grain boundaries. The formation of modified type of precipitates in presence of the alumina nanoparticles may also attribute to the enhancement in toughness, but this needs further investigation by TEM and is beyond the scope of this work.

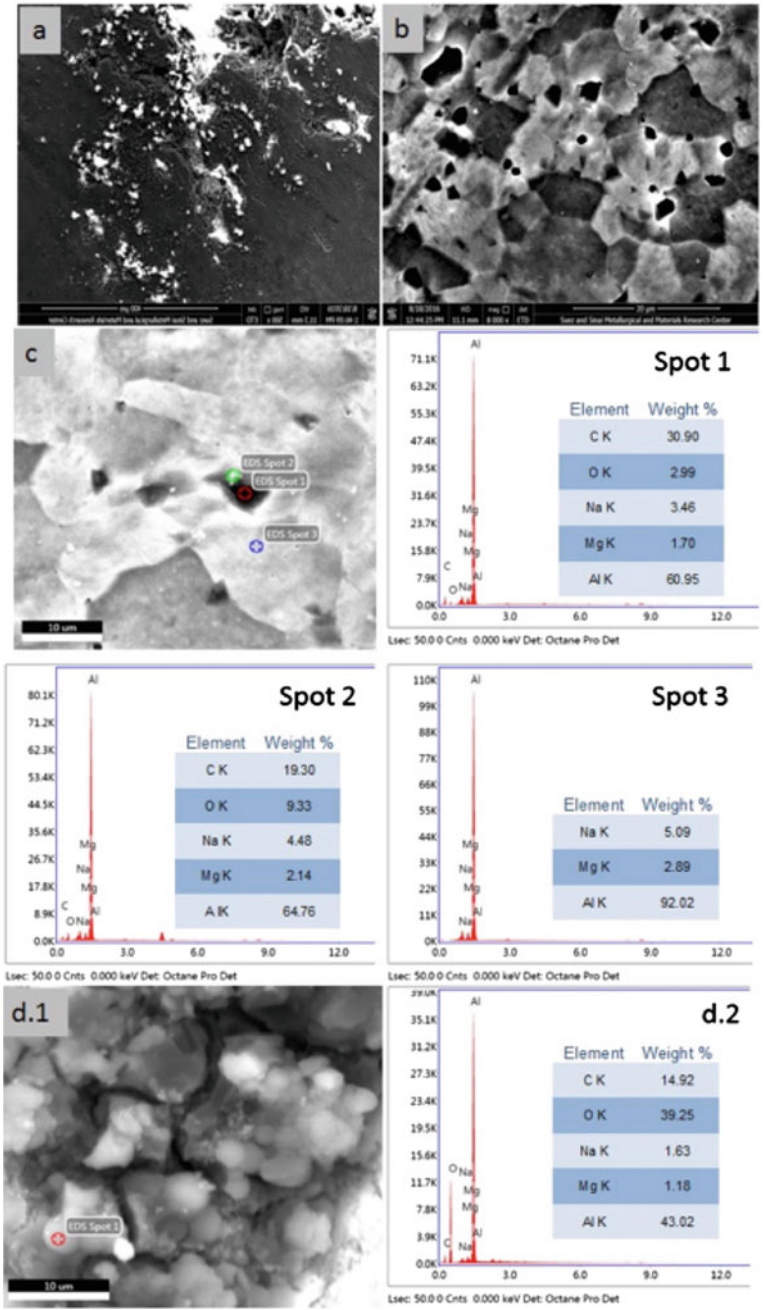


Fig. 7 SEM images for the AA7075 specimen with nanoparticles friction stir processed and aged for 48 h with an EDEX analysis of a nanoparticle

Conclusions

This work has shown that combining nanodispersion and friction stir processing with peak aged condition has shown to be an effective route in enhancing the elongation % of AA2024 alloy to double that of the T6 peak aged condition, and improving the impact toughness of AA7075 by 35% compared to the peak aged condition, with insignificant change of the hardness. The presence of nanodispersions affects the precipitation behavior of both AA2024 and AA7075 in peak aged condition, where the precipitates attach themselves to the nanoparticles and spinel type precipitates form resulting de-acceleration of the aging process.

References

1. King F (1987) Aluminum and its Alloys. Ellis Harwood Series in Metals Materials. Ellis Harwood, Chichester, England, p 193
2. Cobden R, Banbury A (1994) Aluminium: physical properties, characteristics and alloys. TALAT Lecture 1501. European Aluminium Association
3. Hatch E (1984) Aluminium—properties and physical metallurgy (metals park. American Society for Metals, Ohio. ISBN 0-87179-176-6
4. Ringer SP, Hono K (2000) Microstructural evolution and age hardening in aluminium alloys: atom probe field-ion microscopy and transmission electron microscopy studies. *Mater Charact* 44:101–131
5. Santosh Kumar, Namboodhiri TKG (2011) Precipitation hardening and hydrogen embrittlement of aluminum alloy AA7020. *Bull Mater Sci* 34(2):311–321
6. Berg LK, Gjnnes J, Hansen V, XZ Li, Knutson-Wedel M, Waterloo G (2001) GP zones in Al–Zn–Mg alloys and their role in artificial ageing. *Acta Mater* 49:3443–3451
7. Abdel-Azim AN, Shash Y, Mostafa SF, Younan A (1995) Casting of 2024-Al alloy reinforced with Al₂O₃ particles. *J Mater Process Technol* 55:199–205
8. Rahimi B, Khosravi H, Haddad-Sabzevar M (2015) Microstructural characteristics and mechanical properties of Al-2024 alloy processed via a rheocasting route. *Int J Min Metall Mater* 22(1):1–9
9. Curle UA (2010) Semi-Solid near-net shape rheocasting of heat treatable wrought aluminum alloys. *Trans Nonferrous Met Soc China* 20:1719–1724
10. El-Mahallawi I, Abdelkader H, Yousef L, Amer A, Mayer J, Schwedt A (2012) Influence of Al₂O₃ nano—dispersions on micro structure features and mechanical properties of cast and T6 heat-treated Al Si hypoeutectic alloys. *Mater Sci Eng, A* 556:1–12
11. Ma ZY, Sharma SR, Mishra RS (2006) Effect of friction stir processing on the microstructure of cast A356 aluminum. *Mater Sci Eng* 433:269–278
12. Hu WZ, Yuan S, Wang X, Liu G, Huang Y (2011) Effect of post-weld heat treatment on the microstructure and plastic deformation behavior of friction stir welded 2024. *Mater Des* 32:5055–5060
13. Ahmed MMZ, Refat M, El Mahallawi I (2014) Manufacturing of nano surface AA7075 composites by friction stir processing. *Light Met* 1417–1422
14. Naeem Haider T, Mohammed Kahtan S, Ahmad Khairil R (2015) Effect of friction stir processing on the microstructure and hardness of an aluminum–zinc–magnesium–copper alloy with nickel additives. *Phys Met Metall* 116(10):1035–1046
15. Aydin GH, Bayram A, Aguz A, Akay KS (2009) Tensile properties of friction stir welded joints of 2024 aluminium alloys in different heat-treated- state. *Mater Des* 30:2211–2221

16. Singh RKR, Shanna Chaitanya, Dwivedi DK, Mehta NK, Kumar P (2011) The microstructure and mechanical properties of FSWed Al-Zn-Mg alloy in welded and heat treated conditions. *Mater Des* 32:682–687
17. Sivaraj P, Kanagarajan D, Balasubram V (2014) Effect of post weld heat treatment on tensile properties and microstructure characteristics of friction stir welded armour grade AA7075-T651aluminium alloy. *Defence Technol* 10:1–8
18. Hoziefa W, Toschi S, Ahmed MMZ, Morri Al, Mahdy AA, El-Sayed Seleman MM, El-Mahallawi I, Ceschini L, Atlam A (2016) Influence of friction stir processing on the microstructure and mechanical properties of a compocast AA2024-Al₂O₃ nanocomposite. *Mater Des* 106:273–284
19. Hoziefa W, Ahmed MMZ, Mahdy AA, El-Mahallawi I, Atlam A (2016) Fabrication and development of aluminium 2024 composite reinforced with alumina nano particles using compocasting and friction stir processing. Ph.D. thesis, Faculty of Engineering, Al-Azhar University
20. Refat M, Abdelmotagaly AMM, Ahmed MMZ, El-Mahallawi I (2015) The effect of heat treatment on the properties of friction stir processed AA7075-O with and without nano alumina additions. In: *Friction stir welding and processing VIII*, TMS. Wiley
21. Ardakani M, Amirkhanlou S, Khorsand S (2014) Cross accumulative roll bonding—A novel mechanical technique for significant improvement of stir-cast Al/Al₂O₃ nanocomposite properties. *Mater Sci Eng, A* 591:144–149
22. Abdel-Azim AN, Shash Y, Mostafa SF, Younan A (1995) Ageing behaviour of 2024-Al alloy reinforced with Al₂O₃ particles. *J Mater Process Technol* 55:140–145
23. Refat M, Elashery A, Toschi S, Ahmed MMZ, Morri A, El-Mahallawi I, Ceschini L Microstructure, hardness and impact toughness of heat treated surface nanodispersed and friction stir processed aluminum alloy AA7075”, *JMEP*. doi:[10.1007/s1166501623463](https://doi.org/10.1007/s1166501623463)

Numerical Analysis of FSW Employing Discrete Element Method

Kenta Mitsufuji, Masahito Nambu and Fumikazu Miyasaka

Abstract The Friction Stir Welding (FSW) is known as the non-melting joining technique. The numerical analysis methods employing grid methods for FSW process have been developed. However, the FSW includes the complex phenomena as plastic flow of the substances, temperature flow and a phase transformation. Some complex processes are required to analyze the substances of different physical properties on the bonded interface and the dissimilar joining. This paper proposes the analysis technique for the FSW employing the Discrete Element Method (DEM). The DEM is the analysis technique for that analyze the powders behavior. In this report, a proposal analysis model of plasticity body for FSW simulation is described. Finally, the usefulness is discussed through the analysis result of FSW process.

Keywords Friction stir welding · Discrete element method · Mesh free method

Introduction

The FSW [1] that shown in Fig. 1 is known as the non-melting joining. Therefore, the FSW has been applied to the joining of aluminum for the train body. However, it is difficult to detecting a deflection that is spawned in the substances during the FSW process. As a one approach for the mentioned problem, the numerical analysis models for FSW have been developed and there are many papers about it [2–4]. These methods which use the mesh or grid are difficult to handle such surface deformation. The most frequency used method to calculate the deformation of materials in these papers is Finite Element Method (FEM) [2, 3]. Recently, the analysis method employing Particle method [5] for the plastic flow during the FSW process has been proposed [6]. In the method, the substances are modeled as highly

K. Mitsufuji (✉) · M. Nambu · F. Miyasaka
Department of Adaptive Machine Systems, Graduate School of Engineering,
Osaka University, Osaka 565-0871, Japan
e-mail: kenta.mitsufuji@ams.eng.osaka-u.ac.jp

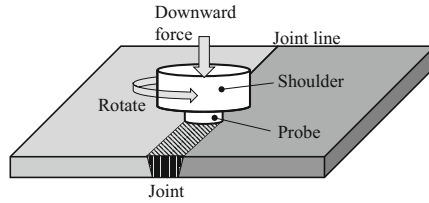


Fig. 1 The schematic diagram friction stir welding

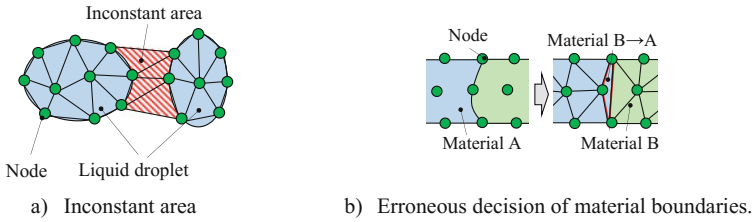


Fig. 2 The topology of mesh in FEM

viscous fluid, a material flow is calculated by MPS method. The stress inside the materials is calculated by FEM. However, FEM requires calculation points in analyzed space. Also, the remeshing process have to be required whenever structural boundaries of material moves. As an example, divided liquid droplets are shown in Fig. 2. In Fig. 2a, the material types of elements between each droplet (the shaded areas) are indefinite. As the result, the analysis for large deformation of materials breaks down during the remeshing process in FEM.

In this paper, the Discrete Element Method (DEM) is employed for analysis technique for solving mentioned problems. This method is the meshless method that does not require grid. The plasticity model to analyze FSW is proposed. Also, the heat flow analysis method is described. Finally, the proposal method is applied to FSW process, the results are shown.

The Discrete Element Method

The Discrete Element Method [7] is the analysis technique that simulates a granular flow. The method treats the contact between the granules and the rotate of granules. The motion equations are shown in Eqs. (1) and (2).

$$ma + cv + kx = F \tag{1}$$

$$I \frac{d^2p}{dt^2} + cr^2 \frac{dp}{dt} + kr^2 p = T \tag{2}$$

Fig. 3 The schematic diagram of Voigt model

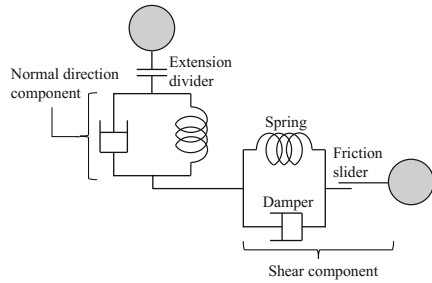
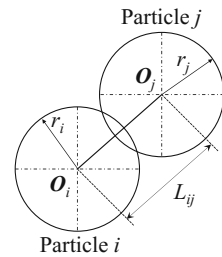


Fig. 4 Positional relationship of the particles



where, in Eq. (1), m is the mass of granules, \mathbf{a} is the acceleration, c is the damping factor, v is the velocity, k is the spring coefficient, \mathbf{x} is the displacement between the contacted granules, \mathbf{F} is the external force. Also, in Eq. (2), I is the inertia, r is the radius of the granule, \mathbf{p} is the rotational displacement and \mathbf{T} is the torque by the external force. These equations are modeled by Voigt model that is shown in Fig. 3. The Voigt model is constructed by the spring-damper systems. However, the tension force between the materials are not transferred by extension divider.

Now, the forces due to collisions between the particles i and j are modeled. The collision is modeled by penetration of the particles during collision. In Fig. 4, two particle collision is shown. Then, the penetration between the particles i and j is presented by the overlap of the particles δ .

$$\delta = (r_i + r_j) - L_{ij}. \tag{3}$$

Also, the normal direction component of the overlap and relative velocity are presented by Eqs. (4)–(6).

$$\delta_n = \delta \mathbf{n}_{ij} \tag{4}$$

$$\mathbf{v}_n = (\mathbf{v} \cdot \mathbf{n}_{ij}) \mathbf{n}_{ij}. \tag{5}$$

$$\mathbf{n}_{ij} = \frac{\mathbf{O}_i - \mathbf{O}_j}{|\mathbf{O}_i - \mathbf{O}_j|}. \tag{6}$$

where, \mathbf{v} is the relative velocity between the particles i and j . Also, The share direction component of the displacement and relative velocity are presented by

$$\delta_s = \int_{t_s}^{t_e} \mathbf{v}_s dt \quad (7)$$

$$\mathbf{v}_s = \mathbf{v} - \mathbf{v}_n + \left(r_i \frac{d\mathbf{p}_i}{dt} + r_j \frac{d\mathbf{p}_j}{dt} \right) \times \mathbf{n}_{ij}. \quad (8)$$

where $t_e - t_s$ is the time during collision of the particles, r is the radius of the particles. Finally, the each components of the contact force and torque of particles i is obtained by

$$\mathbf{f}_n = -k\delta_n - c\mathbf{v}_n \quad (9)$$

$$\mathbf{f}_s = -k\delta_s - c\mathbf{v}_s \quad (10)$$

$$\mathbf{T} = r\mathbf{n}_{ij} \times \mathbf{f}_s. \quad (11)$$

Heat Flow Analysis Method

In the analysis method for FSW process, the heat flow analysis method is important. The heat transfer equation is shown in Eq. (12).

$$\frac{DT}{Dt} = \frac{\kappa}{c\rho} \nabla^2 T + \frac{q}{c\rho} \quad (12)$$

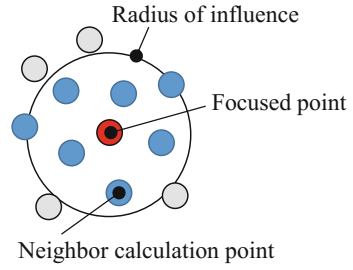
where, T is the temperature, κ is the heat-transfer coefficient, c is the specific heat, r is the density and q is the internal heat generation. In proposal analysis method, Eq. (12) is discretized by mesh-free method based on the Weighted Least Square Method (WLSM) [8].

Then, the distribution of temperature in the analyzed space is able to be assumed as a second order polynomial function. The function of temperature as follows:

$$T_i(x, y, z) = \tau + a_1x + a_2y + a_3z + a_4x^2 + a_5xy + a_6y^2 + a_7yz + a_8z^2 + a_9xz \quad (13)$$

where T_i is the temperature at the calculation point i , a_k ($k = 1-9$) are the coefficients of the function and x, y, z are coordinates of neighbor calculation points on a coordinate system with the origin at the coordinate of calculation point i . Then, the weighted square sum of the error between the approximated distribution and the real distribution is presented by

Fig. 5 Influence radius and neighbor calculation points



$$E = \sum w_{ij} \{T_i(x_j, y_j, z_j) - T_j\}^2. \tag{14}$$

where x_j, y_j, z_j are coordinates of the calculation point j and the T_j is the temperature at the calculation point j . The weight w_{ij} is presented by spline weight function as shown in Eq. (15).

$$w_{ij} = 1 - 6\left(\frac{r_{ij}}{R}\right)^2 + 8\left(\frac{r_{ij}}{R}\right)^3 - 3\left(\frac{r_{ij}}{R}\right)^4 \tag{15}$$

where r_{ij} is the distance between the calculation point i and j , R is the influence radius. The neighbor calculation points are selected by the radius (in Fig. 5).

The derivative of T_i as the coordinate of calculation point i is presented by the coefficient a_k . The laplacian of T_i is presented by

$$\nabla^2 T_i = \frac{\partial^2 T_i}{\partial x^2} + \frac{\partial^2 T_i}{\partial y^2} + \frac{\partial^2 T_i}{\partial z^2} = 2(a_4 + a_6 + a_8). \tag{16}$$

After that, the temperature is updated by following formula.

$$T_i^{t+1} = T_i^t + \left(\frac{\kappa}{\rho c} 2(a_4 + a_6 + a_8) + \frac{q}{\rho c}\right) dt. \tag{17}$$

Heat Generation

In FSW, the main heat source is the friction between materials and tool, plastically flow. The plastically flow is the obtained by the equivalent plastic strain and equivalent stress. The equivalent strain velocity is shown in Eq. (18).

$$\dot{\epsilon} = \sqrt{\frac{2}{3} \dot{\epsilon}_{ij} \dot{\epsilon}_{ij}}. \tag{18}$$

where $\dot{\epsilon}_{ij}$ is the strain velocity tensor as shown in (19).

$$\dot{\epsilon}_{ij} = \frac{1}{2} \left(\frac{dv_i}{dx_j} + \frac{dv_j}{dx_i} \right). \quad (19)$$

The equivalent stress is obtained by the temperature and equivalent strain velocity as shown in Eqs. (20) and (21).

$$\sigma = \frac{1}{\alpha} \ln \left\{ \left(\frac{Z}{A} \right)^{\frac{1}{n}} + \left[\left(\frac{Z}{A} \right)^{\frac{2}{n}} + 1 \right]^{\frac{1}{2}} \right\} \quad (20)$$

$$Z = \dot{\epsilon} \exp \left(\frac{Q}{RT} \right). \quad (21)$$

where α , A , n and Q are unique value of material, R is the gas constant. The heat generation by the plastically flow is obtained by Eq. (22).

$$q = \gamma \sigma \dot{\epsilon} \quad (22)$$

where γ is the heat-transduction ratio. In this case, 90% of the work for plastic deformation is transformed into heat. It was chosen based on the experimental rules [6].

Analysis Result

In this section, the analyzed model is described. In DEM process, the damping factor η that is related with temperature is considered. In this case, the damping factor is presented by Eq. (23).

$$\eta = \eta_0 \exp \left(- \frac{T}{\lambda} \right) \quad (23)$$

where, λ is the constant value, T is the temperature. On DEM, the plastic body is modeled by Voigt model as shown in Fig. 6. In the Fig. 6a, the particles are covered with a viscosity region. In the Fig. 6b, the extension divider is replaced with the damper. The damping factor of the damper is given by Eq. (23). The plastic flow in the FSW process is simulated by DEM employed this model.

The analyzed model and analysis conditions are shown in Fig. 7 and Table 1. The properties of A1100 are obtained by [9]. The particles are placed in the cubic closest packing. Also, the edge of material (water colored) is the temperature

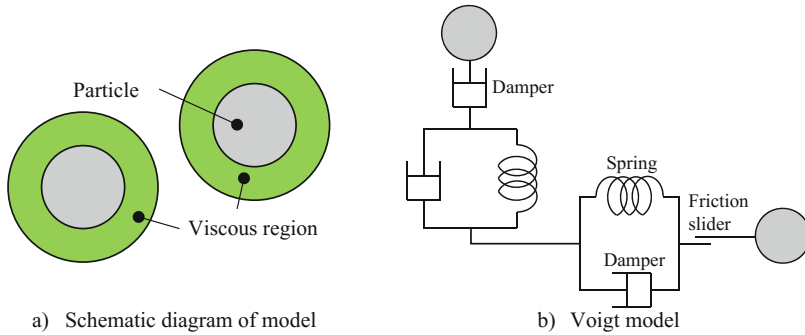
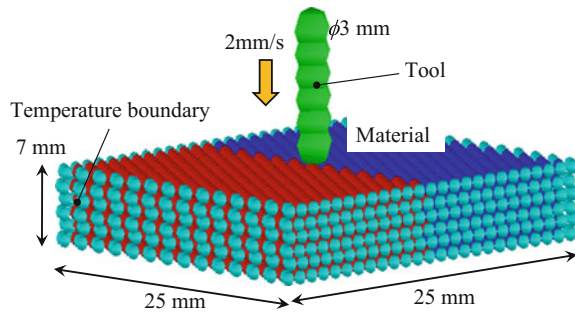


Fig. 6 The elastic plastic body model

Fig. 7 Schematic diagram of the analyzed model



boundary. The temperatures on the boundaries are room temperature. In this analysis, the bonded materials are the same. The material is the pure aluminum.

The particle size was chosen in consideration of the calculation time and the stability.

As the analyzed results, the physical value distributions are shown in Fig. 8. Then, Fig. 8a shows the temperature distribution, b shows the calorific value, c shows the equivalent stress and d shows the strain velocity. In the Fig. 8a, the temperature around the tool is increased. The calorific value has the distribution as same as the strain velocity. Therefore, the calorific value from plastic flow is the more dominant than friction heat. It seems that the material temperature will reach to mechanical melting temperature. Also, the bias of the distribution is produced by the initial placement of particles, and low resolution. According to Fig. 8c, the equivalent velocity is distributed on the center part and edge of material. It was occurred by the fine vibration of particles by the propagation of contact forces.

Table 1 Analysis conditions

Material	A1100
Density (kg/m ³)	2700
Thermal conductivity (W/m · K)	236
Specific heat (J/Kg · K)	880
α (MPa ⁻¹)	0.045
A	exp(24.67)
n	5.66
Q	158300
Number of particles	4026
Particle diameter (mm)	1.0
Spring coefficient k (N/m)	1000
Damping factor c (Pa · s · m)	0.012
Damping factor η_0 (Pa · s · m)	0.5
Friction coefficient	0.4
Room temperature (K)	300
Time interval (μ s)	2
Rev. of tool (rpm)	520
Diameter of tool (mm)	3.0
Number of steps	500000
CPU time/step (ms)	150

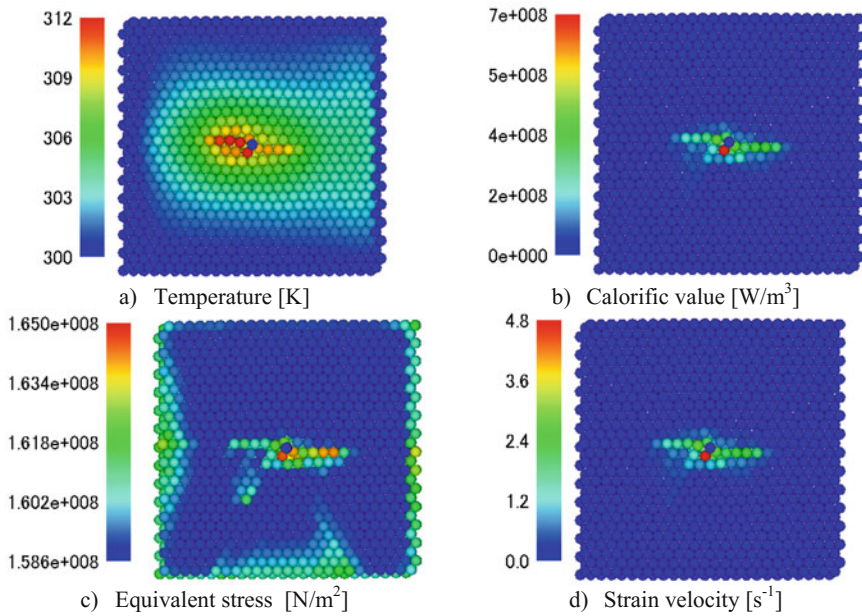


Fig. 8 The distributions of the physical value at 150 ms

Conclusion

In this paper, the analysis technique employed DEM for analysis of FSW process is proposed. The proposal method does not required the mesh through the analysis. Thus, the mentioned problems on the reported analysis techniques are resolved. The method treats the model of elastic plastic deformation with spring-damper system. Therefore, plastic flow is calculated easily. The method is applied to the simple model of FSW, carried out the analysis of the insertion of tool on the FSW process. Also, in this method, the friction between the materials and tool can be considered. However, DEM is computationally expensive. Therefore, it is difficult to increase analysis resolution. Additionally, the particles placement is the sensitivity of the matter. In future work, the clearly articulated problems must be improved.

Acknowledgements This work was (partly) supported by the New Energy and Industrial Technology Development Organization (NEDO) under the “Innovative Structural Materials Project (Future Pioneering Projects)”.

References

1. Guerdoux S, Fourment L. A 3D numerical simulation of different phases of friction stir welding. *Model Simul Mater Sci Eng* 17(7), art no 075001
2. Ulysse P (2002) Three-dimensional modeling of the friction stir-welding process. *Int J Mach Tools Manuf* 42:1549–1557
3. Guerdoux S, Fourment L (2009) A 3D numerical simulation of different phases of friction stir welding. *Model Simul Mater Sci Eng* 17:075001 (32 pp)
4. Song M, Kovacevic R. Numerical and experimental study of the heat transfer process in friction stir welding. *Proc Inst Mech Eng Part B J Eng Manuf* 217(1):73–85
5. Koshizuka S, Oka Y (1995) Moving-particle semi-implicit method for fragmentation of incompressible fluid. *Nucl Sci Eng Soc* 123:421–434
6. Yoshikawa G, Miyasaka F (2012) Hirata Y, Katayama Y, Fuse T (2012) Development of numerical simulation model for FSW employing particle method. *Sci Tech Weld Join* 17 (4):255–263
7. Mishra BK, Rajamani RK (1992) The discrete element method for the simulation of ball mills. *Appl Math Model* 16(11):598–604
8. Matsuzawa S, Mitsufuji K, Miyake Y, Hirata K, Miyasaka F (2015) Numerical analysis of electromagnetic levitation employing meshless method based on weighted least square method. *J Manuf Sci Prod* 29–34
9. Sheppard T, Jackson A (1979) Constitutive equations for use in prediction of flow stress during extrusion of aluminum alloys. *Mater Sci Technol* 13(3):203–209

Author Index

A

Abdelmotagaly, A.M.M., 297
Ahmed, M.M.Z., 297
Aldanondo, Egoitz, 109
Aoki, Yasuhiro, 119
Arruti, Ekaitz, 109

B

Barker, Erin Iesulauro, 261
Benfer, Sigrid, 179
Bergmann, Jean Pierre, 211, 277
Boettcher, Eric, 147
Boldsaikhan, Enkhsaikhan, 237
Brown, Brian, 237
Bui, Phuonghanh, 237
Busuttill, Peter, 147

C

Cannell, Gary, 39
Carlson, Blair, 147
Catalini, David, 269
Cederqvist, Lars, 249
Champagne, Victor K., 221
Chen, Z.W., 157
Chougule, Sandip, 53
Conrad, Christian, 179
Cook, George E., 79, 91
Couch, Robert, 39
Curtis, Todd R., 3, 221

D

Darsell, Jens, 269
Duncan, Brent, 237
Dymek, Stanisław, 167

E

Echeverria, Alberto, 109
El-Mahallawi, I., 297
Evans, William Todd, 79

F

Field, David P., 125
Frederick, Greg, 39
Fujii, Hidetoshi, 119
Fujimoto, Mitsuo, 237
Fukada, Shintaro, 237
Fürbeth, Wolfram, 179

G

Garpinger, Olof, 249
Gerken, Jan Ansgar, 211
Grant, Glenn, 39, 269
Grätzel, Michael, 277
Gunasekaran, G., 289
Gunter, C., 13

H

Hamilton, Carter, 167
Handyside, Alan, 237
Harrison, Nia R., 197
Hasieber, Michael, 277
Hilton, A., 157
Hovanski, Yuri, 67, 147, 125, 261
Hoziefia, W., 297

I

Ikegaya, Akihiko, 47
Imam, Murshid, 119
Ishida, Kiyohito, 29
Ishizuka, Hiroshi, 47

J

Jarrell, Adam W., 91
Jasthi, Bharat K., 3
Jha, Kaushal, 53

K

Kamimuki, Kenichi, 237
Kashyap, B.P., 53, 289

Kellogg, Brendan, 3
 Kokawa, Hiroyuki, 23, 29, 47
 Kopyściański, Mateusz, 167

L

Littlefair, Guy, 137
 Liu, F., 13

M

Mahdy, A.A., 297
 MA, Ninshu, 119
 Martin, Jonathan Peter, 99
 McDonnell, Martin, 67
 Miles, M.P., 13
 Mishra, M.K., 289
 Mitsufuji, Kenta, 311
 Miyamori, Tomoko, 23
 Miyasaka, Fumikazu, 311
 Moriguchi, Hideki, 47
 Murakawa, Hidekazu, 119

N

Nadeau, François, 197
 Nakazawa, Tatsuya, 29
 Nambu, Masahito, 311
 Nelson, T.W., 13
 Nielsen, Isak, 249

O

Okada, Hideki, 237
 Omori, Toshihiro, 29

P

Parningotan, D., 157
 Pasang, T., 157
 Pietras, Adam, 167
 Prabhu, N., 53, 289

R

Rao, A.G., 289
 Refat, M., 297
 Regensburg, Anna, 211, 277
 Reza-E-Rabby, Md., 67
 Rokni, Reza, 221

Ross, Ken, 39, 67, 269
 Ruokolainen, Robert, 147

S

Sakairi, Koichi, 29
 Sato, Yutaka S., 23, 29, 47
 Schürer, René, 211, 277
 Sheed, Digvijay, 53
 Shibata, Akinori, 47
 Singh, R.K.P., 53
 Steinberg, Helmut, 211
 Straß, Benjamin, 179
 Strauss, Alvin M., 79, 91
 Sun, Xin, 261
 Sun, Yufeng, 119
 Susukida, Shinichi, 47
 Sutton, Ben, 39

T

Takida, Tomohiro, 47
 Tanaka, Kunihiro, 29
 Tarrant, M., 157
 Thomä, Marco, 179
 Tsuji, Ayuri, 47
 Tsutsumi, Seiichiro, 119

U

Upadhyay, Piyush, 125, 147, 261

W

Wagner, Guntram, 179
 Wang, Xiaoming, 137
 Węglowska, Aleksanda, 167
 West, Michael K., 3, 221
 Whalen, Scott, 67
 Widener, Christian A., 3, 221
 Wolter, Bernd, 179

Y

Yan, David P., 137
 Yeshiambel, Michael, 237

Z

Zhang, Jingyi, 125

Subject Index

A

AA2024, 297, 299, 301, 302, 306, 308
AA6022, 151, 154
AA7075, 126, 129, 198, 199, 202, 206, 208,
297, 300, 302–304, 306–308
AA7075-T6, 109, 110, 116
Aerospace aluminum alloys, 237
Aluminum, 67, 68, 70, 72, 76, 79, 80, 82, 86,
88, 109, 110, 114, 116
6061 aluminum alloy, 138
Aluminum alloys, 277, 279, 285
Aluminum to steel joining, 155
Automatic control, 259, 260

C

Carbon steel, 23, 24, 27
Cold spray, 222, 224, 225, 227–229, 231–234
Copper, 250, 253
Corrosion, 126, 127, 129, 132, 134, 180, 181,
186, 187, 191, 192
Crack healing, 16, 17

D

Discrete Element Method (DEM), 311, 312,
316, 319
Dissimilar joints, 212, 215
Dissimilar metal joining, 223, 228, 233
Dissimilar metals, 1, 2, 6, 68, 168, 180, 186
Donor/Acceptor density, 294

E

Electrical contacts, 212
Electron Backscatter Diffraction (EBSD), 127,
128, 131
Eutectic reaction, 215
EXCO, 125, 127, 132

F

Force control, 269, 271–274

Friction stir, 39, 40, 45, 270, 273
Friction Stir Dovetailing (FSD), 67–69, 71–73,
76
Friction Stir Extrusion (FSE), 1, 2
Friction stir lap welding (FSLW), 157–162,
164, 165
Friction Stir Processing (FSP), 13–15, 54–57,
61, 62, 79, 290–292, 295, 297, 298, 301,
306, 308
Friction Stir Scribe (FSS), 148, 150, 154
Friction stir scribe joining, 262
Friction stir spot joining, 211, 219
Friction Stir Spot Welding (FSSW), 29, 30,
32–34
Friction Stir Welding (FSW), 1, 2, 4, 6–8, 23,
24, 26, 27, 47, 48, 51, 52, 67–69, 80, 100,
101, 104–112, 114, 117, 125, 126, 130,
138, 139, 142, 148–150, 152, 155, 168,
170, 172–175, 179, 180, 182, 198, 199,
204, 208, 222, 225, 228, 232, 233, 250,
252, 277, 279, 280, 311, 312, 315, 316, 319

H

Hot stamping, 198, 208

I

Iridium (Ir), 30, 35

J

Joining, 80, 81

L

Lap joints, 109, 111, 112, 114, 117
Low carbon steel, 2
304L stainless steel, 13–16

M

Maraging steel, 3, 4, 6
Material flow, 167, 168, 171–173, 175, 176

Mesh free method, 314
Microstructure, 54, 55, 57, 59, 62, 125, 127,
128, 130, 134
Mild steel, 150, 151, 154
Modeling, 170

N

Nano-surface composite, 301
New techniques, 101
Ni-base superalloy, 31
Nondestructive testing, 193

P

Potentiodynamic polarization, 291, 292, 295
Process control, 270
Process forces, 278, 279, 283, 284
Process parameter, 54, 55

R

Refill Friction Stir Spot Joining (RFSJ),
237–239, 242, 243
Repair, 40, 44–46
Robotic spot welding, 237
Rolled Homogeneous Armor (RHA), 67, 68,
70, 72, 76

S

Scaling effects, 278, 284

Scroll tool, 137, 138, 142
SEM, 127–129, 134
Sensitization, 40, 44, 45
Shoulder zone flow patterns, 139, 142
Stainless steel, 48, 52
Stranded wire, 211, 219
Stress Corrosion Cracking (SCC), 39–43, 45
Surfalex 6s, 149, 153

T

Tailor welded blanks, 198
Temperature control, 40, 43, 269–271, 273,
274
Thick section, 99, 100, 103, 108
Ti-6Al-4V alloy, 54–57
Titanium, 79, 80, 82, 85, 86, 88
Transition joint, 1, 2, 6, 225, 226, 233
Tungsten-based alloy, 48–50, 52

U

Ultrasonic welding, 211
Ultrasound enhancement, 180, 182, 184, 186
Underwater operation, 23
Usibor, 150, 153

W

Welding tool, 29, 30, 48
W-Re pin tool, 4, 7